



**HAL**  
open science

# Méthodologie instrumentale à l'échelle atomique pour une meilleure compréhension des mécanismes de ségrégation intergranulaire dans les aciers : application au phosphore.

Alfia Akhatova

## ► To cite this version:

Alfia Akhatova. Méthodologie instrumentale à l'échelle atomique pour une meilleure compréhension des mécanismes de ségrégation intergranulaire dans les aciers : application au phosphore.. Science des matériaux [cond-mat.mtrl-sci]. Normandie Université, 2017. Français. NNT : 2017NORMR131 . tel-01767494

**HAL Id: tel-01767494**

**<https://theses.hal.science/tel-01767494>**

Submitted on 16 Apr 2018

**HAL** is a multi-disciplinary open access archive for the deposit and dissemination of scientific research documents, whether they are published or not. The documents may come from teaching and research institutions in France or abroad, or from public or private research centers.

L'archive ouverte pluridisciplinaire **HAL**, est destinée au dépôt et à la diffusion de documents scientifiques de niveau recherche, publiés ou non, émanant des établissements d'enseignement et de recherche français ou étrangers, des laboratoires publics ou privés.



Normandie Université

## THÈSE

**Pour obtenir le diplôme de doctorat**

**Spécialité: Physique – Sciences des Matériaux**

**Préparée au sein d'Université de Rouen Normandie**

**Méthodologie instrumentale à l'échelle atomique pour une meilleure compréhension des mécanismes de ségrégation intergranulaire dans les aciers : application au phosphore**

**Présentée et soutenue par  
Alfiia AKHATOVA**

**Thèse soutenue publiquement le 20 Decembre 2017  
devant le jury composé de**

M. Frédéric CHRISTIEN	Professeur, MINES – Saint-Étienne	Rapporteur
Mme. Brigitte DECAMPS	Directrice de Recherches, CNRS – Orsay	Rapporteur
M. Eric van WALLE	Professeur, SCK•CEN – Mol, Belgium	Président
Mme. Marta SERRANO	Directrice de Recherches, CIEMAT – Madrid, Espagne	Examineur
M. Bertrand RADIGUET	Maître de conférences, GPM – Rouen	Encadrant de thèse
M. Philippe PAREIGE	Professeur, GPM – Rouen	Directeur de thèse
M. Laurent LEGRAS	Ingénieur Chercheur, EDF – Les Renardières	Invité

**Thèse dirigée par Pr. Philippe PAREIGE, co-encadrée par Dr. Bertrand RADIGUET**

**Groupe de Physique des Matériaux**

**UMR CNRS 6634 – Université de Rouen Normandie**





This thesis is dedicated to my uncle Alfir



## Acknowledgement

Completion of this PhD thesis was possible with the support of several people. I would like to express my sincere gratitude to all of them. First and foremost, I wish to thank my supervisors, Prof. Philippe Pareige and Dr. Bertrand Radiguet. You have created the invaluable space for me to do this research and develop myself as a researcher in the best possible way. I greatly appreciate the freedom you have given me to find my own path and the guidance and support you offered at key moments in my work.

I sincerely thank my thesis committee: Prof. Eric van Walle, Prof. Frédéric Christien, Dr. Brigitte Decamps, Dr. Marta Serrano, Dr. Laurent Legras. Thank you for investing time and providing interesting and valuable feedback. I feel proud and honoured that you have accepted to be on my committee. I would especially like to thank Prof. Frédéric Christien for his cooperation in comparison of Atom Probe Tomography with Auger Electron Spectroscopy measurements.

I am particularly grateful to Dr. Xavier Sauvage for all the support he has shown me during three years. Thank you very much for welcoming me into the GPM for 5 months internship and for helping me to adjust to new surroundings.

I want to thank my colleagues for the great working environment and friendly atmosphere during all these years. I would like to thank Dr. Emmanuel Cadet and Fabien Cuvilly for their guidance in SEM/FIB/TKD experiments. My grateful thanks are also extended to Dr. Auriane Etienne for her help in doing STEM experiments, to Beatrice Foulon and Charly Vaudolon for their help with preparation of samples, and to David Gibouin and Laurence Chevalier for their great effort on NanoSIMS analysis. I am grateful to Dr. Antoine Vaugeois and Dr. Constantinos Hatzoglou for providing me information related to grain boundaries, using computer simulation.

I want to take a moment and say that I had a lot of fun and pleasure with the best musicians in Rouen: Charly, Fabien, Martin, Aurélien, Jean Baptiste, Tanguy. That was a Rock 'n' Roll, yeah!

My life is so blessed with some of the most amazing people. Thank you for being part of my journey. Special thanks to all my friends: Yana and Sasha, Olha, Begoña, Martin, Gilles, Linda, Arantxa, Mykola, Mohit, Solene, Alexander, Sana for giving me the amazing memories. My friends, you help to make the bad stuff bearable, and the good stuff much more fun. TYFBA – thank you for being so awesome!

I would like to thank my husband Misha for all his love, support and faith in my strengths. You've always found a way to cheer me up and encourage me to do my best. Thanks to you, I have learned to love and accept myself the way I really am.

Last but certainly not least, I would like to thank my uncle Alfir, who raised me with a love of science and supported me in all my pursuits.

## Abbreviations and Acronyms

ASTM	American Society for Testing and Materials
APT	Atom Probe Tomography
AES	Auger Electron Spectroscopy
BSE	Backscattered Electrons
BM	Base Material
BCC	Body Centered Cubic
BF	Bright Field
CGHAZ	Coarse Grain Heat Affected Zone
CSL	Coincidence Site Lattice
CEA	Commissariat à l'énergie Atomique
CL	Core-Loss
DF	Dark Field
DoF	Degrees of Freedom
DFT	Density Functional Theory
DTE	Displacement Threshold Energy
dpa	displacements per atom
DBTT	Ductile-to-Brittle Transition Temperature
EBSD	Electron Backscatter Diffraction Analysis
EELS	Electron Energy Loss Spectroscopy
EAM	Embedded-Atom Method
EDX/EDS	Energy-Dispersive X-ray spectroscopy
EMIR	Réseau National d'accélérateurs pour l'Etudes des Matériaux sous IRradiation
EAEC	European Atomic Energy Community
FS	Finnis-Sinclair
FIB	Focused Ion Beam
GIS	Gas Injection System
GB	Grain Boundary
GPM	Groupe de Physique des Matériaux
HAZ	Heat Affected Zone
HAADF	High Angle Annular Dark Field

HAGB	High-Angle Grain Boundary
IPF	Inverse Pole Figure
IGF	Intergranular Fracture
JANNuS	Joint Accelerators for Nanoscience and Nuclear Simulation
LWR	Light Water Reactor
LEAP	Local Electrode Atom Probe
LAGB	Low-Angle Grain Boundary
LL	Low-Loss
MTR	Materials Test Reactors
MD	Molecular Dynamics
NRT	Norgett, Robinson and Torrens
OES	Optical Emission Spectrometry
PISA	Phosphorus Influence on Steel Ageing
PWHT	Post Weld Heat Treatment
PE	Primary Electrons
PKA	Primary Knock-on Atom
PWR	Pressurized Water Reactor
QA	Quasi particle Approach
RES	Radiation Enhanced Segregation
RIS	Radiation Induced Segregation
RPV	Reactor Pressure Vessel
RIS	Radiation-Induced Segregation
SEM	Scanning Electron Microscopy
STEM	Scanning Transmission Electron Microscopy
SE	Secondary Electrons
SIA	Self-Interstitial Atom
SRHT	Stress Relieve Heat Treatment
SRIM	Stopping and Range of Ions in Matter
SAW	Submerged Arc Welded
TKD	Transmission Kikuchi Diffraction
VASP	Vienna Ab initio Simulation Package
WM	Weld Metal

XPS	X-ray Photoelectron Spectroscopy
ZL	Zero-Loss
ZLP	Zero-Loss Peak



# Table of Contents

Introduction .....	1
Chapter 1. Bibliography .....	3
1.1    Description of reactor pressure vessel (RPV) .....	4
1.1.1    French RPV materials and their fabrication .....	4
1.1.2    Service condition: actual and test reactors .....	6
1.1.3    Effect of irradiation on mechanical properties of RPV steel .....	7
1.1.4    Effect of phosphorus in RPV steel .....	8
1.2    Point defects production and their interaction with solutes .....	13
1.2.1    Primary radiation damage .....	13
1.2.2    Point-defect – impurity complexes .....	18
1.2.3    Radiation induced segregation .....	22
1.3    Grain-boundary structure and segregation behavior .....	25
1.3.1    Crystallography of grain boundaries .....	25
1.3.2    GB structure and GB energy .....	28
Conclusion.....	32
References .....	33
Chapter 2. Material and experimental techniques .....	42
2.1    Materials: model alloy.....	43
2.1.1    Elaboration .....	43
2.1.2    Thermal aging .....	46
2.1.3    Ion irradiation.....	47
2.2    Atom probe tomography .....	48
2.2.1    Principle of atom probe tomography.....	49
2.2.2    Experimental conditions.....	51
2.2.3    Optimization of reconstruction parameters .....	52
2.2.4    Measurement of grain boundary composition.....	56
2.3    Analytical electron microscopy.....	63
2.3.1    Principle of imaging on STEM mode .....	63
2.3.2    Two beam conditions .....	64
2.3.3    Electron energy-loss spectroscopy .....	65

2.3.4	Energy dispersive X-ray spectroscopy .....	67
2.4	Scanning electron microscopy .....	70
2.4.1	Principle of SEM imaging.....	70
2.4.2	Focused ion beam and gas injection system.....	71
2.4.3	Electron Backscatter Diffraction and Transmission Kikuchi Diffraction.....	73
2.4.4	Site-specific sample preparation .....	74
2.4.5	Determination of grain boundary nature from APT and TKD techniques.....	77
	Conclusion.....	81
	References .....	82
Chapter 3.	Equilibrium grain boundary segregation in Fe-P-C alloy .....	87
3.1	APT measurement of equilibrium grain boundary segregation .....	89
3.2	Comparison of Auger Electron Spectroscopy with Atom Probe measurement of phosphorus grain boundary segregation .....	92
3.2.1	Principle of Auger electron spectroscopy .....	92
3.2.2	AES and APT measurements of GB concentration .....	95
3.3	Modelling of equilibrium grain boundary segregation .....	99
3.3.1	The theories of grain boundary segregation.....	99
3.3.2	Kinetics of grain boundary segregation .....	107
3.3.3	Position of phosphorus atoms in the GB core and their interaction with carbon atoms .....	110
3.3.4	Modeling versus experiments and discussion .....	113
	Conclusions .....	120
	References .....	122
Chapter 4.	Solute segregation under ion irradiation in Fe-P-C model alloy .....	127
4.1	Radiation-induced segregation related to the grain boundary structure.....	128
4.1.1	Phosphorus segregation as a function of irradiation depth .....	128
4.1.2	Radiation-induced segregation at grain boundaries .....	130
4.1.3	Intragranular segregation and precipitation of phosphorus atoms.....	134
4.2	Modeling of radiation induced grain boundary segregation .....	137
4.2.1	Radiation-induced segregation.....	138
4.2.2	Thermal equilibrium segregation under irradiation temperature .....	142

4.2.3	Comparison of experimental and theoretical results .....	143
4.3	Discussion .....	147
	Conclusion.....	152
	References .....	153
	Conclusion and Perspectives .....	160
	Appendices .....	166
	Appendix 1. Field evaporation model .....	166
	Appendix 2: Nanoscale secondary ion mass spectrometry .....	168
	References .....	171



# Introduction

The vessel is an important barrier between the nuclear reactor core and the near environment in a Nuclear Power Plant. The exposure to irradiation and long term thermal ageing can promote the segregation of phosphorus to grain boundaries (GBs) in vessel steels. This, in turn, reduces the cohesive energy of GBs and leads to a much higher ductile-to-brittle transition temperature (DBTT), determined by Charpy V-notched impact tests. For the purpose of safe nuclear power plant operation, it is necessary to gain a fundamental understanding of the role of phosphorus in irradiation embrittlement.

In the past few decades, the effect of phosphorus segregation on the embrittlement of vessel steel has been extensively studied. The phosphorus intergranular segregation was found to be linearly related to the percentage of intergranular failure and the increase of DBTT. However, very few studies focus on the dependence between the segregation intensity and the GB nature. This remains an open question often ignored in the literature, whereas the intergranular segregation value may strongly vary from one GB to another.

This study aims to describe the influence of irradiation and thermal ageing conditions and GB nature on the intergranular phosphorus segregation in a Fe-P-C model alloy. Separate examinations of the model alloy after thermal and irradiation ageing are intended to allow better differentiation between thermal and radiation-induced/enhanced segregations in irradiated material. For an effective investigation of the mechanisms of intergranular segregation it is necessary to develop a methodology which combines complementary techniques giving an accurate and representative description of GBs before and after ageing. This is the first objective of this thesis. The second one is to apply the approach developed to the study of the influence of ageing conditions and GB geometry on intergranular segregation in model alloys thermally aged or ion irradiated. The third one is to investigate the mechanisms of equilibrium and non-equilibrium segregation of phosphorus to GBs to improve the predictability of irradiation embrittlement in reactor pressure vessel (RPV) steel.

The document is divided in four chapters. The first chapter gives a brief description of the RPV fabrication and operation conditions of French pressurized water reactors (PWRs). A review of experimental observations and theoretical works was undertaken to highlight the phosphorous behavior in irradiated materials and the effect of phosphorus on mechanical properties of low alloyed steels.

The second chapter illustrates physical principles of the experimental techniques extensively used in this work, namely: Atom Probe Tomography (APT), Electron Backscatter Diffraction Analysis (EBSD), Transmission Kikuchi Diffraction (TKD), Scanning Electron Microscopy / Focused Ion Beam (SEM/FIB) and Energy-Dispersive X-ray spectroscopy (EDX). Also, the method used to identify the five crystallographic degrees of freedom that define a GB, using correlative TKD and APT is described in details.

The third chapter presents the study of equilibrium GB segregation of phosphorus and carbon atoms after stresses relieve heat treatment and after thermal ageing at the temperature of irradiation. These experimental results are important to separate the different origins of phosphorus GB segregation in irradiated material.

The fourth chapter reports on the characterization of intergranular segregation after self-ion irradiation of Fe-P-C model alloy at three different doses and its possible relationship with GB geometry. An experimental evidence of the relation between the GB plane orientation and phosphorus GB segregation is provided. In order to gain a better understanding of the mechanism of intergranular segregation, Faulkner's radiation-induced segregation model for dilute alloys is applied. At the end a general conclusion and perspectives for future work are given.

## Chapter 1. Bibliography

Reactor Pressure Vessel (RPV) is an important barrier between the nuclear reactor core and environment, its integrity defines the operation time of the entire nuclear power plant. The 16MND5 steel is a key material used for the fabrication of French RPVs. In the past 40 years, the 16MND5 steel has been extensively studied to understand the factors with respect to the mechanical properties degradation, e.g. the ductile-to-brittle transition temperature shift to higher values. In this field, the segregation of impurities, more specifically phosphorus, at grain boundaries are known to favor the intergranular embrittlement of RPVs.

In the first part of the current chapter, the in service reactor vessel conditions and their effects on mechanical properties evolution of the steel are described.

The second section focuses on the microstructural changes occurring in  $\alpha$ -Fe alloys under ion irradiation, simplified representation of the vessel steel under service condition. Computer simulation is a powerful tool for understanding the primary defect formation, single defects and complexes migration as well as the interaction of solute atoms with point defects. Attention will be paid here to the mobility of phosphorus atoms and the effect of the conditions of irradiation on that mobility.

Besides of irradiation conditions (temperature, dose, dose rate), intergranular segregation under irradiation depends on GB structure. The definition of GB crystallography and its influence to the GB segregation level is discussed in the third part of this chapter.

## 1.1 Description of reactor pressure vessel (RPV)

### 1.1.1 French RPV materials and their fabrication

Nuclear energy is the main source of energy for electricity production in France: 58 nuclear power plants produce 72.3% of the electricity in the country [1]. All of them are Pressurized Water Reactors (PWRs), one of three types of Light Water Reactor (LWR). In a PWR, the water in primary loop is pumped under high pressure to the reactor core and heated up to 300-350°C by nuclear fission energy. The core is enclosed in a large container called Reactor Pressure Vessel (RPV). Then the primary heated water transfers the thermal energy to a not-pressurized water loop in order to generate steam, which is then injected in a steam turbine and drives an electrical generator (Fig. 1.1) [2].

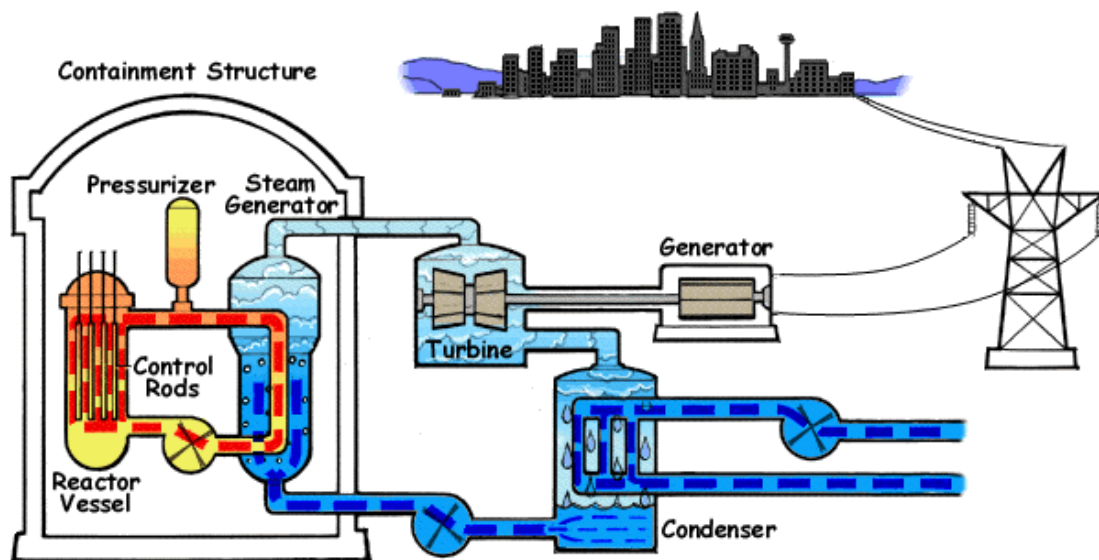
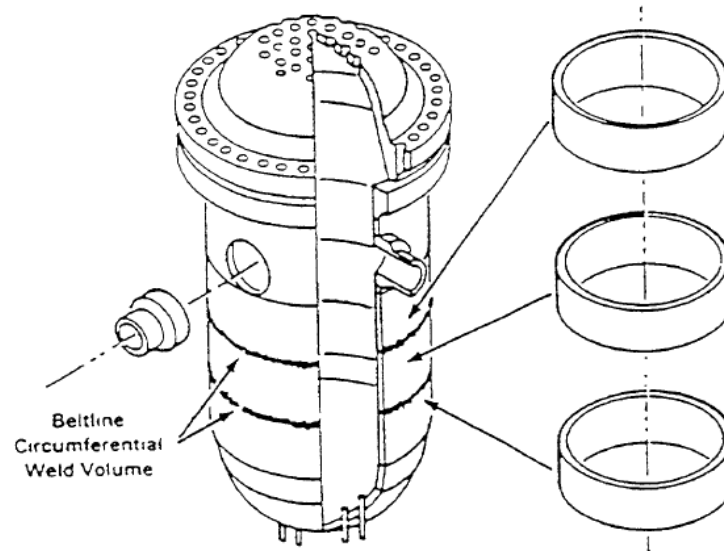


Fig. 1.1. Schematic presentation of Pressurized Water Reactor [3]

The RPV is the most important part of PWR, and it determines the lifespan of the whole nuclear power plant. The RPV is a large and heavy component, which is practically irreplaceable and must remain completely safe under conditions of high pressure, temperature and irradiation.

Western-type RPV (Fig. 1.2.) has a cylindrical body with a hemispherical bottom head and a flanged and gasketed upper head. The bottom head is welded to the cylindrical shell while the top head is bolted to the cylindrical shell via the flanges. The body of the vessel is manufactured by submerged-arc welding of ring forging sections. To protect the inner surface in contact with the coolant water from corrosion, a 3 to 10 mm thick clad of austenitic

stainless steel, usually type 308 or 309, is deposited [4]. During its fabrication, the RPV undergoes non-destructive tests and is submitted to a hydrostatic pressure test above operating limit. During the nuclear power plant operation, the RPV is subjected to exhaustive periodic in-service inspection, including material radiation damage evaluation via the surveillance program [4].



**Fig. 1.2.** Schematic illustration of Western-type RPV [4]

The French RPVs are designed by Framatome and manufactured by Creusot-Loire. The PWR RPV design pressure is about 17 MPa and the operating pressure is about 15.5 MPa. The design temperature is 343°C, while the operating temperature is typically 280–325 °C [5,6].

The material of French RPV core is a low alloyed 16MND5 steel (equivalent to SA 508 Class 3). The chemical requirements for this material are given in Table 1.1. The heat treatment and minimum material properties for 16MND5 are listed in Table 1.2.

**Table 1.1.** Chemical requirements for 16MND5 RCC-M 2111 forging for reactor core region [4]

Elements	C	Si	Mn	P	S	Cr	Mo	Ni	V	Cu	Al
wt %	max	0.10	1.15	max	max	max	0.43	0.50	max	max	max
	0.20	0.30	1.55	0.008	0.008	0.25	0.57	0.80	0.01	0.20	0.04
at %	max	0.20	1.16	max	max	max	0.24	0.48	max	max	max
	0.92	0.60	1.57	0.014	0.014	0.27	0.33	0.77	0.01	0.18	0.08

**Table 1.2.** Heat treatment and minimum material properties for 16MND5 [4]

Austenitization	850-925°C
Tempering	635-668°C
Stress relief	600-630°C
Yield stress at 20°C	> 400 MPa
Tensile strength at 20°C	550-670 MPa
Total elongation at 20°C	> 20%

High concentrations of copper, nickel and phosphorus in the beltline region can have a strong effect on radiation sensitivity of RPV steels. The contribution of other elements such as molybdenum, manganese and chromium to the radiation induced degradation of RPV steels are not uniquely identified [6]. Modern RPV steels contain much lower levels of copper and phosphorus, but there are many operating vessels fabricated before the early 1970s [7]. So the question of lifetime extension of PWRs requires the understanding of the mechanisms responsible for embrittlement of RPV steels.

### 1.1.2 Service condition: actual and test reactors

Typical French PWRs operate at temperatures in the range 280-325°C and under a neutron flux about  $6 \times 10^{10} \text{ n/cm}^2/\text{s}$  leading to a fluence close to  $6 \times 10^{19} \text{ n/cm}^2$  ( $E > 1 \text{ MeV}$ ) and a dose about 0.1 dpa for 32 years of full power operation [5].

To understand the radiation and temperature effects on material structure and properties the Materials Test Reactors (MTRs) were designed. The two main types of research reactors in France are:

- Pool reactors, in which the reactor core is immersed in an open water pool, where the water acts as a neutron moderator, cooling agent and radiation shield. This type of disposition has low pressurization of the reactor coolant system, limited power density of the reactor, but provides fast access to the materials;
- Tank reactors with higher pressurization (5-20 bars), and subsequently, higher power density and flux levels, but more difficult access to the analyzed materials.

Depending on selected core configuration, the material can be exposed to low-energy neutrons, so-called “thermal” neutrons ( $E < 0.625 \text{ eV}$ ) or to high-energy “fast” neutrons ( $E > 1 \text{ MeV}$ ). The neutron flux in different research reactors varies from  $10^{13} \text{ n} \cdot \text{cm}^{-2} \cdot \text{s}^{-1}$  to more than  $10^{15} \text{ n} \cdot \text{cm}^{-2} \cdot \text{s}^{-1}$  [8].

### 1.1.3 Effect of irradiation on mechanical properties of RPV steel

The defects created during irradiation (vacancy and interstitial clusters, solute clusters and precipitates, dislocation loops...) act as obstacles to the dislocations glide. Therefore the minimum stress under which a material deforms permanently (yield stress) becomes higher. The increase of yield stress due to the irradiation-induced defects, i.e. irradiation hardening, typically is associated with a decrease of tensile elongation and fracture toughness [5].

The relation between irradiation hardening and the cleavage fracture stress is schematically shown in Fig. 1.3. Two *yield stress-temperature* curves are plotted for irradiated and unirradiated materials and superimposed with *fracture stress-temperature* line. Irradiation strengthening leads to an upward shift of the temperature required to keep the yield stress below the cleavage fracture stress. This temperature is called ductile-to-brittle transition temperature (DBTT) and is determined using standard Charpy impact tests.

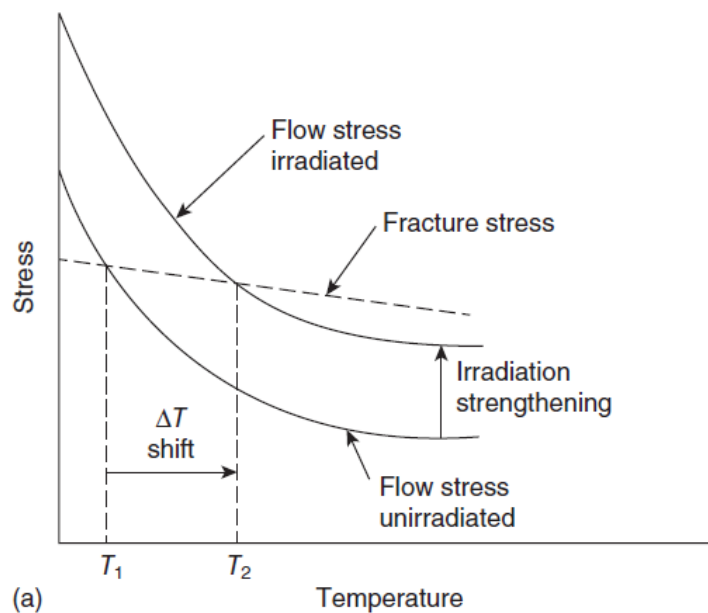


**Fig. 1.3.** Effect of irradiation-induced strengthening on an upward shift in the Charpy impact toughness transition temperature [5].

Apart from the hardening mechanism, the DBTT shift can be caused by intergranular segregation of embrittling elements such as phosphorus. Previous studies have shown appreciable level of phosphorus intergranular segregations on former austenitic grains boundaries of RPV steel irradiated with high values of fast neutrons fluence even at low bulk concentration of phosphorus (below 0.006 wt.%) [9–11].

Despite progress in predicting irradiation embrittlement, the contribution of the non-hardening mechanism is still not clear. Development of a physically reasonable model of

radiation embrittlement requires the understanding of the mechanisms responsible for degradation of properties in materials under irradiation.

### 1.1.4 Effect of phosphorus in RPV steel

The decrease of fracture toughness due to phosphorus intergranular segregation was clearly established for many thermally aged steels [12–16]. For most of them, a linear relationship between the DBTT and the phosphorus grain boundary (GB) concentration was found. For example, Fig. 1.4 shows the empirical relation between the DBTT and GB concentration of phosphorus in a 2.25Cr-1Mn steel doped with phosphorus and isothermally aged at temperatures from 480°C to 650°C [17]. As this relationship is linear, Song et al. suggested to use this graph to predict the DBTT in the 2.25Cr-1Mn steel.

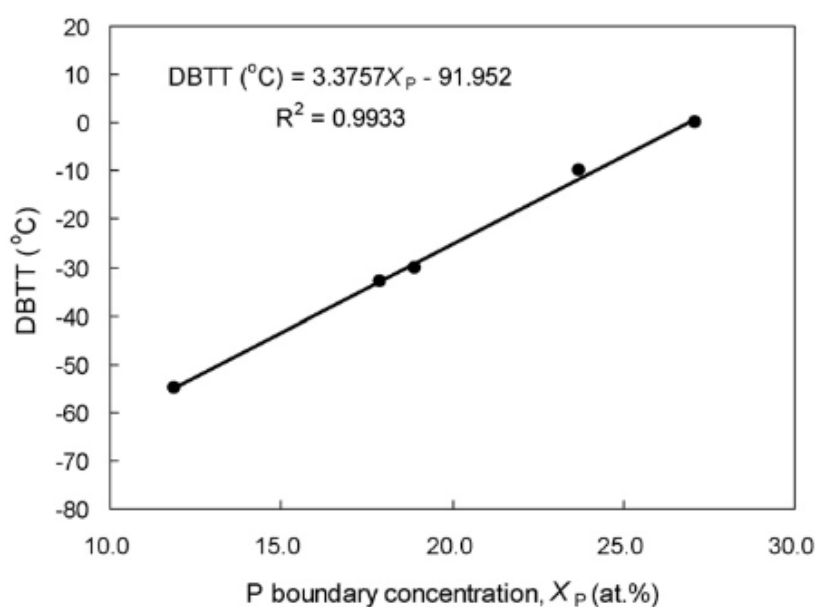


**Fig. 1.4.** Dependence of DBTT to the GB concentration of phosphorus in thermally aged 2.25Cr-1Mn steel [17]

Segregation of phosphorus at GBs makes them brittle, i.e. decreases the cohesive strength of GBs. The explanation of this phenomenon is based on the suggestion that the presence of solute atoms changes the chemical bonding in GB. Hashimoto et al. [18] reported that when phosphorus atoms segregate at the GB of iron the strong bonding orbitals are formed between Fe(3d) and P(3p) orbitals in  $Fe_xP$  clusters, and thus, the metallic bonds between  $Fe_xP$  clusters and surrounding iron atoms are weakened. Wu et al. [19] have studied the charge density distribution at GB and displayed that the polar-covalent P-Fe bonding is weaker in the GB environment; also phosphorus atoms diminish the magnetic polarization in the GB. In the more recent work of Migal et al. [20] it was shown that phosphorus, silicon, sulfur and copper

atoms weaken the bond between grains, since they have lower binding energy with iron than iron atoms with themselves.

Based on previous observations of the phosphorus effect on the temper embrittlement, a similar effect is expected in RPV steels due to the inevitable presence of phosphorus and radiation-enhanced diffusion. According to the literature review given in a technical report of PRW Materials Reliability Project (PWRMRP-2000) [21], segregation of phosphorus at GBs and associated intergranular fracture were observed in all RPV steel zones: base material (BM), weld metal (WM), Heat Affected Zone (HAZ) and Coarse Grain Heat Affected Zone (CGHAZ) (Fig. 1.5). However, studies have shown that the coarse-grain regions of the weld HAZ are more susceptible to GB embrittlement than base metal and other weld zones [22,23].

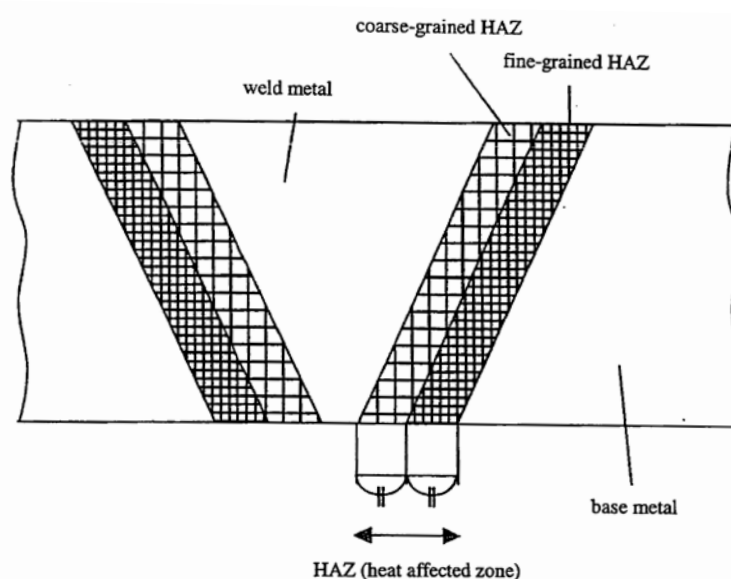


**Fig. 1.5.** Welded zone of RPV: base material, weld metal, Heat Affected Zone (HAZ)[24]

Most studies of phosphorus segregation on HAZs has been done using simulated HAZ and Auger Electron Spectroscopy (AES), therefore the results may deviate from that of the real HAZ where more complexity is expected. Druce et al. [22] have simulated the structure of CGHAZ by austenitization of base material at 1000-1300°C with subsequently post-weld heat-treatment (PWHT) at 600-650°C. To follow the evolution of GB chemistry under RPV operation condition, the materials were thermally aged in the temperature range 300-500°C. The quantification of GB concentration was performed by AES.

The embrittlement of different RPV steels as a function of phosphorus segregation is shown in Fig. 1.6. Fig. 1.6a presents the DBTT shift as a function of the phosphorus peak height ratio measured by AES for simulated CGHAZ in A533esB Class 1 steel (bulk

phosphorus 50 wt ppm) in the range of temperatures from 300°C to 500°C. It clearly appears that the DBTT shift is proportional to the phosphorus segregation level.

A similar dependence was observed for CGHAZ from 235-mm thick PWR submerged-arc weldment in an A508 Class 3 ring forging (bulk phosphorus 60 wt ppm) after ageing in the temperature range 325°C-525°C until 20000 hours (Fig. 1.6b) [25]. The scatter in data for the material from real HAZ material (Fig. 1.6b) is larger than for simulated one (Fig. 1.6a) due to variations in the microstructure of the samples.

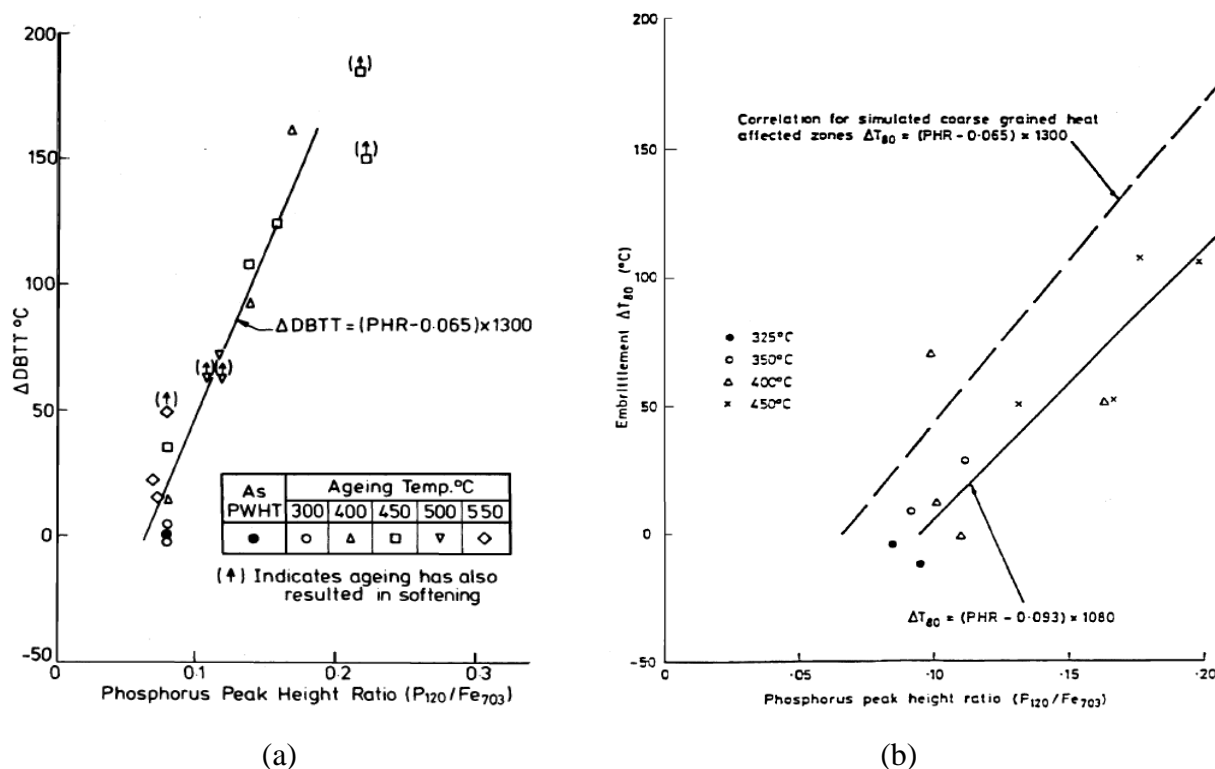


**Fig. 1.6.** DBTT shift as a function of phosphorus segregation in (a) simulated CGHAZ of A533B [22], (b) CGHAZ of A508 welds [25]

Thus, it is possible to conclude that the increasing of intergranular phosphorus segregation under temperature and irradiation exposure leads to DBTT shift towards higher temperatures.

However, understanding the behavior of phosphorus in irradiated materials becomes more complicated due to the parallel irradiation-induced processes such as hardening-effect of defect clusters and solute-rich clusters. During irradiation (heavy ions, neutrons) solutes, including phosphorus, can form precipitates and clusters in the iron matrix. These clusters work as obstacles for the dislocation movement [26].

Nishiyama and co-workers [27] have studied phosphorus doped A533B steels irradiated by neutrons with energy  $> 1$  MeV in a range of neutron fluence from  $2.3$  to  $12 \times 10^{23}$   $neutron \cdot m^{-2}$  at 290°C. The minimum of phosphorus content (130 ppm) is in the steel

called PB, the maximum phosphorus concentration (570 ppm) is in PH steel (Fig. 1.7a). The Charpy impact tests along with AES measurements revealed the linear dependence of DBTT from intergranular phosphorus segregation (Fig. 1.7a).

The linear correlation between DBTT and irradiation hardening (Fig. 1.7b) indicates that an embrittling effect of phosphorus is associated with the hardening mechanism, except for PH steel, which reveals the higher DBTT shift at the same irradiation condition than others. This means that non-hardening mechanism of embrittlement, caused by intergranular segregation of phosphorus was observed only in high-phosphorus (570 ppm) containing steel irradiated to high neutron fluence ( $2.6 \times 10^{23} \text{ nm}^{-2}$ ).

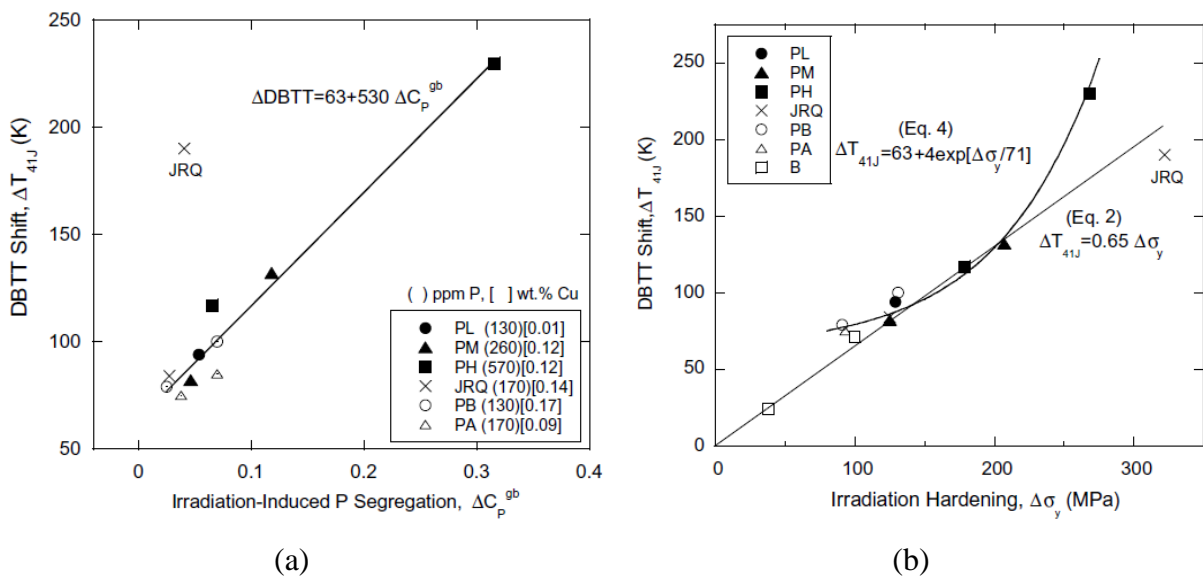


**Fig. 1.7.** Relationships between (a) Charpy DBTT shift and radiation-induced phosphorus segregation at GBs for various steel, (b) Charpy DBTT shift and irradiation hardening for various steel[27]

The European Atomic Energy Community (EAEC) program of Phosphorus Influence on Steel Ageing (PISA) [28,29] has investigated the effect of irradiation ageing on simulated CGHAZ materials of three model steels based on LWR RPV A533B with varying phosphorus content (maximum 0.017 wt% P). The simulated CGHAZ microstructure was obtained by heat-treatment at 1200°C for 30 minutes, followed by oil quenching and subsequent post-weld heat treatment (PWHT) for 25 hours at 615°C. After PWHT, model alloys were aged for 2000 hours at 450°C. The characteristics of all three alloys in as-PWHT and aged conditions are shown in Table 1.3.

The thermal ageing increases both intergranular fracture (IGF) content and phosphorus GB segregation level. In the model steel containing 0.007 wt.% phosphorus, the proportion of

IGF and GB phosphorus were found to be the lowest in both as-PWHT and aged condition. The DBTT shift is also much greater in the two higher phosphorus containing alloys.

**Table 1.3.** Intergranular fracture (IGF) content, GB phosphorus segregation and DBTT shift measured in thermally aged JPC, JPB and JPG model alloys

Alloy	IGF content (%)		P segregation (monolayer)		Embrittlement $\Delta$ DBTT ( $^{\circ}$ C)
	As-PWHT	Aged	As-PWHT	Aged	
JPC (0.007 wt.% P)	8	86	<0.05	0.15	118
JPB (0.017 wt.% P)	35	98	0.10	0.35	174
JPG (0.017P/0.16Cu)	20	96	0.08	0.35	209

Also, as-PWHT and aged alloys were subjected to irradiation at approximately  $290^{\circ}$ C to doses 17.4, 7.3, and 11.5 mdpa for steels JPC, JPB and JPG, respectively. The irradiation promoted an increase of both the IGF content and GB phosphorus concentration in both as-PWHT and aged alloys. Authors have shown that experimental results can be fitted by McLean model for segregation kinetics (Fig. 1.8).

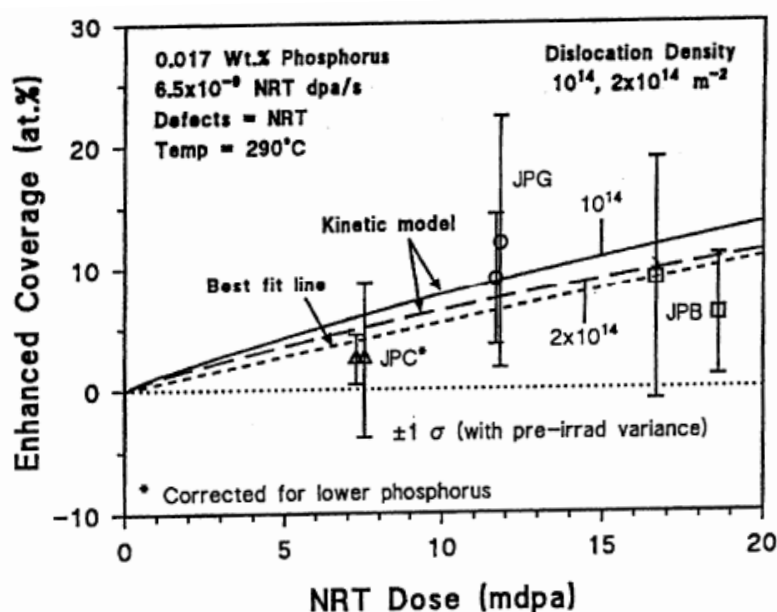


**Fig. 1.8.** Comparison of experimental measurement of GB phosphorus segregation in model alloys after irradiation with kinetic model [29]

As a summary of the aforesaid information, it is possible to assert that the increasing of intergranular phosphorus segregation under temperature and irradiation ageing leads to increasing of intergranular fracture percentage in RPV steels.

However, embrittlement of CGHAZ through phosphorus segregation during irradiation requires further work. It is necessary to undertake additional experiments and do modeling to clarify three important points. First of all, at which conditions the intergranular fracture becomes the dominant fracture mechanism? Further what is the influence of primary heat treatment and HAZ macrostructure? And the last one, what is the effect of GB structure to the segregation level? The answers to specified questions are needed for prediction of embrittlement of RPV under operation. In the current work, we focus on the effect of GB structure to the segregation level.

## 1.2 Point defects production and their interaction with solutes

Radiation-induced segregation (RIS) is a kinetic process controlled by fluxes of vacancy and interstitial point defects towards point defect sinks such as grain boundaries, dislocations and voids [30–33]. As a consequence, it is necessary to describe the formation of point defects under irradiation and their interaction with solutes.

### 1.2.1 Primary radiation damage

Radiation damage in metals and alloys occurs as a result of displacement of atoms from their lattice site (Fig. 1.9). In the first step, an incident particle (neutron from nuclear disintegration or ion in a case of ion irradiation) interacts with a target lattice atom. If the kinetic energy transmitted to the target atom (the primary knock-on atom - PKA) exceeds a critical value, called the threshold displacement energy, a Frenkel pair is formed.

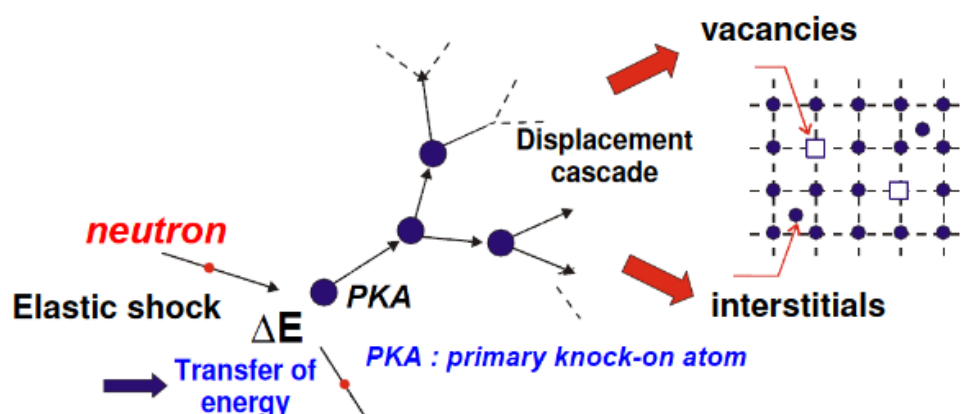
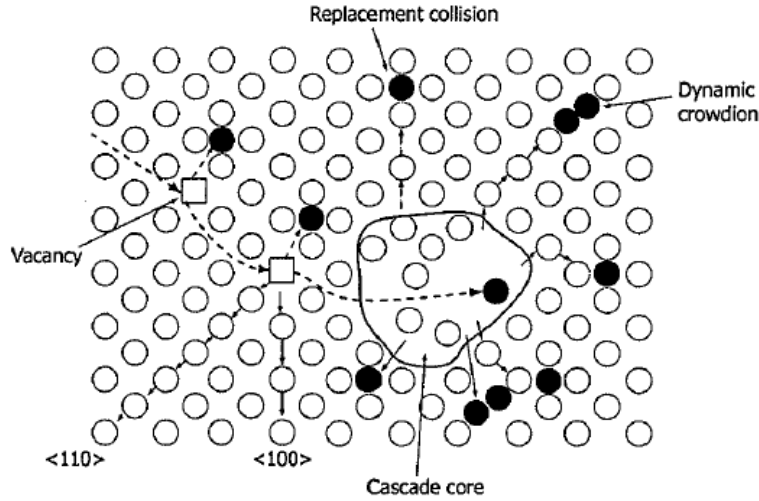


Fig. 1.9. Schematic view of displacement cascade formation after impact of a neutron or a heavy ion [34]

If the kinetic energy of PKA is high enough, it becomes a projectile itself and can cause new displacements. This phenomenon is called a displacement cascade. The displacement cascade has a dimension in the order of a few tens cubic nanometers and more or less consists of vacancies and small vacancy clusters in the core and self-interstitial atoms (SIAs) and small SIA clusters around [35] (Fig. 1.10). Above a certain energy (30-50 keV), the cascade breaks up into separated subcascades [36].



**Fig. 1.10.** Schematic representation of a displacement cascade: white circles are atoms in lattice position, white squares are vacancies and black circles are self-interstitial atoms [39]

The radiation damage is characterized by the number of *displacements per atom*. It is the average number of times that an atom is displaced from its lattice site due to ballistic collisions [37]. The number of displaced atoms is usually estimated using the Kinchin-Pease [38] model:

$$\begin{aligned}
 N_d &= 0 & T_d < E_d \\
 N_d &= 1 & E_d \leq T_d < 2E_d \\
 N_d &= \frac{T_d}{2E_d} & T_d \geq 2E_d
 \end{aligned} \tag{1}$$

where  $N_d$  is the number of displaced atoms or vacancy-interstitial pairs,  $T_d$  is the kinetic energy of the PKA and  $E_d$  is the displacement threshold energy.

Later Norgett, Robinson and Torrens (NRT) proposed modification to the Kinchin and Pease model [38] in order to take into account the energy used for electronic excitation. According to the NRT model, the number of displacements produced per PKA,  $\nu_{NRT}$ , is given by:

$$\nu_{NRT} = 0.8 E_{PKA}/2E_d \tag{2}$$

where  $E_{PKA}$  is the kinetic energy of PKA considering the energy lost by electron excitation (i.e. the PKA energy available to produce displacements) and  $E_d$  is the threshold energy. The factor 0.8 was determined from binary collision models to account for realistic (i.e. not hard sphere) scattering. The NRT model is generally accepted as the international standard to evaluate the displacement rate [40].

According to the American Society for Testing and Materials (ASTM) standard [41], an energy transfer of 40 eV is required to displace an iron atom from its lattice position. This value and modified Kinchin-Pease model of displacement cascade have been used for the SRIM simulation in the current research. However, recently published Density Functional Theory Molecular Dynamics (DFT-MD) study of Olsson et al. [42] provided a significantly lower average value of displacement threshold energy (DTE) in iron, closer to 30 eV. The discrepancy was explained by the approximation of the interatomic forces that have been previously applied to calculate the standard value of DTE and by the stronger localization of the defects (crowdion and vacancy) along high-symmetry directions as predicted by DFT-MD.

The second issue with NRT displacement model is that the retained point defect concentration is not equal to the calculated dpa value. The atomic configuration in a displacement cascade is not stable: indeed both SIAs and vacancies are mobile at irradiation temperature. Due to the high mobility and small distances between SIAs and vacancies in the displacement cascades a large fraction of them is annihilated by mutual recombination. The fraction of defects that survive after intracascade recombination is about 0.04 for 1 MeV heavy ion irradiation [37].

The point defect surviving after recombination can migrate, create clusters, trap impurities and contribute to the radiation-enhanced diffusion. Over the last few decades, stability and mobility of vacancies and SIAs have been extensively studied by ab initio techniques. With regards to the experimental work, it was noted that the reliable experimental values for point defect formation and migration are difficult to obtain due to the phase transition and magnetism [43].

The values of vacancy formation energy,  $E_V^f$ , given in literature lie within a range 1.4 to 2.14 eV, and the migration energy of single vacancy,  $E_V^m$ , for the nearest neighbor jump, from 0.11 to 1.45 eV depending on the interatomic potential and vacancy formation energies [43,44]. As reported by Domain et al. [45] this data scattering is due to the difficulty to obtain very pure Fe crystals. The impurities in an iron matrix can trap the vacancies and decrease the

vacancy diffusion coefficient. This suggestion is supported by the fact, that much smaller experimental value of about 0.55 eV was measured for high-purity  $\alpha$ -Fe [46]. Thus, for prediction of defect kinetics in Fe-P-C alloy the high vacancy migration energy is used.

The five main configuration of SIA in bcc iron are schematically shown in Fig. 1.11:  $\langle 110 \rangle$  and  $\langle 100 \rangle$  dumbbells,  $\langle 111 \rangle$  crowdion, tetrahedral and octahedral. The majority of authors calculating the SIA formation energies agree on the fact that the most stable configuration of SIA in bcc iron is the  $\langle 110 \rangle$  dumbbell [45,47–49] (Fig. 1.11a).

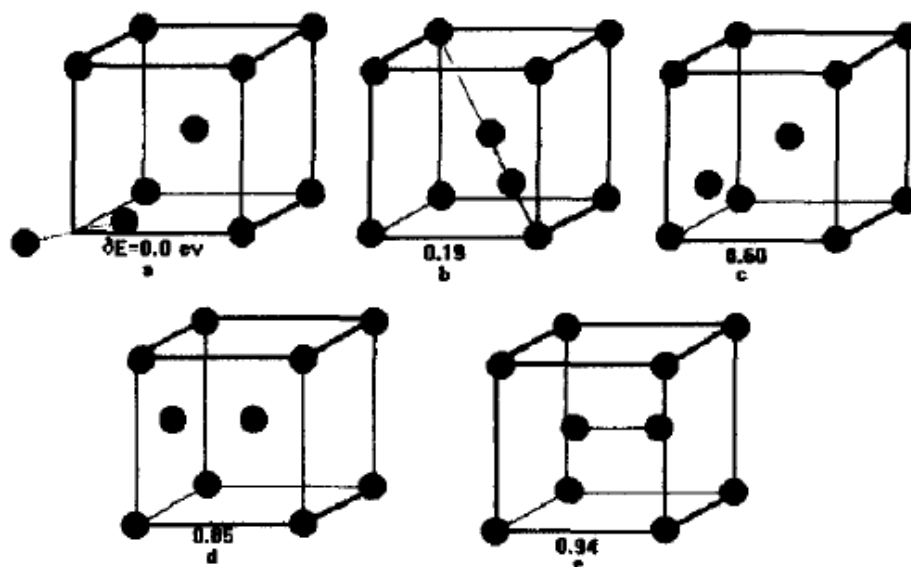


**Fig. 1.11.** SIA configuration in BCC iron: a)  $\langle 110 \rangle$  dumbbell, b)  $\langle 111 \rangle$  crowdion, c) tetrahedral, d) octahedral and e)  $\langle 100 \rangle$  dumbbell [47]

But different calculation methods, potentials and even size of supercell can influence the value of the formation energy. Fig. 1.12a shows the formation energies of the five high symmetry configurations, calculated using the SIESTA ab initio method [50] for two supercell sizes (55 and 129 atoms), the Vienna ab initio simulation package (VASP) [45], and the molecular dynamic (MD) simulation with Finnis-Sinclair (FS) and embedded-atom method (EAM) type empirical potentials. All of them have the same trend with most favorable  $\langle 110 \rangle$  configuration, but the values are shifted relative to each other. In a work of Domain and Becquart [45], it is presented the convergence of the formation energies vs supercell size, calculated using MD simulation with EAM potential. Fig. 1.12b shows a decrease in the  $\langle 110 \rangle$  dumbbell formation energy with the number of atoms in supercell.

Since there is a large variation of the formation energies in the literature, the value used to predict the RIS of phosphorus in Fe-P-C model alloy (Chapter 4) was chosen by the fitting of the theoretical curve with the experimental values.

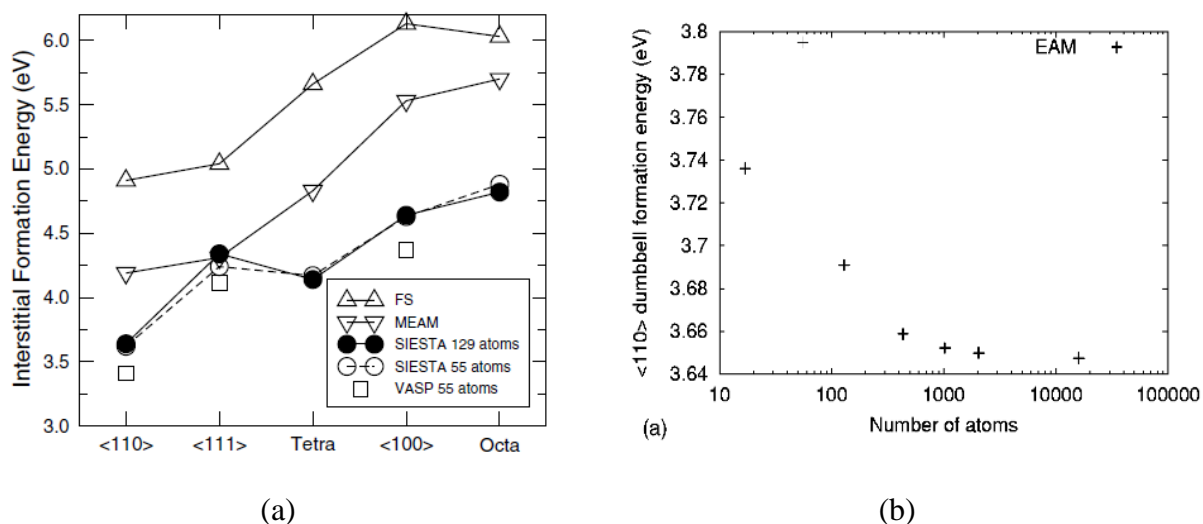


**Fig. 1.12.** SIA formation energies in bcc iron: comparison of SIESTA ab initio results for two supercell sizes with plane-wave (VASP) and empirical potential (FS and MEAM) calculations [51], b) <110> dumbbell formation energy depending on supercell size calculated using embedded atom method (EAM) potential [45]

The most favorable migration mechanism of <110> self-interstitial dumbbell is the nearest-neighbor translation-rotation jump (Fig. 1.13a) with a migration energy of 0.34 eV [48,51,52]. This value is in good agreement with experimental value 0.3 eV [53,54].

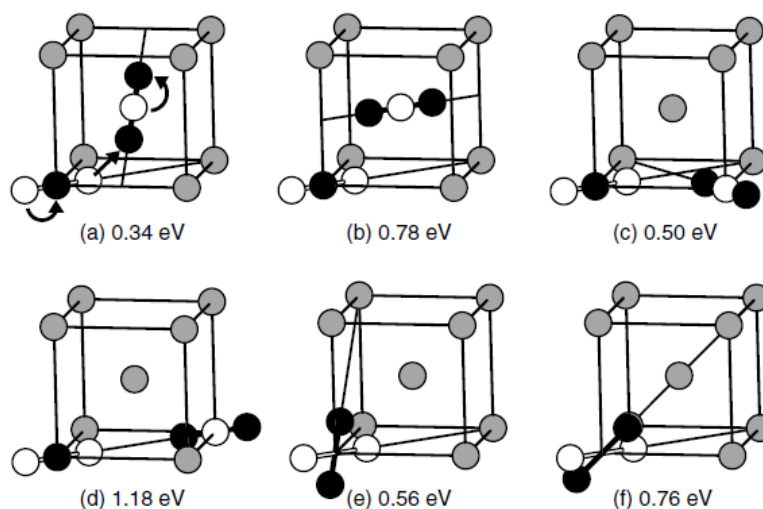


**Fig. 1.13.** Mechanisms of SIA migration with their respective activation energies [51]

Overall, a computer simulation provides us information about formation, configuration and mobility of primary defects in irradiated samples. The good agreement between calculated and experimental energies (formation, migration) strongly supports the theoretical interpretation. These parameters are important in predicting kinetics of defect accumulation and elimination and irradiation-related structural changes in metals and alloys (Chapter 4).

## 1.2.2 Point-defect – impurity complexes

Point-defect solute interaction is usually reported as the formation of defect-solute complexes that can migrate over appreciable distances. The distance travelled by each pair is determined essentially by the magnitude of the binding energy relative to the migration energy of the pair. This ratio appears to be a critical parameter in modelling the segregation of phosphorus in iron [55]. The formation and migration energies given here are used in Chapter 4 to predict the radiation-induced segregation of phosphorus under ion-irradiation of Fe-P-C model alloy.

### a) Phosphorus-SIA complexes

Phosphorus, as an undersized atom, has a strong interaction with SIA. One of the first experimental confirmation was given by Perks et al. [56]. They studied the movement of phosphorus in pure nickel and austenitic steel at room temperature, where vacancies are essentially immobile, making depth profiling using Secondary Ion Mass Spectroscopy (SIMS). They have found that phosphorus atoms migrate in the same direction than the interstitials and that their diffusion (or velocity) depends on the initial concentration of SIAs [56,57]. A similar result was observed by Vasiliev and coworkers [47], which have found an increase of the phosphorus mobility under low-temperature irradiation when the vacancy migration mechanism is not valid.

According to simulation results, the substitutional position is the most stable for phosphorus atoms in  $\alpha$ -iron [47]. A direct transition of the P atom from substitutional ( $P_{sub}$ ) to an interstitial site ( $P_{int}$ ) with a vacancy ( $V$ ) appearance ( $P_{sub} = P_{int} + V$ ) is energetically not efficient [47]. But during neutron or heavy ion irradiation the recoiling iron atom kick-out the P atom from the substitutional site, and P atoms subsequently forms a  $\langle 110 \rangle$  dumbbell with the nearby Fe atom (Fig. 1.14i) or the incident Fe atom (Fig. 1.14ii) [58].

According to ab initio calculation of Meslin et al. [59] the binding energy of  $\langle 110 \rangle$  Fe-P dumbbell,  $E_{\langle 110 \rangle Fe-P}^b \sim 1$  eV, is the energy gain corresponding to the formation of a P interstitial from Fe-Fe  $\langle 110 \rangle$  dumbbell and a substitutional P atom.

Another possible mechanism of mixed  $\langle 110 \rangle$  Fe-P dumbbell formation is the attraction of migrated SIAs by the strain field around substitutional P atoms [47,58,60]. The formation of the mixed dumbbell out of a SIA and a phosphorus atoms give an energy gain of 0.96 eV [60].

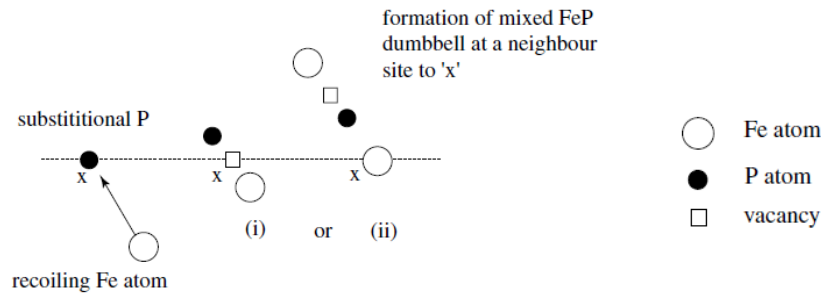


**Fig. 1.14.** The formation of a mixed Fe–P dumbbell during the collisional phase is shown here. A substitutinal P atom which is dislodged from its site can then form a dumbbell with the incident atom itself (i) or a neighboring Fe atom (ii) [58]

The phosphorus atoms become more mobile when displaced from substitutional sites to form Fe–P dumbbells. The long-distance diffusion of  $\langle 110 \rangle_{Fe-P}$  is possible by the translation-rotation (Path 1), the rigid translation (Path 2), the second nearest neighbor jump mechanisms (Path 3) (Fig. 1.15a) and two kinds of on-site rotation mechanisms (Fig. 1.15b).

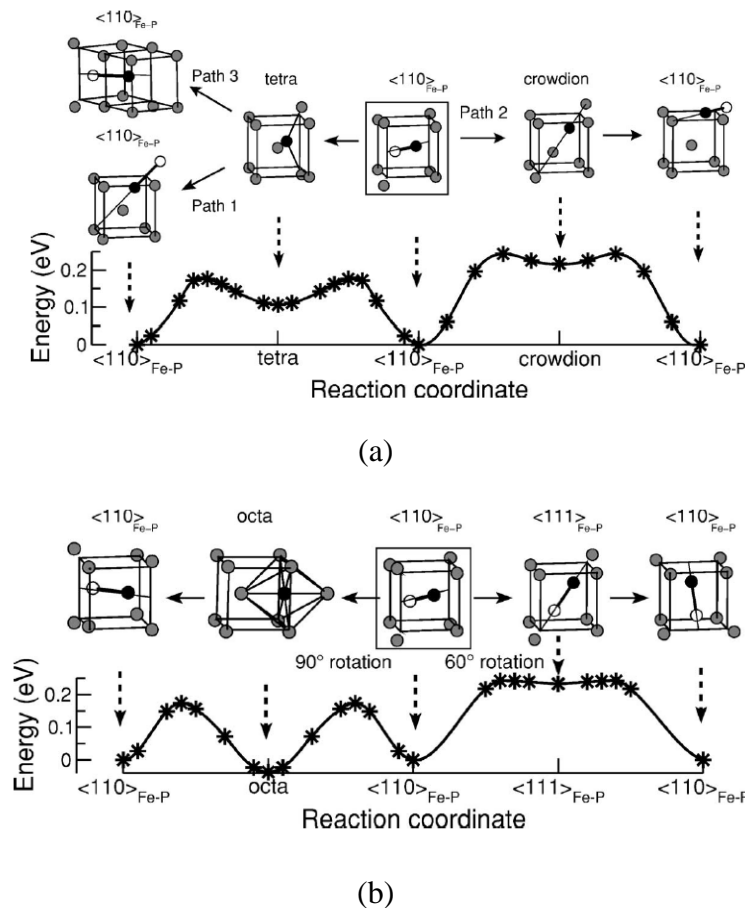


**Fig. 1.15.** Ab initio calculation of activation energy for different mechanisms of  $\langle 110 \rangle_{Fe-P}$  mixed dumbbell migration. (a) Path 1, 2 and 3 are the translation-rotation, the rigid translation, and the second nearest neighbor jump, respectively; (b) two on-site rotation mechanisms [59]

Ab initio and MD calculations of Meslin et al. [59] revealed that the translation-rotation with the activation energy 0.27 eV is the most probable mechanism of the  $\langle 110 \rangle_{Fe-P}$  dumbbell migration.

In its turn, the translation-rotation mechanism consists of the rotation of the Fe-P dumbbell to a tetrahedral site (Fig. 1.16a-b) and a jump from the tetrahedral back to the dumbbell configuration (Fig. 1.16b-c). According to Gordon et al. [61] the transition from dumbbell to tetrahedral has an activation energy 0.29 eV and jump from the tetrahedral back to the dumbbell configuration would cost 0.26 eV [61].

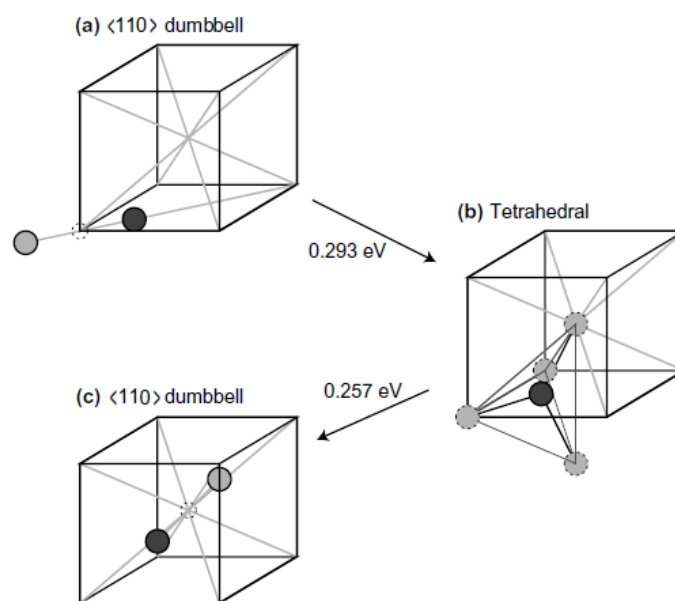


**Fig. 1.16.** Migration mechanism of  $\langle 110 \rangle$  Fe-P dumbbell: from a dumbbell position (a), the P atom move to tetrahedral site (b), and then form the dumbbell in the center of the cell (c)[61]

Faulkner and coworkers [62–67] have assumed that the dissociation together with translation is a more favorable mechanism for the Fe-P complex migration rather than translation-rotation. The complex migration activation energy is determined as the sum of SIA migration energy and Fe-P complex binding energy and equal to 0.87 eV [66]. This value is close to the experimentally determined activation energy for Fe-P complex diffusion in Fe-0.027 at.% P alloy irradiated with 1 MeV electrons (0.79 eV) [43].

### ***b) Phosphorus-vacancy complexes***

Although earliest works have neglected the phosphorus-vacancy (P-V) complexes migration, recent studies have reported the relatively high binding energy of stable P-V complex (from 0.25 to 0.4 eV), when the vacancy is situated at the first or second nearest

neighbor position from the P atom [47,60,68,69]. The P-V complex binding energy is a result of the relaxation of some of the strain energy related to both species individually when they occupy nearest neighbor sites [65]. It characterizes the possibility of solute atoms to be dragged by vacancies [70]. The long-range P-V interaction in BCC iron makes it possible for a vacancy to move around phosphorus atom, while remaining bound as a complex, and consequently drag phosphorus atoms to sinks of point defects [69].

Despite the strong P-V binding energy, the analysis of the P-V diffusivity indicated that the pairs have a small free path [60] (Fig. 1.17).

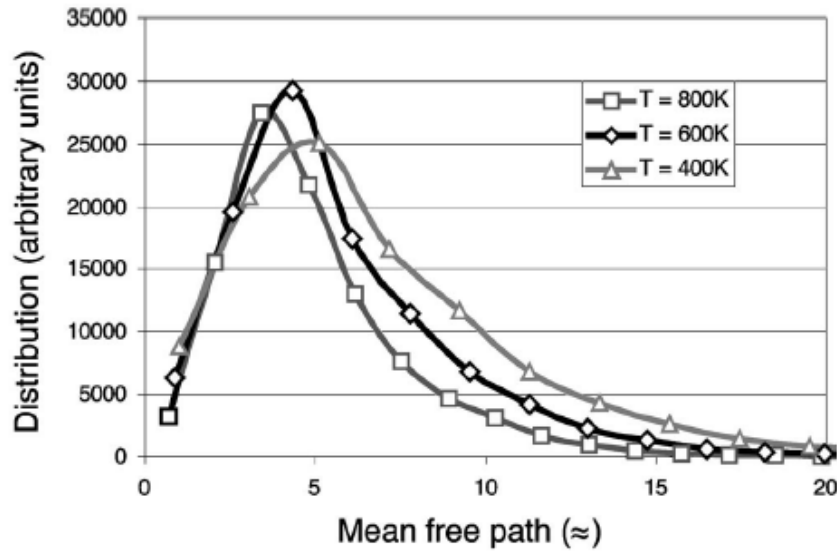


**Fig. 1.17.** Phosphorus-vacancy pair mean free path (in Å) distribution for three different temperatures [60]

The result of ab initio calculation offered by Messina [71] suggests that phosphorus transport is dominated by the mixed dumbbell over the vacancy mechanism. This conclusion based on calculation of interstitial factor  $\chi^I$ :

$$\chi^I = 1 - \frac{D_{PDV}^V}{D_{PDC}^I} \quad (3)$$

where  $D_{PDV}^V$  is the partial diffusion coefficient of P-V complex,  $D_{PDC}^I$  is the partial diffusion coefficient of P-SIA complexes.

Fig. 1.18 shows the temperature dependence of the interstitial factor  $\chi^I$  for different solute atoms. As seen, the interstitial factor of phosphorus in all range of temperature is equal to one, which indicates that vacancy contribution to the phosphorus migration is negligible.

Since the phosphorus-interstitial complex migrates much more easily than the phosphorus-vacancy complex, it is considered that phosphorus-interstitial should play a dominant role in radiation-induced phosphorus segregation in Fe-P-C model alloy

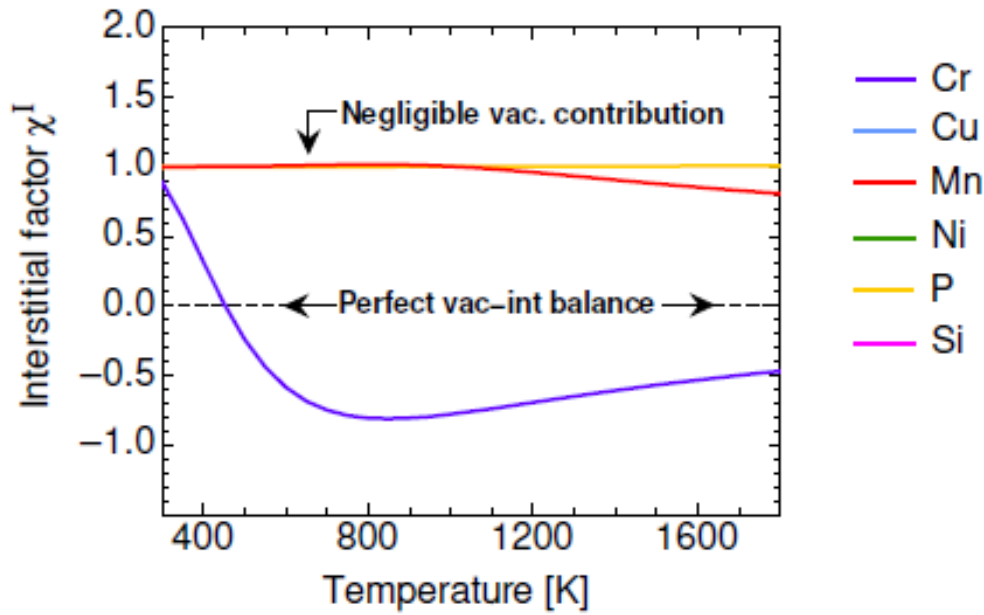


**Fig. 1.18.** Interstitial factor  $\chi^I$  as a function temperature for different solutes ( $\chi^I = 1$  when the contribution of vacancies in solute drag is negligible)

### 1.2.3 Radiation induced segregation

#### a) Radiation induced segregation mechanisms

Irradiation produces an excess of point defects which can be eliminated by recombination, clustering or adsorption at sinks such as surfaces, grain boundaries, dislocations and voids [72]. Current theoretical models describe the solute segregation in irradiated alloys as a result of coupling between fluxes of defects and solute elements.

If there is no solute-vacancy or solute-SIA complexes in irradiated material, the RIS can be simply described with the inverse Kirkendall mechanism, where the vacancy flux toward the sink,  $J_V$ , induces the equal flux of atoms ( $J_A^V + J_B^V$ ) in the opposite direction (Fig. 1.19a). If A atoms exchange faster with vacancies than B atoms, i.e.  $D_B^V < D_A^V$ , the vacancy sink becomes depleted in A atoms and appears enriched in B atoms.

If B atoms are strongly bounded to vacancies, vacancies can drag B atoms toward the sink (Fig. 1.19b). The dragging effect can also be induced by self-interstitial atoms (SIA) (Fig. 1.19c), when the interstitial flux and associated atom flux move in the same direction. The interstitial-solute fluxes  $J_A^I$  and  $J_B^I$  being proportional to the local atomic fraction,  $C_A$  and  $C_B$ , the faster component will be preferentially transported toward to the sink [72].

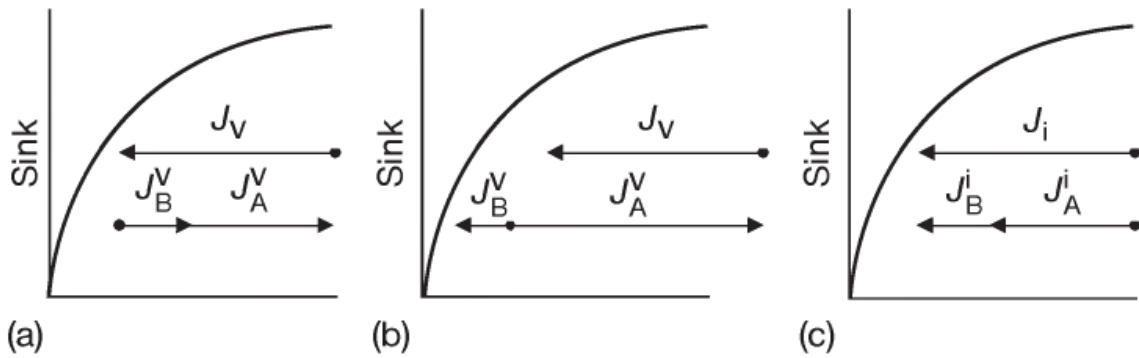


**Fig. 1.19.** Radiation-induced segregation mechanisms due to coupling between point defect and solute fluxes in a binary A-B alloy. An enrichment B occurs (a) when A atoms diffuse faster than B atoms, i.e.  $D_B^V < D_A^V$ , (b) when vacancies drag B atoms, (c) when interstitials drag B atoms towards GB [37,72]

The contribution of these different mechanisms to RIS phenomena in industrial steels is still under discussion. It is considered that solute size effect plays a key role in determining the magnitude and the direction of segregation [73]. In general, undersized solutes are dragged by SIAs toward to sinks, while oversized atoms have repulsion interaction with SIAs [74]. Moreover, the oversize atoms will preferentially exchange with vacancies, so radiation-induced depletion (RID) of these solutes at GBs is expected [37].

This effect, first noted by Okamoto and Wiedersich [75] in ion irradiated Fe-Cr-Ni-Si alloy, has been confirmed for austenitic steels containing oversized Cr [31,76,77] and undersized Ni, P, S, Si [78–81] solute elements. However, several works have reported that Cr atoms can segregate at GBs in ferritic/martensitic steels under irradiation [82–84]. Lu et al. [85] summarized the intergranular segregation behavior in high Cr ferritic/martensitic and austenitic steels and suggested that Cr atoms in ferritic steels may be oversized or undersized, depending on concentration and electronic/magnetic effects. For undersized Cr atoms, Cr-SIA complexes may be preferentially formed by the positive binding energy and Cr atoms are dragged towards grain boundaries. Whereas oversized Cr atoms drift away from grain boundaries against the vacancy flux.

Messina et al. [71] have reported that Cr atoms in FeCr alloys under irradiation form the stable and mobile mixed dumbbells, and have a negative coupling with vacancies. At low temperatures, the interstitial-drag mechanism dominates over the vacancy-diffusion mechanism, which leads to Cr enrichment at GB. As the temperature increases, Cr transport is dominated by the vacancy-diffusion mechanism, so the segregation behavior changes from enrichment to depletion.

For minor solutes such as P, S, Si which are always undersized, as pointed by Ardell [86], no case of depletion has ever been reported. The segregation of undersized elements under irradiation either can be the result of supersaturation of vacancies that enhance the diffusion in the matrix, or induced by flux coupling between point defect and solutes, or the driving force most likely contains both mechanisms [59].

**b) Effect of irradiation dose, dose rate and temperature on phosphorus segregation**

Generally, the concentration of undersized elements at GB increases monotonically as the irradiation dose increases [55,64,87–89]. The neutron dose dependence of phosphorus intergranular segregation in various steels is presented in Fig. 1.20. It shows the dose dependence of radiation-induced evolution of phosphorus GB monolayer coverage, normalized with respect to the bulk atomic phosphorus concentration for C-Mn Light-Water Reactor (LWT) plates, welds and coarse heat affected zone (HAZ) structures and for VVER base metal and weld is reported. Irradiation temperatures are 270 – 290°C excepted for the Magnox submerged arc welded (SAW), which cover the range 186 – 311°C [37]. Segregation of phosphorus increases with increasing neutron dose in all steels.

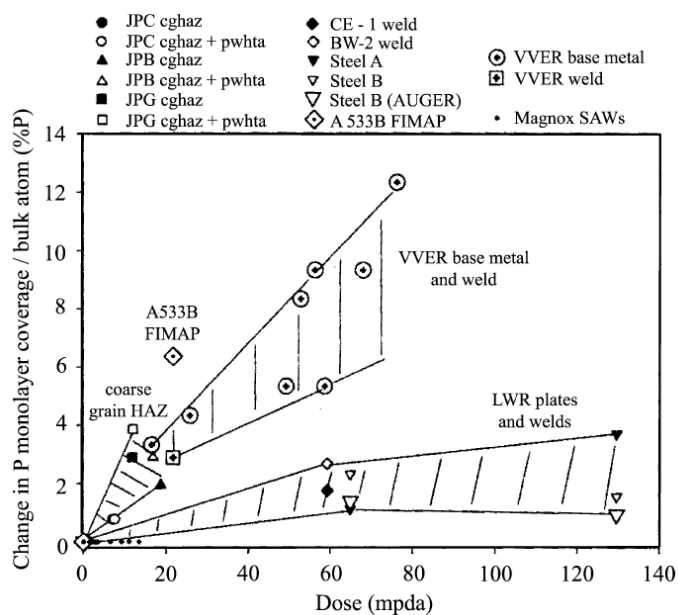


**Fig. 1.20.** Dose dependence of radiation-induced change in GB phosphorus monolayer for C-Mn Light-Water Reactor (LWT) plates, welds and coarse heat affected zone (HAZ) structure and VVER base metal and weld [37].

Besides of irradiation dose, radiation-induced segregation level depends on dose rate and temperature. The effect of dose rate,  $K_0$  in dpa/s and temperature,  $T$  is schematically represented in Fig. 1.21. Radiation-induced segregation (RIS) requires enough amounts of

point-defects, which can drag solute atoms toward GB. The maximum level of RIS is typically observed at temperatures between 0.3 and 0.6 times the melting point,  $T_m$  [37]. At lower temperatures, the low mobility of point defects leads to high mutual recombination more than annihilation at point defect sinks. At high temperatures, the equilibrium vacancy concentration is high, so the back diffusion of segregated alloying elements from GB to the matrix and a lower vacancy supersaturation reduce the segregation [72]. So that, increasing dose rate, or radiation flux, results in rising the point defect concentration and shifts the transition between RIS zones toward a higher temperature.

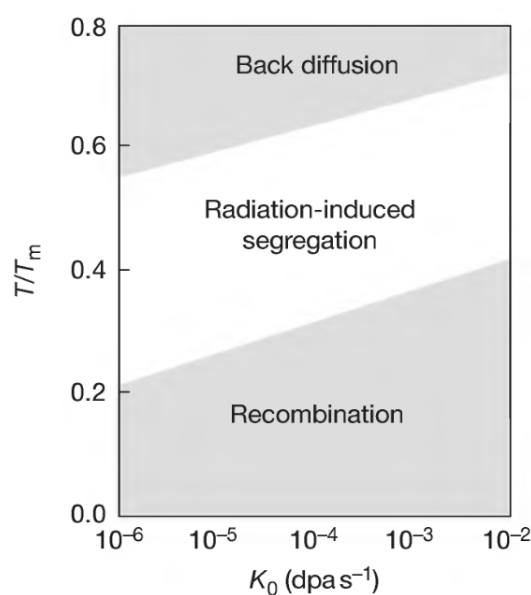


**Fig. 1.21.** Temperature (related to the melting point) and dose rate effect on the radiation-induced segregation [72].

The Fe-0.034 at.%P-0.01 at.% C model alloy used in the current work was subjected to ion irradiation at  $T = 450^\circ\text{C}$  ( $T_m = 1538^\circ\text{C}$ ) and dose rate of  $10^{-5}\text{dpa/s}$ . Based on Fig. 1.21, we expect to observe significant RIS of phosphorus in our material.

### 1.3 Grain-boundary structure and segregation behavior

#### 1.3.1 Crystallography of grain boundaries

A grain boundary (GB) is the interface between two grains in a polycrystalline material. The GB structure is defined by the misorientation between two grains and the orientation of the boundary plane. Five independent macroscopic parameters (degrees of freedom) are needed to specify the GB structure: two for the rotation axis  $[uvw]$ , one for the rotation angle  $\theta$  between the two crystals, and two for the GB plane  $(h_1k_1l_1)/(h_2k_2l_2)$ . In

addition, four microscopic parameters describe the rigid translation of one grain with respect to the other, parallel or perpendicular to the grain boundary plane [90]. In total, a GB possesses nine geometrical degrees of freedom. However, the five macroscopic degrees of freedom (DOFs) are sufficient to give a complete geometrical description by the notation  $\theta^\circ [uvw](h_1k_1l_1)/(h_2k_2l_2)$ . In the current work, we are available to estimate all five macroscopic DOFs and link it with the segregation level of phosphorus.

Based on the relationship among individual DOFs, the GBs can be categorized into groups. According to the misorientation angle, grain boundaries can be divided into *low-angle grain boundaries* (LAGBs), generally with  $\theta < 15^\circ$  and *high-angle grain boundaries* (HAGBs). The relationship between rotation axis  $[uvw]$  and the GB plane normal,  $n$  classifies three different types of grain boundaries: *tilt grain boundary*, where rotation axis is parallel to the boundary plane; *twist grain boundary* (Fig. 1.22a), where this axis is perpendicular to the boundary plane; *general grain boundary* in any other configuration of rotation axis with respect to the grain boundary plane. If a tilt GB plane has the same indexes in crystals I and II,  $\{h_1k_1l_1\} = \{h_2k_2l_2\}$ , the GB is called *symmetrical tilt grain boundary* (Fig. 1.22c). If the GB plane has a different Miller indexes in the two adjacent crystals,  $\{h_1k_1l_1\} \neq \{h_2k_2l_2\}$ , the GB is called *asymmetrical* (Fig. 1.22b).

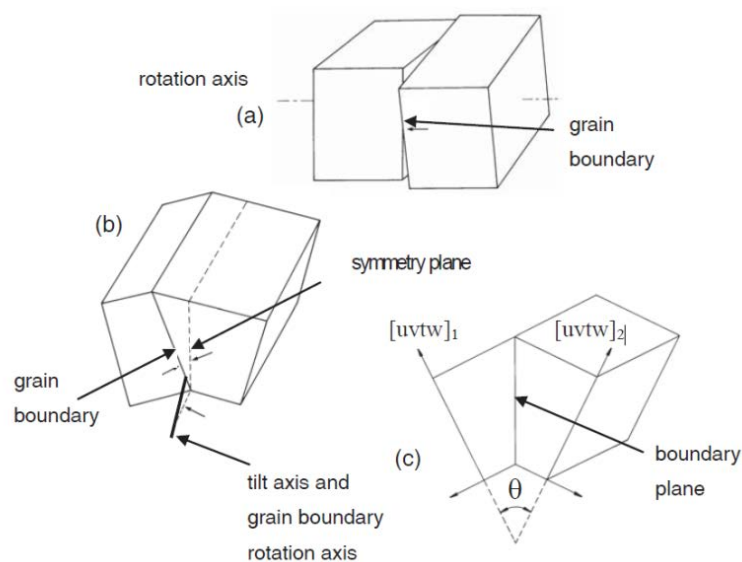


**Fig. 1.22.** Schematic representation of a) a twist grain boundary, b) an asymmetrical tilt grain boundary and c) symmetrical tilt boundary [93]

The symmetrical/asymmetrical distinction only concerns straight GB plane defined by its five macroscopic parameters and does not take into account the faceting phenomenon that often occurs in real GBs [91]. A symmetrical tilt GBs structure is usually described using

*coincidence site lattice* (CSL) model [92]. At certain misorientations between two grains, one can get the perfect overlap of the lattice sites in the grains, i.e. certain atomic positions in the GB coincide with ideal positions in both neighboring crystallites. These specific positions are called coincidence sites and the super lattice containing these sites is a *coincidence site lattice* (CSL) [92]. The CSL is characterized by the density of coincidence sites  $\Sigma$ , which is defined as [91]:

$$\Sigma = \frac{\text{Coincidence unit cell volume}}{\text{Crystal primitive unit cell volume}} \quad (4)$$

In cubic lattices,  $\Sigma$  could be defined from the Miller indices of the symmetrical tilt GB plane,

$$\Sigma = \delta(h^2 + k^2 + l^2) \quad (5)$$

where  $\delta = 1$  if  $(h^2 + k^2 + l^2)$  is odd and  $\delta = 1/2$  if  $(h^2 + k^2 + l^2)$  is even because in cubic system all  $\Sigma$  values are odd. The GBs with a high density of coincidence sites are called *special grain boundaries*. Until now, the knowledge of the GB structures and on the relations between structures and GB properties mainly concerns symmetrical tilt GBs. Recently, some symmetrical twist and asymmetrical tilt GBs have been experimentally and theoretically studied [94–99].

The structure of *general grain boundaries* is too complicated to be defined only by *coincidence site lattice* (CSL) model. In fact, the geometrical description of *real grain boundaries* in a polycrystal is a very difficult task. Their geometrical parameters are uncontrollable and are generally determined with less accuracy than those of the bicrystals (i.e. a sample containing two grains with the required orientation of the planar separating interface) [91]. The GB planes cannot be precisely defined because of the presence of curvature and/or faceting at GB. Furthermore, the structure of general GBs is rarely observed by high-resolution transmission microscopy due to the narrow focus on GB region. The detailed review of experimental and theoretical works on GBs structure is given in the books of Priester [91] and Lejcek [100].

In the current work, the majority of investigated interfaces are high-angle general GBs, as a main type of GB in the Fe-0.034 at.% P-0.01 at.% C ferritic model alloy after hot rolling at 1200° followed by air cooling. The geometry of them is described using the five macroscopic degrees of freedom.

### 1.3.2 GB structure and GB energy

The increase of the internal energy in a single crystal, due to the addition of a GB under constant temperature and chemical potentials,  $\mu_i$  of components  $i = 1, 2, \dots, N$ , according to the first and second principles of thermodynamics is:

$$dU = TdS - PdV + \sum_{i=1}^N \mu_i dn_i + \gamma dA \quad (6)$$

where  $S$  is the entropy of the system,  $V$  is the volume of system,  $n_i$  is the amount of  $i = 1, 2, \dots, N$  components,  $A$  is the GB area and  $\gamma$  is the interfacial (GB) energy per unit area.

Therefore, the GB energy per unit area,  $\gamma$ , represents the change of the internal energy of the closed system with the change of GB area at constant entropy and volume,

$$\gamma = \left( \frac{\partial U}{\partial A} \right)_{S, V, n_i} \quad (7)$$

In accordance with the fundamental relationship among the thermodynamic state functions,  $H = U + PV$ ,  $F = U - TS$ ,  $G = U + PV - TS$ , we get:

$$\gamma = \left( \frac{\partial U}{\partial A} \right)_{S, V, n_i} = \left( \frac{\partial H}{\partial A} \right)_{S, P, n_i} = \left( \frac{\partial F}{\partial A} \right)_{T, V, n_i} = \left( \frac{\partial G}{\partial A} \right)_{T, P, n_i} \quad (8)$$

where  $H$  is the enthalpy of the system,  $F$  is the Helmholtz energy and  $G$  is the Gibbs energy.

Extrapolating the Gibbs-Duhem [101] equation to the interfacial region gives:

$$-\frac{S}{A} dT + \frac{V}{A} dP - \sum_{i=1}^N \frac{n_i}{A} d\mu_i - d\gamma = 0 \quad (9)$$

or

$$d\gamma = -s^\phi dT + v^\phi dP - \sum_{i=1}^N \Gamma_i^\phi d\mu_i \quad (10)$$

where  $s^\phi$ ,  $v^\phi$  and  $\Gamma_i^\phi$  are the entropy, the volume and the amount of the  $i$  solute at the grain boundary  $\phi$ , respectively, normalized by the GB area. The term  $\Gamma_i^\phi$  is called *Gibbsian interfacial excess* of solute  $i$ .

This is well-known Gibbs equation, which shows the change of interfacial energy with the variation in temperature, pressure and chemical potentials of the bulk. The energy of GB is not only function of temperature and pressure, also the five macroscopic DOFs which define the structure of GB. Finally, the function of GB energy can be written as:

$$\gamma = \gamma(T, P, \mu_i, \theta, o, n_1, n_2) \quad (11)$$

where  $\theta$  is a misorientation angle,  $o$  is the direction of rotation axis and  $n_1, n_2$  are normal to the boundary plane in two crystal.

Changes in the GB energy affects the values of the chemical potentials of the solute and matrix elements at the GB and thus the standard Gibbs energy of segregation,  $\Delta G_I$ . In its turn, the standard Gibbs energy of segregation defines the level of GB segregation (more details are given in Chapter 3).

Thus, different GB structures in material results in *anisotropy of GB segregation*, i.e. the dependence of GB segregation level on the GB structure. The example of GB segregation anisotropy is given in Fig. 1.23 as a dependence of phosphorus GB segregation from the misorientation angle  $\theta$  of [100] symmetric tilt GB in Fe-3.5 at% Si-0.009 at% P alloy. We can see the presence of anisotropy of GB segregation, characterized by minima of GB concentration at special  $\{012\}$ ,  $\{013\}$  and  $\{015\}$  symmetrical tilt GBs. At high temperatures, however, the orientation dependence of GB enrichment qualitatively changes and the maxima of GB concentration are observed at special GBs with high-coincidence (low  $\Sigma$ ).

Due to the complicated structure of GBs in polycrystal (5 DOFs, GB curvature, faceting), there is no simple rule which may link a GB geometrical parameter to the segregation level [91]. The segregation anisotropy has been first attributed to the different GB plane orientations.

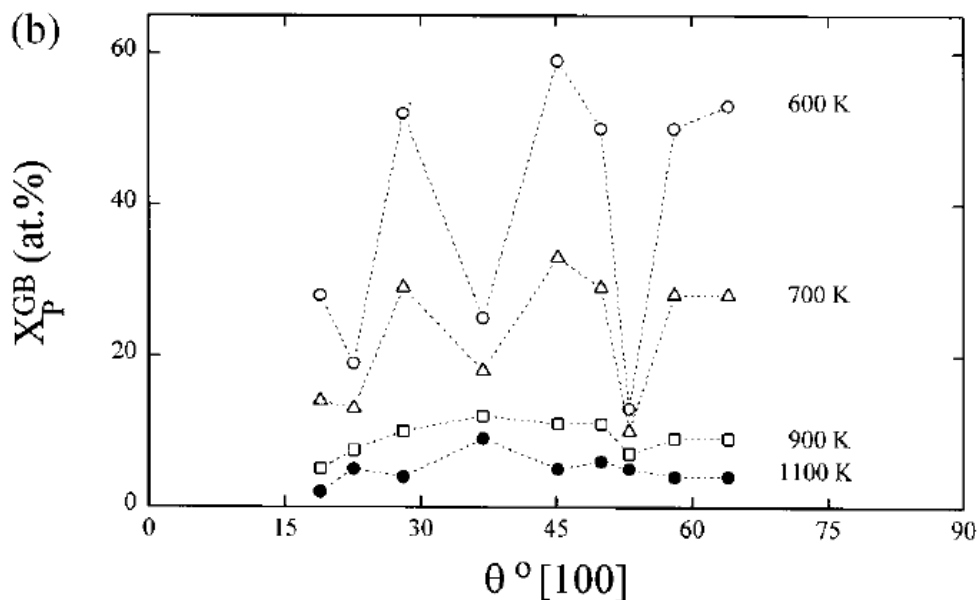


**Fig. 1.23.** GB concentration dependence for phosphorus on the misorientation angle  $\theta$  of both crystals in [100] symmetrical tilt bicrystals of an Fe-3.5 at.% Si-0.009 at.% P alloy at different temperatures

For example, Fig. 1.24 shows the changing of GB concentration of Ti and Si along curved GB in  $\text{Al}_2\text{O}_3$ . There is a clear predominance of titanium segregation in the region of the boundary with rhombohedral  $(01\bar{1}2)$  plane and of silicon in the region with basal  $(0001)$  plane. The result indicates the important role of GB plane orientation, while other geometrical parameters are fixed. In the current work, two samples from one GB were prepared in order to check the distribution of phosphorus along curved GB plane (see Chapter 4).

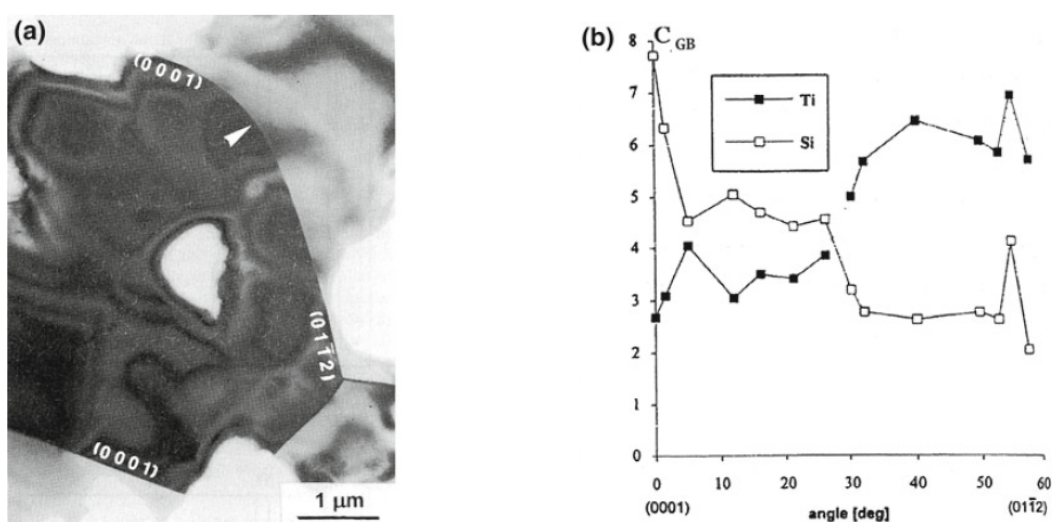


**Fig. 1.24.** (a) Curved GB in  $\text{Al}_2\text{O}_3$  with GB plane orientation changing from the basal  $(0001)$  to the rhombohedral  $(01\bar{1}2)$  plane. (b) Variation of Si and Ti concentration at the GB as a function of GB plane orientation [102]

Suzuki et al. [103] have studied intergranular segregation of phosphorus in polycrystalline BCC iron using Auger Electron Spectroscopy (AES). As it is shown in Fig. 1.25, the level of segregation was found to be larger on the high-index GB planes and lower on the low-index planes, independently from the misorientation angle. The relationship between the crystallography of intergranular cracks and the segregation also has been investigated by Williams et al. [104]. They studied the phosphorus and carbon segregations in thermally aged Fe-0.06 wt.% P-0.002 wt.% C alloy. Phosphorus segregation was measured using AES. The nearest low Miller index plane (deviation angle less than  $10^\circ$ ) was determined using Electron Backscatter Diffraction (EBSD) analysis. Fig. 1.26 shows the proportion of segregated phosphorus and carbon as a function of increasing Miller index. It can be seen an inverse relationship between two solutes, indicating the site competition between them. No carbon or phosphorus segregation at  $\{100\}$  facets was detected, since they are transgranular. The lower phosphorus/higher carbon were detected on the GB planes close

to  $\{110\}$  plane. The concentration of phosphorus at other GBs is higher, but there is no clear correlation as in the work of Suzuki (Fig. 1.25) [103].

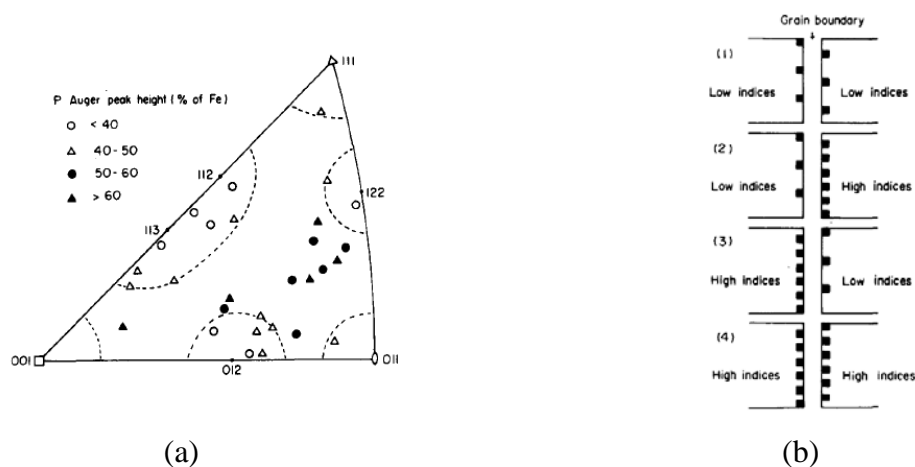


**Fig. 1.25** (a) Relationship between P segregation (Auger peak-to-peak ratios between P and Fe in fractured surface) and crystallographic orientation of GB planes, (b) Correspondance between P segregation (dark marks schematically depict amount of segregated P) and GB planes [103]

From the literature review, it is suggested that the GB plane orientation is an important factor, which can control the amount of phosphorus segregation to GBs. In the present work, we determine the orientation of GB plane for both grains and check the relationship between GB plane indices and phosphorus GB concentration.

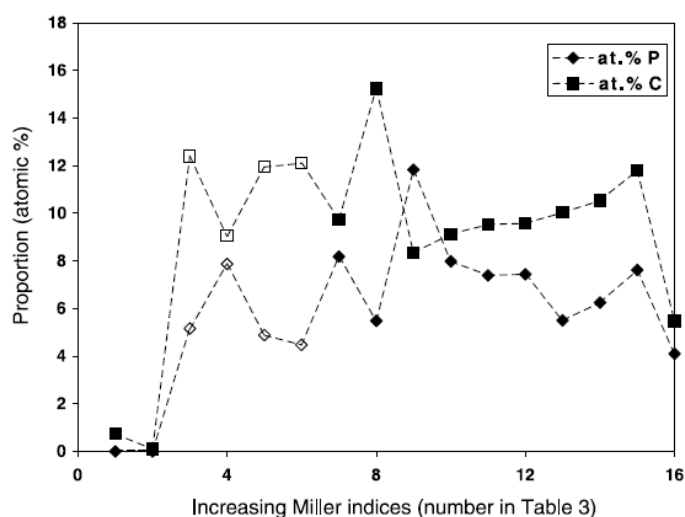


**Fig. 1.26.** Proportion of phosphorus and carbon as a function of increasing Miller indices, labelled according to their number in Table 3, for each of the 16 facets for which both Auger and EBSD information was obtained. The nearest low index Miller indices are: 1,2 –  $\{100\}$ ; 3–6 –  $\{110\}$ ; 7 –  $\{210\}$ ; 8,9 –  $\{211\}$ ; 10 –  $\{221\}$ ; 11 –  $\{311\}$ ; 12 –  $\{321\}$ ; 13 –  $\{331\}$ ; 14 –  $\{332\}$ ; 15 –  $\{411\}$ ; 16 –  $\{432\}$ . Facets near  $\{110\}$  are shown as open symbols [104]

## Conclusion

Neutron irradiation embrittlement of RPV steels is a key issue in the estimation of safety lifespan of the whole nuclear plant. The irradiation embrittlement may be caused by three different mechanisms: matrix damage (hardening mechanism), irradiation-induced/enhanced clustering and precipitation (hardening mechanism) and irradiation induced/enhanced GB segregation of embrittling elements such as phosphorus (non-hardening mechanism). According to the literature review, the dominance of non-hardening mechanism of irradiation embrittlement over hardening mechanism was detected only in high-phosphorus (570 ppm) steels. However, most of the mechanical tests (for example, Charpy impact test) presented in the literature were performed either on thermally aged materials or on samples irradiated in test reactors with high flux (accelerated irradiation). The results obtained in materials from test reactors require extrapolation to low flux service conditions over a wide range of fluences and metallurgical conditions. That is to say that the effect of phosphorus on irradiation embrittlement can become significant after long-term services under low flux, so the further investigation on this subject is necessary.

The current view on mechanisms of irradiation damage in Fe and Fe-based alloys were summarized in the second section of this chapter. The description ranged from primary damage formation, point defect and solute-defect complexes migration and radiation-induced segregation mechanisms. The environmental effects such as temperature, dose and dose rate on defect formation and the phosphorus segregation level were discussed.

The third part of this chapter describes the GB geometry and its relation with the GB energy and thus with GB segregation. Although, due to the complicated structure of GBs in polycrystals (5 DOFs, GB curvature, faceting), there is no simple rule which may link GB crystallography to the segregation level, some correlations of the geometrical parameters with the segregation level were observed earlier. These correlations are investigated experimentally in Chapter 4.

## References

- [1] PRIS – Country Details, (n.d.). <https://www.iaea.org/PRIS/CountryStatistics/CountryDetails.aspx?current=FR> (accessed March 27, 2017).
- [2] J.J. Duderstadt, L.J. Hamilton, *Nuclear Reactor Analysis*, Wiley, 1976.
- [3] The Pressurized Water Reactor (PWR), (n.d.). <https://www.nrc.gov/reading-rm/basic-ref/students/animated-pwr.html> (accessed March 30, 2017).
- [4] Assessment and Management of Ageing of Major Nuclear Power Plant Components Important to Safety: Steam Generators, International Atomic Energy Agency, Vienna, 2011.
- [5] Integrity of Reactor Pressure Vessels in Nuclear Power Plants: Assessment of Irradiation Embrittlement Effects in Reactor Pressure Vessel Steels, International Atomic Energy Agency, Vienna, 2009.
- [6] N. Soneda, *Irradiation Embrittlement of Reactor Pressure Vessels (RPVs) in Nuclear Power Plants*, Elsevier, 2014.
- [7] PRIS – Miscellaneous reports – Operational by Age, (n.d.). <https://www.iaea.org/PRIS/WorldStatistics/OperationalByAge.aspx> (accessed February 5, 2016).
- [8] A. Chabre, *Research nuclear reactors: a nuclear energy division monograph*, CEA Saclay and Groupe Moniteur, Paris, 2012.
- [9] B.A. Gurovich, E.A. Kuleshova, Y.I. Shtrombakh, D.Y. Erak, A.A. Chernobaeva, O.O. Zabusov, Fine structure behaviour of VVER-1000 RPV materials under irradiation, *J. Nucl. Mater.* 389 (2009) 490–496. doi:10.1016/j.jnucmat.2009.02.002.
- [10] E.A. Kuleshova, A.D. Erak, A.S. Kiselev, S.A. Bubyakin, A.P. Bandura, Influence of operation factors on brittle fracture initiation and critical local normal stress in SE(B) type specimens of VVER reactor pressure vessel steels, *J. Nucl. Mater.* 467, Part 2 (2015) 927–936. doi:10.1016/j.jnucmat.2015.10.037.
- [11] D. Erak, B. Gurovich, D. Zhurko, Improvement of radiation embrittlement dependences for VVER-1000 Pressure Vessel materials on service-life extension, in: Manchester, UK, 2015. Available at: [https://repository.lib.ncsu.edu/bitstream/handle/1840.20/33782/SMiRT-23\\_Paper\\_383.pdf?sequence=1&isAllowed=y](https://repository.lib.ncsu.edu/bitstream/handle/1840.20/33782/SMiRT-23_Paper_383.pdf?sequence=1&isAllowed=y).
- [12] F.W. Noble, B.A. Senior, B.L. Eyre, The effect of phosphorus on the ductility of 9Cr-1Mo steels, *Acta Metall. Mater.* 38 (1990) 709–717. doi:10.1016/0956-7151(90)90022-9.

- [13] Q. Li, L. Li, E. Liu, D. Liu, X. Cui, Temper embrittlement dynamics induced by non-equilibrium segregation of phosphorus in steel 12Cr1MoV, *Scr. Mater.* 53 (2005) 309–313. doi:10.1016/j.scriptamat.2005.04.011.
- [14] C.L. Briant, S.K. Banerji, Intergranular failure in steel: the role of grain-boundary composition, *Int. Met. Rev.* 23 (1978) 164–199. doi:10.1179/imtr.1978.23.1.164.
- [15] C. Naudin, J.M. Frund, A. Pineau, Intergranular fracture stress and phosphorus grain boundary segregation of a Mn-Ni-Mo steel, *Scr. Mater.* 40 (1999) 1013–1019. doi:10.1016/S1359-6462(99)00069-X.
- [16] H. Nakata, K. Fujii, K. Fukuya, R. Kasada, A. Kimura, Grain Boundary Phosphorus Segregation in Thermally Aged Low Alloy Steels, *J. Nucl. Sci. Technol.* 43 (2006) 785–793. doi:10.1080/18811248.2006.9711160.
- [17] S.-H. Song, H. Zhuang, J. Wu, L.-Q. Weng, Z.-X. Yuan, T.-H. Xi, Dependence of ductile-to-brittle transition temperature on phosphorus grain boundary segregation for a 2.25Cr1Mo steel, *Mater. Sci. Eng. A.* 486 (2008) 433–438. doi:10.1016/j.msea.2007.09.032.
- [18] M. Hashimoto, Y. Ishida, R. Yamamoto, M. Doyama, T. Fujiwara, Atomic and electronic structures of a grain boundary in iron with impurity segregation, *Surf. Sci.* 144 (1984) 182–195. doi:10.1016/0039-6028(84)90714-3.
- [19] R. Wu, A.J. Freeman, G.B. Olson, On the electronic basis of the phosphorus intergranular embrittlement of iron, *J. Mater. Res.* 7 (1992) 2403–2411. doi:10.1557/JMR.1992.2403.
- [20] Y.F. Migal, V.I. Kolesnikov, I.V. Kolesnikov, Impurity and alloying elements on grain surface in iron: Periodic dependence of binding energy on atomic number and influence on wear resistance, *Comput. Mater. Sci.* 111 (2016) 503–512. doi:10.1016/j.commatsci.2015.10.003.
- [21] S. Rosinski, Review of Phosphorus Segregation and Intergranular Embrittlement in Reactor Pressure Vessel Steels (PWRMRP-19): PWR Material Reliability Project (PWRMRP), EPRI, Palo Alto, CA, 2000.
- [22] S.G. Druce, G. Gage, G. Jordan, Effect of ageing on properties of pressure vessel steels, *Acta Metall.* 34 (1986) 641–652. doi:10.1016/0001-6160(86)90179-3.
- [23] Z. Zhai, Y. Miyahara, H. Abe, Y. Watanabe, Segregation behavior of phosphorus in the heat-affected zone of an A533B/A182 dissimilar weld joint before and after simulated thermal aging, *J. Nucl. Mater.* 452 (2014) 133–140. doi:10.1016/j.jnucmat.2014.05.005.
- [24] M. Tabuchi, H. Okada, M. Kondo, S. Tsukamoto, F. Abe, N.I. for M. Science, L. Sumitomo Metal Industries, L. Mitsubishi, Heavy Industries, Welded joint of tempered

martensite based heat-resistant steel, 2004. Available at: <https://www.google.com/patents/EP1621643A1?cl=en> (accessed March 31, 2017).

[25] Gage G., Druce S.G., Popkiss E.W., Effect of ageing on properties of pressure vessel steels, *Acta Metall.*, vol 34 (1986) pp 641-652. doi: 10.1016/0001-6160(86)90179-3

[26] P.A. Platonov, A.A. Chernobaeva, Formation of radiation induced precipitates in VVER RPV materials, *Int. J. Press. Vessels Pip.* 148 (2016) 36–45. doi:10.1016/j.ijpvp.2016.11.001.

[27] Y. Nishiyama, K. Onizawa, M. Suzuki, J.W. Anderegg, Y. Nagai, T. Toyama, M. Hasegawa, J. Kameda, Effects of neutron-irradiation-induced intergranular phosphorus segregation and hardening on embrittlement in reactor pressure vessel steels, *Acta Mater.* 56 (2008) 4510–4521. doi:10.1016/j.actamat.2008.05.026.

[28] C. English, Final report of the PISA project: phosphorus influence on steels ageing (PISA), European Commission, 2005.

[29] C. English, S. Ortner, G. Gage, W. Server, S. Rosinski, Review of Phosphorus Segregation and Intergranular Embrittlement in Reactor Pressure Vessel Steels, in: S. Rosinski, M. Grossbeck, T. Allen, A. Kumar (Eds.), *Eff. Radiat. Mater. 20th Int. Symp.*, ASTM International, 100 Barr Harbor Drive, PO Box C700, West Conshohocken, PA 19428-2959, 2001: pp. 151-151–23. doi:10.1520/STP10531S.

[30] C. Lu, T. Yang, K. Jin, N. Gao, P. Xiu, Y. Zhang, F. Gao, H. Bei, W.J. Weber, K. Sun, Y. Dong, L. Wang, Radiation-induced segregation on defect clusters in single-phase concentrated solid-solution alloys, *Acta Mater.* 127 (2017) 98–107. doi:10.1016/j.actamat.2017.01.019.

[31] C.M. Barr, G.A. Vetterick, K.A. Unocic, K. Hattar, X.-M. Bai, M.L. Taheri, Anisotropic radiation-induced segregation in 316L austenitic stainless steel with grain boundary character, *Acta Mater.* 67 (2014) 145–155. doi:10.1016/j.actamat.2013.11.060.

[32] H. Wiedersich, P.R. Okamoto, N.Q. Lam, A theory of radiation-induced segregation in concentrated alloys, *J. Nucl. Mater.* 83 (1979) 98–108. doi:10.1016/0022-3115(79)90596-8.

[33] T.R. Allen, J.T. Busby, G.S. Was, E.A. Kenik, On the mechanism of radiation-induced segregation in austenitic Fe–Cr–Ni alloys, *J. Nucl. Mater.* 255 (1998) 44–58. doi:10.1016/S0022-3115(98)00010-5.

[34] V. Kuksenko, Model oriented irradiation experiments in Fe-Cr model alloys, PhD thesis, Université de Rouen, 2011.

[35] W.G. Wolfer, 1.01 - Fundamental Properties of Defects in Metals A2 - Konings, Rudy J.M., in: *Compr. Nucl. Mater.*, Elsevier, Oxford, 2012: pp. 1–45.

- [36] R.E. Stoller, L.R. Greenwood, Subcascade formation in displacement cascade simulations: Implications for fusion reactor materials, *J. Nucl. Mater.* 271–272 (1999) 57–62. doi:10.1016/S0022-3115(98)00730-2.
- [37] G.S. Was, *Fundamentals of Radiation Materials Science: Metals and Alloys*, Springer, 2007.
- [38] G.H. Kinchin, R.S. Pease, The mechanism of the irradiation disordering of alloys, *J. Nucl. Energy* 1954. 1 (1955) 200–202. doi:10.1016/0891-3919(54)90016-9.
- [39] Seeger A., On the theory of radiation damage and radiation hardening, in: *Proc. Second U. N. Int. Conf. Peac. Uses At. Energy*, Geneva, 1958.
- [40] R.E. Stoller, 1.11 - Primary Radiation Damage Formation A2 - Konings, Rudy J.M., in: *Compr. Nucl. Mater.*, Elsevier, Oxford, 2012: pp. 293–332.
- [41] ASTM standart E521-96. Standard practice for neutron radiation damage simulation by charged-particle irradiation, 2009.
- [42] P. Olsson, C.S. Becquart, C. Domain, Ab initio threshold displacement energies in iron, *Mater. Res. Lett.* 4 (2016) 219–225. doi:10.1080/21663831.2016.1181680.
- [43] A. Hardouin Duparc, C. Moingeon, N. Smetniansky-de-Grande, A. Barbu, Microstructure modelling of ferritic alloys under high flux 1 MeV electron irradiations, *J. Nucl. Mater.* 302 (2002) 143–155. doi:10.1016/S0022-3115(02)00776-6.
- [44] L. Malerba, Molecular dynamics simulation of displacement cascades in  $\alpha$ -Fe: A critical review, *J. Nucl. Mater.* 351 (2006) 28–38. doi:10.1016/j.jnucmat.2006.02.023.
- [45] C. Domain, C.S. Becquart, Ab initio calculations of defects in Fe and dilute Fe-Cu alloys, *Phys. Rev. B.* 65 (2001). doi:10.1103/PhysRevB.65.024103.
- [46] A. Vehanen, P. Hautojärvi, J. Johansson, J. Yli-Kauppila, P. Moser, Vacancies and carbon impurities in  $\alpha$  - iron: Electron irradiation, *Phys. Rev. B.* 25 (1982) 762–780. doi:10.1103/PhysRevB.25.762.
- [47] A.A. Vasiliev, V.V. Rybin, A.A. Zisman, The nature of the phosphorus atom mobility in bcc iron irradiated at low temperatures, *J. Nucl. Mater.* 231 (1996) 249–253. doi:10.1016/0022-3115(96)00201-2.
- [48] R.A. Johnson, Interstitials and Vacancies in  $\alpha$  Iron, *Phys. Rev.* 134 (1964) A1329–A1336. doi:10.1103/PhysRev.134.A1329.
- [49] G.J. Ackland, D.J. Bacon, A.F. Calder, T. Harry, Computer simulation of point defect properties in dilute Fe—Cu alloy using a many-body interatomic potential, *Philos. Mag. A.* 75 (1997) 713–732. doi:10.1080/01418619708207198.

- [50] J.M. Soler, E. Artacho, J.D. Gale, A. García, J. Junquera, P. Ordejón, Daniel Sánchez-Portal, The SIESTA method for ab initio order- N materials simulation, *J. Phys. Condens. Matter.* 14 (2002) 2745. doi:10.1088/0953-8984/14/11/302.
- [51] C.-C. Fu, F. Willaime, P. Ordejón, Stability and Mobility of Mono- and Di-Interstitials in  $\alpha$ -Fe, *Phys. Rev. Lett.* 92 (2004). doi:10.1103/PhysRevLett.92.175503.
- [52] F. Willaime, C.C. Fu, M.C. Marinica, J. Dalla Torre, Stability and mobility of self-interstitials and small interstitial clusters in  $\alpha$ -iron: ab initio and empirical potential calculations, *Nucl. Instrum. Methods Phys. Res. Sect. B Beam Interact. Mater. At.* 228 (2005) 92–99. doi:10.1016/j.nimb.2004.10.028.
- [53] P. Paufler, R. W. Cahn, P. Haasen (eds). *Physical metallurgy* 3rd revised and enlarged edition. North-Holland physics publishing, Amsterdam, Oxford, New York, Tokyo 1983. doi:10.1002/crat.2170200229.
- [54] H. Ullmaier, ed., *Atomic Defects in Metals*, Springer-Verlag, Berlin, 1991. doi:10.1007/b37800.
- [55] Druce S.G., English C.A., Foreman A.J.E., McElroy R.J., Vatter E.A., Bolton C.J., Buswell J.T., Jones R.B., The modelling of irradiation-enhanced phosphorus segregation in neutron irradiated reactor pressure vessel submerged-arc weld, in: *Eff. Radiat. Mater.* 17th Int. Symp. ASTM, West Conshohocken, PA, 1996.
- [56] J.M. Perks, C.A.English, M.L.Jenkins, 14th Symp. *Eff. Radiat. Mater.* ASTM. West Conshohocken, PA, 1989.
- [57] S.M. Murphy, J.M. Perks, Analysis of phosphorus segregation in ion-irradiated nickel, *J. Nucl. Mater.* 171 (1990) 360–372. doi:10.1016/0022-3115(90)90382-W.
- [58] H. Hurchand, S.D. Kenny, C.F. Sanz-Navarro, R. Smith, P.E.J. Flewitt, The influence of P solutes on an irradiated  $\alpha$ -Fe matrix, *Nucl. Instrum. Methods Phys. Res. Sect. B Beam Interact. Mater. At.* 229 (2005) 92–102. doi:10.1016/j.nimb.2004.11.010.
- [59] E. Meslin, C.-C. Fu, A. Barbu, F. Gao, F. Willaime, Theoretical study of atomic transport via interstitials in dilute Fe – P alloys, *Phys. Rev. B.* 75 (2007). doi:10.1103/PhysRevB.75.094303.
- [60] C. Domain, C.S. Becquart, Diffusion of phosphorus in  $\alpha$ -Fe: An ab initio study, *Phys. Rev. B.* 71 (2005) 214109. doi:10.1103/PhysRevB.71.214109.
- [61] S.M.J. Gordon, H. Hurchand, S.D. Kenny, R. Smith, Diffusion of radiation damage in Fe–P systems, *Nucl. Instrum. Methods Phys. Res. Sect. B Beam Interact. Mater. At.* 228 (2005) 131–136. doi:10.1016/j.nimb.2004.10.034.

- [62] S. Song, R.G. Faulkner, Diffusion Characteristics of Interstitial and Vacancy Based Complexes, Defect Diffus. Forum. 143–147 (1997) 149–154. doi:10.4028/www.scientific.net/DDF.143-147.149.
- [63] Z. Lu, R.G. Faulkner, Irradiation Assisted Grain Boundary Segregation in Steels, Materials Research Society, Warrendale, PA, USA, 2008.
- [64] R.G. Faulkner, S. Song, P.E.J. Flewitt, A model describing neutron irradiation-induced segregation to grain boundaries in dilute alloys, Metall. Mater. Trans. A. 27 (1996) 3381–3390. doi:10.1007/BF02595431.
- [65] S. Song, Radiation-induced grain boundary segregation in dilute alloys, PhD thesis, Loughborough University, UK, 1995. Available at: <https://dspace.lboro.ac.uk/dspace-jspui/handle/2134/10475> (accessed April 28, 2017).
- [66] R.G. Faulkner, N.C. Waite, E.A. Little, T.S. Morgan, Radiation-induced grain boundary segregation in dilute alloys, Mater. Sci. Eng. A. 171 (1993) 241–248. doi:10.1016/0921-5093(93)90411-7.
- [67] R.G. Faulkner, S. Song, P.E.J. Flewitt, M. Victoria, P. Marmy, Grain boundary segregation under neutron irradiation in dilute alloys, J. Nucl. Mater. 255 (1998) 189–209. doi:10.1016/S0022-3115(98)00022-1.
- [68] R.G. Faulkner, S.-H. Song, P.E.J. Flewitt, Determination of impurity–point defect binding energies in alloys, Mater. Sci. Technol. 12 (1996) 904–910. doi:10.1179/mst.1996.12.11.904.
- [69] G.J. Ackland, M.I. Mendeleev, D.J. Srolovitz, S. Han, A.V. Barashev, Development of an interatomic potential for phosphorus impurities in  $\alpha$ -iron, J. Phys. Condens. Matter. 16 (2004) S2629–S2642. doi:10.1088/0953-8984/16/27/003.
- [70] L. Messina, M. Nastar, T. Garnier, C. Domain, P. Olsson, Exact ab initio transport coefficients in bcc Fe – X ( X = Cr , Cu , Mn , Ni , P , Si ) dilute alloys, Phys. Rev. B. 90 (2014). doi:10.1103/PhysRevB.90.104203.
- [71] L. Messina, M. Nastar, P. Olsson, Ab initio-based investigation of solute-dumbbell transport and radiation induced segregation in Fe-X (X= Cr, Cu, Mn, Ni, P, Si) dilute alloys, (2015).
- [72] M. Nastar, F. Soisson, 1.18 - Radiation-Induced Segregation, in: R.J.M. Konings (Ed.), Compr. Nucl. Mater., Elsevier, Oxford, 2012.
- [73] L.E. Rehn, P.R. Okamoto, D.I. Potter, H. Wiedersich, Effect of solute misfit and temperature on irradiation-induced segregation in binary Ni alloys, J. Nucl. Mater. 74 (1978) 242–251. doi:10.1016/0022-3115(78)90363-X.

- [74] P.R. Okamoto, L.E. Rehn, Radiation-induced segregation in binary and ternary alloys, *J. Nucl. Mater.* 83 (1979) 2–23. doi:10.1016/0022-3115(79)90587-7.
- [75] P.R. Okamoto, H. Wiedersich, Segregation of alloying elements to free surfaces during irradiation, *J. Nucl. Mater.* 53 (1974) 336–345. doi:10.1016/0022-3115(74)90267-0.
- [76] H. Takahashi, S. Ohnuki, T. Takeyama, Radiation-induced segregation at internal sinks in electron irradiated binary alloys, *J. Nucl. Mater.* 104 (1981) 1415–1419. doi:10.1016/0022-3115(82)90798-X.
- [77] Z. Lu, R.G. Faulkner, N. Sakaguchi, H. Kinoshita, H. Takahashi, P.E.J. Flewitt, Effect of hafnium on radiation-induced inter-granular segregation in ferritic steel, *J. Nucl. Mater.* 351 (2006) 155–161. doi:10.1016/j.jnucmat.2006.02.026.
- [78] J.L. Brimhall, D.R. Baer, R.H. Jones, Radiation induced phosphorus segregation in austenitic and ferritic alloys, *J. Nucl. Mater.* 122 (1984) 196–200. doi:10.1016/0022-3115(84)90595-6.
- [79] E.A. Little, Microstructural evolution in irradiated ferritic-martensitic steels: transitions to high dose behaviour, *J. Nucl. Mater.* 206 (1993) 324–334. doi:10.1016/0022-3115(93)90131-H.
- [80] A. Etienne, B. Radiguet, N.J. Cunningham, G.R. Odette, P. Pareige, Atomic scale investigation of radiation-induced segregation in austenitic stainless steels, *J. Nucl. Mater.* 406 (2010) 244–250. doi:10.1016/j.jnucmat.2010.08.043.
- [81] R.G. Faulkner, R.B. Jones, Z. Lu, P.E.J. Flewitt, Grain boundary impurity segregation and neutron irradiation effects in ferritic alloys, *Philos. Mag.* 85 (2005) 2065–2099. doi:10.1080/14786430412331331853.
- [82] S. Ohnuki, H. Takahashi, T. Takeyama, Void swelling and segregation of solute in ion-irradiated ferritic steels, *J. Nucl. Mater.* 104 (1981) 1121–1125. doi:10.1016/0022-3115(82)90751-6.
- [83] R.E. Clausing, L. Heatherly, R.G. Faulkner, A.F. Rowcliffe, K. Farrell, Radiation-induced segregation in HT-9 martensitic steel, *J. Nucl. Mater.* 141–143 (1986) 978–981. doi:10.1016/0022-3115(86)90128-5.
- [84] G. Gupta, Z. Jiao, A.N. Ham, J.T. Busby, G.S. Was, Microstructural evolution of proton irradiated T91, *J. Nucl. Mater.* 351 (2006) 162–173. doi:10.1016/j.jnucmat.2006.02.028.
- [85] Z. Lu, R.G. Faulkner, G. Was, B.D. Wirth, Irradiation-induced grain boundary chromium microchemistry in high alloy ferritic steels, *Scr. Mater.* 58 (2008) 878–881. doi:10.1016/j.scriptamat.2008.01.004.

- [86] A.J. Ardell, Radiation-Induced Solute Segregation in Alloys, in: V. Ghetta, D. Gorse, D. Mazière, V. Pontikis (Eds.), *Mater. Issues Gener. IV Syst.*, Springer Netherlands, Dordrecht, 2008: pp. 285–310. doi:10.1007/978-1-4020-8422-5\_15.
- [87] E.A. Kuleshova, B.A. Gurovich, Z.V. Lavrukhina, M.A. Saltykov, S.V. Fedotova, A.N. Khodan, Assessment of segregation kinetics in water-moderated reactors pressure vessel steels under long-term operation, *J. Nucl. Mater.* 477 (2016) 110–122. doi:10.1016/j.jnucmat.2016.04.060.
- [88] K. Ebihara, M. Yamaguchi, Y. Nishiyama, K. Onizawa, H. Matsuzawa, Effect of carbon on irradiation-induced grain-boundary phosphorus segregation in reactor pressure vessel steels using first-principles-based rate theory model, *J. Nucl. Mater.* 414 (2011) 328–335. doi:10.1016/j.jnucmat.2011.05.001.
- [89] Bischler P.J., Wild R.K., A microstructural study of phosphorus segregation and intergranular fracture in neutron irradiated reactor pressure vessel submerged-arc weld, in: *Eff. Radiat. Mater. 17th Int. Symp. ASTM STP 1270 Gelles RK Nanstad Kumar EA Little*, American Society for Testing and Materials, West Conshohocken, PA, 1996.
- [90] A.P. Sutton, R.W. Balluffi, *Interfaces in Crystalline Materials*, OUP Oxford, 2006.
- [91] L. Priester, *Grain boundaries from theory to engineering*, Springer, Dordrecht; New York, 2013. <http://dx.doi.org/10.1007/978-94-007-4969-6> (accessed February 17, 2017).
- [92] M.L. Kronberg, F.H. Wilson, Secondary recrystallization in copper, *AIME TRANS.* 185 (1949) 501–514.
- [93] C. Günster, *Magnetically and Capillary Driven Grain Boundary Motion in Zinc Bicrystals*, Cuvillier Verlag, 2013.
- [94] D. Wolf, Structure and energy of general grain boundaries in bcc metals, *J. Appl. Phys.* 69 (1991) 185–196. doi:10.1063/1.347741.
- [95] D. Wolf, Structure-energy correlation for grain boundaries in f.c.c. metals—IV. Asymmetrical twist (general) boundaries, *Acta Metall. Mater.* 38 (1990) 791–798. doi:10.1016/0956-7151(90)90031-B.
- [96] K.L. Merkle, D. Wolf, Low-energy configurations of symmetric and asymmetric tilt grain boundaries, *Philos. Mag. A.* 65 (1992) 513–530. doi:10.1080/01418619208201536.
- [97] M.A. Tschopp, D.L. McDowell, Structural unit and faceting description of  $\Sigma 3$  asymmetric tilt grain boundaries, *J. Mater. Sci.* 42 (2007) 7806–7811. doi:10.1007/s10853-007-1626-6.
- [98] T. Schober, R.W. Balluffi, Quantitative observation of misfit dislocation arrays in low and high angle twist grain boundaries, *Philos. Mag.* 21 (1970) 109–123. doi:10.1080/14786437008238400.

- [99] Z.-H. Liu, Y.-X. Feng, J.-X. Shang, Characterizing twist grain boundaries in BCC Nb by molecular simulation: Structure and shear deformation, *Appl. Surf. Sci.* 370 (2016) 19–24. doi:10.1016/j.apsusc.2016.02.097.
- [100] P. Lejcek, *Grain Boundary Segregation in Metals*, Springer Berlin Heidelberg, Berlin, Heidelberg, 2010. [101] J.W. Gibbs, *The collected works of J. Willard Gibbs.*, Yale University Press, New Haven, 1948.
- [102] S. Hofmann, P. Lejček, J. Adámek, Grain boundary segregation in [100] symmetrical tilt bicrystals of an Fe-Si alloy, *Surf. Interface Anal.* 19 (1992) 601–606. doi:10.1002/sia.7401901112.
- [103] W. Swiatnicki, S. Lartigue-Korinek, J.Y. Laval, Grain boundary structure and intergranular segregation in  $\text{Al}_2\text{O}_3$ , *Acta Metall. Mater.* 43 (1995) 795–805. doi:10.1016/0956-7151(94)00256-H.
- [104] S. Suzuki, K. Abiko, H. Kimura, Phosphorus segregation related to the grain boundary structure in an Fe-P alloy, *Scr. Metall.* 15(1981)1139–1143. doi:10.1016/0036-9748(81)90175-7.
- [105] G.O. Williams, V. Randle, J.R. Cowan, P. Spellward, The role of misorientation and phosphorus content on grain growth and intergranular fracture in iron–carbon–phosphorus alloys, *J. Microsc.* 213 (2004) 321–327. doi:10.1111/j.0022-2720.2004.01301.x.



## Chapter 2. Material and experimental techniques

This work is dedicated to understand the influence of ageing conditions and GB geometry on the intergranular segregation of phosphorus in the Fe-0.034 at.% P-0.01 at.% C model alloy. The description of the investigated model alloy is given in the first section of this chapter: the elaboration, chemical composition and the microstructure in the as-received state and ageing conditions.

The second part of this chapter describes Atom Probe Tomography (APT), which is the main tool in this research to determine the relationship between GB structure and the level of GB segregation. The working principles and application of APT to study the intergranular segregation are given in the second part of this chapter.

Scanning Transmission Electron Microscopy (STEM), described in the third section, was used to characterize crystal defects and to measure the GB segregation along irradiation profile using Energy-Dispersive X-ray Spectroscopy (EDS).

To provide the atomic-scale study of GB segregation, the site-specific sample extraction was used. The specimen preparation using SEM-FIB (Scanning Electron Microscopy/Focused Ion Beam) lift-out process is given in the fourth section of this chapter. Finally, the determination of GB geometry using correlative Transmission Kikuchi Diffraction (TKD) and APT is described in details.

## 2.1 Materials: model alloy

### 2.1.1 Elaboration

The material studied in this work is a high purity Fe-0.034 at.% P-0.01 at.% C model alloy. The ingot of  $110 \times 110 \times 80 \text{ mm}^3$  supplied by OCAS (Belgium) was cast in a vacuum induction furnace. After reheating at  $1200^\circ\text{C}$ , it was hot rolled in 6 passes to 20 mm thickness. Then it was air-cooled down to the room temperature. The nominal chemical composition of the model alloy, which was measured in OCAS using optical emission spectrometry (OES) and X-ray fluorescence is given in Table 2.1.

**Table 2.1.** Chemical composition of the Fe-0.034 at.% P-0.01 at.% C alloy determined by OES (at.%, Fe bal.)

P	C	Si	Mn	S	Cr	Ni	Al	Ti	O	N
0.0343	0.007	0.004	0.0014	0.0009	0.0037	0.0068	0.0093	0.0017	0.0105	0.002

The composition of the as-received model alloy was checked by Atom Probe Tomography (APT) analysis before any treatment (Table 2.2).

**Table 2.2.** Chemical composition of the Fe-0.034 at.% P-0.01 at.% C alloy determined by APT (at.%, Fe bal.)

P	C	Si	Mn	S	Cr	Ni	Al	Ti	O	N
$0.032 \pm 0.01$	$0.007 \pm 0.004$	-	0.0048	-	0.0039	-	0.010	-	0.025	0.011

The concentration of phosphorus ( $0.032 \pm 0.01$  at.%) and carbon atoms ( $0.007 \pm 0.004$  at.%) in the bulk is close to the nominal composition. However, both phosphorus and carbon concentrations vary from one volume to another (Fig. 2.1). Since these fluctuations are larger than the standard error of the APT analysis, it indicates that the bulk concentration of phosphorus and carbon can vary through volume. This can be caused by a number of complex processes during casting and hot-rolling. We will not discuss them further and assume that the initial bulk concentration of phosphorus and carbon atoms is non-variable and equal to the average value.

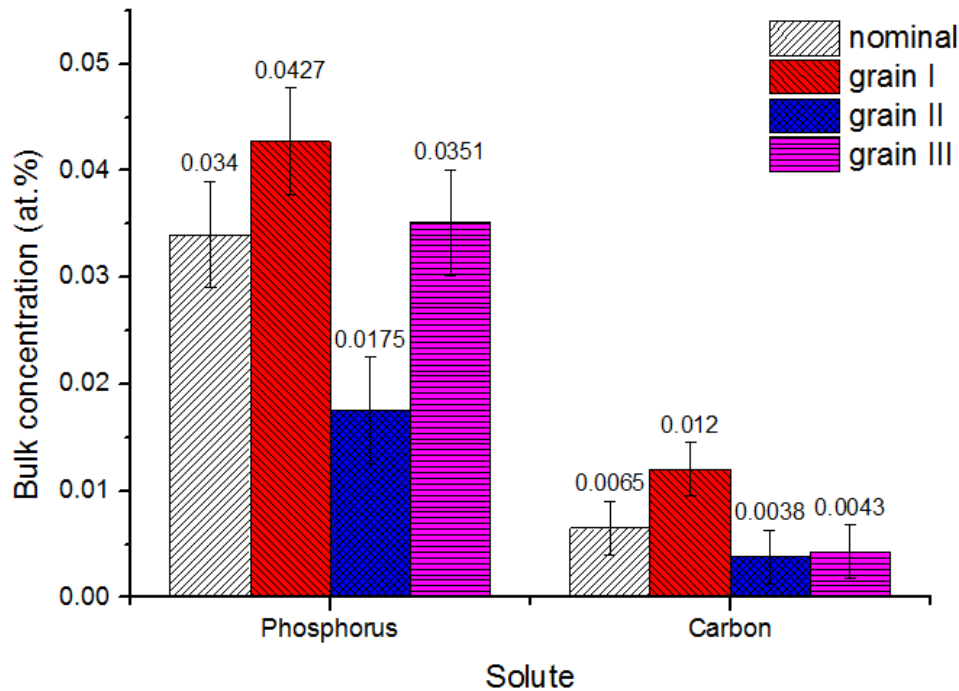


**Fig. 2.1.** Bulk concentrations of phosphorus and carbon atoms measured by APT from the different volumes (grains)

APT mass spectrum analysis revealed a small peak at 14 a.m.u. (atomic mass unit). The absence of peaks at 14.5 and 15 a.m.u. (minor isotopes of Si) suggests that it is  $^{14}\text{N}^+$ . However, due to the low concentration of this element in a bulk ( $0.01 \pm 0.005$  at.%), the presence of some Si cannot be excluded unambiguously. The concentration of other detected elements (Cr, Al, O) is less than  $< 0.01$  at.% and is in good agreement with OES measurement, excepted for O and Mn. The O concentration measured by APT ( $0.025 \pm 0.005$  at.%) is higher than the one measured by OES (0.0105 at.%). It is possible that the APT value is slightly overestimated due to the oxidation of the tip. The amount of Mn detected by APT (0.0048 at%) is three times larger than measured by OES (0.0014 at%). In comparison with OES, no S, Ni and Ti are detected.

Specimens in the form of plates of  $4 \times 4 \times 2$  mm<sup>3</sup> were cut and polished with abrasive paper down to 4000 grit, followed by polishing using a diamond paste of 3  $\mu\text{m}$  and 1  $\mu\text{m}$  size. In the final step, the samples were polished using an aluminum oxide polishing paste of 0.1  $\mu\text{m}$  grit size and cleaned in ethanol in an ultrasonic cleaner.

The as-received Fe-0.034 at.% P-0.01 at.% C model alloy has a coarse-grained ( $\sim 200$   $\mu\text{m}$ ) ferritic microstructure. Fig. 2.2 shows the surface images of the same area obtained using Scanning Electron microscope (SEM) in the secondary electrons (SE) mode and the Electron Backscatter Diffraction (EBSD) grain orientation map.

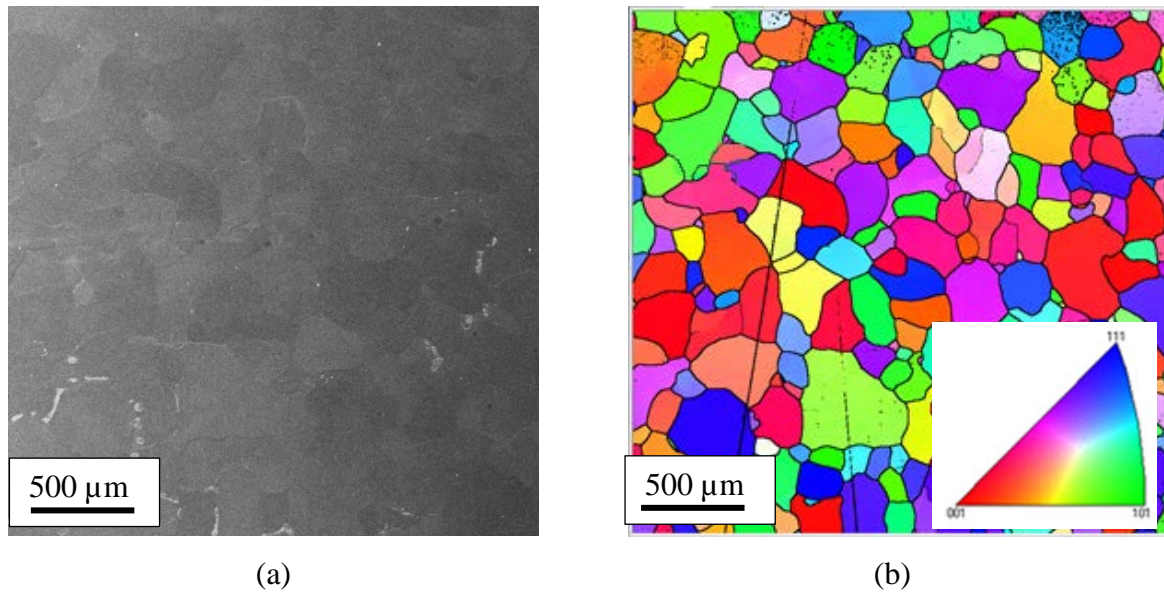


**Fig. 2.2.** (a) SEM-SE image and (b) EBSD grain orientation map displayed in inverse pole figure (IPF) coloring of the as-received Fe-0.034 at.% P-0.01 at.% C model alloy

The distribution of phosphorus and carbon atoms in the bulk was analyzed by APT and has been found to be homogenous at nm scale (Fig. 2.3), considering that the continuous enrichment along the crystallographic poles is a well-known reconstruction artefact. More details related to the APT reconstruction artefacts are given in section 2.2.

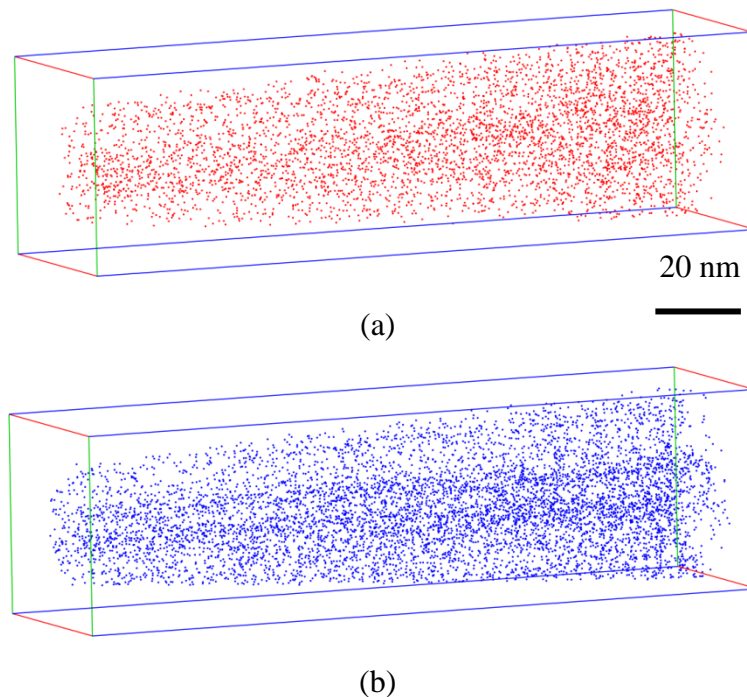


**Fig. 2.3.** Distribution of (a) carbon (red) and (b) phosphorus (blue) atoms in the as-received Fe-0.034 at.% P-0.01 at.% C model alloy. Considering the enrichment along crystallographic poles as a well-known reconstruction artefact, the distributions of P and C atoms are homogeneous.



### 2.1.3 Ion irradiation

The samples for irradiation experiments were prepared in the form of plates of  $4 \times 4 \times 2$  mm<sup>3</sup> and preliminarily polished and cleaned as described in section 2.1.1. The specimens were placed in a particular holder, specially made for such irradiations (Fig. 2.5).

The ion irradiations were performed at JANNuS-Saclay (Joint Accelerators for Nanoscience and Nuclear Simulation) at CEA (Commissariat à l'énergie atomique et aux énergies alternatives) and supported by the French Network EMIR (Réseau National d'accélérateurs pour l'Etudes des Matériaux sous IRradiation) [6]. Irradiations were performed with Epyméthée accelerator in the 3F chamber. In this chamber, the angle of incidence of ions is 15° and the vacuum was 10<sup>-7</sup> mBar.

10 MeV Fe<sup>5+</sup> ions were used for the production of self-ion displacement damage in order to avoid the introduction of foreign atoms which could interact with the solute atoms and change the GB segregation level. The ion irradiation temperature (450°C) is higher than the neutron irradiation temperature of RPV steel in the test reactors (300°C). This higher temperature allows

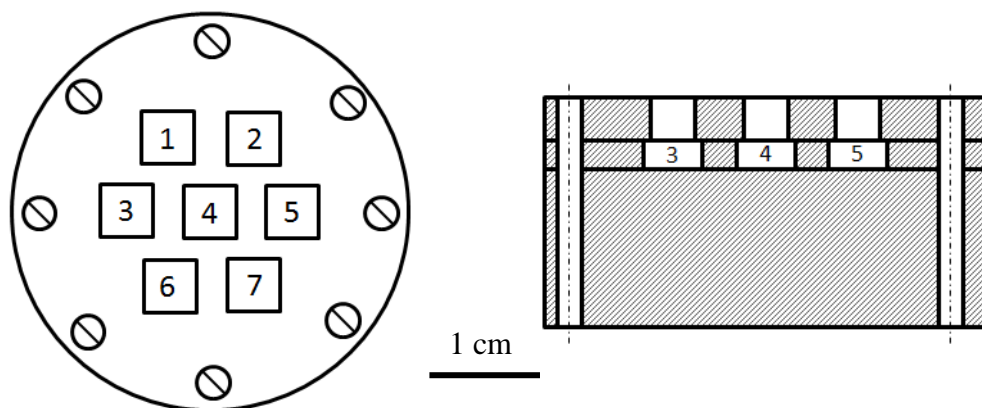


Fig. 2.5. Schematic image of the specimens holder used for irradiation

to compensate dose rate effect and thus facilitate the comparison of these results to the ones reported in literature about neutron irradiated materials [7].

The target flux was  $\sim 10^{11}$  ions.cm<sup>-2</sup>.s<sup>-1</sup>. However, the measurement of flux in JANNUS-Saclay was biased due to inaccurate Faraday cups detector and the flux and fluences were overestimated. The correction factor to get the true values was estimated by CEA from 0.4 to 0.8. Finally, the ion flux during or irradiation range between  $0.8 \times 10^{11}$  to  $1.6 \times 10^{11}$  ions/cm<sup>2</sup>/s. We will consider the average value in the following sections:  $(1.2 \pm 0.4) \times 10^{11}$  ions/cm<sup>2</sup>/s. Three irradiation durations were used (2500s, 12500s, 25000s),

corresponding to three different fluences:  $3 \times 10^{14} \text{ ions/cm}^2$ ,  $1.5 \times 10^{15} \text{ ions/cm}^2$  and  $3 \times 10^{15} \text{ ions/cm}^2$ , respectively.

The SRIM (Stopping and Range of Ions in Matter) software [8] was used to estimate the dose rate and dose in terms of displacements per atoms (dpa). Calculations were performed using a displacement threshold energy of 40eV as recommended by ASTM [9]. According to [10], the "Quick calculation" mode was used. The results are reported in Fig. 2.6. As it will be shown in the 4<sup>th</sup> section of this chapter, APT samples are taken at a depth of about 750nm. At this depth, the average value of irradiation flux is  $3.0 \times 10^{-5} \text{ dpa/s}$ . The average irradiation doses are 0.075 dpa, 0.375 dpa and 0.75 dpa.

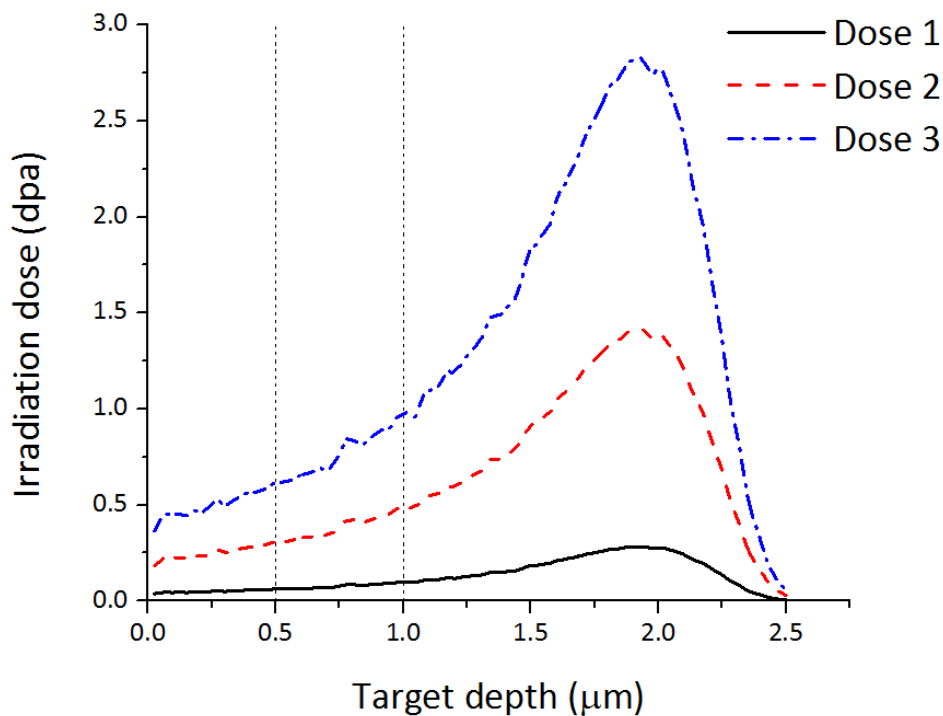


**Fig. 2.6.** Dose (in dpa) as a function of depth during irradiations by 10MeV  $\text{Fe}^{5+}$  ions. The analysed area is highlighted by two vertical dash lines. The calculation was done with SRIM 2013 software using "Quick Calculation" mode.

## 2.2 Atom probe tomography

Atom Probe Tomography (APT) is one of the most powerful analytical technique to study the chemical heterogeneities in materials at sub-nm scale [11,12]. The capabilities of APT to combine three-dimensional (3D) visualization of microstructure at atomic scale with accurate quantitative data analysis make the APT attractive for investigation of GB segregation. With the development of site-specific focused ion-beam (FIB) specimen

preparation, which is more precise than conventional methods using electro-polishing, it became possible to explore individual grain boundaries and other areas of interest [13-20].

In this work, a Local Electrode Atom Probe (LEAP) was used to map the position of single solute atoms in the bcc iron matrix and to image the grain boundary segregation in three dimensions. This section gives a brief introduction to the underlying principles of atom probe tomography, the reconstruction artefacts and the GB segregation analysis.

### 2.2.1 Principle of atom probe tomography

The schematic geometry of LEAP is shown in Fig. 2.7. The sharp needle-shaped specimen (radius of tip < 100 nm) is placed in the analytical chamber under high vacuum (residual pressure <  $10^{-8}$  Pa) at cryogenic temperature (< 80K).

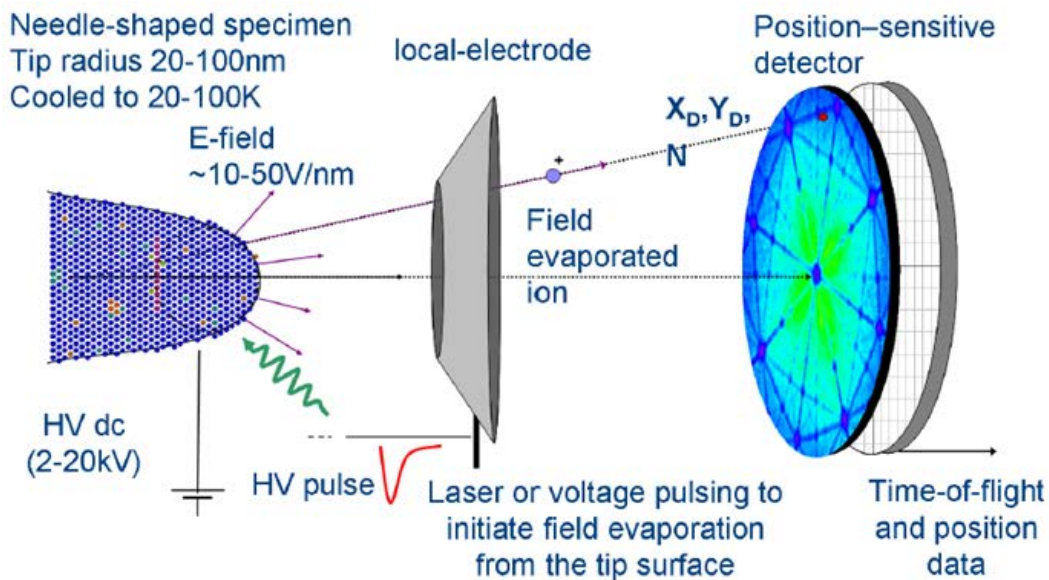


**Fig. 2.7.** Schematic geometry of an atom probe (image not to scale) [21]

During the analysis, a positive electrical potential  $V_{DC}$  is applied to the specimen and induces an electric field at the sample surface. The field generated is described by the simple equation [11]:

$$F = \frac{V}{k_f R} \quad (12)$$

where  $V$  is the total applied voltage,  $R$  is the tip radius and  $k_f$  is a field factor which characterizes the deviation of the tip shape from the hemisphere.

If this field is higher than the evaporation field of the atoms, surface atoms are ionized and are removed from the needle surface. The phenomenon is called “field evaporation”. In practical, the field generated by  $V_{DC}$  is too small to evaporate atoms. In addition, short duration negative electrical pulses,  $V_p = (0.2 \text{ to } 0.25) V_{DC}$ , are applied on the local electrode. Only the total voltage ( $V_{DC}$  and  $V_p$ ) generates a sufficient electrical field to evaporate surface atoms. This allows to control the time of departure of atoms from the sample surface (only during pulses).

The evaporated ions are accelerated by the electric field toward a delay line detector with microchannel plates. The detector provides information about the time of flight and impact position of each ion.

To determine the chemical nature of a detected ion, time-of-flight mass spectrometry is used. The time-of-flight of each ion is measured as the difference between the moment of detection of ions on the microchannel plate and the moment at which the pulse is applied to generate the evaporation. Assuming that the potential energy of an ion is completely converted into kinetic energy, the mass-to charge ratio is determined from energy conservation relationship:

$$neV = \frac{1}{2}mv^2 = \frac{1}{2}m \frac{L^2}{t^2} \quad (13)$$

where  $n$  is the ion charge state,  $e$  is the electrical elementary charge,  $V$  is the total applied voltage,  $m$  is the ion mass,  $v$  is the velocity, given by  $v = L/t$ , where  $L$  is the flight length and  $t$  is the time-of-flight.

Hence, the mass-to-charge-state ratio of detected ion is given by:

$$\frac{m}{n} = 2eV \frac{t^2}{L^2} \quad (14)$$

The detected atoms are represented in the form of a mass spectrum (Fig. 2.8). After identification of each isotope and background removing, the total concentration of elements is simply calculated from the proportion of atoms.

The uncertainty on the measured concentration of the element  $i$ , considering only statistical variation, is given by:

$$\sigma_i = \sqrt{\frac{X_i(1 - X_i)}{N_{at}}} \quad (15)$$

where  $X_i$  is the measured concentration of  $i$ -atoms and  $N_{at}$  is the total number of atoms in analyzed volume.

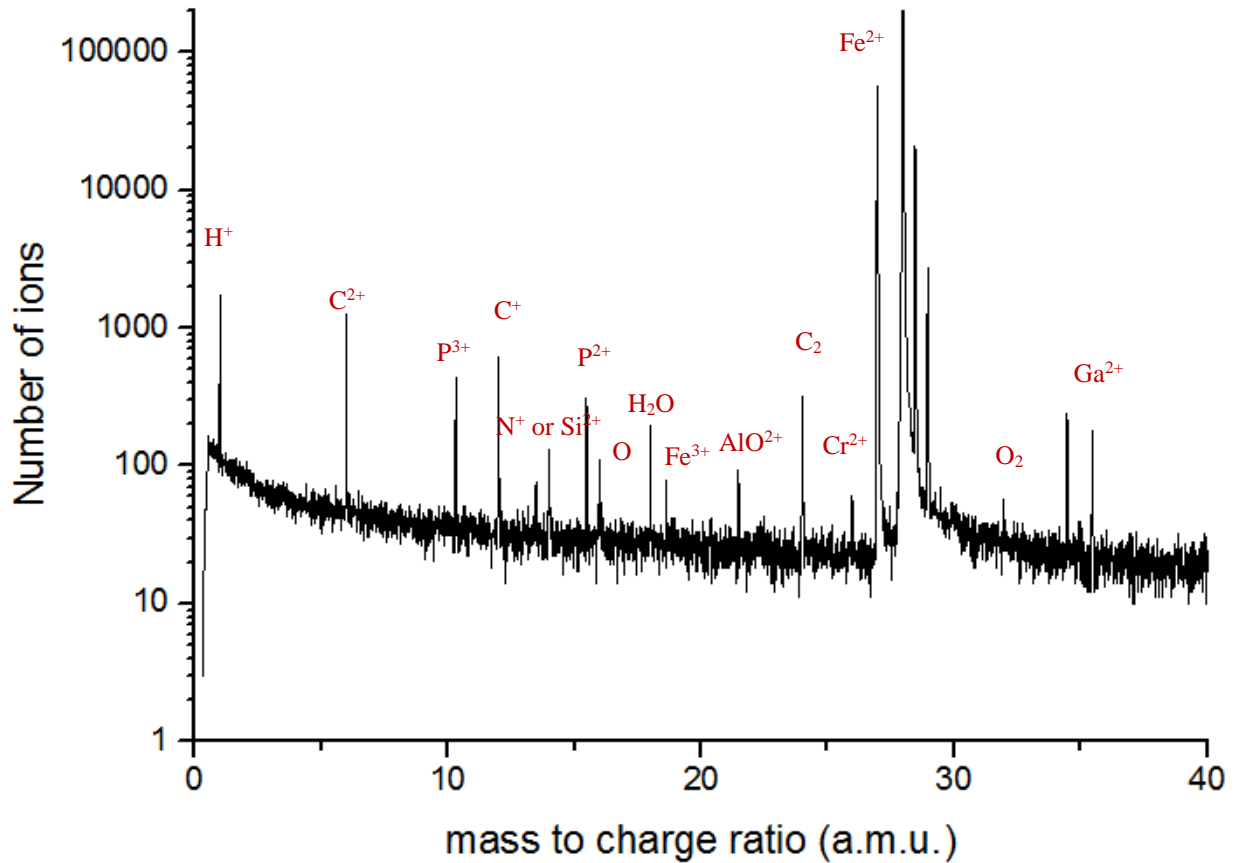


Fig. 2.8. Mass spectrum obtained from an analysis of the Fe-0.034 at.% P-0.01 at.% C model alloy

### 2.2.2 Experimental conditions

In the present work, a LEAP 4000 HR, from Cameca has been used. The analyses were performed in voltage mode. The pulse fraction and the pulse repetition rate were 20% and 200 kHz, respectively. To remove the surface oxides, the initial evaporation temperature was around 80 K, and then cooled down to 50 K.

To ensure that the experimental conditions provide reliable compositions, calibration experiments were performed at pulse fractions equal to 15% and 20% with a range of specimen temperature from 20 K to 80 K. The results are summarized on Fig. 2.9. The material used for the calibration was a Fe-0.018 at.% P-0.007 at.% C model alloy after hot-rolling with subsequent tempering at 650°C during 2h. The microstructure of the material is coarse-grained iron-based BCC. The distributions of phosphorus and carbon in the 3D reconstructed volumes are homogeneous.

No influence of pulse fraction and temperature was observed at temperatures below 60 K. Thus, the temperature of analysis was fixed to 50 K to get the reliable compositions and to limit the risk of fracture of the samples.

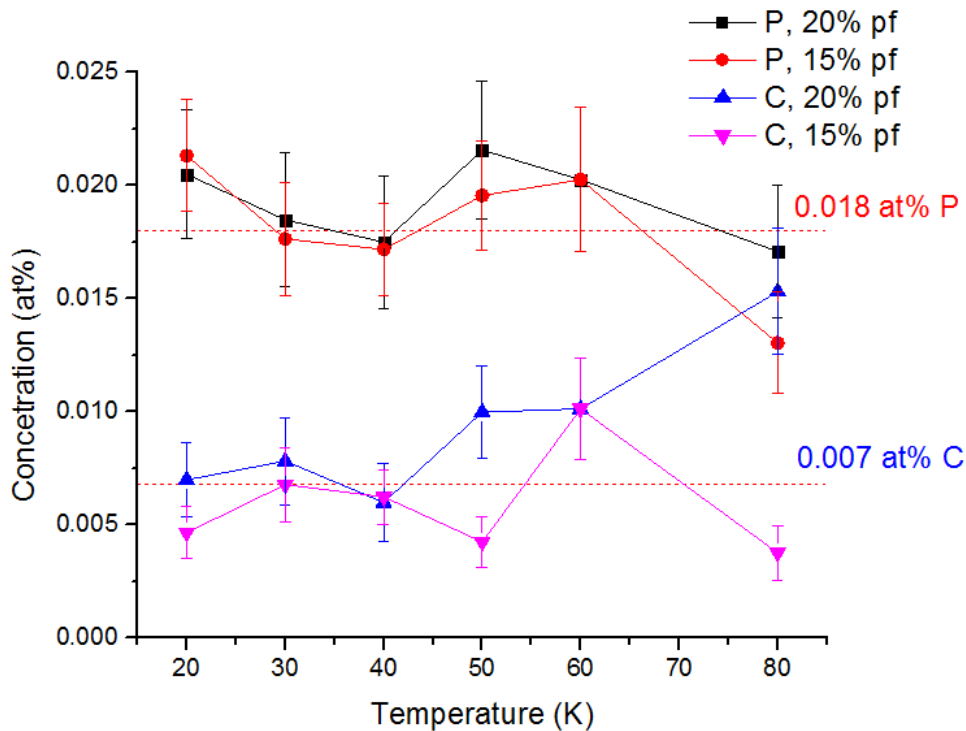


**Fig. 2.9.** Temperature dependence of measured P and C bulk concentrations in the Fe–0.018 at.% P–0.007 at.% C model alloy at pulse fractions (pf) of 20% and 15%. The nominal bulk concentrations are shown with dashed lines

### 2.2.3 Optimization of reconstruction parameters

In order to obtain reliable three-dimensional reconstructions of atoms distribution, the projection law of each ion has to be known. Due to the specific shape of the specimen (shank), the ion trajectory is progressively compressed after a distance corresponding to few times the radius of curvature of the specimen and becomes linear in the final section. The commonly used model to describe the projection of ions and image formation during APT reconstruction is the point-projection model, which is schematically shown in Fig. 2.10.

This model assumes that ions follow a straight trajectory from the surface toward the detector. The centre of projection, called point  $P$ , is situated behind the centre,  $O$ , of the spherical cap. The distance between tip apex and projection point is expressed in the radius of curvature units as  $(m + 1)R$ , where  $mR$  is the distance between  $O$  and  $P$ .

The factor  $(m + 1)$  is called image compression factor and is related to the specimen shape and electrostatic configuration of the microscope. Using the point projection model (Fig. 2.10), the compression factor is determined as:

$$\theta = \theta' + \arcsin(m \sin \theta') \quad (16)$$

where  $\theta$  is the angle between the tip axis and the radial trajectory of the ion and  $\theta'$  is the angle observed after compression of the ion trajectories. For small angles between two crystallographic directions, the image compression factor can be defined as:

$$m + 1 \approx \frac{\theta_{crys}}{\theta_{obs}} \quad (17)$$

where  $\theta_{crys}$  is the theoretical angle between two crystallographic directions, and  $\theta_{obs}$  is the angle between the poles observed on the projected image.

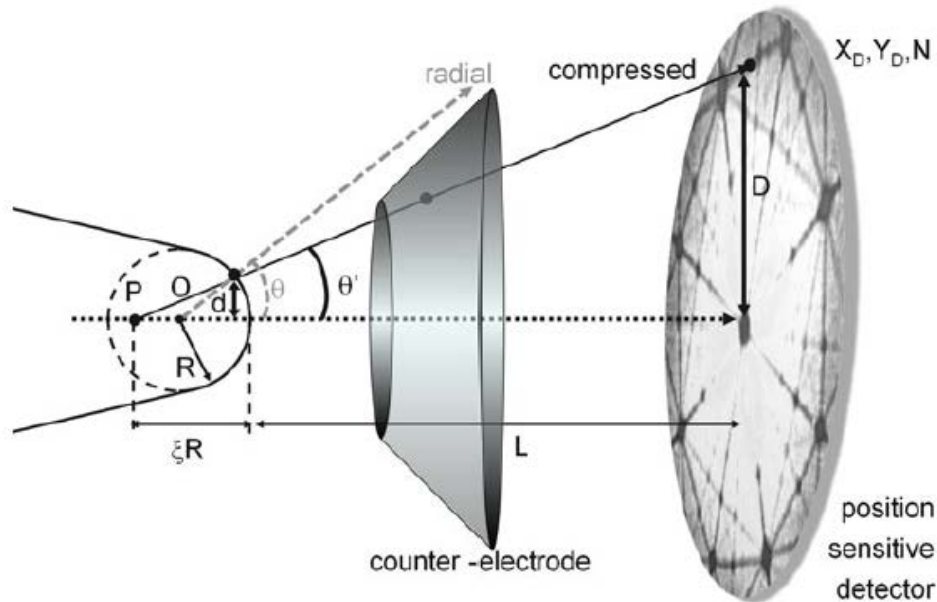


Fig. 2.10. Schematic view of ion trajectory in an atom probe experiment [12]

Considering that the distance between the sample and detector ( $L = 49.4$  mm) is much greater than the radius of curvature of the specimen,  $R$ , the magnification  $M$  is given by:

$$M = \frac{D}{d} \approx \frac{L}{(m + 1)R} \quad (18)$$

The radius of curvature  $R$  is determined directly from the applied voltage  $V$  as:

$$R = \frac{V}{k_f F} \quad (19)$$

where  $F$  is the evaporation field and  $k_f$  is the *field reduction factor* or more simply *field factor*.

The reconstruction parameters  $m + 1$  and  $k_f$  can be determined using the following approach.

**Step 1.** The first step is the identification of crystallographic directions (poles), using the map of impacts on detector (Fig. 2.11a) or map of impact density on detector (Fig. 2.11b and c). Concerning the two-dimensional density map, only single or multiple events (detection of several ions on the same pulse) can be filtered. The multiple hits map highlights the crystallographic directions in which high electric field gradient exist between edges and the center of a pole [22]. Different poles appear more clearly on one map or another. For example, (011) pole appears as a hole surrounded by two high-density regions in the map of impacts (Fig. 2.11a) and all (single and multiple) events density map (Fig. 2.11b). Multiple events map (Fig. 2.11c) clearly highlights the (002) pole.

**Step 2.** The image compression factor,  $m + 1$ , can be estimated from the distance,  $D$  between two poles on the detector impact map. Indeed, the observed angle between two poles is simply given by:

$$\theta_{obs} \sim \arctan \frac{D}{L} \quad (20)$$

where  $L$  is the equivalent linear distance between the tip and the detector. Since the poles are indexed, the crystallographic angle between them is known, so the image compression factor is calculated using relation (17).

In the LEAP 4000 HR used in this work,  $L$  is about 49.4 mm. Hence, on the example given in Fig. 2.11, the observed angle between (011) and (112) poles is equal to  $19.2^\circ$ , while the theoretical value is equal to  $30^\circ$ . The ratio between them gives the compression factor  $m+1 = 1.56$ .

**Step 3.** Considering that the reconstructed inter-reticular distance  $(d_{hkl})^{measured}$  is proportional to the field factor squared [12], the field factor,  $k_f$  can be adjusted until the measured lattice spacing in known crystallographic directions becomes equal to the theoretical value. The interplanar spacing can be measured either in GPM 3D software, or in IVAS software using the Spatial Distribution Map [23].

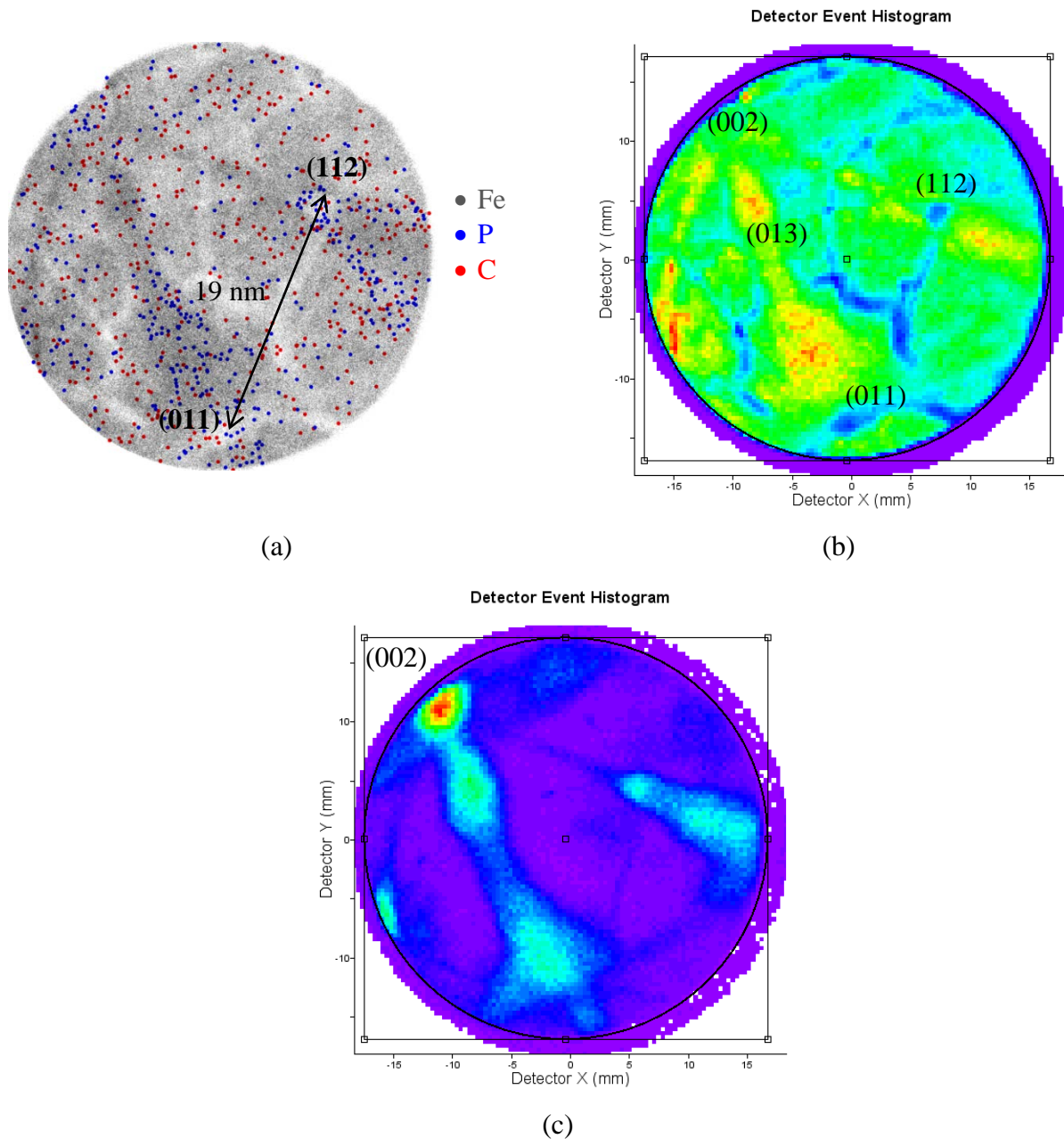


**Fig. 2.11.** (a) 2D slice of APT reconstruction of the small volume of the Fe-0.034 at.%P-0.01 at.% C alloy presenting the distribution of P (blue), C (red) and Fe (black) atoms on the detector, (b) 2D all events map with identified crystallographic poles, (c) 2D multiple events map

Fig. 2.12 shows a small APT subvolume of the Fe-0.034 at.% P-0.01 at.% C alloy indicating the distribution of iron atoms in the [011] direction after adjustment of field factor. Several reconstructions with different field factors were done to obtain the interplanar spacing at [011] direction ( $0.200 \pm 0.030$  nm) close to the theoretical value (0.203 nm). In the example given on Fig. 2.12, the field factor is 4.4. The reconstruction parameters were calculated for each specimen following this method. The correct reconstruction is necessary to determine the GB plane orientation and quantify GB segregation.

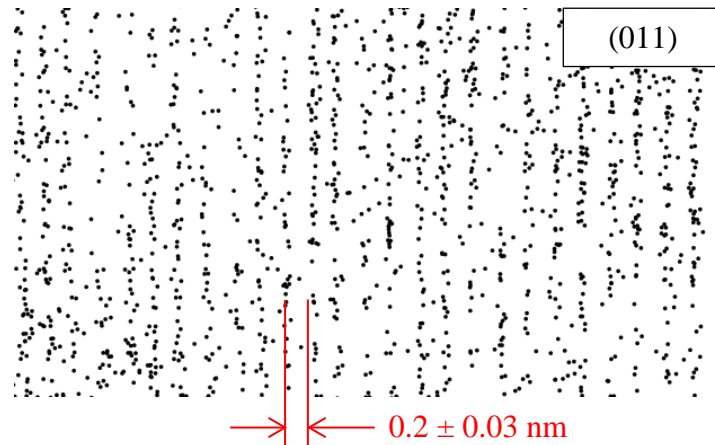


**Fig. 2.12.** Small APT subvolume of a Fe-0.034 at.% P-0.01 at.% C model alloy indicating the distribution of Fe atoms in the [011] direction. The reconstruction was done with  $m+1 = 1.56$  and  $k_f = 4.4$

## 2.2.4 Measurement of grain boundary composition

An APT reconstruction of a volume of the Fe-0.034 at.% P-0.01 at.% C model alloy containing phosphorus and carbon segregations at a GB is shown in Fig. 2.13a. The GB segregation is quantitatively determined using a one-dimensional composition profile across the GB. First, a region from which the composition profile will be extracted is defined by positioning a sampling volume perpendicular to the GB plane (Fig. 2.13a). The sampling volume is then subdivided along its axis into subvolumes (boxes). The measured composition in each box is used to plot the concentration profiles (Fig. 2.13b). In this work, the sampling boxes are 0.28 nm in length along the volume (close to the bcc lattice constant of a 0.286 nm).

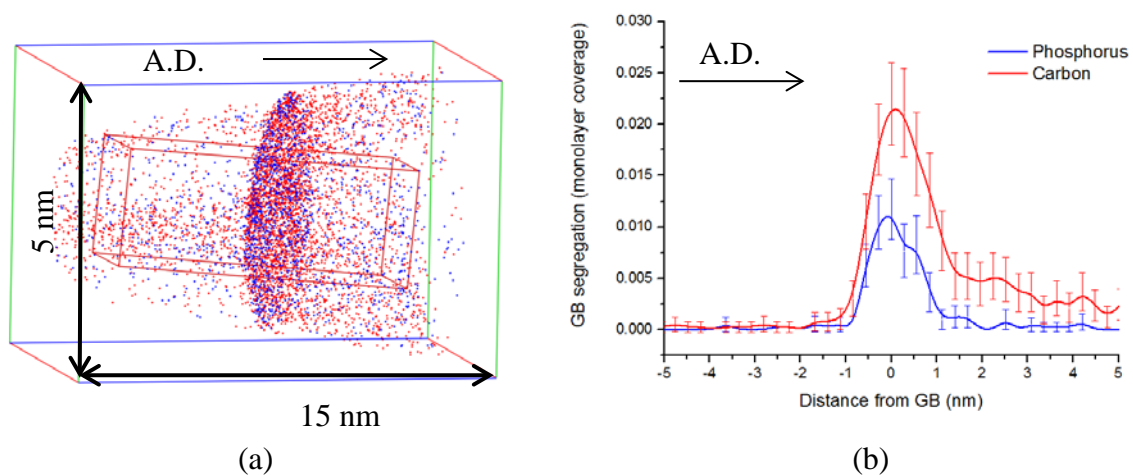


**Fig. 2.13.** (a) Reconstructed 3D volume of Fe-0.034 at.% P-0.01 at.% C model alloy containing a GB reveals the segregation of C (red) and P atoms (blue), (b) GB concentration profile across GB represents the concentration of C (red) and P atoms versus distance from GB. (A.D. = analysis direction)

As shown in Fig. 2.13b, the linear profile of carbon concentration exhibits an asymmetric shape with respect to the GB plane. In all the experiments, the solute “tail” stretching up to several nanometers is systematically observed after the GB, following the analysis direction (A.D.). The concentration profiles of phosphorus also tend to have this asymmetrical shape but to a less extent. Thus, it is clear that concentration profiles are biased by some aberration due to the field evaporation effect.

If the segregation elements have an evaporation field different from the matrix one, local magnification can also occur [24,25]. In this case, the trajectory of ions is modified. The presence of high evaporation field elements at GB results in a smaller local curvature of the tip surface and a defocusing of ion trajectories. In that case, the atomic density at GB is lower than expected (Fig. 2.14a). If the evaporation field at GB is lower than the matrix one, the trajectory of ions is overfocused, resulting in a higher density of atoms at GB (Fig. 2.14b).

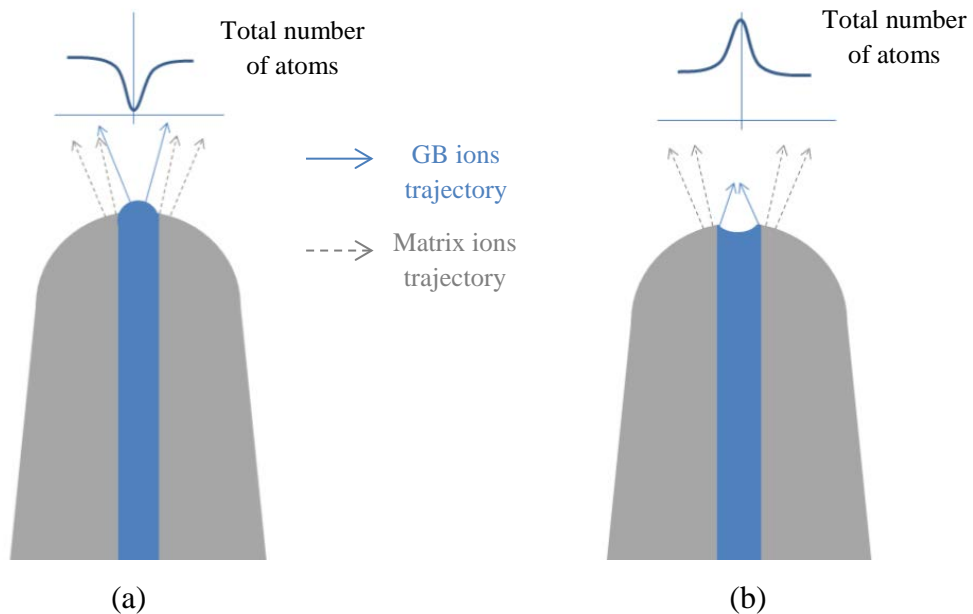


**Fig. 2.14.** Schematic representation of trajectory of ions from (a) low-field GB and (b) high-field GB and the atomic density at GB in the reconstructed volume

In the absence of segregation, the evaporation field at GB is lower than for the matrix atoms. The GB structure is less regular and the boundary atoms may be more easily evaporated. Experimentally, we always observed an increase of atomic density (Fig. 2.15) at GB indicating *lower evaporation field*, even in the presence of carbon segregation with high-field evaporation (103 V/nm [12]). Fig. 2.15 represent phosphorus and carbon segregations (right axis) and iron atomic density (left axis) at HAGB in the Fe-0.034 at.% P-0.01 at.% C alloy. An increase in atomic density at GB is apparent.

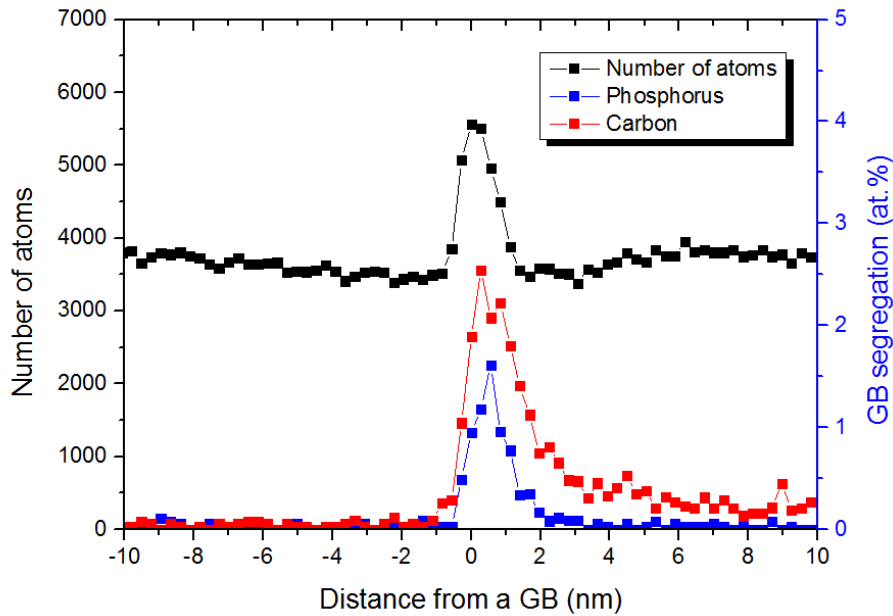


**Fig. 2.15.** The typical linear profiles across HAGB in the Fe-0.034 at.%P-0.01 at.% C model alloy representing the phosphorus (blue) and carbon (red) concentrations (right axis) and iron atomic density (black, left axis). An increase in atomic density at GB is apparent.

In order to minimize an eventual local magnification effect, the GB plane should be perpendicular to the analysis direction [25-27]. However, it is rather difficult to perfectly align the GB plane perpendicularly to the tip axis. In most cases the GB normal is not perfectly aligned with the analysis direction. Fig. 2.16 shows the thickness of the phosphorus segregated layer in annealed (equilibrium segregation) and irradiated (non-equilibrium segregation) samples as a function of the angle  $\theta$  between the GB plane and the tip axis. The measured thickness of the segregation varies from 4.5 down to 1.7 nm when the angle varies from  $55^\circ$  to  $90^\circ$ . Maximum thickness of the phosphorus GB segregation (4.7 nm) correspond to  $\theta \approx 60^\circ$ ; while the minimum thickness (1.7 nm) is observed at the nearly perpendicular GBs ( $\geq 80^\circ$ ). Thus, the perpendicular position of a GB relatively to the evaporation direction reduces the local magnification effect.

However, no difference between the equilibrium and non-equilibrium (under irradiation) segregation thicknesses was observed. It can be noticed here that this result does support previous works, in which it is reported that the equilibrium segregation is found within few atomic layers, whereas non-equilibrium segregation has a wider and smooth concentration profile across a GB [28-30]. In the current work, the minimum width of the equilibrium phosphorus segregation measured directly from the APT concentration profile across GB is 1.7 nm, which is approximately equal to the 8 atomic layers (if  $d_{hkl} = 0.203$  nm).

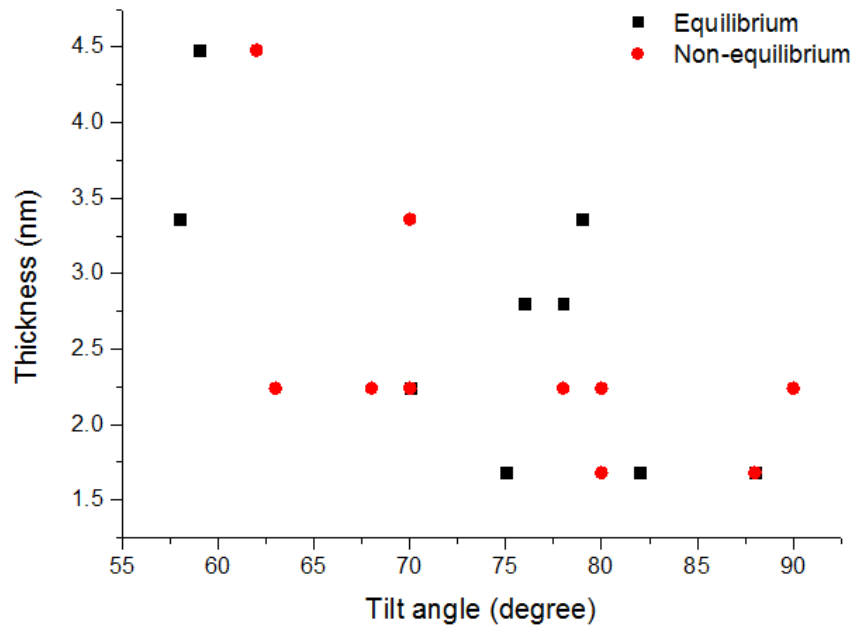
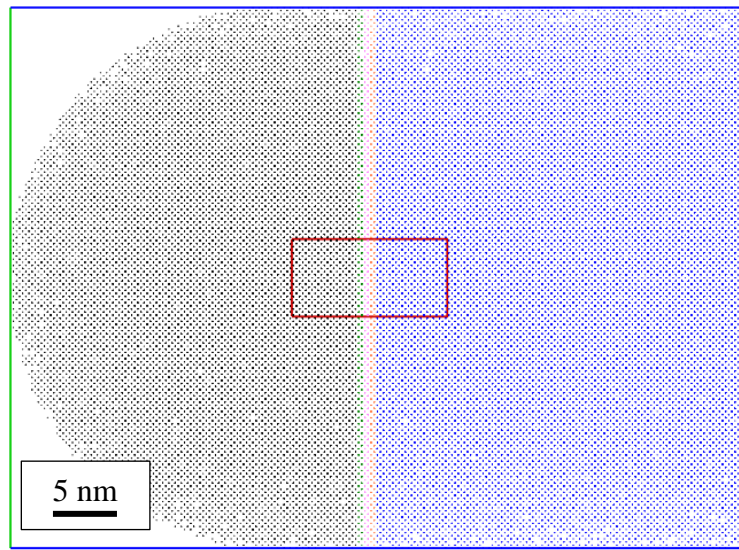


**Fig. 2.16.** Apparent thickness of the phosphorus segregated layer as a function of the angle  $\theta$  between the GB plane and the tip axis

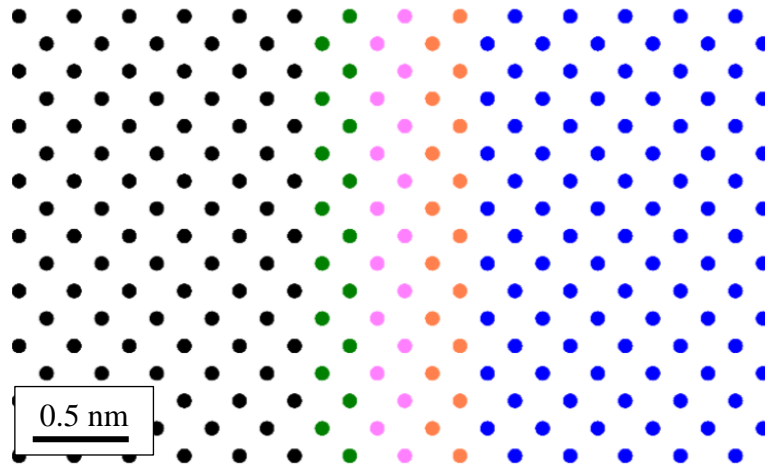
In order to evaluate the contributions of local magnification effect on the enlargement of phosphorus segregations width, modeling was used. A model developed by Pr. F.Vurpillot and M.Gruber [31], allows to simulate the field evaporation of atoms from a tip apex and to calculate the ion trajectories. The basic principle of the model is described in Appendix 1. The results are treated with the 3D GPM soft. Calculations adapted to the case of a tip containing a GB were performed by Dr. Constantinos Hatzoglou, Post Doctoral student at GPM, University of Rouen Normandy.

Due to the highly defective nature of GBs, iron atoms at the GB are expected to have a lower evaporation field than iron atoms in the perfect crystal lattice. However, the GBs contain phosphorus and carbon atoms characterized by a relatively high evaporation field (field evaporations are 103 V/nm and 33 V/nm for carbon and iron atoms, respectively [12]).

The simulated tip in Fig. 2.17a has a  $0^\circ$  shank angle and contains a GB described with two segregated atomic layers perpendicular to the tip axis. Fig. 2.17b shows the small subvolume (Fig. 2.17b) from the simulated tip. Black atoms indicates the atoms of the first grain (evaporation field  $E_{G1} = 1$  V/nm), green atoms are matrix atoms at GB ( $E_{GB} = 0.8$  V/nm), pink atoms are solute atoms with the high evaporation field ( $E_S = 1.2$  V/nm), orange atoms are matrix atoms at GB ( $E_{GB} = 0.8$  V/nm) and blue atoms are atoms of the second grain ( $E_{G2} = 1$  V/nm).



(a)



(b)

**Fig. 2.17.** (a) The simulated APT tip at the initial state before evaporation. (b) The small subvolume taken from the simulated tip contains black matrix atoms with the evaporation field  $E_{G1} = 1$  V/nm, two layers of green matrix atoms at GB ( $E_{GB} = 0.8$  V/nm), two layers of pink solute atoms with high evaporation field ( $E_S = 1.2$  V/nm), two layers of orange matrix atoms at GB ( $E_{GB} = 0.8$  V/nm), blue matrix atoms with the evaporation field  $E_{G1} = 1$  V/nm

The simulated volume after evaporation and reconstruction is shown in Fig. 2.18. As seen from Fig. 2.18, the lower evaporation field of matrix atoms at GB leads to a higher atomic density near the GB, which is in agreement with our experimental observations. Also, the simulation reveals that solute atoms with the higher evaporation field hold longer at the specimen surface, leading to their detection deeper in the tomographic reconstruction in the analysis direction [32].

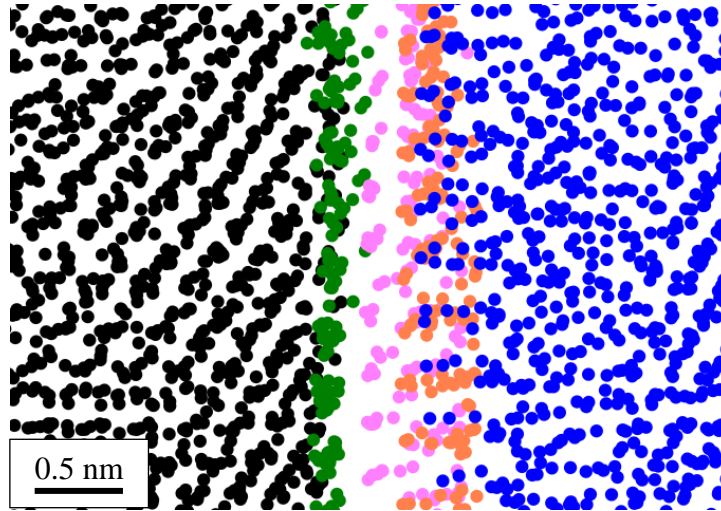


**Fig. 2.18.** The simulated APT reconstruction obtained by modeling ion trajectories of evaporated atoms from the tip surface to the detector. From the right to the left: black matrix atoms in the bulk ( $E_{G1} = 1$  V/nm), green matrix at the GB ( $E_{GB} = 0.8$  V/nm), pink solute atoms at GB ( $E_S = 1.2$  V/nm), orange matrix atoms at the GB ( $E_{GB} = 0.8$  V/nm) and blue matrix atoms in the bulk ( $E_{G2} = 1$  V/nm).

These effects result in an asymmetrical concentration profile just as it is in the experiments (Fig. 2.19) and enlargement of the segregated layer thickness from 0.203 nm to  $0.7 \pm 0.1$  nm.

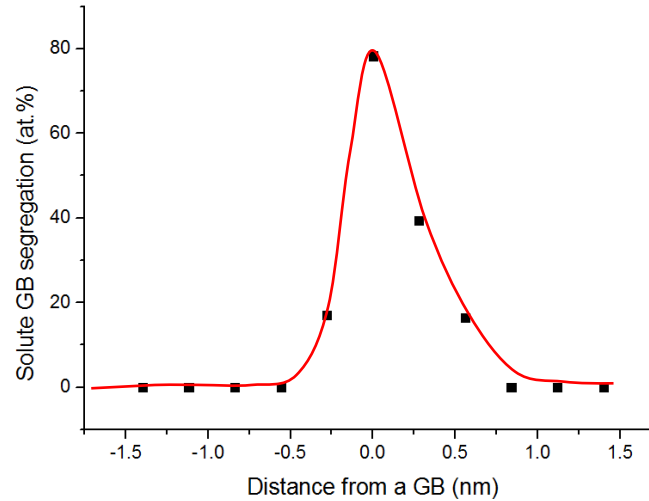


**Fig. 2.19.** Solute concentration profile across GB plotted from the simulated APT reconstruction

As reported in [33], the sampling effect, resulting from the convolution of the actual profile and the sampling box, can also contribute to an artificial enlargement of the intergranular segregation. In the current work, the sample box size is 0.28 nm. According to [23], it can cause a maximum enlargement of one atomic layer (if  $d_{hkl} = 0.203$  nm). Thus, it is supposed that the enlargement of the phosphorus GB segregation thickness is mainly caused by the reconstruction artifacts. The lower evaporation field of matrix atoms at GB leads to a

higher atomic density near a GB, while the higher evaporation field of solute atoms (phosphorus and carbon) results in an asymmetrical concentration profile across a GB.

In order to minimize the influence of APT artifacts, it is preferred to standardise the segregation measurement using the so called Gibbsian interfacial excess of solute at GBs [101,136,137]. The Gibbsian interfacial excess of element  $i$ ,  $\Gamma_i$ , can be determined from APT data using the following equation:

$$\Gamma_i = \frac{N_i^{excess}}{\eta A} \quad (21)$$

where  $N_i^{excess}$  is the excess number of atoms associated with an interface,  $A$  is the interfacial area and  $\eta$  is the detection efficiency. The detection efficiency of the LEAP 4000 HR used here is equal to 0.36. The excess number of atoms is determined from a cumulative profile, as shown in Fig. 2.20. If there is no segregation, the cumulative number of atoms of element  $i$  will increase proportionally to the cumulative number of all atoms (the slope of the line is the concentration of solute). If there is an intergranular segregation of element  $i$ , the slope will change as sketched in Fig. 2.20. The number of segregated (interfacial excess) atoms is defined directly from the plot. The error due to manual slope fitting was estimated using an upper and lower bounds approach [18,37].

The measured Gibbsian interfacial excess can be converted to a fraction of a monolayer assuming that the phosphorus atoms reside in a single close-packed (110) plane of a BCC  $\alpha$ -iron. This assumption is used for comparison purpose and is irrelevant to the real position of phosphorus atoms at the GB.

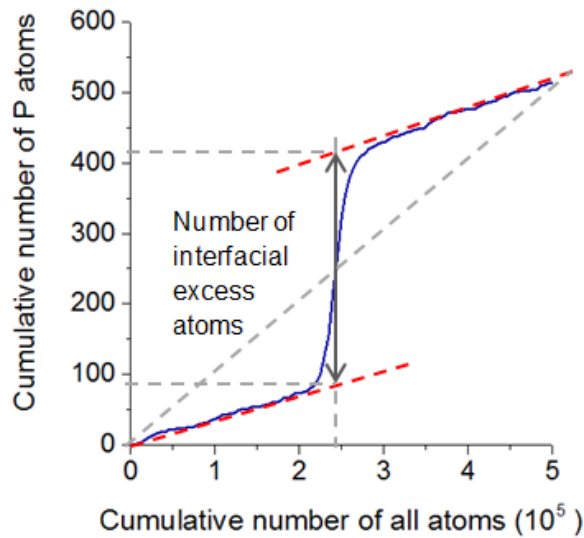


**Fig. 2.20.** Cumulative concentration profiles of phosphorus atoms determined from a parallelepipedic region perpendicular to a GB.

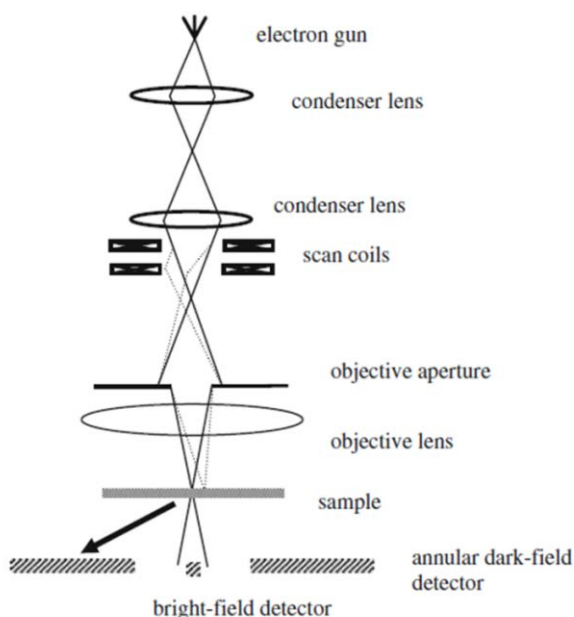
## 2.3 Analytical electron microscopy

High resolution analytical electron microscope JEM-ARM 200F 200 kV FEG-STEM/TEM was used to characterize the microstructure and chemistry of the Fe-0.034 at.% P-0.01 at.% C model alloy after irradiation with a high spatial resolution. Phosphorus GB segregation was examined as a function of irradiation depth in order to verify that segregation is homogeneous along GB in the direction of irradiation, especially in the range from 0.5 to 1  $\mu\text{m}$ .

The thickness of specimens was controlled by electron energy loss spectroscopy (EELS). The chemical segregations were measured using energy dispersive X-ray spectroscopy (EDX).

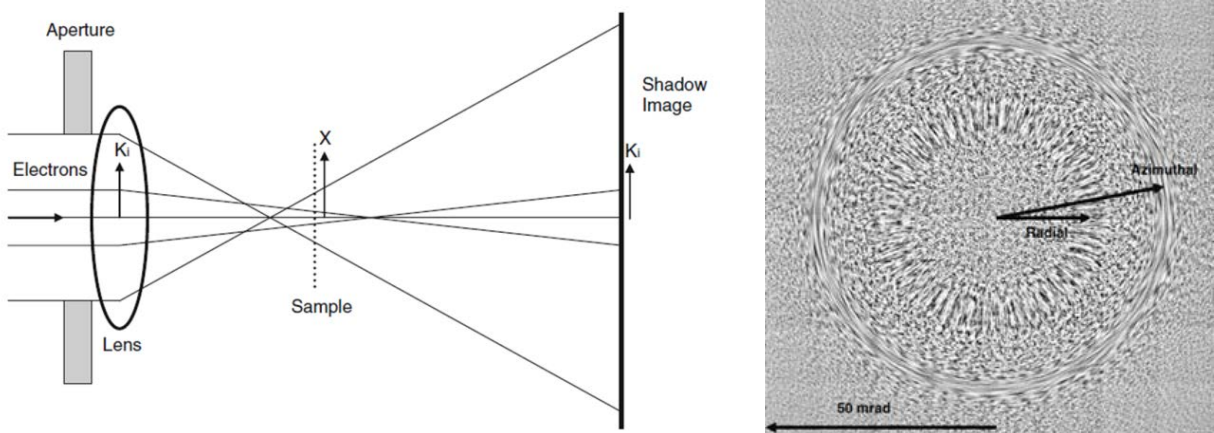
### 2.3.1 Principle of imaging on STEM mode

Fig. 2.21 shows the main components of an aberration-corrected Scanning Transmission Electron Microscopy (STEM). Electrons are accelerated from a field-emission gun and focused into a point of the specimen by a set of condenser lenses and an objective lens. The size of the probe is defined by the objective aperture, which limits the maximum illumination angle. The scanning across the sample is carried by a set of scan coils. The commonly used detectors include a bright field (BF) detector that intercepts the transmitted beam and an high angle annular dark field (HAADF) to collect scattered electrons [38].



**Fig. 2.21.** A schematic diagram of a STEM instrument [39]

Aberration correction of the incident beam is very important for all type of analysis because the spatial resolution is dramatically improved with a smaller probe. The shadow image of the specimen, called Ronchigram, is used to set the aberration correction. A schematic figure of the formation of the Ronchigram image is shown in Fig. 2.22. Ronchigram is the projected image of the specimen in the diffraction plane obtained with a convergent incident electron beam focused near the specimen. When the convergence point is focused exactly on the specimen, the magnification of the Ronchigram is infinite, its intensity is uniform and its shape is circular.



**Fig. 2.22.** A schematic diagram for the formation of Ronchigram [39]

### 2.3.2 Two beam conditions

STEM technique offers many possibilities to visualize the defects of interest. The irradiation created dislocations near a GB were characterized using two beam conditions [40].

Under two-beam conditions, the foil is tilted so that one set of diffracting planes ( $hkl$ ) is at the Bragg condition. The Ewald sphere construction and diffraction patterns for this condition are shown in Fig. 2.23. Under two-beam conditions the intensity of the diffraction pattern (the (200) in Fig. 2.23b) is similar to that of forward-scattered beam (the (000)). The image is formed by placing an objective aperture around either the forward-scattered beam to form a bright-field (BF) image or around the diffracted beam to form a dark-field (DF) image [41].

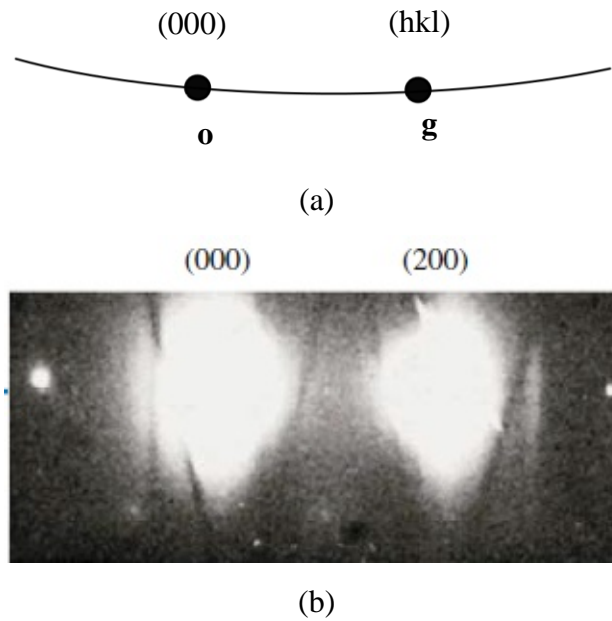


**Fig. 2.23.** (a) Ewald sphere construction for two-beam conditions. The reciprocal vector  $\mathbf{g}$  is the diffraction vector joining the (000) to (hkl) spot in the diffraction pattern. The curvature of the Ewald sphere is exaggerated for clarity. (b) Two strong beams, the direct (000) on-axis beam and the diffracted (200) beams from Al-3wt.%Li taken under two-beam conditions [40]

The experimental procedure to obtain a two-beam condition described in [40,41] is first to tilt the specimen in BF diffraction mode until the desired (hkl) reflection ( $g$ ) is strong. The DF diffraction mode is then selected and the  $(\bar{h}\bar{k}\bar{l})$  reflection ( $-g$ ) is tilted to the optical axis with the beam-tilt coils. When  $-g$  is on the axis, switch off the DF deflectors, insert and center the objective aperture around (000) or (hkl) for a BF or a DF image, respectively. Switch to image mode. In the current work, the dislocations were visualized using (110) reflection from  $\langle 111 \rangle$  oriented grain.

### 2.3.3 Electron energy-loss spectroscopy

To determine the number density of dislocations, it is necessary to know the thickness of the specimen. In this work, Electron Energy-loss Spectroscopy (EELS) was used to determine the local specimen thickness in each specimen from the low-loss spectra. In the ARM 200F, EELS instrumentation is located after the viewing screen (Fig. 2.24). The electrons pass through a thin sample, interacting either elastically or inelastically with the atoms. As a consequence of the different energy losses they occupy different parts of the Electron Energy-Loss (EEL) spectrum.

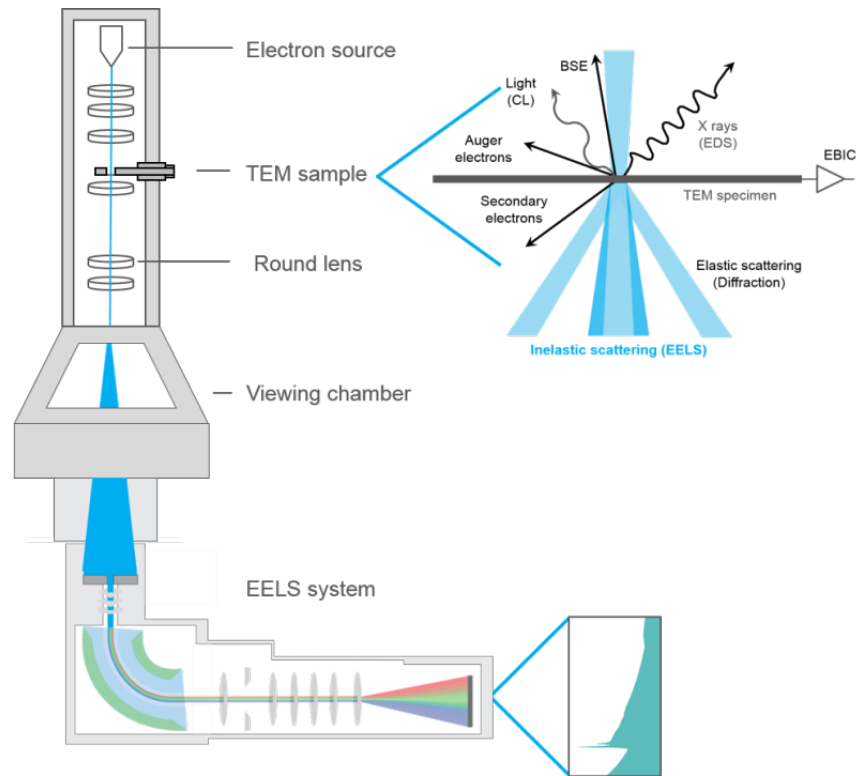


**Fig. 2.24.** Schematic view of EELS installation in TEM [42]

An EEL spectrum is composed of three main parts: the zero-loss (ZL), the low-loss (LL) and the core-loss (CL) regions, as shown in Fig. 2.25. The zero-loss peak (ZLP) represents electrons which are scattered elastically. The position of ZLP is used for adjust the position of total spectrum.

The low-loss region with energy losses  $\Delta E \leq 50 \text{ eV}$  contains electrons which have interacted with the weakly bound, outer-shell electrons of the atoms.

The core-loss region with energy typically  $\geq 100 \text{ eV}$  shows electrons that have lost energy by excitation of specimen electrons from relatively deeply bound initial core states to final electronic states above the Fermi level [43]. The exact value of the transition energy is highly dependent on the electronic structure and atom type.

The natural logarithm of the ratio of the integrated low-loss region to the zero-loss, often referred as “ $t/\lambda$ ”, is a good indication of the thickness,  $t$  of the sample in units of the electron mean free path for inelastic scattering [44], i.e.:

$$t = \lambda \ln \frac{I_t}{I_0} \quad (22)$$

where  $I_0$  is the ZLP intensity,  $I_t$  is the total intensity in the low-loss spectrum out to 50eV, including  $I_0$  and  $\lambda$  is the average mean free path for these low-energy losses.

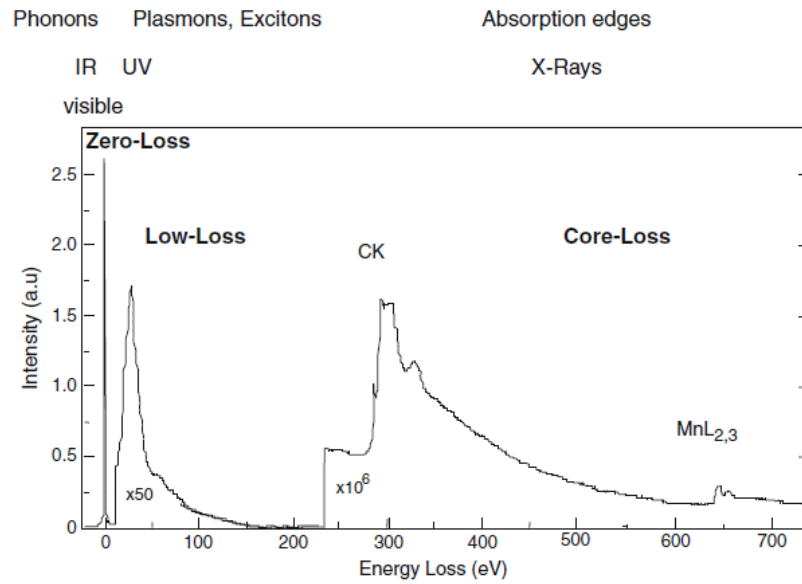


**Fig. 2.25.** A typical EELS spectrum [140] separated into three regions: electrons that have no lost energy (zero-loss peak), electrons interacted with the weakly bound electrons in the specimen (low-loss region), and electrons interacted with the strongly bound core electrons of the atoms (core-loss region)

### 2.3.4 Energy dispersive X-ray spectroscopy

Energy dispersive X-ray spectroscopy is a qualitative and quantitative technique used with both SEM and STEM techniques. It provides information about the chemical composition of a sample and allows chemical mapping. The electron beam is focused on the specimen and excites an electron from an inner shell of a specimen atom. This electron is ejected from the shell, leaving an electron hole. De-excitation is ensured by an electron from an higher-energy shell that fills the hole. The difference in energy between the higher-energy shell and the lower energy shell may be released in the form of an X-ray [45].

The STEM-EDS analysis was performed using JEOL JED-2300 Analysis Station. Spectra and line scans were obtained using the JEOL genesis software. For EDS analysis the probe size used was 0.2 nm (6C) and the CL aperture size was 40 $\mu$ m.

In order to obtain reliable quantitative information about segregation, it is important to optimize and control the experimental conditions. First, the GB must be aligned closely parallel to the electron beam. Second, the sample thickness has to be thick enough to have good counting statistics but also thin enough to minimize the beam broadening. In this work, the thickness of specimens was in a range 50 to 100 nm. The focused probe is then positioned sequentially at a series of points sampling the specimen across the boundary, as shown in Fig. 2.26.



**Fig. 2.26.** STEM bright-field image of the series of EDX points across the GB in a thin foil from the Fe-0.034at%P-0.01at.%C alloy (irradiated to 0.75 dpa)

A typical spectrum at GB reveals the significant intensities from iron, phosphorus, carbon and copper atoms (Fig. 2.27). Only phosphorus and iron atoms were quantified from the spectrum. The peaks of copper come from the lamellar holder. In the case of carbon, reliable measurement is very difficult because it is difficult to confirm whether the carbon signal is from the sample itself or from the contamination accumulated during analysis.

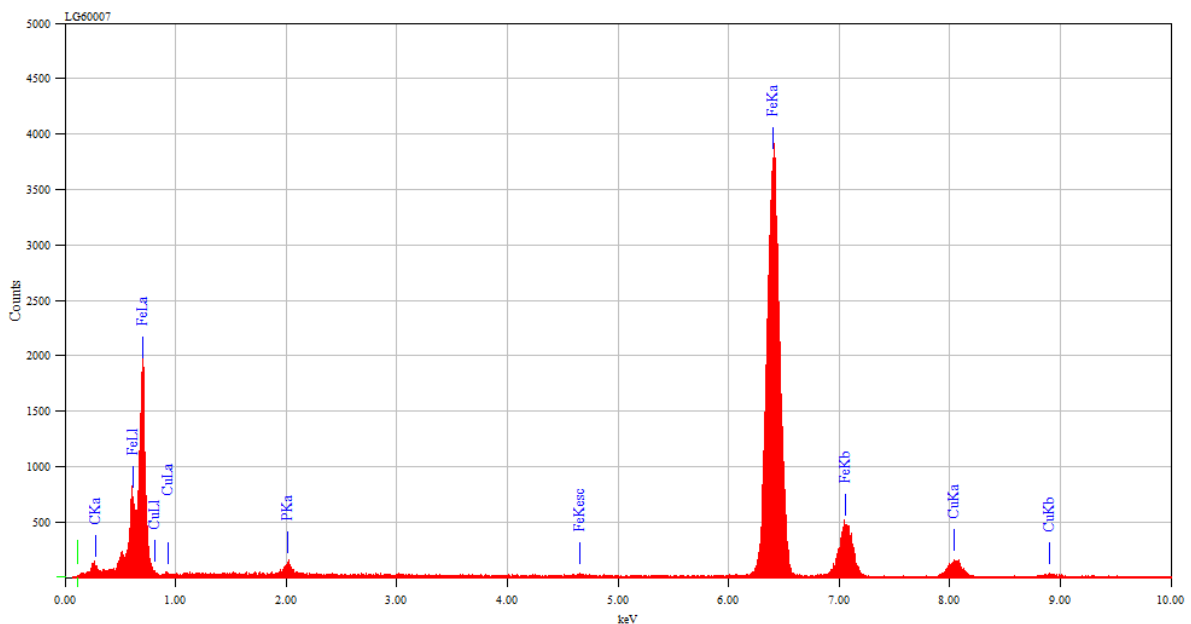


**Fig. 2.27.** EDS spectrum from a high-angle GB in the Fe-0.034 at.% P-0.01 at.% C model alloy irradiated to 0.75 dpa. Characteristic X-ray peaks ( $K_{\alpha}$  and  $K_{\beta}$ ) for Fe, P, C and Cu are evident.

The X-ray intensities  $I_{Fe}$  and  $I_P$  from iron and phosphorus atoms respectively, are related to the concentration local  $C_{Fe}$  and  $C_P$  by the Cliff-Lorimer equation [46]:

$$\frac{C_P}{C_{Fe}} = k_{FeP} \frac{I_P}{I_{Fe}}$$

where  $k_{AB}$  is a sensitivity factor which takes into account differences in the generation and detection characteristics of the X-rays from different elements. This equation ignores X-rays absorption and fluorescence effects. This assumption is a reasonable first-order approximation in a thin-foil sample.

After quantification of each dote in the line across a GB using JEOL Analysis Station (ZAF, standardless), the composition profile of phosphorus across GB can be plotted (Fig. 2.28).

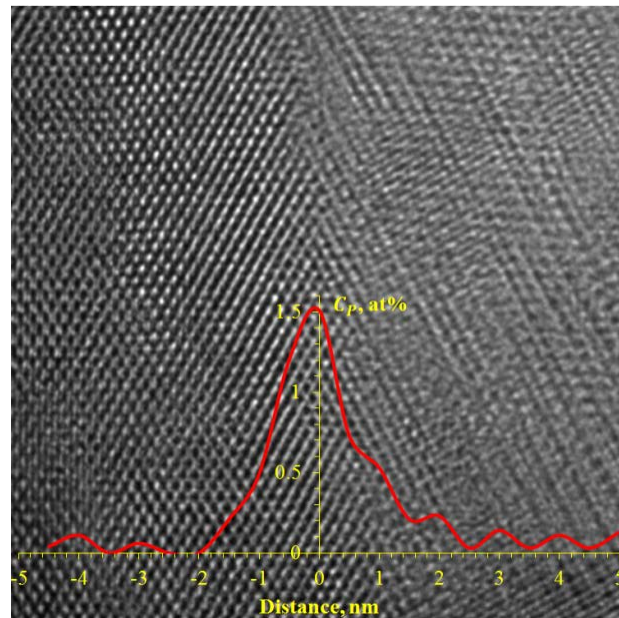


**Fig. 2.28.** Measured concentration profile of phosphorus across a GB overlapped with the HRTEM image of the analyzed region

The measured concentration profile is a result of the convolution of the actual GB concentration profile with the broadened electron beam as it traverses the thickness of the foil [47]. In order to obtain the actual GB segregation profile, the interaction volume between the electron beam and the specimen has to be known. In the literature, several approaches have been proposed to transform the measured (convoluted) profile to the actual (deconvoluted) one.

In the current work, the quantification of the GB segregation using EDS is not principal task. The aim is to control the segregation level along GB, which is located parallel to the irradiation direction. In this case, for the sample with homogenous thickness, the GB

concentration is calculated by numerical integration of concentration profile, as it is shown in Fig. 2.29. The interval between the measured points in the line profile is always 0.5 nm.

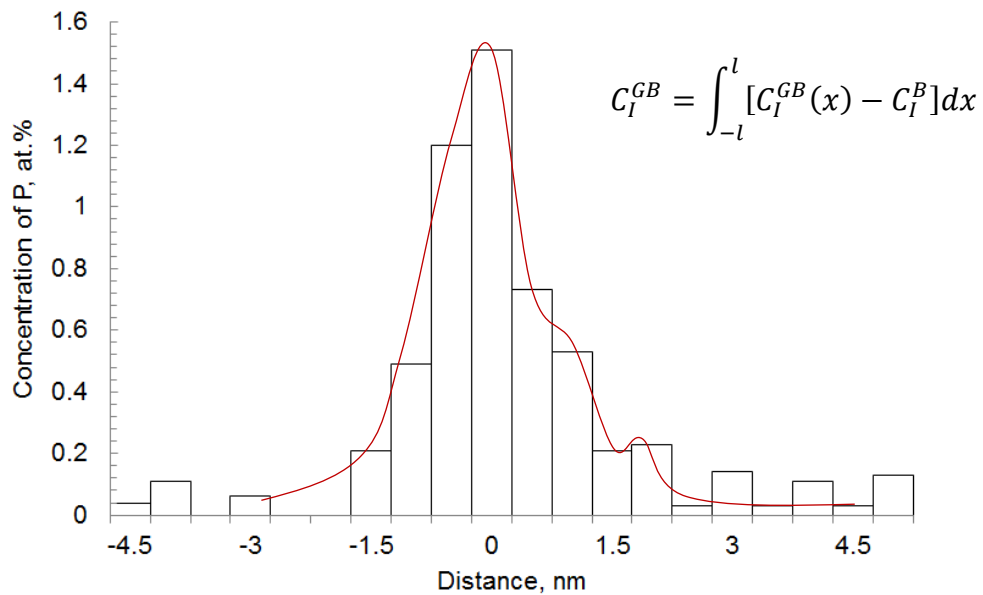


**Fig. 2.29.** Measured concentration profile of phosphorus across the GB. The equation represents how to calculate the integral concentration of P at GB.

## 2.4 Scanning electron microscopy

Scanning Electron Microscope (SEM) equipped with Electron Backscattering Diffraction (EBSD) camera and Focused Ion-Beam (FIB) system has been used to make the atom probe tips and TEM lamellar containing the GB. In this section, the principles of SEM and FIB imaging, the deposition and milling processes, the SEM/FIB specimen preparation, and the principle of EBSD and transmission Kikuchi diffraction (TKD) are described. Also, the method to identify five crystallographic degrees of freedom (DOF's) of a GB using correlative TKD and APT is given in details.

### 2.4.1 Principle of SEM imaging

SEM is equipped with an electron gun, generating the high energy electrons (0.1-30 keV), and magnetic lenses, which focus the beam at the specimen surface and scan it across the surface of a specimen (Fig. 2.30).

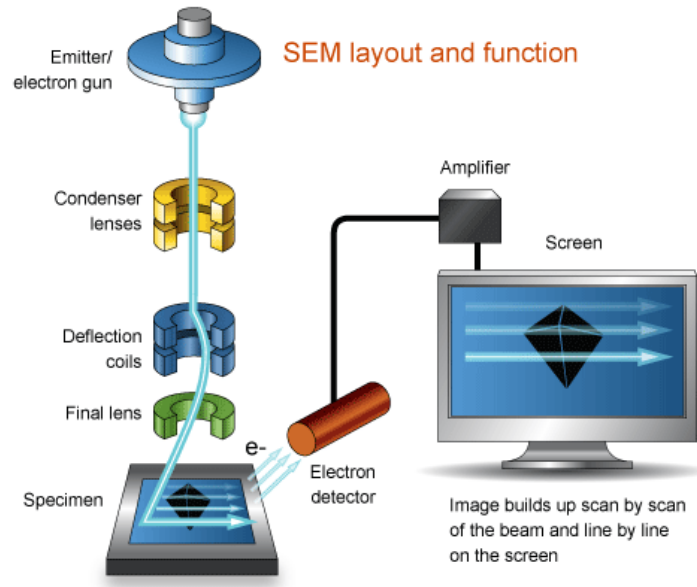


**Fig. 2.30.** Schematic view of SEM instrument [48]

Several types of electrons are generated during the bombardment of the specimen by the primary electrons (PE) (Fig. 2.31a). SEM imaging is performed using either secondary electrons (SE), which are formed by inelastic scattering and have an energy lower than 50eV or using backscattered electrons (BSE) produced through an elastic scattering interaction of primary electrons with the atoms of the sample and having an energy higher than 50 eV (Fig. 2.31b).

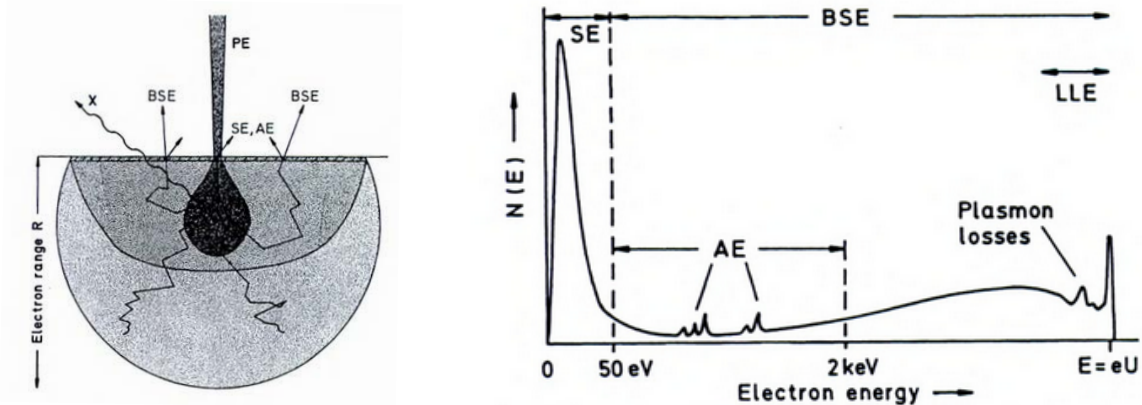


**Fig. 2.31.** (a) The interaction volume,  $R$  displaying the origin of secondary electrons (SE), backscattered electrons (BSE), Auger electrons (AE) and X-rays (X); (b) schematic energy spectrum of emitted electrons consisting of secondary electrons (SE) with  $E < 50\text{ eV}$  and backscattered electrons (BSE) with  $E > 50\text{ eV}$  [49]

## 2.4.2 Focused ion beam and gas injection system

The FIB system generates and directs a stream of high-energy ions (usually  $\text{Ga}^+$ ), focusing them onto a surface for milling, or deposition, or implantation and imaging (Fig.

2.32a) [50]. Milling is a process of digging under the surface as a result of bombardment with heavy ions (Fig. 2.32b). Deposition results from an ion beam assisted chemical vapor deposition process (Fig. 2.32c) [51]. Metal ions, such as W and Pt are delivered in the form of an organometallic molecule ( $\text{W}(\text{CO})_6$ ) via the gas injection system (GIS). These molecules are cracked under the ion beam, and metallic ions are deposited on the sample surface [50].

Both APT and TEM samples were prepared using SEM/FIB dual beam technique. Besides many advantages (such as highly site-specific area preparation and uniform thinning), this method is not free of some shortcomings. In particular, the high energy  $\text{Ga}^+$  beam (up to 30 kV) may seriously damage the structure of the material in the same manner as an ion irradiation at low temperature [52].

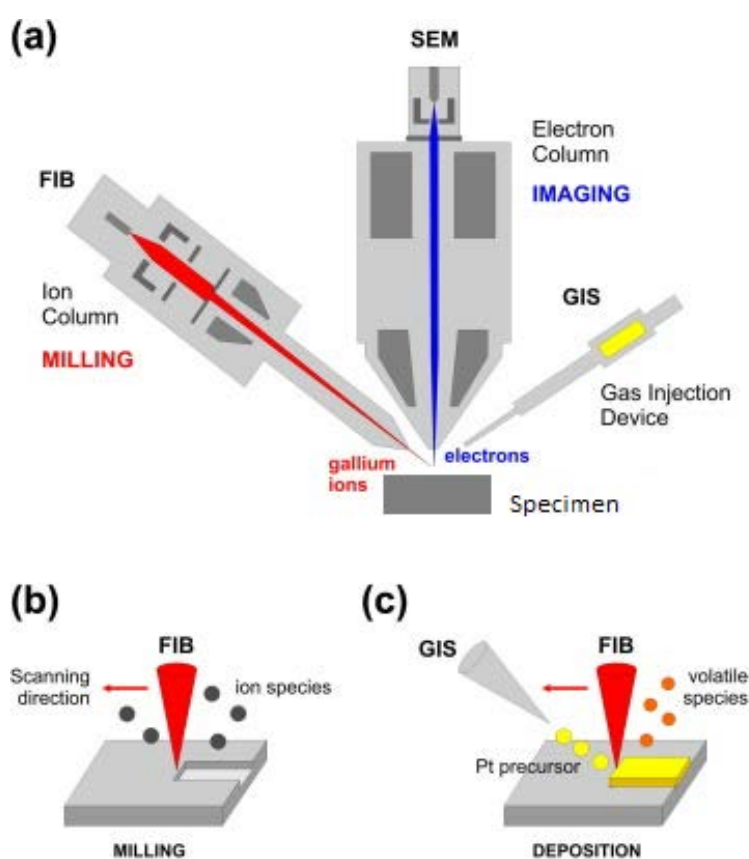


**Fig. 2.32.** (a) Schematic view of a SEM chamber with FIB and GIS systems, (b) ion beam milling: atoms of the specimen are ejected by ion-atom collision, (c) ion beam assisted deposition: the ion beam is used to deposit molecules released from a GIS onto the specimen surface [53]

However, comparison of irradiated and unirradiated thin foils prepared with the same SEM/FIB dual beam technique has shown that the sort of damages is different. The FIB milling leads to the formation of large number of black dots, while ion irradiation up to 0.75 dpa results in the appearance of the dislocation arrays and voids.

### 2.4.3 Electron Backscatter Diffraction and Transmission Kikuchi Diffraction

EBSD is a microstructural-crystallographic technique used for crystallographic orientation mapping, defect studies, phase identification, grain boundary orientation, micro-strain mapping [45].

In this work EBSD mapping and GB study are performed using a Zeiss NVision 40 SEM equipped with an EBSD camera. A flat well-polished specimen is placed in the SEM chamber at a highly tilted angle ( $70^\circ$  from horizontal) toward the EBSD camera. The incident beam is diffracted by crystal planes forming two diffracting large-angle cones (Fig. 2.33a).

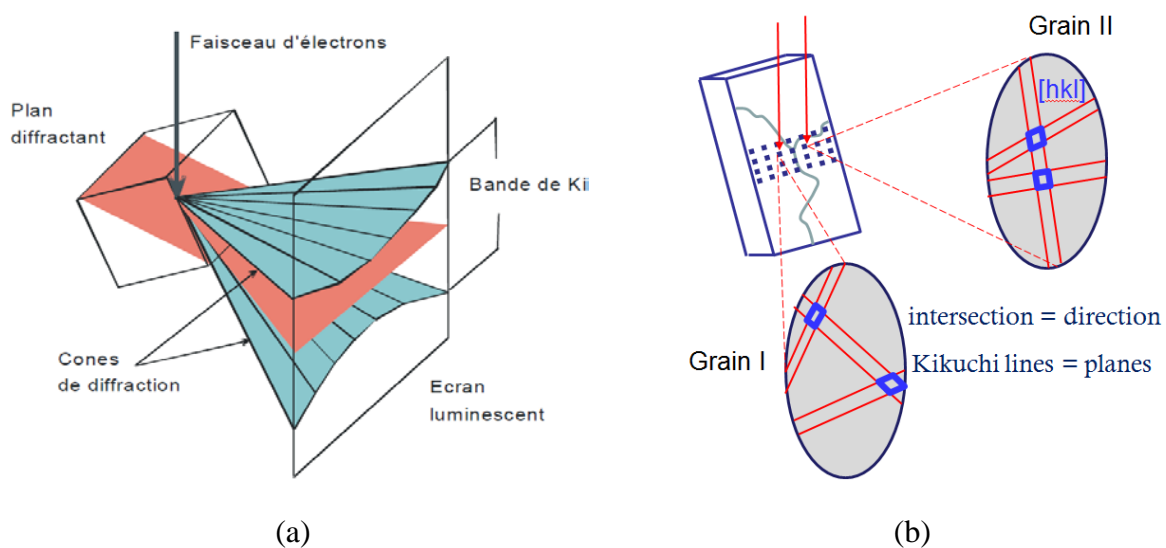


**Fig. 2.33.** (a) The incident beam is diffracted from the crystallographic plane resulting two diffracting cones. This large-angle and thus almost parallel cones project onto the phosphorus screen and form the Kikuchi bands. (b) The middle of Kikuchi bands and their intersection correspond with crystallographic planes and zone axis, respectively.

The cones are projected onto a phosphorus screen and form the Kikuchi bands. The middle of a Kikuchi pair (2 projected lines) corresponds to diffracting crystal planes and the intersections of Kikuchi bands correspond to zone axes. A Hough transform is used to identify the position of Kikuchi bands and calculate the angles between them. The calculated angles are compared with a standard and are indexed for each pixel generating orientation map [54].

The results of EBSD measurements are shown in the so-called crystal orientation map on selected viewing direction (Fig. 2.34), where the crystallographic orientations are assigned to different colors. The crystal orientation map is interpreted using the inverse pole figure

(IPF). In the case of a cubic crystal symmetry red is assigned to the directions near [011] corner, green to the directions near [01 $\bar{1}$ ], and blue to the directions near [111] corner. Also the crystal orientation map is often called IPF map.

From the EBSD map, the GB misorientation angle and rotation axis can be calculated (three DOFs). Therefore, using 2D EBSD map the GB with the desired misorientation and length ( $< 10 \mu\text{m}$ ) is chosen. Since the position of a GB plane under the sample surface is unknown, the definition of a GB plane orientation requires additional experiments. In this work, the GB plane is characterized correlating Transmission Kikuchi Diffraction (TKD) and Atom Probe 3D reconstruction (see 2.4.5)

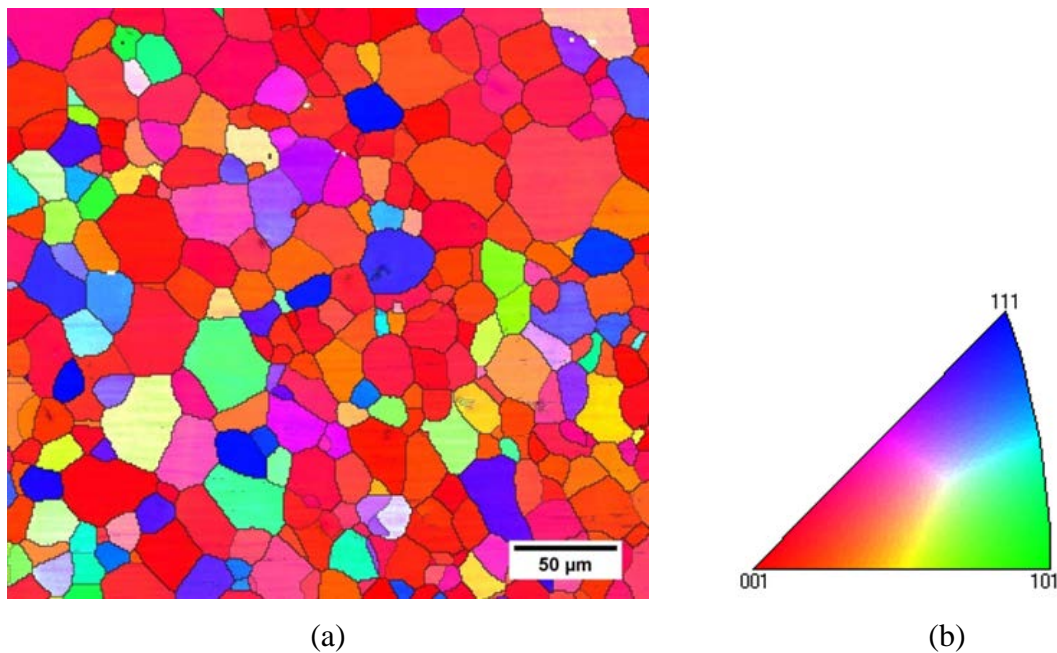


**Fig. 2.34.** (a) A typical crystal orientation map in Z direction (normal to the surface) for a sample of the Fe-0.034 at.% P-0.01 at.% C alloy in which the colours are defined by the (b) inverse pole figure (IPF)

TKD is a method used in a SEM with the EBSD detector. The method was proposed by Keller and Geiss [55] as a variation of EBSD analysis with better spatial resolution. The main difference from conventional EBSD is that the TKD works with diffracted transmitted electrons. In the current work, TKD is used for the site-specific preparation of APT specimens with GB.

#### 2.4.4 Site-specific sample preparation

The specimens containing GBs are made using FIB lift-out method in a Zeiss NVision 40 microscope equipped with a Kleindiek micromanipulator [13]. First a GB for site-specific preparation is selected from EBSD orientation map. Then, small chunk ( $2 \times 2 \times 8 \mu\text{m}^3$ )

containing the GB is cut from the sample (Fig. 2.35A) and lifted-out thanks to the micromanipulator (Fig. 2.35B). As it is said in the APT section, the GB has to be nearly perpendicular to the tip axis to minimise the local magnification effect [25]. However, it is not possible to avoid a small deviation of GB from the perpendicular position. The chunk is welded to a W pre-tip employing Pt deposition. Finally, annular milling is performed to form the APT microtip with  $\sim 10$  nm radius of curvature (Fig. 2.35 C, D).

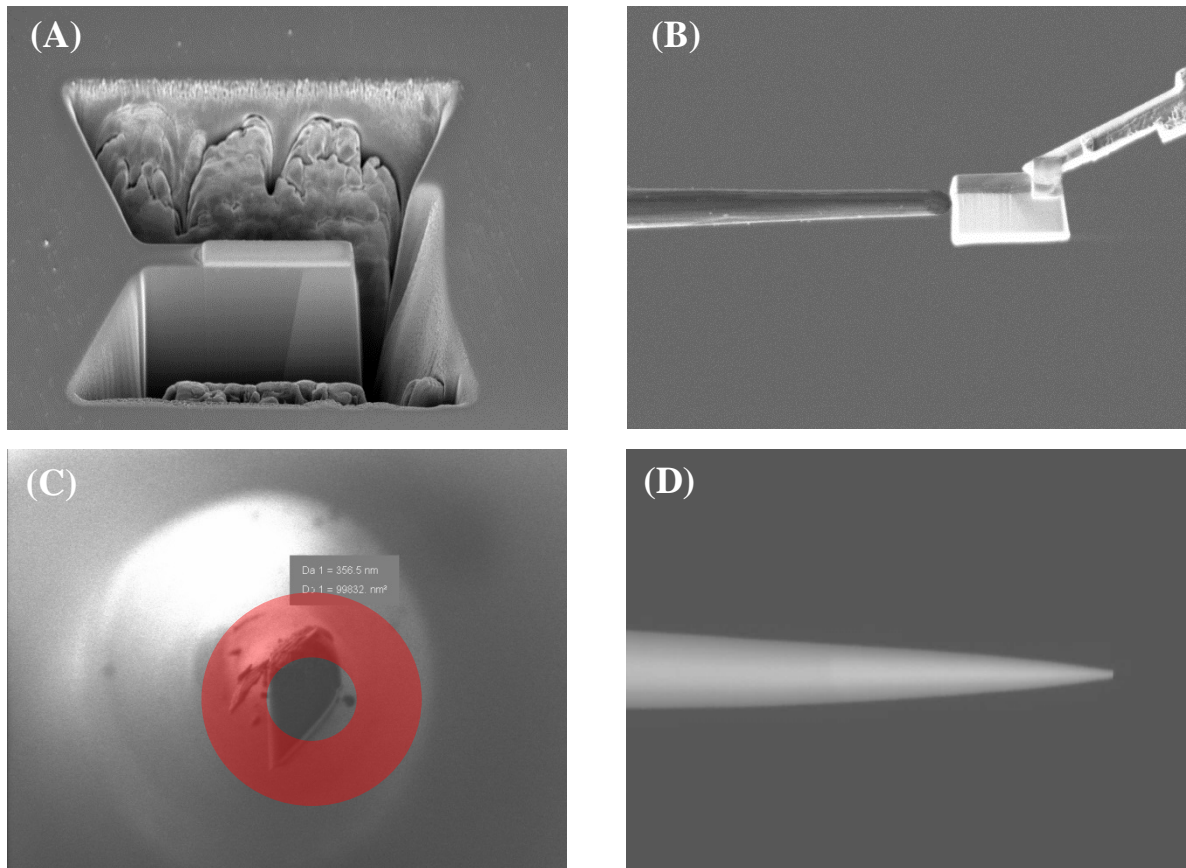


**Fig. 2.35.** SEM and FIB images showing different steps of the GB containing specimen preparation for APT: (A) the deposition of a Pt protection layer perpendicular to the GB plane on the surface and milling of three trenches around Pt layer, (B) the lift-out and mounting of the chunk on a support tip with the micromanipulator, (C) the milling pattern superimposed with FIB image of the tip, (D) APT tip after several steps of FIB annular milling

The milling process is controlled thanks to TKD (Fig. 2.36). Indeed, the idea is to perform TKD orientation map and to identify the GB position after each annular milling step [56]. Several repetitions of FIB annular milling with consequent TKD mapping is required to place the GB close ( $< 50$  nm) to the tip apex. Final milling is performed at 2kV to “clean” the sample from  $\text{Ga}^+$  ions and damaged zone and to decrease the speed of process in order to control accurately the distance between GB and tip apex.

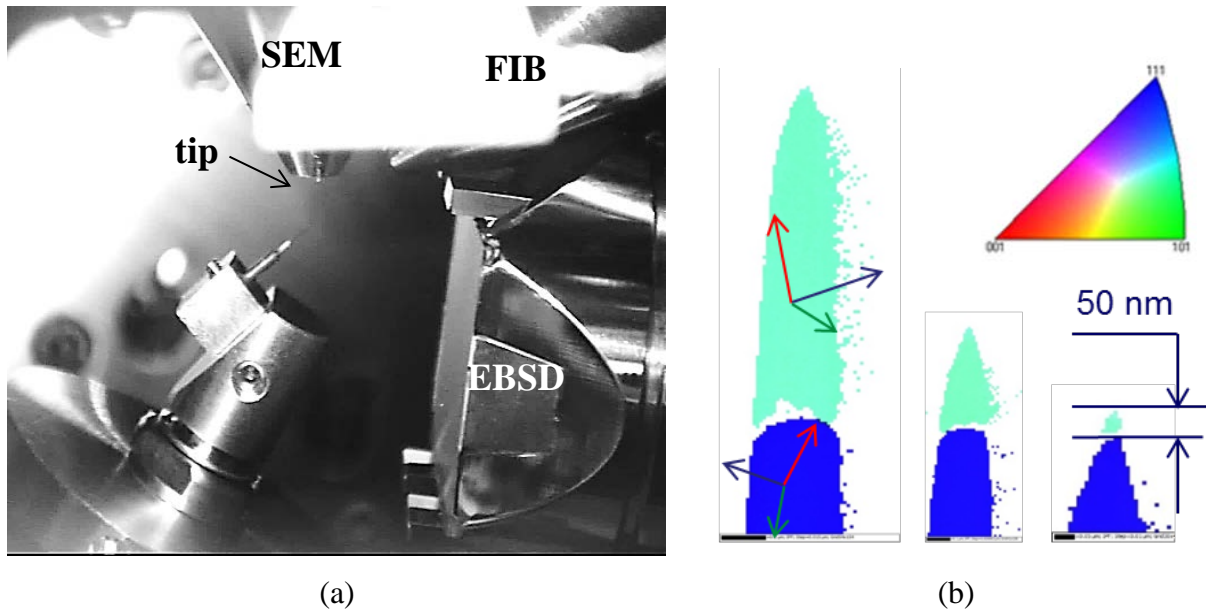


**Fig. 2.36.** Experimental setup for SEM-TKD with the pre-tilted APT tip holder, the electron gun (SEM), the ion gun (FIB) and the EBSD detector. The APT tip is mounted parallel to FIB beam at the crossing of electron and ion beams. (b) The IPF Z color map shows the GB position and allows to control the annular milling of tip by FIB

The lift-out process for TEM lamella preparation is the same as for APT tips. The chunk is situated onto a copper grid (Fig. 2.37a), and thinned using 30 kV  $\text{Ga}^+$  beam (Fig. 2.37b). At the last step, the specimen is tilted an angle of  $\pm 5^\circ$  and “cleaned” using a very low beam current ( $\sim 30$  pA at 2 kV) for a short period of time on the whole surface. This procedure is employed in order to remove re-deposition and to reduce the number of FIB artifacts.

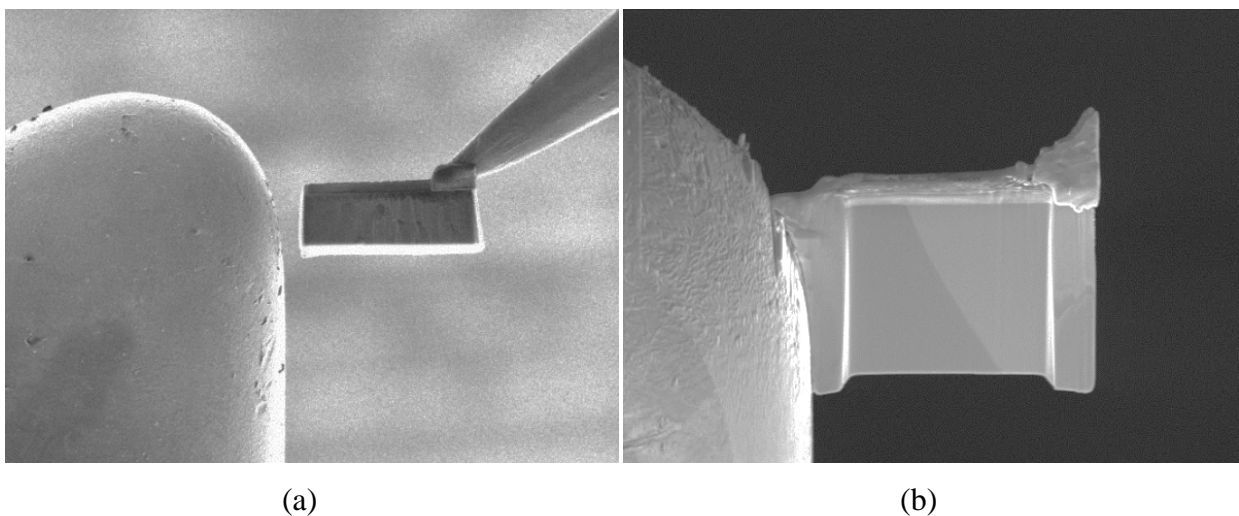


**Fig. 2.37.** SEM images of TEM lamellar (a) during mounting on a Cu-grid, (b) after several steps of FIB milling

## 2.4.5 Determination of grain boundary nature from APT and TKD techniques

The conventional 2D EBSD technique allows to determine the misorientation angle and the rotation axis of a GB. To find the GB plane orientation, both TKD and APT data are needed. The method is based on the works of Babinsky [57], Herbig [18] and Mandal [58].

Fig. 2.38a shows the schematic set-up for TKD mapping of the APT specimen at the last preparation step. The APT specimen remains at the same position as it was for annular milling. The coordinate system used to identify the crystal directions with TKD is specified in the acquisition program as shown on Fig. 2.38. The X axis is parallel to EBSD screen, the Y axis is the tip axis and the Z axis is the axis perpendicular to tip axis giving a direct marker.

Fig. 2.38b shows inverse pole figure (IPF) map of the APT specimen close to the last step of milling. The tip containing  $11^\circ[4\bar{4}3]$  GB was prepared from the Fe-0.034 at.% P-0.01 at.% C alloy irradiated up to 0.75 dpa.

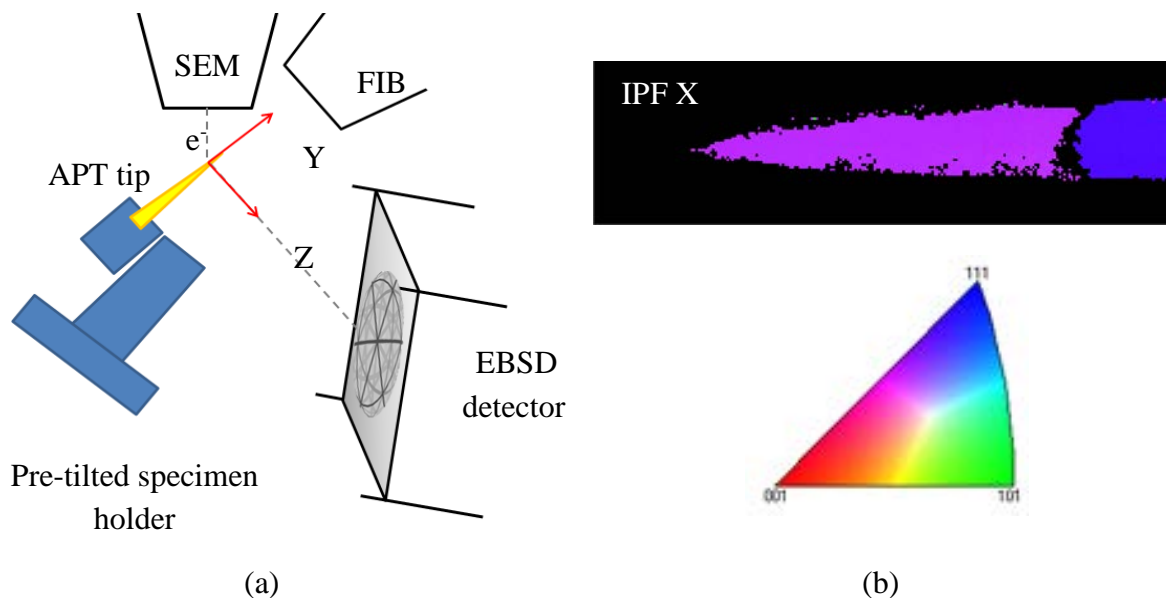


**Fig. 2.38.** (a) Schematic set-up in the microscope chamber for TKD analysis. The tip axis is located parallel to the FIB at the intersection point with SEM beam. X, Y and Z axis are respectively the axis parallel to EBSD screen, the tip axis and the axis perpendicular to tip axis giving a direct marker; (b) Inverse pole figure (IPF) map of APT sample containing  $11^\circ[4\bar{4}3]$  GB indicates the crystallographic directions lying along X axis

From the TKD indexing, the crystal orientation of each grain is calculated and displayed in the form of spherical and stereographic projections (Fig. 2.39). The stereographic projection is a projection of points from the surface of a sphere onto its equatorial plane [59].

To find, for example, the stereographic projection of  $[100]$  direction crossing the spherical surface at point  $P$ , join  $P$  with the south pole  $S$  and the intersection of  $PS$  with the equatorial plane will be the stereographic projection of  $[100]$  direction.

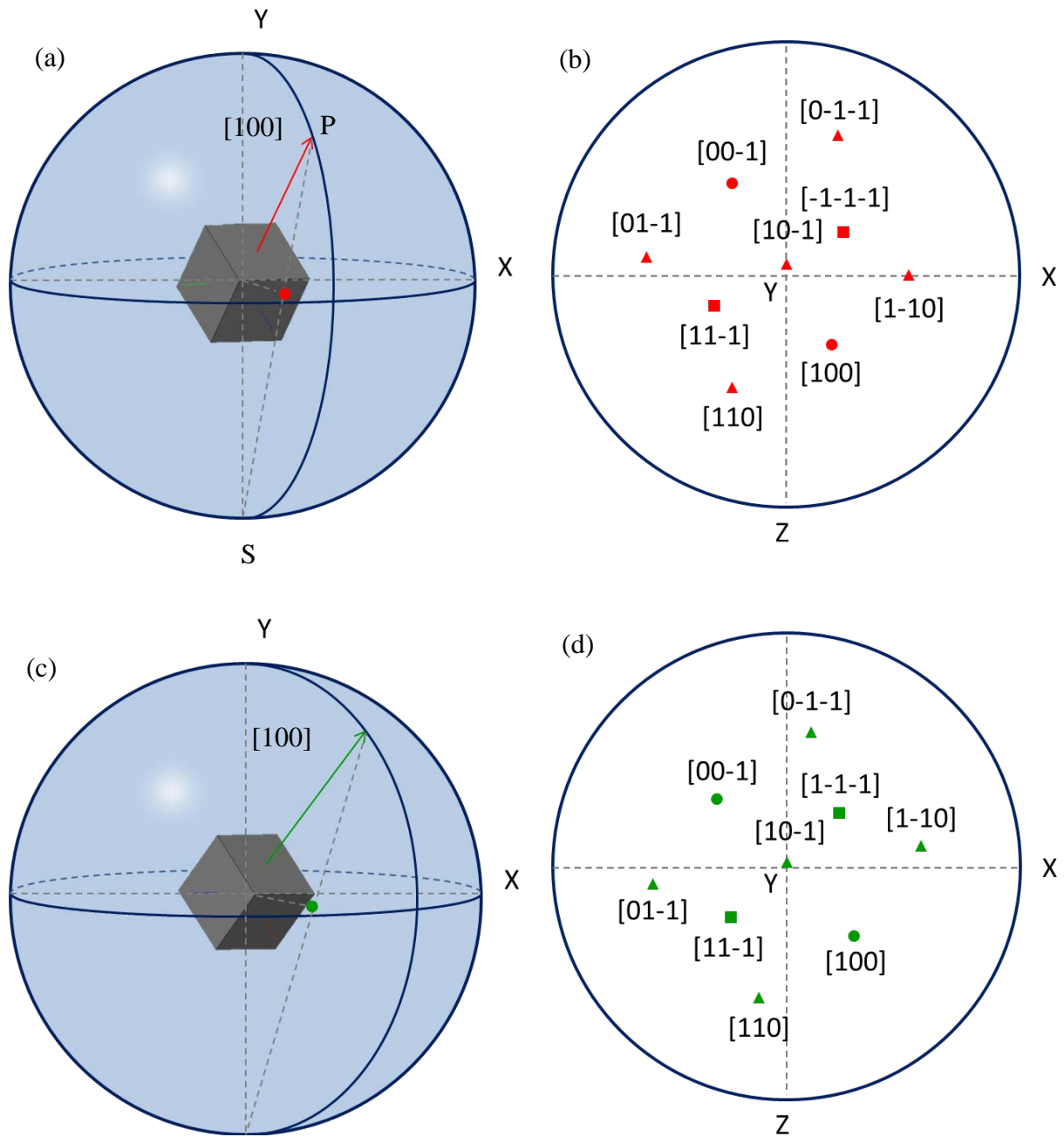


**Fig. 2.39.** (a) The spherical and (b) the stereographic projections of grain I (upper); (c) the spherical and (d) the stereographic projections of grain II (lower) of APT sample containing  $11^\circ[4\bar{4}3]$  GB

The first step is to plot the 3D APT reconstruction and, guided by the GB position, turn the reconstruction so that the GB is located exactly as on the IPF map (Fig. 2.40).

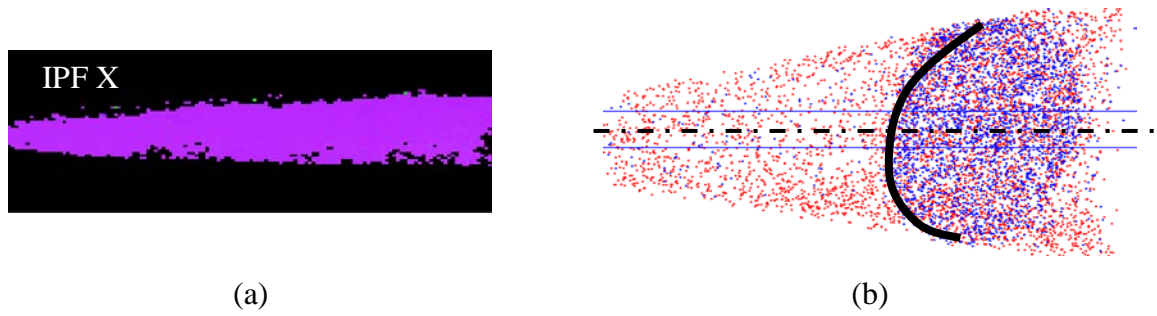


**Fig. 2.40.** (a) IPF X color map and (b) 3D APT reconstruction of the sample containing the  $11^\circ[4\bar{4}3]$  GB. The reconstruction is turned so that the GB is located as well as on the IPF map

Second, the APT reconstruction is rotated around tip axis (defined previously as the Y axis in TKD) until the GB projection appears as a straight line (Fig. 2.41a). Doing this, the angle of rotation around Y axis needed to get a straight projection, noted  $\alpha$ , is measured. In the example given in figures Fig. 2.40b and Fig. 2.41a it is about  $70^\circ$ .

Then, the angle between the GB plane normal and the Y-axis can be directly measured, as it is shown in Fig. 2.41b. This angle, noted  $\beta$ , is the angle of inclination of the GB plane from the perpendicular position relative to the tip axis. In the example given here, it is about  $30^\circ$ .

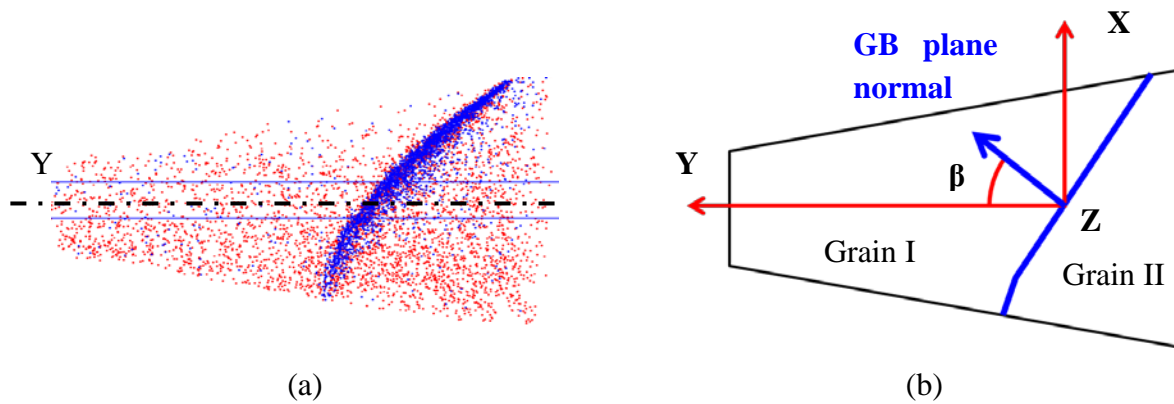


**Fig. 2.41.** (a) 3D APT reconstruction of sample containing  $11^\circ[4\bar{4}3]$  GB after rotation to the angle  $\alpha = 70^\circ$ , (b) schematic image of APT reconstruction with position of GB plane relatively to the coordinate system. The Y axis is parallel to the tip axis, the GB plane normal is inclined from the Y axis to the angle  $\beta$

The knowledge of angles  $\alpha$  and  $\beta$  allows to determine Miller indexes of the GB plane in both grains, as shown in Fig. 2.42. Thus, the complete geometry of the analysed GB is known. It is here  $11^\circ[4\bar{4}3](\bar{3}44)/(\bar{4}55)$ .

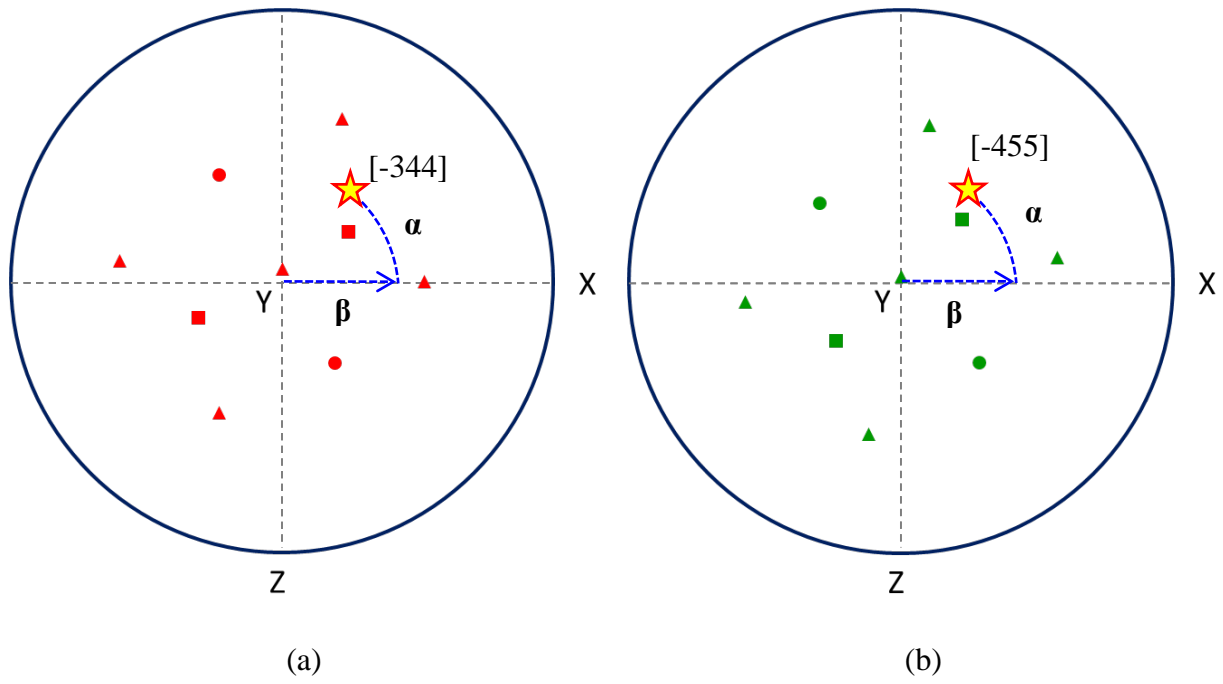


**Fig. 2.42.** Scheme for determination of the GB plane normal in (a) Grain I and (b) Grain II

## Conclusion

The methodology, combining different techniques such as Atom Probe Tomography, Scanning Transmission Electron Microscopy and Scanning Electron Microscopy / Focused Ion Beam / Transmission Kikuchi Diffraction to get accurate and representative information about intergranular segregation and grain boundary geometry was described. The principles of different techniques, the optimization of parameters, the data treatment and GB segregation quantification were detailed in this chapter.

The first part detailed the chemical composition and microstructure in the as-received state and ageing conditions. The measured bulk concentration of phosphorus and carbon is close to the expected nominal composition. The distribution of species in the atom probe volume is homogenous. However, there is a fluctuation of phosphorus and carbon concentrations from one analyzed volume to another.

The second part describes the underlying principles of Atom Probe Tomography and the way to adjust the reconstruction parameters. The simulation of GB evaporation process reveals that the lower evaporation field of matrix atoms at GB leads to their higher atomic density near a GB, and that, solute atoms with the higher evaporation field hold longer over the specimen surface, appearing at deeper position in the APT reconstruction in the analysis direction (asymmetrical concentration profile across GB). These results are in good agreement with our experiments. In order to minimize the influence of APT artifacts, the Gibbsian interfacial excess is measure from the cumulative diagram and is converted to a fraction of a monolayer assuming that the phosphorus atoms reside in a single close-packed (110) plane of the BCC  $\alpha$ -iron lattice.

The third part describes the principles of Scanning Transmission Electron Microscopy. In the current work, it is used to study if dependence between irradiation depth and phosphorus GB segregation levels exists and also to estimate the number density of irradiation-created defects such as dislocations and voids. The GB segregation was measured using energy dispersive X-ray spectroscopy. The dislocation and voids were visualized under two-beam conditions.

The fourth part presents the principles of SEM and FIB imaging, the deposition and milling processes, the SEM/FIB specimen preparation, the EBSD and TKD mapping. Also, the method to identify five crystallographic DOF's of GB using correlative TKD and APT is given in details.

## References

- [1] ASTM A508 / A508M-04, Standard Specification for Quenched and Tempered Vacuum-Treated Carbon and Alloy Steel Forgings for Pressure Vessels, ASTM International, West Conshohocken, PA, 2004, [www.astm.org](http://www.astm.org), doi: 10.1520/A0508\_A0508M-04.
- [2] C. Miller, F. Champigny, J.M. Frund, Manufacturing Conditions of French Reactor Pressure Vessels to Avoid the Occurrence of Hydrogen Flakes, in: ASME, 2016: p. V01AT01A063. doi:10.1115/PVP2016-63881.
- [3] Suzuki, Z. Für Met. 83 (1992).
- [4] B. Radiguet, Etude de la formation d'amas diffus de solutés sous irradiation dans des alliages modèles ferritiques, PhD thesis, Université de Rouen, 2004.
- [5] O.K. von Goldbeck, IRON—Binary Phase Diagrams, Springer Berlin Heidelberg, Berlin, 1982.
- [6] Y. Serruys, M.-O. Ruault, P. Trocellier, S. Henry, O. Kaïtasov, P. Trouslard, Multiple ion beam irradiation and implantation: JANNUS project, Nucl. Instrum. Methods Phys. Res. Sect. B Beam Interact. Mater. At. 240 (2005) 124–127. doi:10.1016/j.nimb.2005.06.100.
- [7] N.H. Packan, K. Farrell, J.O. Stiegler, Correlation of neutron and heavy-ion damage, J. Nucl. Mater. 78 (1978) 143–155. doi:10.1016/0022-3115(78)90513-5.
- [8] J.F. Ziegler, J.P. Biersack, The Stopping and Range of Ions in Matter, in: D.A. Bromley (Ed.), Treatise Heavy-Ion Sci., Springer US, 1985.
- [9] ASTM standart E521-96. Standard practice for neutron radiation damage simulation by charged-particle irradiation, ASTM International, West Conshohocken, PA, 2009.
- [10] R.E. Stoller, M.B. Toloczko, G.S. Was, A.G. Certain, S. Dwaraknath, F.A. Garner, On the use of SRIM for computing radiation damage exposure, Nucl. Instrum. Methods Phys. Res. Sect. B Beam Interact. Mater. At. 310 (2013) 75–80. doi:10.1016/j.nimb.2013.05.008.
- [11] M.K. Miller, Atom Probe Tomography, Springer US, Boston, 2000. doi:10.1007/978-1-4615-4281-0.
- [12] B. Gault, M.P. Moody, J.M. Cairney, S.P. Ringer, Atom Probe Microscopy, Springer New York, New York, 2012. doi:10.1007/978-1-4614-3436-8.
- [13] M.K. Miller, K.F. Russell, G.B. Thompson, Strategies for fabricating atom probe specimens with a dual beam FIB, Ultramicroscopy. 102 (2005) 287–298. doi:10.1016/j.ultramic.2004.10.011.

- [14] M.I. Hartshorne, D. Isheim, D.N. Seidman, M.L. Taheri, Specimen preparation for correlating transmission electron microscopy and atom probe tomography of mesoscale features, *Ultramicroscopy*, 147 (2014) 25–32. doi:10.1016/j.ultramic.2014.05.005.
- [15] E.A. Marquis, R. Hu, T. Rousseau, A systematic approach for the study of radiation-induced segregation/depletion at grain boundaries in steels, *J. Nucl. Mater.* 413 (2011) 1–4. doi:10.1016/j.jnucmat.2011.03.023.
- [16] A. Etienne, B. Radiguet, N.J. Cunningham, G.R. Odette, P. Pareige, Atomic scale investigation of radiation-induced segregation in austenitic stainless steels, *J. Nucl. Mater.* 406 (2010) 244–250. doi:10.1016/j.jnucmat.2010.08.043.
- [17] M.L. Taheri, J.T. Sebastian, B.W. Reed, D.N. Seidman, A.D. Rollett, Site-specific atomic scale analysis of solute segregation to a coincidence site lattice grain boundary, *Ultramicroscopy*, 110 (2010) 278–284. doi:10.1016/j.ultramic.2009.11.006.
- [18] M. Herbig, M. Kuzmina, C. Haase, R.K.W. Marceau, I. Gutierrez-Urrutia, D. Haley, D.A. Molodov, P. Choi, D. Raabe, Grain boundary segregation in Fe–Mn–C twinning-induced plasticity steels studied by correlative electron backscatter diffraction and atom probe tomography, *Acta Mater.* 83 (2015) 37–47. doi:10.1016/j.actamat.2014.09.041.
- [19] Y.J. Li, D. Ponge, P. Choi, D. Raabe, Segregation of boron at prior austenite grain boundaries in a quenched martensitic steel studied by atom probe tomography, *Scr. Mater.* 96 (2015) 13–16. doi:10.1016/j.scriptamat.2014.09.031.
- [20] B. Färber, E. Cadel, A. Menand, G. Schmitz, R. Kirchheim, Phosphorus segregation in nanocrystalline Ni–3.6 at.% P alloy investigated with the tomographic atom probe (TAP), *Acta Mater.* 48 (2000) 789–796. doi:10.1016/S1359-6454(99)00397-3.
- [21] [www.atomprobe.materials.ox.ac.uk](http://www.atomprobe.materials.ox.ac.uk)
- [22] L. Yao, B. Gault, J.M. Cairney, S.P. Ringer, On the multiplicity of field evaporation events in atom probe: A new dimension to the analysis of mass spectra, *Philos. Mag. Lett.* 90 (2010) 121–129. doi:10.1080/09500830903472997.
- [23] B.P. Geiser, T.F. Kelly, D.J. Larson, J. Schneir, J.P. Roberts, Spatial Distribution Maps for Atom Probe Tomography, *Microsc. Microanal.* 13 (2007) 437–447. doi:10.1017/S1431927607070948.
- [24] F. Vurpillot, G. Da Costa, A. Menand, D. Blavette, Structural analyses in three-dimensional atom probe: a Fourier transform approach, *J. Microsc.* 203 (2001) 295–302. doi:10.1046/j.1365-2818.2001.00923.x.
- [25] D. Blavette, A. Bostel, J.M. Sarrau, B. Deconihout, A. Menand, An atom probe for three-dimensional tomography, *Nature* 363 (1993) 432–435. doi:10.1038/363432a0.

- [26] P. Maugis, K. Hoummada, A methodology for the measurement of the interfacial excess of solute at a grain boundary, *Scr. Mater.* 120 (2016) 90–93. doi:10.1016/j.scriptamat.2016.04.005.
- [27] P.J. Felfer, C.R. Killmore, J.G. Williams, K.R. Carpenter, S.P. Ringer, J.M. Cairney, A quantitative atom probe study of the Nb excess at prior austenite grain boundaries in a Nb microalloyed strip-cast steel, *Acta Mater.* 60 (2012) 5049–5055. doi:10.1016/j.actamat.2012.06.013.
- [28] L. Karlsson, H. Nordén, Overview no. 63. Non-equilibrium grain boundary segregation of boron in austenitic stainless steel-II. Fine scale segregation behaviour, *Acta Metall.* 36 (1988) 13–24. doi:10.1016/0001-6160(88)90024-7.
- [29] H. Erhart, H.J. Grabke, Equilibrium segregation of phosphorus at grain boundaries of Fe–P, Fe–C–P, Fe–Cr–P, and Fe–Cr–C–P alloys, *Met. Sci.* 15 (1981) 401–408. doi:10.1179/030634581790426877.
- [30] M. Tomozawa, Y. Miyahara, K. Kako, Solute segregation on  $\Sigma 3$  and random grain boundaries in type 316L stainless steel, *Mater. Sci. Eng. A.* 578 (2013) 167–173. doi:10.1016/j.msea.2013.04.048.
- [31] F. Vurpillot, Three-Dimensional Reconstruction in Atom Probe Tomography, in: *Atom Probe Tomogr.*, Elsevier, 2016: pp. 183–249. doi:10.1016/B978-0-12-804647-0.00007-3.
- [32] P.J. Felfer, B. Gault, G. Sha, L. Stephenson, S.P. Ringer, J.M. Cairney, A New Approach to the Determination of Concentration Profiles in Atom Probe Tomography, *Microsc. Microanal.* 18 (2012) 359–364. doi:10.1017/S1431927611012530.
- [33] R. Lard, L. Lechevallier, A. Zarefy, A. Bostel, J. Juraszek, J.M. Le Breton, B. Rodmacq, B. Dieny, Structural analysis of a (Pt/Co)<sub>3</sub>/IrMn multilayer: Investigation of sub-nanometric layers by tomographic atom probe, *J. Appl. Phys.* 105 (2009). doi:10.1063/1.3106636.
- [34] J.W. Gibbs, *The collected works of J. Willard Gibbs.*, Yale University Press, New Haven, 1948.
- [35] B.W. Krakauer, D.N. Seidman, Absolute atomic-scale measurements of the Gibbsian interfacial excess of solute at internal interfaces, *Phys. Rev. B.* 48 (1993) 6724–6727. doi:10.1103/PhysRevB.48.6724.
- [36] M.K. Miller, K.F. Russell, APFIM characterization of a high phosphorus Russian RPV weld, *Appl. Surf. Sci.* 94–95 (1996) 378–383. doi:10.1016/0169-4332(95)00400-9.
- [37] M. Hazewinkel, ed., *Encyclopaedia of mathematics: an updated and annotated translation of the Soviet “Mathematical encyclopaedia,”* Reidel; Sold and distributed in the

U.S.A. and Canada by Kluwer Academic Publishers, Dordrecht ; Boston : Norwell, MA, U.S.A, 1988.

[38] S.J. Pennycook, A.R. Lupini, M. Varela, A. Borisevich, Y. Peng, M.P. Oxley, K.V. Benthem, M.F. Chisholm, Scanning Transmission Electron Microscopy for Nanostructure Characterization, in: W. Zhou, Z.L. Wang (Eds.), Scanning Microsc. Nanotechnol., Springer New York, 2006: pp. 152–191. doi:10.1007/978-0-387-39620-0\_6.

[39] S.J. Pennycook, P.D. Nellist, eds., Scanning Transmission Electron Microscopy, Springer New York, New York, NY, 2011.

[40] D.B. Williams, C.B. Carter, The Transmission Electron Microscope, in: Transm. Electron Microsc., Springer US, 2009: pp. 3–22. doi:10.1007/978-0-387-76501-3\_1.

[41] M.L. Jenkins, M.A. Kirk, Characterisation of Radiation Damage by Transmission Electron Microscopy, Taylor & Francis, 2000.

[42] <http://www.eels.info/>

[43] J. Silcox, Core-loss EELS, Curr. Opin. Solid State Mater. Sci. 3 (1998) 336–342. doi:10.1016/S1359-0286(98)80042-9.

[44] T. Malis, S.C. Cheng, R.F. Egerton, EELS log-ratio technique for specimen-thickness measurement in the TEM, J. Electron Microsc. Tech. 8 (1988) 193–200. doi:10.1002/jemt.1060080206.

[45] A.D. Gianfrancesco, Materials for Ultra-Supercritical and Advanced Ultra-Supercritical Power Plants, Woodhead Publishing, 2016.

[46] G. Cliff, G.W. Lorimer, The quantitative analysis of thin specimens, J. Microsc. 103 (1975) 203–207. doi:10.1111/j.1365-2818.1975.tb03895.x.

[47] R.D. Carter, D.L. Damcott, M. Atzmon, G.S. Was, S.M. Bruemmer, E.A. Kenik, Quantitative analysis of radiation-induced grain-boundary segregation measurements, J. Nucl. Mater. 211 (1994) 70–84. doi:10.1016/0022-3115(94)90282-8.

[48] Layout MyScope, (n.d.).

<http://www.ammrf.org.au/myscope/sem/practice/principles/layout.php#detail> (accessed June 15, 2017).

[49] L. Reimer, Scanning Electron Microscopy, Springer Berlin Heidelberg, Berlin, Heidelberg, 1998. doi:10.1007/978-3-540-38967-5.

[50] N. Yao, Focused ion beam systems: basics and applications, Cambridge University Press, 2007.

- [51] L.A. Giannuzzi, F.A. Stevie, eds., *Introduction to Focused Ion Beams*, Kluwer Academic Publishers, Boston, 2005. doi:10.1007/b101190.
- [52] A. Aitkaliyeva, J.W. Madden, B.D. Miller, J.I. Cole, J. Gan, Comparison of preparation techniques for nuclear materials for transmission electron microscopy (TEM), *J. Nucl. Mater.* 459 (2015) 241–246. doi:10.1016/j.jnucmat.2015.01.042.
- [53] A. Rigort, J.M. Plitzko, Cryo-focused-ion-beam applications in structural biology, *Arch. Biochem. Biophys.* 581 (2015) 122–130. doi:10.1016/j.abb.2015.02.009.
- [54] A.J. Schwartz, M. Kumar, B.L. Adams, D.P. Field, eds., *Electron Backscatter Diffraction in Materials Science*, Springer US, Boston, MA, 2009.
- [55] R.R. Keller, R.H. Geiss, Transmission EBSD from 10 nm domains in a scanning electron microscope: TRANSMISSION EBSD IN THE SEM, *J. Microsc.* 245 (2012) 245–251. doi:10.1111/j.1365-2818.2011.03566.x.
- [56] K. Babinsky, R. De Kloe, H. Clemens, S. Primig, A novel approach for site-specific atom probe specimen preparation by focused ion beam and transmission electron backscatter diffraction, *Ultramicroscopy.* 144 (2014) 9–18. doi:10.1016/j.ultramic.2014.04.003.
- [57] K. Babinsky, W. Knabl, A. Lorich, R. De Kloe, H. Clemens, S. Primig, Grain boundary study of technically pure molybdenum by combining APT and TKD, *Ultramicroscopy.* 159 (2015) 445–451. doi:10.1016/j.ultramic.2015.05.014.
- [58] S. Mandal, K.G. Pradeep, S. Zaefferer, D. Raabe, A novel approach to measure grain boundary segregation in bulk polycrystalline materials in dependence of the boundaries' five rotational degrees of freedom, *Scr. Mater.* 81 (2014) 16–19. doi:10.1016/j.scriptamat.2014.02.016.
- [59] Whittaker E.J.W., *The stereographic projection*, University Colledge Cardiff Press, Cardiff, United Kingdom, 1984.



## Chapter 3. Equilibrium grain boundary segregation in Fe-P-C alloy

Segregation of phosphorus to the grain boundaries (GBs) in reactor pressure vessel (RPV) steel can occur both during fabrication (stress relieve post-weld heat treatment) and exploitation (thermal ageing, irradiation). In order to separate the different origins of phosphorus GB segregation the as-received model alloys were subjected to a stress relieve heat treatment (SRHT) and a thermal ageing at the irradiation temperature. The first part of this chapter presents the atomic scale investigation of the intergranular phosphorus segregation at low-angle and high-angle GBs in a Fe-0.034 at.% P-0.01 at.% C model alloy heat treated at 650°C and subsequently thermally aged at 450°C.

Since the phosphorus GB segregation in steel can cause the temper embrittlement, many experimental and theoretical investigations were performed on this subject [1–6]. Most of them were carried using Auger Electron Spectroscopy (AES). AES studies the composition of fresh fractured surfaces obtained by in-situ impact. During the fracture, the crack preferentially follows GBs with the highest phosphorus segregation (less cohesion), i.e. not all type of GBs is covered by the AES analysis. Also, the identification of the GB crystallography in the fractured polycrystalline material is a difficult task. Since usually one part of a broken sample is retained for the measurement, only one geometrical parameter can be determined (GB plane of retained grain), whereas other characteristics of a GB (the misorientation angle, the rotation axis, the GB plane orientation of second grain) cannot be defined. Besides that, the measured GB segregation is doubled on the assumption that the distribution of phosphorus atoms between two fracture surfaces is equally divided. However, it can be noted that some experiments which compare the solute segregation intensity on both specimen halves have revealed a non-uniform distribution between two surfaces [7,8].

Atom Probe Tomography (APT) has no such drawbacks. Moreover, APT provides more accurate measurement of the GB solute segregation and in combination with other techniques (Transmission Kikuchi Diffraction, Scanning Transmission Electron Microscopy) gives complete information (5 macroscopic degrees of freedom) about the GB structure. Also, APT allows to quantify the intergranular segregation of carbon, in contrast with AES, where the sample surface can be contaminated with carbon during its exposure to the electron beam.

However, it is worth acknowledging that AES is a cheaper and faster method, and is still widely used. Also, the parameters for the prediction of the equilibrium intergranular

segregation given in literature were defined using AES experiments. Thus, the comparison of AES and APT techniques is necessary for our work. The second part describes the basic principles of AES and compares experimental results given by AES and APT for Fe-0.034 at.% P-0.01 at.% C model alloy after SRHT at 650°C during 2h.

The models of equilibrium GB segregation in binary and ternary systems are described in the third part of this chapter. Guttman's model of equilibrium GB segregation in multicomponent system is applied to predict the equilibrium phosphorus GB segregation in the Fe-0.034 at.%P-0.01 at.% C model alloy. The model considers the influence of the GB structure and the phosphorus-carbon interaction at GB.

### 3.1 APT measurement of equilibrium grain boundary segregation

The equilibrium segregation of solute elements at low-angle grain boundaries (LAGBs) and high-angle grain boundaries (HAGBs) was measured by APT in the Fe-0.034 at.% P-0.01 at.% C model alloy after: (1) stress relieve heat treatment (SRHT) at 650°C during 2 h, (2) SRHT at 650°C during 24 h and (3) thermal ageing at 450°C during 1000 hours after SRHT. SRHT during 24 h followed by air-cooling was done to ensure that the equilibrium segregation level is reached after recommended time (2 h). Five degrees of freedom were determined for each GB using combined APT/TKD method.

A typical three-dimensional APT reconstruction of a tip containing HAGB is presented in Fig. 3.1a. The GB with a misorientation of  $41^\circ[010] (-251)/(53-1)$  contains both phosphorus (blue) and carbon (red) atoms. Fig. 3.1b shows that the distribution of phosphorus atoms in the GB plane is homogenous. The same behavior was observed for carbon atoms (Fig. 3.1c).

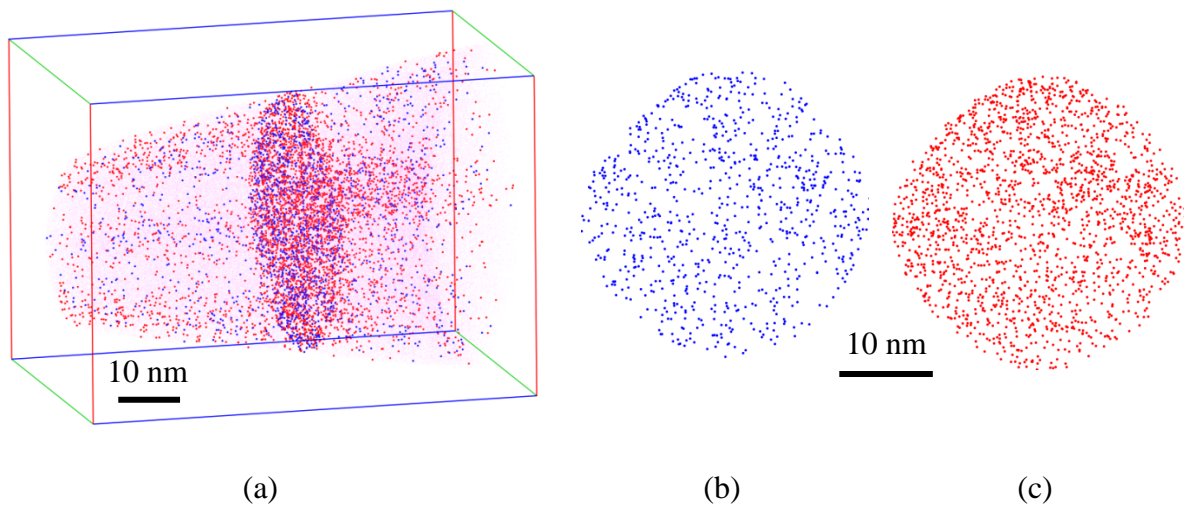


**Fig. 3.1.** APT reconstruction of a small volume of the Fe-0.034 at.% P-0.01 at.% C model alloy after SRHT at 650°C during 2 h demonstrates (a) the segregation of phosphorus (blue) and carbon (red) atoms at  $41^\circ[010] (-130)/(-120)$  GB and homogenous distribution of (b) phosphorus and (c) carbon atoms on the GB plane

The Gibbsian interfacial excess of phosphorus and carbon atoms measured by APT is converted to a fraction of a monolayer, assuming that the phosphorus atoms reside in a single close-packed (110) plane. Monolayer coverages of phosphorus and carbon atoms with the corresponding GB geometries are presented in Table 3.1. Four GBs were analysed from the sample after SRHT during 2 h: two LAGBs and two HAGBs. Since the HAGB structure has a less ordered arrangement of the atoms at the GB plane with large areas of misfits and a

relatively more excess volume [9], there is more phosphorus segregation at HAGBs ( $\sim 0.12$  monolayer) than at LAGBs ( $\sim 0.04$  monolayer).

Two HAGBs were analyzed from the sample after 24h of SRHT. The average value of phosphorus GB segregation is  $0.12 \pm 0.01$  monolayer, which is similar to the value measured from the sample annealed at the same temperature ( $650^\circ\text{C}$ ) but during shorter time (2h). Since the phosphorus GB segregation does not change with an increasing of the annealing time from 2h to 24 h, it is supposed, that the value of  $0.12 \pm 0.01$  monolayer is the equilibrium phosphorus GB segregation at  $650^\circ\text{C}$ . The time needed to reach the equilibrium GB concentration is less than or equal to 2h.

The samples after SRHT were subjected to the thermal ageing at  $450^\circ\text{C}$  during 1000 h and this increases the average phosphorus segregation from  $0.12 \pm 0.01$  to  $0.14 \pm 0.01$  monolayer at HAGBs and from  $0.04 \pm 0.01$  to  $0.10 \pm 0.01$  monolayer at LAGBs.

**Table 3.1.** Five degrees of freedom and solute segregation information for GBs from different heat treated samples.  $C_p^\Phi$  and  $C_c^\Phi$  are the GB segregation of phosphorus and carbon atoms, respectively, given in a fraction of the (110) plane monolayer

Heat treatment	GB	$C_p^\Phi$ (monolayer)	$C_c^\Phi$ (monolayer)
SRHT 2h	$6^\circ[41-2] (01-2)/(02-3)$	$0.04 \pm 0.01$	$0.31 \pm 0.01$
	$8^\circ[03-3] (-542)/(34-2)$	$0.04 \pm 0.01$	$0.29 \pm 0.01$
	$41^\circ[010] (-251)/(53-1)$	$0.13 \pm 0.02$	$0.34 \pm 0.02$
	$35^\circ[014] (031)/(241)$	$0.12 \pm 0.01$	$0.29 \pm 0.01$
SRHT 24h	$35^\circ[143] (-321)/(54-1)$	$0.11 \pm 0.02$	$0.02 \pm 0.02$
	$42^\circ[31-1] (41-4)/(010)$	$0.13 \pm 0.01$	$0.04 \pm 0.01$
Thermal ageing at $450^\circ\text{C}$ , 1000 h	$11^\circ[412] (1-41)/(1-65)$	$0.10 \pm 0.01$	$0.21 \pm 0.02$
	$33^\circ[121] (53-1)/(-331)$	$0.14 \pm 0.01$	$0.31 \pm 0.01$
	$43^\circ[4-10] (2-21)/(-140)$	$0.15 \pm 0.02$	$0.25 \pm 0.01$
	$48^\circ[11-2] (3-61)/(-612)$	$0.14 \pm 0.01$	$0.30 \pm 0.02$

With regards to the carbon GB segregation, its level significantly decreases after additional SRHT during 24h. The average carbon GB segregation in the sample after 2h of SRHT is  $0.30 \pm 0.01$  monolayer and only  $0.03 \pm 0.01$  monolayer after 24h of SRHT. Fast diffusion of carbon atoms in bcc iron at  $650^\circ\text{C}$  ( $6.4 \times 10^{-8} \text{cm}^2/\text{s}$  from [10]) results on very

short time (few seconds) needed to reach equilibrium carbon GB segregation. Thus, the increasing of the annealing time should not affect the GB segregation level.

The probably explanation of different carbon segregation is the difference in size of the annealed samples. A SRHT during 2h was performed on the specimen with the size of  $20 \times 20 \times 20 \text{ mm}^3$ , while additional SRHT during 24 h was done on the  $4 \times 4 \times 20 \text{ mm}^3$  sample. Both treatments were followed by air-cooling. The bigger size of the specimen annealed during 2h could lead to the slower cooling rate and to GB segregation of small solutes (carbon) during cooling.

Cowan et al. [11] have shown that in the Fe-0.06 wt.% P-0.002 wt.% C alloy the carbon atoms due to their high mobility even at low temperatures continue to segregate to GBs during air-cooling of the specimen with the size of  $30 \times 100 \times 700 \text{ mm}^3$  from  $600^\circ\text{C}$  to the room temperature (Fig. 3.2). Slight de-segregation of phosphorus at the intermediate temperatures ( $200\text{-}400^\circ\text{C}$ ) with the simultaneously 20% increase of carbon indicates the site competition between phosphorus and carbon atoms at GB.

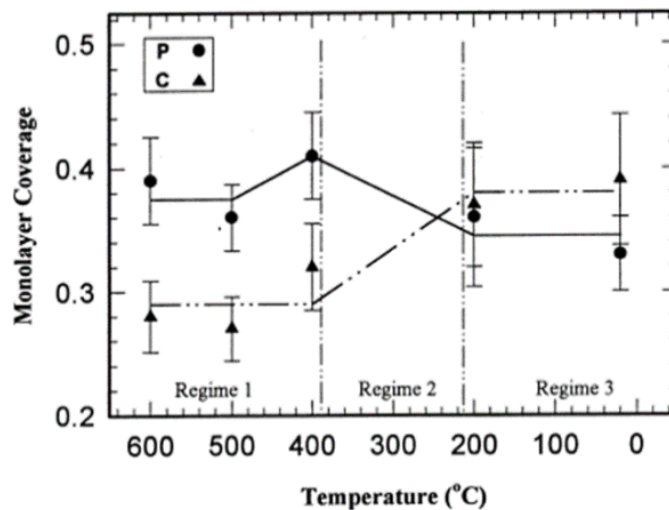


**Fig. 3.2.** The change of phosphorus and carbon GB segregations in the Fe-0.06 wt.% P-0.002 wt.% C alloy during air cooling from  $600^\circ\text{C}$  to the room temperature [11]

In the current work, no phosphorus de-segregation during air-cooling was observed. However, the experimental conditions in the current work are quite close to the conditions in the work of Cowan et al. (the alloy composition, the sample size, the quenching temperature) to suppose that the greater carbon GB segregation in the sample after 24 h SHRT is the result of the bigger sample size. Therefore, the lowest value of carbon GB segregation ( $0.03 \pm 0.01$  monolayer) obtained after fast air-quenching of the small sample ( $4 \times 4 \times 20 \text{ mm}^3$ ) is close to the equilibrium GB segregation of carbon at  $650^\circ\text{C}$ .

Since the sample aged at 450°C during 1000h is also small ( $4 \times 4 \times 20 \text{ mm}^3$ ), the carbon GB segregation equal to  $0.25 \pm 0.04$  monolayer is considered to be the equilibrium GB segregation of carbon at 450°C.

## 3.2 Comparison of Auger Electron Spectroscopy with Atom Probe measurement of phosphorus grain boundary segregation

Auger Electron Spectroscopy (AES) is the most extensively used technique for the last four decades to study GB segregation of impurity elements in iron and ferritic steels in connection to their temper embrittlement [12]. The basic advantages of this technique are the rapid and quantitative identification of segregated elements, the high sensitivity for chemical analysis in the 5-20 Å region near the surface, and the ability to detect all elements above He [13].

In the current work, the equilibrium GB segregation in the Fe-0.034 at.% P-0.01 at.% C model alloy at 450°C is predicted using the thermodynamic parameters from literature, mainly from the works of Lejček et al. These parameters (segregation enthalpy, segregation entropy, interaction coefficients) were obtained from AES analysis of fractured polycrystals or bicrystals [14–16].

Since the experimental part of the current work based on the APT study of the GB segregation, the comparison of two techniques is necessary. Moreover, although until now both APT and AES have been widely used to study GB segregation, however, there are only a few works comparing them [17].

### 3.2.1 Principle of Auger electron spectroscopy

The process of Auger electron formation is shown in Fig. 3.3. A primary electron beam with sufficiently high energy (1-20 keV) irradiates the sample. The primary electrons penetrate in the sample up to 0.1-1µm depth, depending on their energy [18]. If target atom is ionized by the removal of an inner shell electron, electrons from the higher shell can fill up the ionized states. This is accompanied by the release of energy  $E(K) - E(L_1)$ , which may occur in the form of a photon, as in X-ray fluorescence, or may transmit to another electron in an outer level that escapes from the atom as an Auger electron [19].

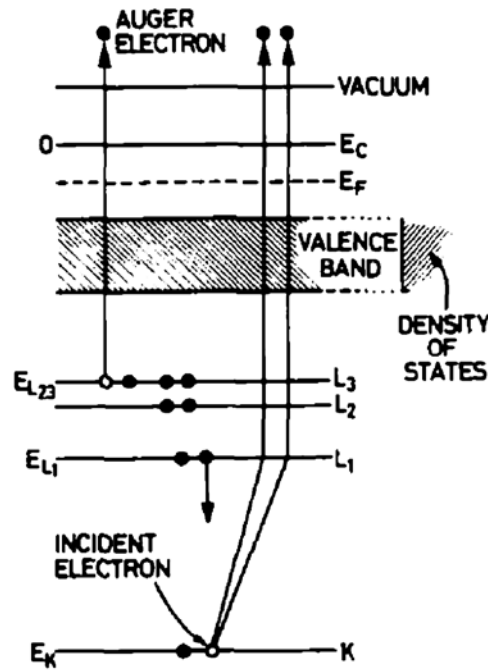


**Fig. 3.3.** The  $KL_1L_2$  Auger process. The incident electron from K shell leaves the atom. Then the electron from  $L_1$  fills up the ionized state. The release of energy  $E_K - E_{L_1}$  transmits to the electron in the outer  $L_{23}$  shell. As a result, the electron from  $L_{23}$  escapes from the atom as Auger electron [19]

The kinetic energy,  $E(Z)$ , of the  $KL_1L_2$  Auger electron can be written as [19,20]

$$E(Z) = E_K(Z) - E_{L_1}(Z) - E_{L_2}(Z) - \phi \quad (23)$$

where  $Z$  is the atomic number of the atom,  $E_K$ ,  $E_{L_1}$ ,  $E_{L_2}$  are the binding energies of electron in the K,  $L_1$  and  $L_2$  energy levels and  $\phi$  is a term containing both the sample and spectrometer work functions as well as many-body corrections, which account for energy shift during the Auger process and other electronic effects. The  $\phi$  term is often small ( $< 10$  eV) and varies with the chemical state [20].

A typical Auger Electron Spectrometer consists of a stainless-steel ultra-high vacuum chamber with an electron gun and an electron kinetic energy analyzer, a data-acquisition and the analysis computer. In the current research, AES analysis was performed using the cylindrical mirror analyzer (Fig. 3.4).

The sample is fixed on a carousel target holder and in situ fractured by the impact hammer. All practical fracture stages provide for the liquid nitrogen cooled sample to attempt a brittle fracture. The fractured surface is bombarded by an electron beam focused to a spot size of less than  $1 \mu\text{m}$ . Auger electrons escaped from the sample pass through an entrance split in the center of two concentric cylinders. A negative potential  $V$  is applied to the outer

cylinder and electrons are deflected through the exit split and collected using an electron multiplier. By sweeping  $V$  over the desired range, a spectrum can be generated [19].

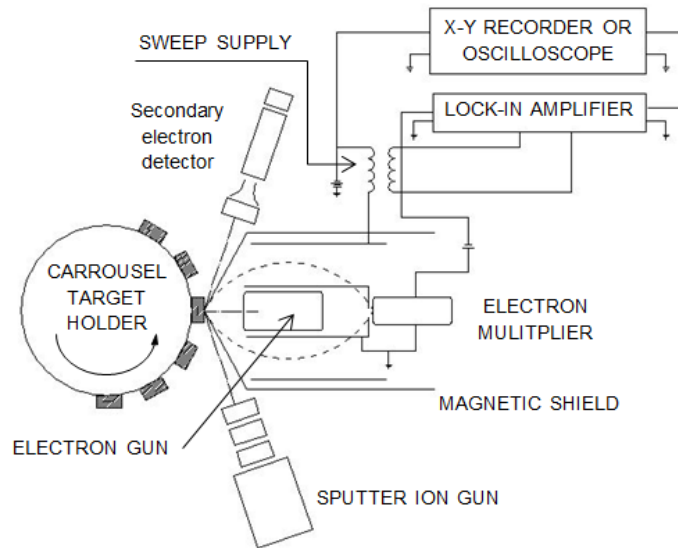


**Fig. 3.4** Schematic diagram of an Auger system based on a cylindrical mirror analyzer [19]

Fig. 3.5 shows schematically an Auger spectrum in which the number of emitted electrons  $N$  is given as a function of their kinetic energy  $E_{kin}$ . The Auger peaks are superimposed on a large and smoothly varying background consisting of inelastically scattered primary and secondary electrons. Because of this fact, Auger spectra are usually taken in the derivative mode  $dN(E)/dE$ . The area under the peak after background removal is approximately proportional to the number of atoms in a volume given by the primary beam diameter and the Auger electrons formation depth of a few monolayer from the surface [18].

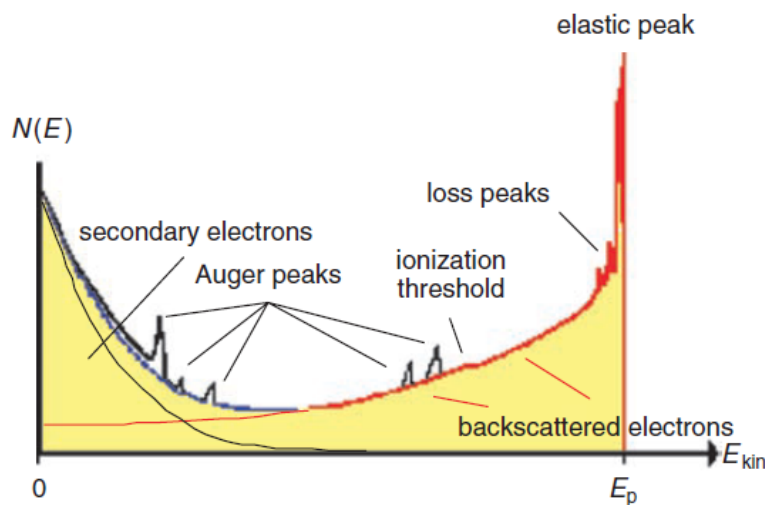


**Fig. 3.5.** Schematic representation of an Auger spectrum[21]

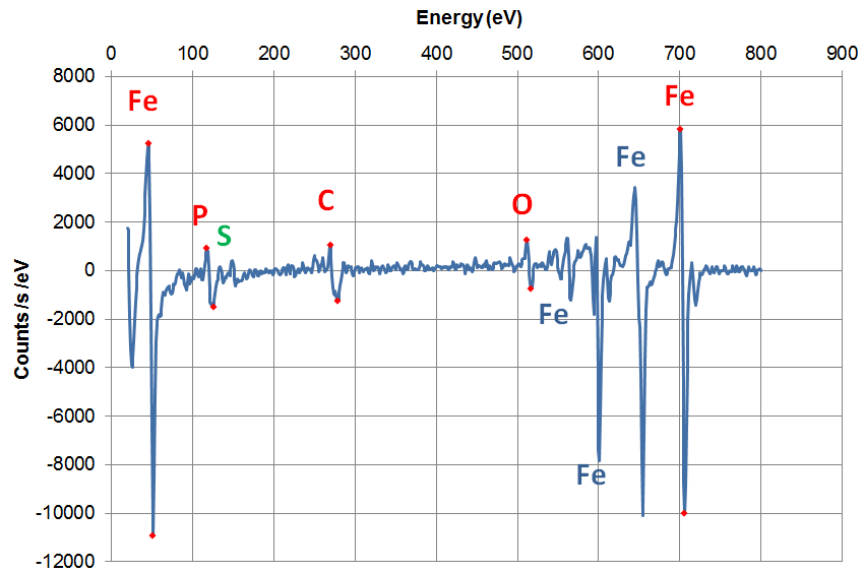
Several methods have been developed and used to transform the Auger signals to the intergranular solute segregation, which is usually given in atomic fraction (at.%) or mole fraction of the elements. They all can be divided to two main groups. The first group of methods is concerned with the comparison of the signal intensity of an element from the analysed sample with the signal intensity from a standard material of known composition under identical measurement conditions. The second group uses basic physical equations with appropriate materials and instrumental parameters. Also, a combination of both is applied in practice [18].

The method used in this work was developed (but not yet published) by V. Barnier, Ecole des Mines, Saint Etienne, France. This approach bases on a calibration of Auger intensity by an angle-resolved X-ray photoelectron spectroscopy (XPS). The XPS and AES measurements were carried out on the same specimen. The method does not require the standard sample and needs less number of parameters using in the quantification procedure comparing with the conventional methods. The results are given in the number of phosphorus atoms per unit surface.

### 3.2.2 AES and APT measurements of GB concentration

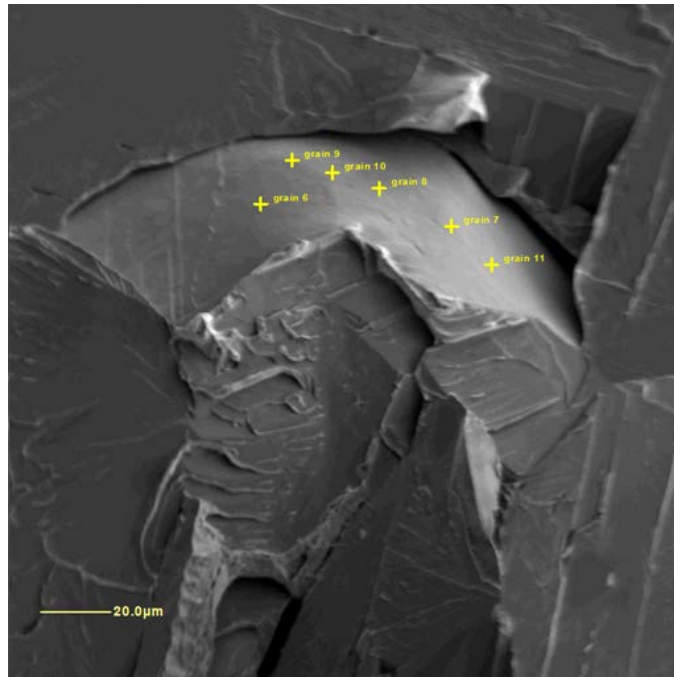
AES experiments were performed in the École des Mines de Saint-Étienne, Saint-Étienne, France. The material of study is the Fe-0.034 at.% P-0.01 at.% C model alloy annealed at 650°C during two hours. The samples, approximately  $1 \times 1 \times 15 \text{ mm}^3$ , with a notch at the midpoint were maintained by liquid nitrogen at  $-90^\circ\text{C}$  inside the AES chamber. They were then fractured by impact in a vacuum of  $2 \times 10^{-8} \text{ Pa}$  and one of fracture face presented to the Auger analysis. Analyses were performed in spot mode, where spots are randomly chosen by the operator. The values for the surface concentration on an intergranular fracture surface were multiplied by factor two, in order to account for the distribution of the segregated atoms on two fracture surfaces [15].

A typical AES spectrum (Intensity vs. kinetic energy) is presented in Fig. 3.6. As seen, it exists apparent phosphorus and carbon GB segregations. However, carbon, as well as oxygen, can be the result of contamination during AES analysis. It was occasionally found S, N and B traces on certain GB facets. The quantification procedure was provided only for phosphorus segregation as for the main segregated element.



**Fig. 3.6.** A typical AES spectra of fractured surface in the Fe-0.034 at.% P-0.01 at.% C alloy after 2h of SRHT

A fractograph of the first fractured sample is shown in Fig. 3.7. In order to study the phosphorus distribution on the fractured surface of one GB, six spectra were acquired from the same GB.



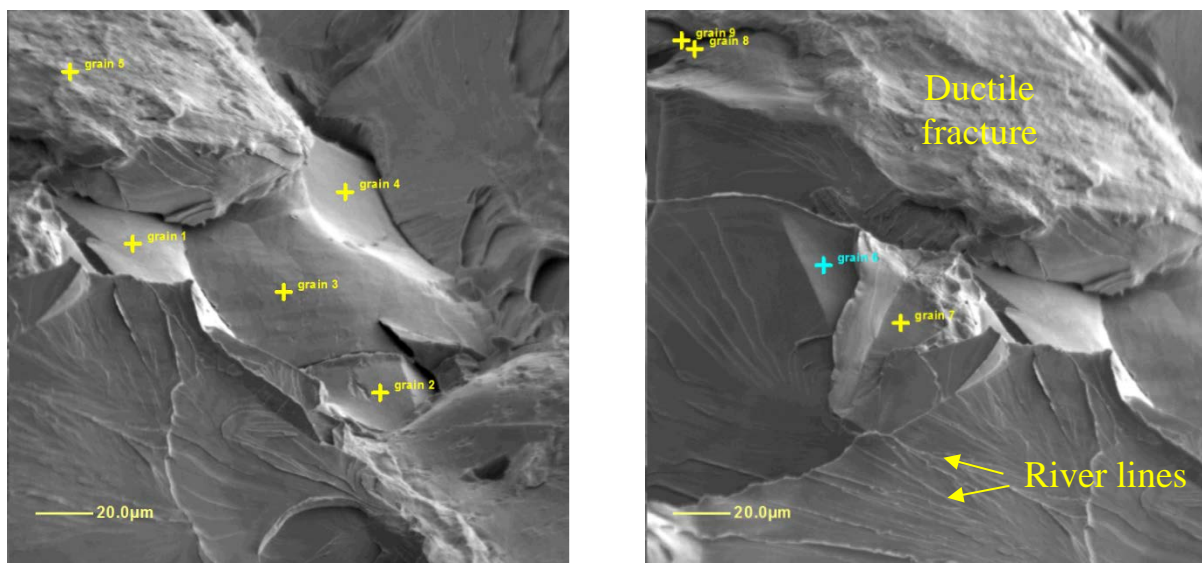
**Fig. 3.7.** Secondary electron image of the fracture surface of the first sample with the position of AES spots. All AES measurements are acquired from the same GB

Table 3.2 presents the phosphorus GB segregations given in the number of phosphorus atoms per unit surface for each AES spot. The average value of phosphorus GB concentration after noise cancelling is equal to  $(1.9 \pm 0.3) \times 10^{14}$  atoms/cm<sup>2</sup>.

**Table 3.2.** AES measurements of phosphorus GB segregation at the same GB facet

Measured location	Phosphorus segregation ( $10^{14}$ atoms / $\text{cm}^2$ )
Spot 6	2.41
Spot 7	1.74
Spot 8	1.58
Spot 9	2.34
Spot 10	1.88
Spot 11	1.90
<b>Average value</b>	$2.0 \pm 0.3$
<b>Average value after noise reduction</b>	$1.9 \pm 0.3$

Fig. 3.8 shows the secondary electron image of two fracture surfaces of the second sample with positions of AES spots. The fracture surface has a complex morphology containing three types of fracture. A ductile fracture has a dimpled surface created by the intensive plastic deformation ahead of crack and the microvoid coalescence. The cleavage facets are the results of transgranular brittle fracture, when the crack follows transgranular crystallographic plane (e.g., the  $\{110\}$  planes in BCC metal). The cleavage facets are recognized by the appearance of “river lines”. The smooth and usually curved surface indicates the intergranular fracture. The large fraction of ductile and cleavage fractures most likely signifies that the intergranular fracture occurs only at GBs with the high level of phosphorus segregation.

**Fig. 3.8.** Secondary electron image of the fracture surface of the second sample with the position of AES spots

On the second sample seven GB facets were analyzed (one spot per facet). AES measurements of the phosphorus segregation at different facets are given in Table 3.3.

**Table 3.3.** AES measurements of phosphorus concentration at fractured GBs of the 2<sup>nd</sup> sample

Measured location	Phosphorus segregation ( $10^{14}$ atoms / cm <sup>2</sup> )
GB sample I	$2.0 \pm 0.3$
GB 1	1.66
GB 2	1.65
GB 3	1.67
GB 4	1.08
GB 6	1.68
GB 7	1.70
<b>Average value</b>	$1.6 \pm 0.5$
<b>Average value after noise reduction</b>	$1.4 \pm 0.5$

The mean value of phosphorus segregation from the two samples analysed by AES is equal to  $1.4 \times 10^{14}$  atoms/cm<sup>2</sup>. This value is compared with phosphorus segregation at HAGBs obtained by APT and given in Table 3.4 in the same unit (atoms/cm<sup>2</sup>).

**Table 3.4.** Phosphorus GB segregation measured by APT and AES techniques

GB	P segregation ( $10^{14}$ atoms/cm <sup>2</sup> )
35°[014](16-1)/(33-1)	2.0
35°[143](-541)/(32-1)	1.7
41°[010] (-130)/(-120)	2.2
42°[31-1](-101)/(15-1)	2.2
6°[41-2](1-24)/(1-34)	0.6
8°[03-3](-252)/(52-3)	0.6
<b>Mean value from APT</b>	$1.6 \pm 0.7$
<b>Mean value from AES</b>	$1.4 \pm 0.5$

The details of GB segregation quantification using APT data are given in Chapter 2. The mean value of phosphorus segregation at HAGBs measured by APT is equal to  $(1.6 \pm$

$0.7)10^{14}$  atoms/cm<sup>2</sup>, which is in good agreement with AES experiment giving  $(1.4 \pm 0.5)10^{14}$  atoms/cm<sup>2</sup>.

Thus, assuming that segregated phosphorus atoms are equally divided between two fracture surfaces, the experimental values obtained from APT and AES are nearly the same. This indicates that APT measurements can be compared to literature and also that the parameters for modeling coming from AES can be used for further calculations.

### 3.3 Modelling of equilibrium grain boundary segregation

#### 3.3.1 The theories of grain boundary segregation

##### a) Langmuir-McLean theory for binary systems

Following Gibbs approach, the segregation of solute elements at the surface (grain boundary) decreases the surface tension, and thus the free energy of the system [22]. The mechanism of this process has been explained by McLean in terms of the lattice distortion energy around solute atoms [23]. He supposed that the GB structure consists of finite numbers of distorted sites. The free energy of solute atoms in this distorted site differs from the energy of a solute atom in the lattice site. The difference between two energies defines the segregation energy. Considering that  $P$  solute atoms distributed among  $N$  undistorted lattice sites and  $p$  atoms can occupy  $n$  distorted sites, the total free energy,  $G$ , is expressed as:

$$G = pe + PE - kT[\ln n! N! - \ln(n-p)! p! (N-P)! P!] \quad (24)$$

where  $e$  and  $E$  are the energies of the solute atoms at GB and in the lattice, respectively, and  $k$  is the configurational entropy of the arrangement of solute atoms in the matrix and at GB. The minimization of the free energy gives:

$$e - E = kT \ln \left( \frac{n-p}{p} \times \frac{P}{N-P} \right) \quad (25)$$

which can be transformed to:

$$\frac{p}{n-p} = \frac{P}{N-P} \exp \left( \frac{E-e}{kT} \right) \quad (26)$$

Writing  $C_i^B = P/N$  for concentration of solute  $i$  in the undistorted region (bulk concentration),  $C_i^\phi = p/n$  for concentration of solute  $i$  in the distorted region (GB concentration) and defining the standard Gibbs energy of segregation as  $\Delta G_i^0 = e - E$ , equation (26) can be expressed as:

$$\frac{C_i^\phi}{1 - C_i^\phi} = \frac{C_i^B}{1 - C_i^B} \exp\left(-\frac{\Delta G_i^0}{RT}\right) \quad (27)$$

**b) Guttman theory for multicomponent systems**

Based on McLean's theory of equilibrium segregation in a binary system and considering the interaction of segregated atoms given by Fowler's theory [24], Guttman [25] has developed a model to describe solute segregation in ternary or higher regular solutions. The model assumes that all solutes occupy the same area on the boundary and have repulsive, neutral or attractive interaction between each other [25–27]. In a manner similar to McLean, a general expression for intergranular segregation of solutes  $i = 1, 2, \dots, m - 1$  in a solvent  $m$  is:

$$\frac{C_i^\phi}{1 - \sum_{j=1}^{M-1} C_j^\phi} = \frac{C_i^B}{1 - \sum_{j=1}^{M-1} C_j^B} \exp\left(-\frac{\Delta G_i}{RT}\right) \quad (28)$$

where  $C_i^\phi$  and  $C_j^\phi$  are the GB segregation of solutes  $i$  and  $j$ , respectively,  $C_i^B$  and  $C_j^B$  are the bulk concentration of solutes  $i$  and  $j$ , respectively,  $\Delta G_i$  is the Gibbs free energy of GB segregation of element  $i$ ,  $R$  is a gas constant,  $T$  is the temperature.

The free Gibbs energy of segregation,  $\Delta G_i$ , is defined as:

$$\Delta G_i = \Delta H_i^0 - T\Delta S_i^0 - 2\alpha_{im}(C_i^\phi - C_i^B) + \sum_{j \neq i}^{M-1} \alpha'_{ij}(C_j^\phi - C_j^B) \quad (29)$$

where  $\Delta H_i^0$  and  $\Delta S_i^0$  are the standard molar enthalpy and entropy of segregation of solute  $i$  in a dilute binary  $m - i$  system, in which no interactions exist,  $\alpha_{im}$  and  $\alpha'_{ij}$  are the interaction coefficients between solute-matrix ( $i - m$ ) and solute-solute ( $i - j$ ), respectively. The solute-matrix interaction coefficient,  $\alpha_{im}$ , is defined as:

$$\alpha_{im} = ZN_A \left[ \varepsilon_{im} - \frac{\varepsilon_{ii} + \varepsilon_{mm}}{2} \right] \quad (30)$$

where  $Z$  is the lateral coordination number for segregant atoms in two-dimensional GB layer,  $N_A$  is the Avogadro's number,  $\varepsilon_{im}$  is the mixing energy between the nearest-neighbour solute atoms  $i$  and the matrix atoms  $m$ . In the case of  $\alpha_{im} > 0$  (repulsive interaction), a GB segregation increase the free energy of a system. On the contrary, if  $\alpha_{im} < 0$  (attractive interaction), the probability of occupation of nearest sites by the same kind of atoms ( $ii$  or  $mm$ ) is high, i.e. the GB segregation decreases the free energy. If there is no interaction between solute and solvent atoms,  $\alpha_{im} = 0$ , the ideal Langmuir-McLean segregation isotherm is obtained. A similar description is given for the solute-solute interaction coefficient  $\alpha'_{ij}$ .

*c) Seah and Hondros model*

Seah and Hondros [28] have used a multilayer gas adsorption theory of Brunauer, Emmett and Teller (truncated BET isotherm) [29] to describe intergranular segregation in a binary alloy. They considered that the GB solute segregation,  $C_i^\phi$ , depends on the solute solubility limit,  $C_i^*$ , of a solute  $i$  in a matrix  $m$  as:

$$\frac{C_i^\phi}{1 - C_i^\phi} = \frac{C_i^B}{C_i^*} \exp\left(-\frac{\Delta G_i^0 - \Delta G_i^*}{RT}\right) \quad (31)$$

where  $C_i^B$  is bulk concentration of segregated element  $i$ ,  $\Delta G_i^0$  is the standard molar Gibbs free energy of segregation consisting of the standard molar enthalpy  $\Delta H_i^0$  and entropy  $\Delta S_i^0$  of segregation of element  $i$  ( $\Delta G_i^0 = \Delta H_i^0 - T\Delta S_i^0$ ) and  $\Delta G_i^*$  is the free energy of solution of  $i$  in a matrix at the solubility limit.

For low GB segregation,  $C_i^\phi \ll 1$ , equation (31) is rewritten into the form:

$$\beta_i = \frac{C_i^\phi}{C_i^B} = \frac{1}{C_i^*} \exp\left(-\frac{\Delta G_i^0 - \Delta G_i^*}{RT}\right) = \frac{K}{C_i^*} \quad (32)$$

where  $\beta_i$  is the GB enrichment ratio and  $K = \exp\left(-\frac{\Delta G_i^0 - \Delta G_i^*}{RT}\right)$ . Seah and Hondros [28] found that  $K$  is a nearly constant for the various systems, so the GB enrichment ratio,  $\beta_i$ , can be predicted using the solubility limit  $C_i^*$ .

Later, the model was repeatedly confirmed for numerous binary systems. Fig. 3.9. shows the dependence of the GB enrichment ratio from solute solubility limit of element  $i$  in Fe, Cu or Ni matrixes.

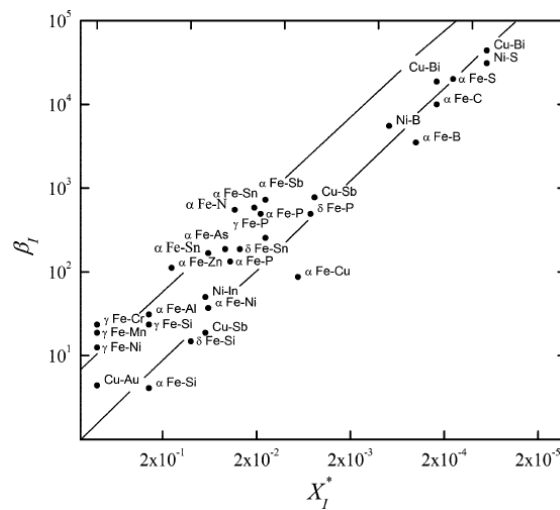


**Fig. 3.9.** Dependence between the experimental GB enrichment ratio  $\beta_i$  (here  $\beta_i$ ) and the solid solubility limit  $X_i^*$  (here  $C_i^*$ ) for various binary systems [14]

Despite the fact that the correlation of the intensity of GB segregation with its solubility limit was experimentally proved, Seah and Hondros model doesn't account the strong influence of the GB structure on the segregation level.

**d) Lejček and Hofmann model: orientation dependence of grain boundary segregation**

Lejček accomplished the thermodynamic analysis of the solute solubility limit dependence of the standard Gibbs energy of interfacial segregation,  $\Delta G_I^0$ , based on work of Seah and Hondros [28], concerning different GB structures [30]. Further, the derivation of the formulas to describe and predict equilibrium segregation to the GBs is shown.

First of all, consider the general relationships of equilibrium segregation in a binary system  $m - i$ . The equilibrium condition of both elements  $i$  and  $m$  can be described through their chemical potentials at the interface  $\mu_i^\phi$  and in the bulk  $\mu_i^B$  as:

$$\mu_i^B = \mu_i^\phi \quad (33)$$

and

$$\mu_m^B = \mu_m^\phi \quad (34)$$

so the basic condition for chemical equilibrium between GB and the bulk is:

$$\mu_i^B + \mu_m^\phi = \mu_m^B + \mu_i^\phi \quad (35)$$

or

$$(\mu_i^B - \mu_i^\phi) - (\mu_m^B - \mu_m^\phi) = 0 \quad (36)$$

For each element  $\xi$  ( $\xi = i, m$ ):

$$\mu_\xi^B = \mu_\xi^{0,B} + RT \ln a_\xi^B \quad (37)$$

and

$$\mu_\xi^\phi = \mu_\xi^{0,\phi} + RT \ln a_\xi^\phi \quad (38)$$

where  $\mu_\xi^{0,B}$  and  $\mu_\xi^{0,\phi}$  are the standard chemical potential of the pure component  $i$  at constant temperature  $T$  and pressure in the bulk ( $B$ ) and GB ( $\phi$ ), respectively;  $R$  is a gas constant;  $T$  is the temperature;  $a_\xi^B$  and  $a_\xi^\phi$  are the activities of component  $\xi$  in the bulk and GB, respectively.

Combination of equilibrium equation (36) and expressions (37), (38) describing the chemical potentials, gives:

$$RT \cdot \ln \frac{a_i^\phi a_m^B}{a_m^\phi a_i^B} = (\mu_i^{0,B} - \mu_i^{0,\phi}) - (\mu_m^{0,B} - \mu_m^{0,\phi}) \quad (39)$$

where the right term is defined as the *standard molar Gibbs energy* of segregation,  $\Delta G_i^0$ , with a minus sign, so that the equation (39) can be rewritten as:

$$\frac{a_i^\phi}{a_m^\phi} = \frac{a_i^B}{a_m^B} \exp\left(-\frac{\Delta G_i^0}{RT}\right) \quad (40)$$

The activities in equation (40) of each element  $\xi$  ( $\xi = i, m$ ) can be replaced by concentration of solute  $C_\xi$ , using the Henry law:

$$a_\xi = k_\xi C_\xi \quad (41)$$

with activity coefficient in ideal dilute alloys  $k_\xi \approx 1$ . After replacing the activities, we obtain the classical view of Langmuir-McLean isotherm [23]:

$$\frac{C_i^\phi}{1 - C_i^\phi} = \frac{C_i^B}{1 - C_i^B} \exp\left(-\frac{\Delta G_i^0}{RT}\right) \quad (42)$$

where  $C_i^\phi$  and  $C_i^B$  are the grain boundary and the bulk concentrations of segregated element  $i$ .

At the solid solubility limit,  $C_i^*$ , the chemical potential,  $\mu_i^*$ , of solute  $i$  is related to its activity  $a_i^*$  as:

$$\mu_i^* = \mu_i^{0,B} + RT \ln a_i^* \quad (43)$$

where the activity at the solute solubility limit does not obey the Henry rule, but the empirical law:

$$a_i^* = (C_i^*)^\nu \quad (44)$$

where  $\nu$  is the constant of the matrix adjusted to fit the experimental results (Fig. 3.10).

Non-linear correlation between the activity and solute concentration at the solute solubility limit was found by Hultgren et al. [31] in various systems (Fig. 3.10). The full lines depict the fitting curves from equation (44). Although the rather limited number of applicable literature values [31] prevents an accurate determination of the exponent  $\nu$  and a clarification of its physical meaning, the general trend seems to confirm the validity of the equation (44).

The Gibbs free energy of solute at the solid solubility limit can then be expressed as:

$$\Delta G_i^* = (\mu_i^{0,\phi} - \mu_i^*) - (\mu_m^{0,\phi} - \mu_m^{0,B}) = \Delta G_i^0 - RT \ln a_i^* \quad (45)$$

Combination of (39), (43) and (45) gives:

$$\Delta G_i^0 = \Delta G_i^* + RT \ln a_i^* = \Delta H_i^* - T\Delta S_i^* + RT \ln a_i^* \quad (46)$$

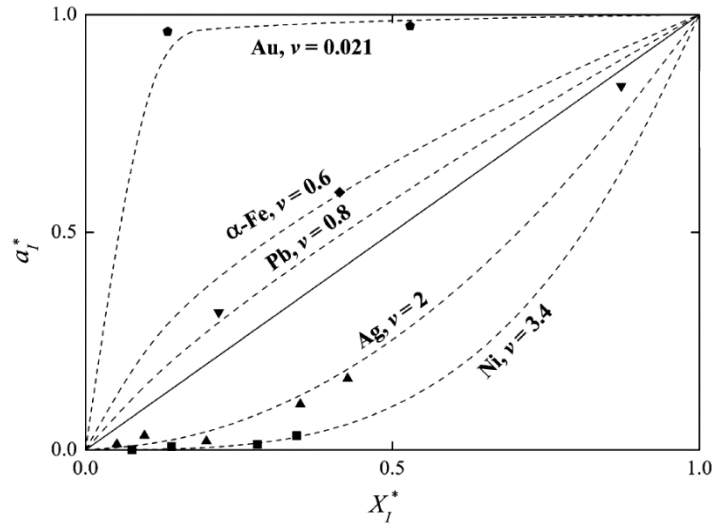


**Fig. 3.10.** Activities of various elements in Au (Co, Fe),  $\alpha$ -Fe (Zn), Pb (Bi, Ti), Ag (Al, Cd, Mg, Sb, Sn, Zn) and Ni (Al, Be, Cr, Mn, Zn) at the solid solubility limits  $X_i^*$  (here  $C_i^*$ ) at different temperatures [30] (data from [31])

Since the corresponding segregation entropies  $\Delta S_i^*$  and  $\Delta S_i^0$  can be expressed as:

$$\Delta S_i^* = - \left( \frac{\partial \Delta G_i^*}{\partial T} \right)_{P, C_i} \quad (47)$$

and

$$\Delta S_i^0 = - \left( \frac{\partial \Delta G_i^0}{\partial T} \right)_{P, C_i} \quad (48)$$

The segregation entropy at the solid solubility limit is written as:

$$\Delta S_i^* = \Delta S_i^0 - R \left( \frac{\partial [T \ln a_i^*]}{\partial T} \right)_{P, C_i} \quad (49)$$

or, using equation (44), as :

$$\Delta S_i^* = \Delta S_i^0 - \nu R \left( \frac{\partial [T \ln C_i^*]}{\partial T} \right)_{P, C_i} \quad (50)$$

Lejček has demonstrated that for many binary systems the term  $T \ln X_i^*$  (here  $\ln C_i^*$ ) is nearly constant with the temperature (Fig. 3.11).

Therefore,

$$\left( \frac{\partial [T \ln C_i^*]}{\partial T} \right)_{P, C_i} \approx 0 \quad (51)$$

and

$$\Delta S_i^* \approx \Delta S_i^0 \quad (52)$$

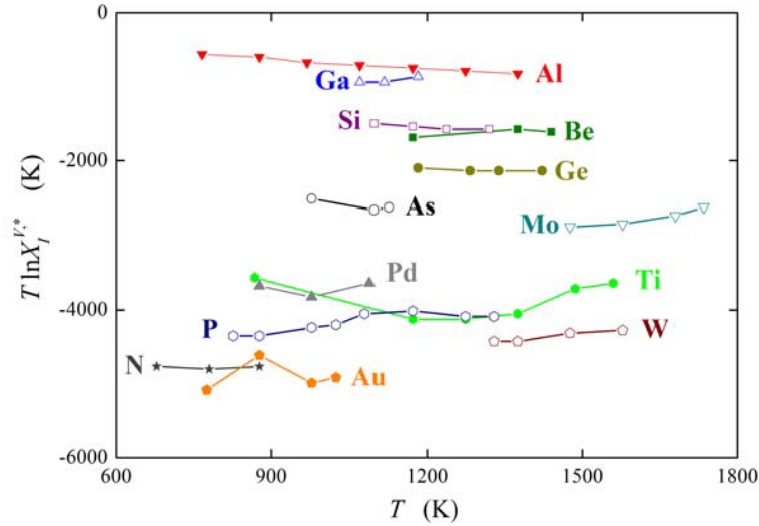


Fig. 3.11. Temperature dependence of  $T \ln X_i^*$  ( $T \ln C_i^*$  here) for various solutes in BCC iron [32]

Consequently, equation (46) can be rewritten as:

$$\Delta H_i^0 = \Delta H_i^* + RT \ln a_i^* = \Delta H_i^* + \nu RT \ln C_i^* \quad (53)$$

As mentioned above, the term  $T \ln C_i^*$  is a practically constant, therefore, the segregation enthalpy,  $\Delta H_i^0$ , is independent of temperature as well as segregation entropy,  $\Delta S_i^0$ . Due to the fact that standard chemical potentials of elements  $i$  and  $m$  at the interface  $\phi$  are involved in description of  $\Delta G_i^*$  (equation (45)) the effect of structure of the interface is included to  $\Delta H_i^*$ .

Extrapolating the equation (53) to  $C_i^* \rightarrow 1$ , gives  $[T \ln C_i^*] \rightarrow 0$  and

$$\Delta H_i^0(C_i^* = 1) = \Delta H_i^* \quad (54)$$

Therefore, we can rewrite equation (53) as:

$$\Delta H_i^0(\Phi, C_i^*) = \Delta H^*(\Phi, C_i^* = 1) + \nu R [T \ln C_i^*(T)] \quad (55)$$

where  $\Delta H^*(\Phi, C_i^* = 1)$  is the structurally dependent segregation enthalpy of a solute  $I$ , which is completely soluble in a matrix  $M$ , characterized by the parameter  $\nu$ .

The average value of  $\nu$  for phosphorus GB segregation in BCC iron is obtained experimentally on bicrystals and equal to  $0.77 \pm 0.06$ . The values of  $\Delta H^*(\Phi)$  range from  $-8 \text{ kJ} \cdot \text{mol}^{-1}$  to  $-4 \text{ kJ} \cdot \text{mol}^{-1}$  for general grain boundaries, and from  $+5 \text{ kJ} \cdot \text{mol}^{-1}$  to  $+8 \text{ kJ} \cdot \text{mol}^{-1}$  for so called special grain boundaries [30]. The values between describe vicinal grain boundaries. According to the general classification based on the grain boundary energy [33], special grain boundaries are characterized by a minimum energy with respect to at least one microscopic degree of freedom. The free energy of vicinal grain boundaries is near a local minimum with respect to at least one degree of freedom. The free energy of

general grain boundary is at or near local maximum with respect to one or more macroscopic degrees of freedom.

To estimate the segregation entropy,  $\Delta S_I^0$ , Lejček has proposed using the *enthalpy-entropy compensation effect*, i.e. the linear dependence between enthalpy and entropy, observed for many processes and states in chemistry [34–36].

Lejček has presented the theoretical thermodynamic background of compensation effect and interpreted it for grain boundary segregation process [37]. He assumes a temperature dependent process or thermodynamic state (chemical reaction, diffusion, interfacial segregation) characterized by a change of its characteristics Gibbs free energy  $\Delta G(\Omega_j)$ , depending on  $N$  independent variables (potentials)  $\Omega_j$ , such as concentration, electric or magnetic fields, specific defect energy, solubility or bond strength.

The total differential  $d\Delta G(\Omega_j)$  can be expressed at constant temperature and pressure as:

$$d\Delta G^0 = \sum_{j=1}^N \left( \frac{\partial \Delta G}{\partial \Omega_j} \right)_{T,P,\Omega_i \neq \Omega_j} d\Omega_j \quad (56)$$

Similarly, the enthalpy and the entropy can be written respectively:

$$d\Delta H^0 = \sum_{j=1}^N \left( \frac{\partial \Delta H}{\partial \Omega_j} \right)_{T,P,\Omega_i \neq \Omega_j} d\Omega_j \quad (57)$$

and

$$d\Delta S^0 = \sum_{j=1}^N \left( \frac{\partial \Delta S}{\partial \Omega_j} \right)_{T,P,\Omega_i \neq \Omega_j} d\Omega_j \quad (58)$$

Author defined a constant temperature  $T_C$  at which  $d\Delta G^0$  does not change with changing of the variables  $\Omega_j$ , i.e.  $d\Delta G^0(T_C) = 0$ , which is expressed as:

$$T_C = \frac{d\Delta H^0}{d\Delta S^0} = \frac{\sum_{j=1}^N \left( \frac{\partial \Delta H}{\partial \Omega_j} \right)_{T,P,\Omega_i \neq \Omega_j} d\Omega_j}{\sum_{j=1}^N \left( \frac{\partial \Delta S}{\partial \Omega_j} \right)_{T,P,\Omega_i \neq \Omega_j} d\Omega_j} \quad (59)$$

Integration of (59) gives:

$$\Delta H^0 = T_C(\Delta S^0 + \Delta S') \quad (60)$$

with the integration constant  $\Delta S'$  with the meaning of entropy, and thus:

$$\Delta S^0 = \frac{\Delta H^0}{T_C} + \Delta S' = \frac{\Delta H^0}{T_C} - \frac{\Delta G_P^0(T_C)}{T_C} \quad (61)$$

The compensation effect in grain boundary segregation has been shown by Lejček for example of BCC iron [37,38]. The segregation of Si, P and C in  $\alpha$ -Fe bicrystals was measured at various grain boundaries using Auger electron spectroscopy [39–44]. The standard Gibbs free energy of phosphorus segregation,  $\Delta G_p^0$ , in  $\alpha$ -iron was determined using equation (29) of Guttman's model. The temperature dependence of the standard Gibbs energy of phosphorus segregation,  $\Delta G_p^0$ , in  $\alpha$ -iron at various grain boundaries is presented in Fig. 3.12.

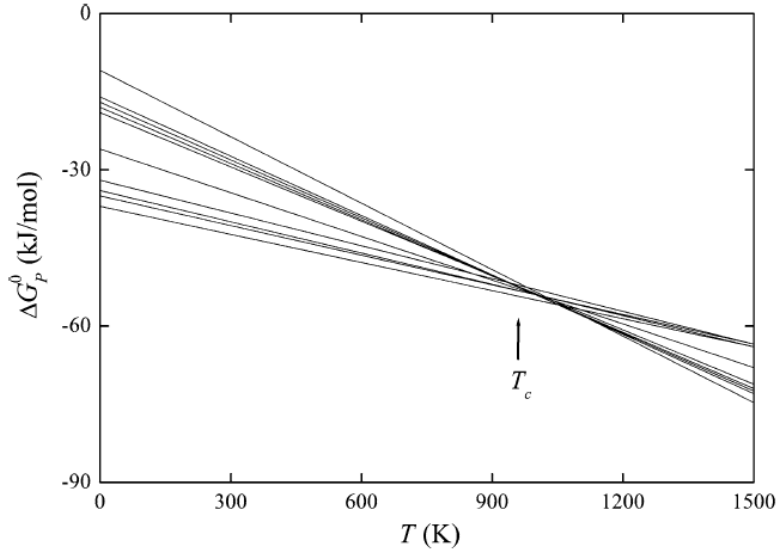


**Fig. 3.12.** Temperature dependence of the standard free Gibbs energy of phosphorus segregation,  $\Delta G_p^0$ , in  $\alpha$ -iron at various grain boundaries [14]

The intersection point occurs at the temperature  $T_c = 930\text{ K}$  and the corresponding term  $\Delta G_p^0(T_c)/T_c$  is equal to  $-56\text{ J}/(\text{mol} \cdot \text{K})$ . Thus, the standard segregation entropy of phosphorus can be determined using the enthalpy-entropy compensation effect as:

$$\Delta S^0 = \frac{\Delta H^0}{930} + 56 \quad (62)$$

### 3.3.2 Kinetics of grain boundary segregation

Following McLean approach [23], solute atoms are assumed to segregate to the boundary from two semi-infinite bulk crystals of uniform solute content. The diffusion of solute  $i$  represented by the changes of its concentration  $C_i$  and described by the second Fick's law [45]:

$$\frac{\partial C_i}{\partial t} = D_i \left( \frac{\partial^2 C_i}{\partial x^2} \right)_{x=0} \quad (63)$$

where  $D_i$  is the diffusion coefficient of solute  $i$ . Assuming that GB with a thickness  $d^\phi$  is located precisely at  $x = 0$  and fed by the crystals on both, the interface condition is:

$$D_i \left( \frac{\partial C_i}{\partial x} \right)_{x=0} = \frac{d^\phi}{2} \left( \frac{\partial C_i^\phi}{\partial t} \right)_{x=0} \quad (64)$$

Diffusion takes place towards grain boundary until equilibrium GB concentration  $C_i^{\phi,\infty}$  is reached. The initial GB concentration is  $C_i^{\phi,0}$  at  $t = 0$ . Concerning that the bulk concentration remains constant during solute segregation, the grain boundary enrichment factor is given by:

$$\beta_i^\phi = \frac{C_i^\phi}{C_i} \quad (65)$$

Hence the GB condition (64) can be written as:

$$D_i \left( \frac{\partial C_i}{\partial x} \right)_{x=0} = \frac{\beta_i^\phi d^\phi}{2} \left( \frac{\partial C_i}{\partial t} \right)_{x=0} \quad (66)$$

Transform equation (63) to

$$\frac{\partial^2 C_i}{\partial x^2} - \frac{1}{D_i} \frac{\partial C_i}{\partial t} = 0 \quad (67)$$

and apply the Laplace transformation [46],

$$L\{C_i(x, t)\} = \bar{C} = \int_0^\infty e^{-pt} C_i dt \quad (68)$$

where  $\bar{C}$  is a convenient short notation to use in the algebra of solution and  $p$  is a number whose real part is positive and large enough to make the integral (68) convergent. The Laplace transformation gives:

$$\int_0^\infty e^{-pt} \frac{\partial^2 C_i}{\partial x^2} dt - \frac{1}{D_i} \int_0^\infty e^{-pt} \frac{\partial C_i}{\partial t} dt = 0 \quad (69)$$

or

$$\frac{\partial^2}{\partial x^2} \int_0^\infty e^{-pt} C_i dt - \frac{1}{D_i} \left[ [e^{-pt} C_i]_0^\infty + p \int_0^\infty e^{-pt} C_i dt \right] = 0 \quad (70)$$

Since  $\bar{C} = \int_0^\infty e^{-pt} C_i dt$ , the equation (70) could be written as:

$$\frac{\partial^2 \bar{C}}{\partial x^2} - \frac{p}{D_i} \bar{C} = -\frac{C_i^{\phi,0}}{D_i} \quad (71)$$

or

$$\frac{\partial^2 \bar{C}}{\partial x^2} - q^2 \bar{C} = -\frac{C_i^{\phi,0}}{D_i} \quad (72)$$

where  $q^2 = p/D_i$  and  $C_i^{\phi,0}$  is the initial concentration of element  $i$  at GB. Using I and II elementary theorems and a table of Laplace transformations, the diffusion equation (72) is solved as:

$$\bar{C} = Me^{-qx} + \frac{C_i^{\phi,0}}{p} \quad (73)$$

Solving (66) by Laplace transform gives:

$$D_i \left( \frac{\partial \bar{C}}{\partial x} \right)_{x=0} = \frac{\beta_i^\phi d^\phi}{2} \left( p\bar{C} - \frac{C_i^{\phi,0}}{p} \right) \quad (74)$$

Substituting equation (73) into (74), we obtain :

$$M = \frac{(1 - \beta_i^\phi) C_i^{\phi,0} d}{D_i q (\beta_i^\phi q d^\phi + 2)} \quad (75)$$

Replacing  $M$  in (73),

$$\bar{C} = \frac{C_i^{\phi,0} \left( \frac{1}{\beta_i^\phi} - 1 \right) e^{-qx}}{D_i q \left( q + \frac{2}{\beta_i^\phi d^\phi} \right)} + \frac{C_i^{\phi,0}}{p} \quad (76)$$

Finally, from the table of Laplace transformations [46], equation (76) can be rewritten as:

$$C_i^\phi(x, t) = C_i^{\phi,0} - C_i^{\phi,0} \left( 1 - \frac{1}{\beta_i^\phi} \right) \exp \left( \frac{2x}{\beta_i^\phi d^\phi} + \frac{4D_i t}{(\beta_i^\phi d^\phi)^2} \right) \operatorname{erfcf} \left( \frac{x}{2\sqrt{D_i t}} + \frac{2\sqrt{D_i t}}{\beta_i^\phi d^\phi} \right) \quad (77)$$

which transform for  $x = 0$  and  $\beta_i^\phi \gg 1$  to

$$\frac{C_i^\phi(t) - C_i^{\phi,0}}{C_i^{\phi,\infty} - C_i^{\phi,0}} = 1 - \exp \left( \frac{4D_i t}{(\beta_i^\phi d^\phi)^2} \right) \operatorname{erfcf} \left( \frac{2\sqrt{D_i t}}{\beta_i^\phi d^\phi} \right) \quad (78)$$

where  $C_{i,t=0}^\phi$  is the initial content of the element  $i$  at GB,  $C_{i,t \rightarrow \infty}^\phi$  is the equilibrium concentration, which achieved after very long time,  $D_i$  is the diffusion coefficient of solute  $I$  in matrix,  $\beta_i^\phi$  is the enrichment ratio of solute  $i$  at GB,  $d^\phi$  is the grain boundary thickness. With this expression we will be able to calculate the GB segregation at any given moment and the time necessary to reach the equilibrium GB segregation.

### 3.3.3 Position of phosphorus atoms in the GB core and their interaction with carbon atoms

The position of segregated atoms in the GB core is one of the most important issues to understand the GB segregation phenomena. According to the atomistic models of GB structure, for example, the structural unit model developed by Sutton and Vitek [47], the hard sphere model proposed by Frost and Spaepen [48], or more general three-dimensional polyhedral unit model of Ashby [49,50], the GB structure is ordered and the position of atoms in such structural units was assumed to deviate little from the perfect lattice positions [51]. Atomic structure of GBs is confirmed using high-resolution transmission electron microscopy (for example, [52]).

Thus, the substitutional sites of GB are created by removing of matrix atoms from their lattice position. The interstitial sites of GB are determined as empty spaces between lattice positions, i.e. sites, which cannot be occupied by the matrix atoms in the equilibrium state but may accept the atoms of other solutes. Due to the presence of structural units and, subsequently, free volume at the interface, the interstitial sites at GB are larger than in regular crystal lattice [48]. Therefore, some solutes, such as phosphorus, tin and antimony, occupying the substitutional sites in BCC iron lattice, can segregate at the interstitial positions [14,53].

Antoine Vaugeois in his PhD thesis (GPM laboratory, University of Rouen Normandy) presents the atomic-scale simulation of phosphorus segregation at GBs in BCC iron using the Quasi particle Approach (QA) [54]. GBs of desired geometry are obtained by crystallizing a liquid layer placed in-between two crystal grain grains of chosen orientation [52]. Due to periodic boundaries condition, two identical GBs are presented in the simulation box.

After GB formation, a second component is introduced in the substitutional positions of the BCC lattice. Fig. 3.13 presents the initial state for the QA modelling: the grey atoms belong to BCC matrix; the red atoms are substitutional solute atoms, distributed homogeneously in a simulation box. The ratio between atomic radii of solute and matrix atoms in the simulation box is similar to the ratio between phosphorus and iron atomic radii. This allows to reproduce the real elastic field of GB.

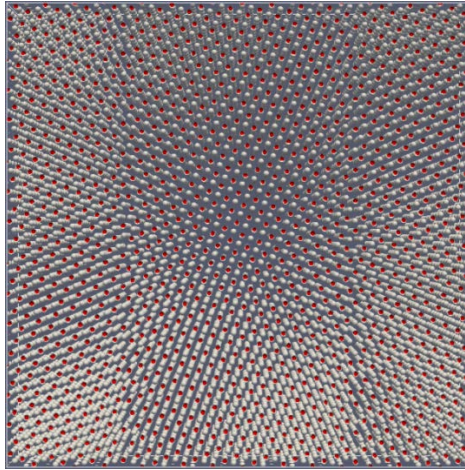


**Fig. 3.13.** The initial state of ADF modelling. The grey atoms belong to BCC matrix, the red atoms are substitutional solute atoms [PhD thesis of Antoine Vaugeois, GPM]

Further, the minimization of the total free energy of the system gives the atomic equilibrium position. The simulation starts from the GBs and the solute atoms spreading further into the matrix (Fig. 3.14a, b, c). Red colored atoms in Fig. 3.14 are interstitial positions occupied by solute atoms during the process of free energy minimization.

In the first step, since the area around GB is expanded, solute atoms around GB start to segregate and change their position from substitutional to interstitial. Further, segregation process continues near GBs. At the end, due to some hypothesis in the QA model (quite big concentration of solute atoms), all simulation box is filled by interstitial solute atoms. The last step of simulation does not reflect the bulk of the real system. However, it reflects the position of segregated atoms near GB.

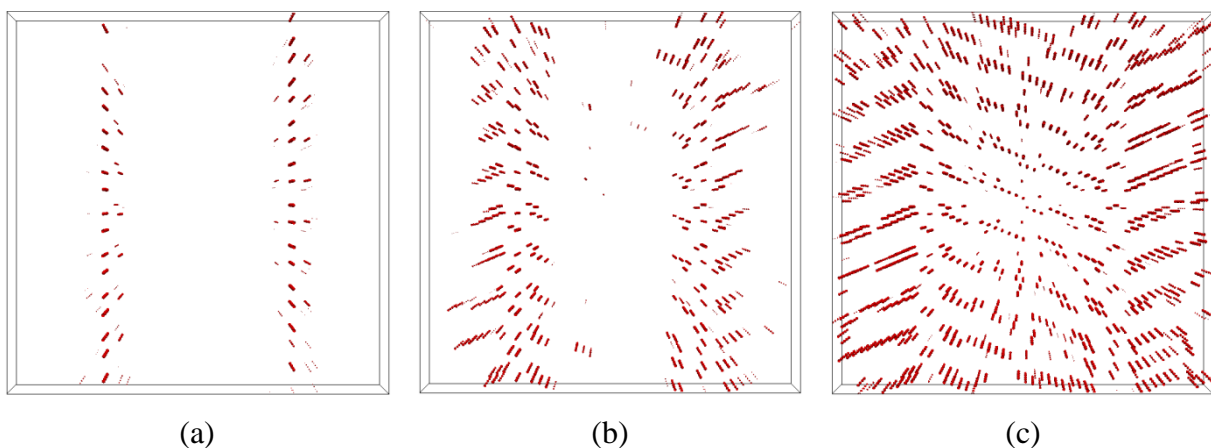


**Fig. 3.14.** Three different steps of free energy minimization using ADF modelling: (a) segregation of substitutional atoms to the interstitial positions at GB, (b) segregation of substitutional atoms to the interstitial positions near GB, (c) due to big concentration of solute atoms all simulation box is filled by interstitial solute atoms. The last step is not in agreement with experiments [PhD thesis of Antoine Vaugeois]

The equilibrium atomic configuration of solute atoms, using this model, at  $46.4^\circ[100](730)/(730)$  symmetrical tilt GB in a BCC lattice after free energy minimization is presented in Fig. 3.15. Black and grey colors refer to two adjacent atomic planes of BCC matrix, red correspond with interstitial solute atoms. As it is seen, the solute atoms are situated in the center of the GB structural units, which are highlighted by the solid black lines and around.

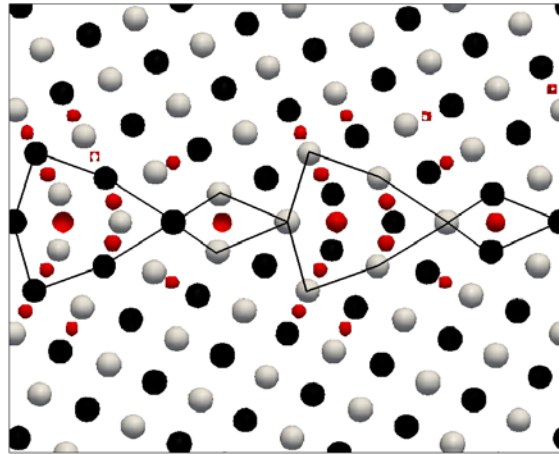


**Fig. 3.15.** QA simulation of interstitials segregation of previously substitutional solute (red) at symmetric tilt  $46.4^\circ[100](730)/(730)$  GB in the BCC lattice (grey and black) [PhD thesis of Antoine Vaugeois, GPM]

Thus, QA modelling confirms that the phosphorus atoms initially situated in the lattice position can move to the interstitial sites close to GB. A possibility of phosphorus to segregate interstitially also was proposed by Lejček. He has plotted the dependence between segregation enthalpy,  $\Delta H_f^0$ , and the segregation entropy,  $\Delta S_f^0$ , to show the enthalpy-entropy compensation effect and found that the data is divided into two branches reflecting two different mechanisms of GB segregation: interstitial (upper branch) and substitutional (lower branch) (Fig. 3.16) [55]. So here, phosphorus and tin are situated on the same branch with carbon and sulfur which always occupy the interstitial positions, while larger elements, such as Al, Si and Cr were determined as substitutional segregants. Later, Lejček [55] has reported that depending on the temperature of thermal ageing phosphorus can segregate both in the interstitial and substitutional sites of GB.

Still there is no experimental high-resolution observation of phosphorus segregation at GB in BCC iron, allowing us to distinguish undoubtedly the position of phosphorus atoms (interstitial or substitutional), so the problem remains open. However, as the repulsive interaction between phosphorus and carbon atoms at GB was repeatedly observed in the literature [15,16,57–60] and, according to the QA simulation, the interstitial segregation of

phosphorus is energetically favorable, both repulsive interaction and site competition between phosphorus and carbon atoms at GB were taken into account in modeling.

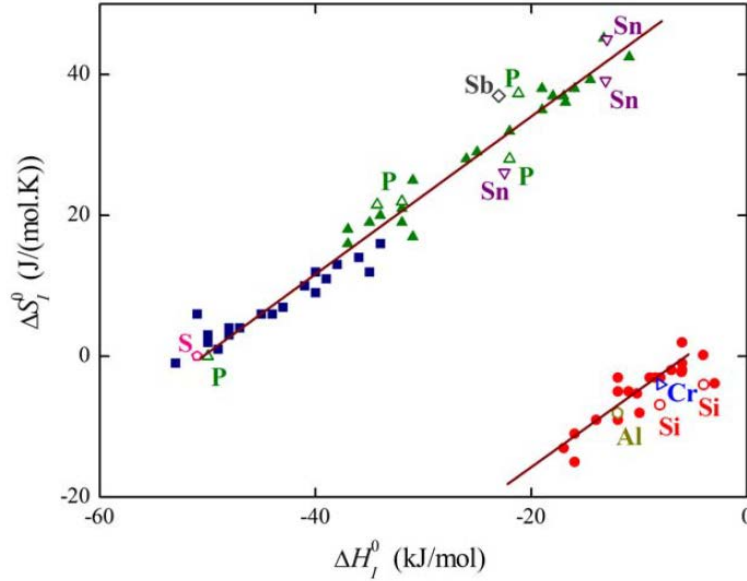


**Fig. 3.16.** Dependence of the standard segregation entropy  $\Delta S_i^0$  and standard segregation enthalpy  $\Delta H_i^0$  in  $\alpha$ -iron. Full symbols depict segregation at individual grain boundaries in bicrystals, the empty symbols represent the data from literature for polycrystalline iron. The upper and lower branches represents the fits of segregation of solute occupied interstitial and substitutional sites, respectively [56]

### 3.3.4 Modeling versus experiments and discussion

Considering all of the issues discussed above, the prediction of GB segregation of solute  $i$  in a matrix  $m$  at temperature  $T$  includes the following steps:

1. The calculation of the standard segregation enthalpy,  $\Delta H_i^0$ , as

$$\Delta H_i^0(\Phi, C_i^*) = \Delta H^*(\Phi, C_i^* = 1) + \nu R [T \ln C_i^*(T)] \quad (79)$$

where  $\Delta H^*(\Phi, C_i^* = 1)$  is the standard enthalpy of segregation of an element with unlimited bulk solid solubility in matrix at a specified GB  $\Phi$ , and  $\nu$  is the parameters correlating the activity,  $a_i^*$ , at the bulk solid solubility limit with corresponding atomic ratio,  $C_i^*$ ,  $a_i^* = (C_i^*)^\nu$

2. The calculation of the standard segregation entropy,  $\Delta S_i^0$ , using the entropy-enthalpy compensation effect,

$$\Delta S_i^0 = \frac{\Delta H_i^0}{T_c} - \frac{\Delta G_i^0(T_c)}{T_c} \quad (80)$$

i.e. that the changes of  $\Delta H_i^0$  are compensated by the changes of  $\Delta S_i^0$  and  $T_c$  is the compensation temperature, at which  $\Delta G_i^0(T_c) = \text{const}$  for all types of GB,  $\Phi$ .

3. The substitution of the segregation enthalpy,  $\Delta H_i^0$ , and entropy,  $\Delta S_i^0$ , values into the Gibbs free energy expression for multicomponent alloy,

$$\Delta G_i = \Delta H_i^0 - T\Delta S_i^0 - 2\alpha_{im}(C_i^\phi - C_i^B) + \sum_{j \neq i}^{M-1} \alpha'_{ij}(C_j^\phi - C_j^B) \quad (81)$$

where  $\alpha_{im}$  and  $\alpha'_{ij}$  are the interaction coefficients between solute-matrix and solute-solute, respectively;  $C_i^\phi$  and  $C_i^B$  are the concentrations of  $i$  atoms at GB and in the bulk, respectively;  $C_j^\phi$  and  $C_j^B$  are the concentrations of  $j$  atoms at GB and in the bulk, respectively.

4. The substitution of the segregation free energy,  $\Delta G_i$ , value into Guttman's equation for equilibrium intergranular segregation in the multicomponent system,

$$\frac{C_i^\phi}{1 - \sum_j^{M-1} C_j^\phi} = \frac{C_i^B}{1 - \sum_j^{M-1} C_j^B} \exp\left(-\frac{\Delta G_i}{RT}\right) \quad (82)$$

This approach was used to predict the equilibrium phosphorus GB segregation in the Fe-0.034 at.% P-0.01 at.% C model alloy at different temperatures. The results of modeling are compared with the experimental data obtained by APT for the HAGBs. Parameters used to calculate the equilibrium GB segregation of phosphorus and carbon in BCC iron and its kinetics are presented in Table 3.5. The bulk concentration is assumed to remain constant during the segregation process.

**Table 3.5.** Data used in the theoretical calculations of phosphorus and carbon GB segregations in the Fe-0.034 at.% P-0.01 at.% C model alloy

Parameter		Value	Reference
$\Delta H^*$ (kJ/mol)	general GBs	-8 to -4	[14]
	vicinal GBs	-2 to +2	
	special GBs	+5 to +8	
$\nu$		0.77	[9]
$T_C$ (K)		930	[14]
$\Delta G_P^0/T_C$ (J/mol · K)		-56	[14]
$\alpha'_{PC}$ (kJ/mol)		7	[43]
$\alpha_{FeP}$ (kJ/mol)		0	[44,58]
$D_P$ (m <sup>2</sup> /s)		$13.8 \exp\left(\frac{-332000}{8.314T}\right)$	[61]

	$2.9 \cdot 10^{-4} \exp\left(\frac{-231000}{8.314T}\right)$	[62]
$D_C (m^2/s)$	$1.67 \cdot 10^{-7} \exp\left(\frac{-78000}{8.314T}\right)$	[10]
$T \ln C_p^* (K)$	$\approx -4200$	[63]
$d^\phi (nm)$	0.2	
$R (J/mol \cdot K)$	8.314	

The overall theoretical predictions are summarized in Table 3.6. Due to the fact that all experimentally observed HAGBs are general (general), the thermodynamic parameters were calculated only for them.

**Table 3.6.** The theoretical prediction of the thermodynamic parameters of the phosphorus and carbon segregations in the Fe-0.034 at.% P-0.01 at.% C model alloy

Parameter	Value
$\Delta H_p^0 (kJ/mol)$	$-32 \pm 2$
$\Delta S_p^0 (J/mol \cdot K)$	$+21.5 \mp 2$
$\Delta H_C^0 (kJ/mol)$	$-50 \pm 2$
$\Delta S_C^0 (J/mol \cdot K)$	$+2 \mp 2$

Using equation (81) with  $\alpha'_{pC} = 7000 kJ/mol$  [43] and  $\alpha_{FeP} = 0$  [44], the free Gibbs energy of phosphorus segregation at general GBs in BCC iron is expressed as

$$\Delta G_p = -32000 - 21.5 \cdot T + 7000 \cdot (C_C^\phi(T) - C_C^B) \quad (83)$$

where  $C_C^\phi(T)$  and  $C_C^B$  are the carbon concentration at GB and in the bulk, respectively.

The equilibrium GB segregation of carbon at 650°C was experimentally determined using APT and found to be equal to  $0.03 \pm 0.01$  monolayer. Thus, the free Gibbs energy of phosphorus segregation at 650°C is  $-51.6 kJ/mol$ . Substituting this energy to equation (82) gives the value of equilibrium phosphorus GB segregation in the Fe-0.034 at.% P-0.01 at.% C model alloy at 650°C, which is equal to  $0.21 \pm 0.01$  monolayer.

As it was mentioned earlier, the phosphorus GB segregation at 650°C reaches the equilibrium value in less than 2h. It was verified with additional annealing at 650°C during 24 h. The mean value of equilibrium phosphorus segregation at HAGB in the Fe-0.034 at.% P-

0.01 at.% C alloy was measured by APT and found to be equal to  $0.12 \pm 0.01$  monolayer. This value is lower than the predicted ( $0.21 \pm 0.01$  monolayer).

Such difference between the theory and our experiments most likely comes from the different quantification methods of the GB solute segregation. The thermodynamic parameters (standard segregation enthalpy and entropy) of phosphorus intergranular segregation were defined by Lejcek using AES measurements on the fracture surfaces of the Fe-Si-P bicrystals with the known GB structure. Further, the experimental data were used to adjust the parameters for the prediction of GB segregation ( $\Delta H^*$ ,  $T_C$ ,  $\alpha'_{PC}$ ).

Since AES and APT experiments reveal the same value of phosphorus atoms per unit surface, as it was shown in part 3.2, the difference between the prediction and the experiments likely comes from the method of converting the excess numbers of atoms per unit surface to a fraction of a monolayer. In the current work, the Gibbsian interfacial excess measured by APT is converted to a fraction of a monolayer, assuming that the phosphorus atoms reside in a single close-packed (110) plane of BCC  $\alpha$ -iron, while Lejcek et al. have estimated the atomic density of GB plane from AES analysis of pure iron surface [44]. Since the (110) plane is the highest density plane in a bcc iron, our assumption underestimates the phosphorus GB segregation in real GB plane with the lower density.

If we assume that the difference between Lejček's and our experiments is always the same, this difference can be considered in equation (83) as a certain value of  $\Delta G'_p$  so that the final expression is rewritten as

$$\Delta G_p = -32000 - 21.5 \cdot T + 7000 \cdot (C_C^\phi - C_C^B) + \Delta G'_p \quad (84)$$

In the current work, the difference between the predicted and experimental free Gibbs energies is about  $\Delta G'_p = 5 \text{ kJ/mol}$  (Fig. 3.17).

The phosphorus equilibrium GB segregation at  $450^\circ\text{C}$ ,  $C_p^\phi$ , determined using equation (84) with substitution of the experimentally measured GB segregation of carbon,  $C_C^\phi$ , ( $0.25 \pm 0.4$  monolayer) is equal to  $0.17 \pm 0.02$  monolayer. The APT measurement of phosphorus GB segregation after 1000 h of ageing at  $450^\circ\text{C}$  gave the mean value at HAGBs of  $0.14 \pm 0.01$  monolayer. This means that the phosphorus GB segregation needs more than 1000 h to reach the equilibrium value.

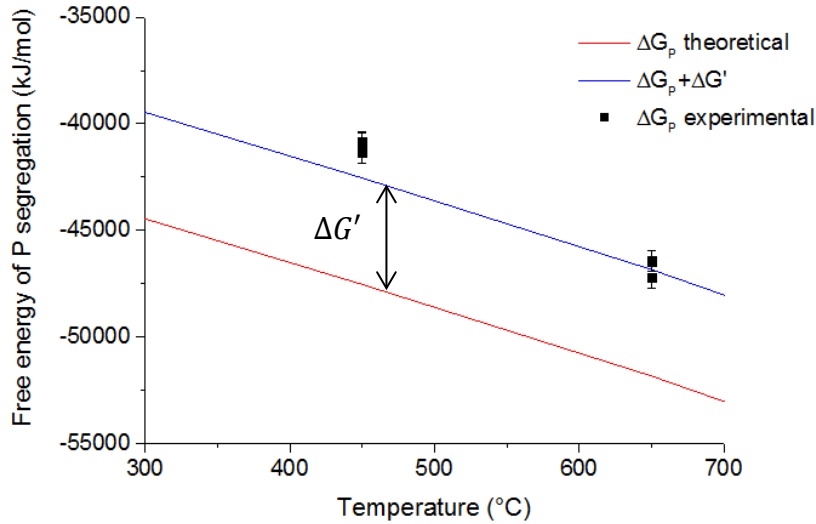


**Fig. 3.17.** Comparison of the theoretical temperature dependence of the standard Gibbs free energy of phosphorus GB segregation in the Fe-0.034 at.% P-0.01 at.% C alloy calculated by equations (83)(red line) and (84)(blue line) with the experimental data

In order to determine the time needed to reach the phosphorus and carbon equilibrium GB segregations at 450°C the segregation kinetics were analysed. The phosphorus and carbon GB segregation kinetics are described by equation (78). Different values of pre-exponential factor and activation energy of phosphorous diffusion are given in literature. In order to cover the whole range of possible diffusion coefficients at a given temperature, kinetics of GB segregation were calculated using two "extreme" diffusion coefficients.

The first coefficient from Matsuyama et al. [61] corresponds to a relatively slow diffusion of phosphorus in  $\alpha$ -iron. It is expressed as:

$$D_p^1 = 13.8 \exp\left(\frac{-332000}{8.314T}\right) \quad (85)$$

The second diffusion coefficient corresponds to a relatively fast diffusion. It was obtained from Qingfen et al. [62] as:

$$D_p^2 = 2.9 \cdot 10^{-4} \exp\left(\frac{-231000}{8.314T}\right) \quad (86)$$

The kinetics curves of phosphorus GB segregation at 650°C and 450°C comparing with the experimental APT data are presented in Fig. 3.18. Red line correspond to the phosphorus segregation kinetics calculated with diffusion coefficient  $D_p^1$ , the black line is the phosphorus segregation kinetics calculated with  $D_p^2$ . The black dots indicate the phosphorus segregation at HAGBs measured by APT. Since the phosphorus GB segregation at 650°C reaches the equilibrium in time less than 2h, the segregation kinetics calculated using the

faster diffusion coefficient  $D_p^2$  more plausibly describes the segregation process at 650°C. Faster segregation kinetics at 450°C also shows the best fit with two APT measurements of phosphorus GB segregation from the sample aged at 450°C during 1000h.

Thus, it is assumed, that the time needed to reach the equilibrium phosphorus GB segregation at 450°C in the Fe-0.034 at.% P-0.01 at.% C model alloy is about 3000h (or 125 days).

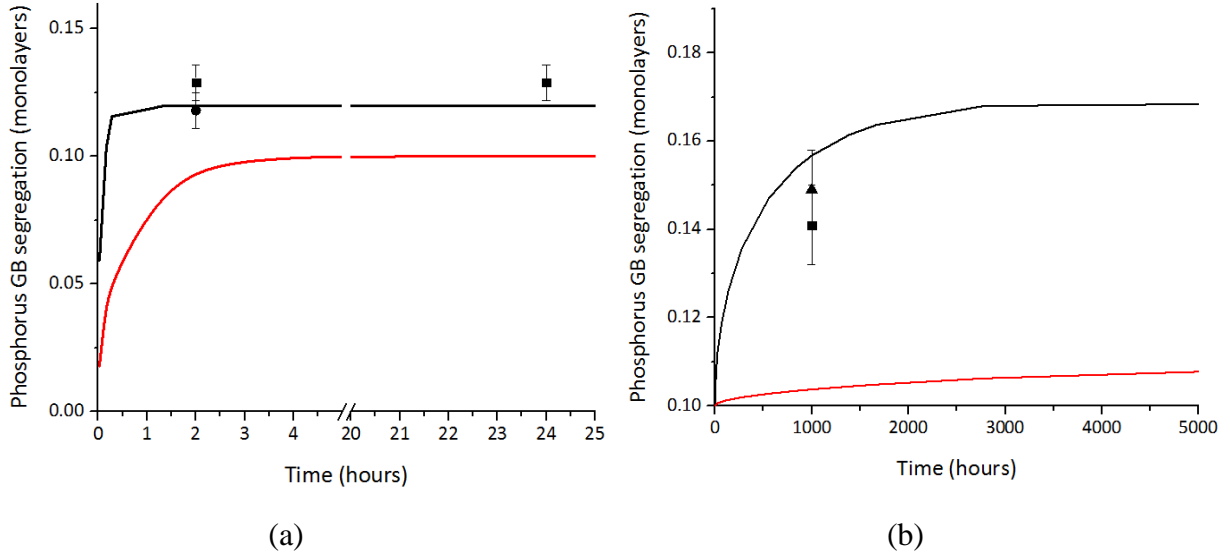


**Fig. 3.18.** Kinetics of phosphorus GB segregation in the Fe-0.034 at.% P-0.01 at.% C model alloy at (a) 650°C and (b) 450°C. Red line correspond to the diffusion coefficient  $D_p^1$ , black line – to  $D_p^2$

Also, the time necessary to reach the equilibrium intergranular carbon segregation was calculated. The diffusivity of carbon is given by [10]:

$$D_c = 1.67 \cdot 10^{-7} \exp\left(\frac{-78000}{8.314T}\right) \quad (87)$$

The equilibrium intergranular segregation of carbon at 450°C and 650°C are  $C_c^\phi = 0.25 \pm 0.4$  monolayer and  $C_c^\phi = 0.03 \pm 0.01$  monolayer, respectively. Thus, the time necessary to reach the equilibrium intergranular carbon segregation is  $< 2$  sec at 650°C and  $< 10$  sec at 450°C.

Analytical approach described above was used to predict the equilibrium GB segregation of phosphorus at 450°C and 650°C in the Fe-0.034 at.% P-0.01 at.% C model alloy. The Lejcek's model allows to consider the variation of the GB segregation with the GB structure. The minimum and maximum values predicted by his model correspond with the segregation at low-energy special GBs and high-energy general GBs, respectively. However,

some questions, such as, the distribution of segregating elements in structurally different GBs, including twist, asymmetrical and mixed ones; the effect of the GB plane; the segregation dependent structural changes (e.g. faceting) are still open and required additional theoretical and experimental studies.

## Conclusions

In this chapter, the equilibrium phosphorus and carbon segregations were investigated in Fe-0.034 at.% P-0.01 at.% C model alloys thermally aged at 650°C during 2h and 450°C during 1000h. The annealing at 650°C during 2h simulates the stress relieve heat treatment (SRHT) of RPV steel in the industry. In the current work, a SRHT during 2h is the reference state of the specimens before thermal ageing and irradiation. The phosphorus GB segregation after 2h of SRHT was measured by APT and the mean value is equal to  $0.12 \pm 0.01$  monolayer. Since the additional SRHT during 24 h did not affect the phosphorus segregation value, this value is supposed to be the equilibrium GB segregation of phosphorus at 650°C.

An additional SRHT didn't change the phosphorus GB segregation value, but significantly reduce the carbon GB segregation. Since the size of specimen annealed at 650°C during 24 h was  $4 \times 4 \times 20 \text{ mm}^3$ , while the previous annealing during 2h was performed on the specimen with the size of  $20 \times 20 \times 20 \text{ mm}^3$ , it was assumed that the higher carbon GB segregation in a bigger specimen is a result of slower cooling rate and thus the segregation of carbon at GB during air-cooling.

A thermal ageing at 450°C was performed to make an atomic-scale investigation of equilibrium phosphorus GB segregation in the Fe-0.034 at.% P-0.01 at.% C model alloys and to compare the results with irradiated samples. The irradiation temperature was the same as the thermal ageing temperature, i.e. 450°C. The study of equilibrium GB segregation helps to separate different mechanisms of GB segregation under irradiation (see Chapter 4). The phosphorus GB segregation after 1000 h of thermal ageing at 450°C is  $0.14 \pm 0.01$  monolayer.

In order to determine the equilibrium GB segregation of phosphorus at 450°C the Guttman's model of equilibrium GB segregation was used. The thermodynamic parameters were taken from the works of Lejček and co-workers. The model was first verified at 650°C. The predicted equilibrium phosphorus GB segregation at 650°C ( $0.21 \pm 0.01$  monolayer) was much higher than the experimentally observed ( $0.10 \pm 0.01$  monolayer).

Since the parameters given by Lejček were obtained by AES experiments, while APT was used in the current work, it was decided to use both techniques to measure the GB segregation in the same material. The comparison of AES and APT measurements of phosphorus GB segregation for specimen annealed at 650°C during 2h demonstrates that the AES experiments, giving  $(1.4 \pm 0.5) \times 10^{14} \text{ atoms/cm}^2$  is in good agreement with APT measurements of phosphorus segregation at GBs ( $(1.6 \pm 1.0) \times 10^{14} \text{ atoms/cm}^2$ ). Based on

that fact, it was supposed that the difference between theoretical prediction and experimental data is a result of GB segregation quantification. In the current work, the Gibbsian interfacial excess measured by APT is converted to a fraction of a monolayer, assuming that the phosphorus atoms reside in a single close-packed (110) plane of BCC  $\alpha$ -iron, while Lejček et al. have estimated the atomic density of GB plane from AES analysis of pure iron surface [44]. Since the (110) plane is the highest density plane in a bcc iron, our assumption underestimates the phosphorus GB segregation.

Considering this fact, the temperature dependence of free Gibbs energy of phosphorus segregation is given by  $\Delta G_P = -27000 - 21.5 \cdot T + 7000 \cdot (X_C^\phi - X_C^B)$ . Thus, the theoretical value of equilibrium GB segregation of phosphorus at 450°C is  $0.17 \pm 0.02$  monolayers. The time needed to reach the equilibrium GB segregation is about 3000h. In the current work, the thermal ageing at 450°C was conducted on the Fe-0.034 at.% P-0.01 at.% C model alloy during 1000h. After 1000h the phosphorus GB segregation reaches  $0.14 \pm 0.01$  monolayer, which is  $\sim 80\%$  from the equilibrium segregation value.

The segregation kinetics of phosphorus is sufficiently well described by McLean's model using the diffusion coefficient of  $D_P = 2.9 \cdot 10^{-4} \exp\left(\frac{-231000}{8.314T}\right)$  from Qingfen [62]. It is necessary to anneal during  $\sim 1$  h at 650°C and  $\sim 3000$  h at 450°C to reach the equilibrium GB segregation.

## References

- [1] S.-H. Song, H. Zhuang, J. Wu, L.-Q. Weng, Z.-X. Yuan, T.-H. Xi, Dependence of ductile-to-brittle transition temperature on phosphorus grain boundary segregation for a 2.25Cr1Mo steel, *Mater. Sci. Eng. A*. 486 (2008) 433–438. doi:10.1016/j.msea.2007.09.032.
- [2] C. English, S. Ortner, G. Gage, W. Server, S. Rosinski, Review of Phosphorus Segregation and Intergranular Embrittlement in Reactor Pressure Vessel Steels, in: S. Rosinski, M. Grossbeck, T. Allen, A. Kumar (Eds.), *Eff. Radiat. Mater. 20th Int. Symp.*, ASTM International, USA, 2001. doi:10.1520/STP10531S.
- [3] Q. Li, L. Li, E. Liu, D. Liu, X. Cui, Temper embrittlement dynamics induced by non-equilibrium segregation of phosphorus in steel 12Cr1MoV, *Scr. Mater.* 53 (2005) 309–313. doi:10.1016/j.scriptamat.2005.04.011.
- [4] S. Rosinski, Review of Phosphorus Segregation and Intergranular Embrittlement in Reactor Pressure Vessel Steels (PWRMRP-19): PWR Material Reliability Project (PWRMRP), EPRI, USA 2000.
- [5] C. Naudin, J.M. Frund, A. Pineau, Intergranular fracture stress and phosphorus grain boundary segregation of a Mn-Ni-Mo steel, *Scr. Mater.* 40 (1999) 1013–1019. doi:10.1016/S1359-6462(99)00069-X.
- [6] J. Kameda, Y. Nishiyama, Combined effects of phosphorus segregation and partial intergranular fracture on the ductile–brittle transition temperature in structural alloy steels, *Mater. Sci. Eng. A*. 528 (2011) 3705–3713. doi:10.1016/j.msea.2011.01.018.
- [7] P.E.J. Flewitt, R.K. Wild, The Distribution of Segregated Elements to Grain Boundaries Measured by Auger Electron Spectroscopy, *Mater. Sci. Forum.* 294–296 (1999) 297–300. doi:10.4028/www.scientific.net/MSF.294-296.297.
- [8] C.L. Brunt, Sources of variability in grain boundary segregation, *Acta Metall.* 31 (1983) 257–266. doi:10.1016/0001-6160(83)90102-5.
- [9] F.C. Campbell, *Elements of Metallurgy and Engineering Alloys*, ASM International, 2008.
- [10] J.R.G. Silva, R.B. McLellan, Diffusion of carbon and nitrogen in B.C.C. iron, *Mater. Sci. Eng.* 26 (1976) 83–87. doi:10.1016/0025-5416(76)90229-9.
- [11] J.R. Cowan, H.E. Evans, R.B. Jones, P. Bowen, The grain-boundary segregation of phosphorus and carbon in an Fe–P–C alloy during cooling, *Acta Mater.* 46 (1998) 6565–6574. doi:10.1016/S1359-6454(98)00295-X.
- [12] V.. Keast, D.. Williams, Grain boundary chemistry, *Curr. Opin. Solid State Mater. Sci.* 5 (2001) 23–30. doi:10.1016/S1359-0286(00)00029-2.

- [13] A.W. Czanderna, *Methods of Surface Analysis*, Elsevier, 2012.
- [14] P. Lejcek, *Grain Boundary Segregation in Metals*, Springer Berlin Heidelberg, Berlin, Heidelberg, 2010. <http://link.springer.com/10.1007/978-3-642-12505-8> (accessed March 9, 2015).
- [15] H. Erhart, H.J. Grabke, Equilibrium segregation of phosphorus at grain boundaries of Fe-P, Fe-C-P, Fe-Cr-P, and Fe-Cr-C-P alloys, *Met. Sci.* 15 (1981) 401–408. doi:10.1179/030634581790426877.
- [16] K. Ebihara, M. Yamaguchi, Y. Nishiyama, K. Onizawa, H. Matsuzawa, Effect of carbon on irradiation-induced grain-boundary phosphorus segregation in reactor pressure vessel steels using first-principles-based rate theory model, *J. Nucl. Mater.* 414 (2011) 328–335. doi:10.1016/j.jnucmat.2011.05.001.
- [17] Y. Koguchi, K. Takahashi, Y. Ishikawa, Impurity segregation of stainless steel studied by atom-probe and auger electron spectroscopy, *J. Phys. Colloq.* 48 (1987) C6-411-C6-416. doi:10.1051/jphyscol:1987667.
- [18] S. Hofmann, *Auger- and X-Ray Photoelectron Spectroscopy in Materials Science*, Springer Berlin Heidelberg, Berlin, Heidelberg, 2013.
- [19] R. Wild, Auger Electron Spectroscopy (AES) for surface analysis, (1981) 183–194. doi:10.1016/S0042-207X(81)80384-3.
- [20] J.C. Riviere, S. Myhra, *Handbook of Surface and Interface Analysis: Methods for Problem-Solving*, CRC Press, 2009.
- [21] J.C. Vickerman, I. Gilmore, *Surface analysis: the principal techniques*, John Wiley & Sons, 2011.
- [22] E.D. Hondros, M.P. Seah, The theory of grain boundary segregation in terms of surface adsorption analogues, *Metall. Trans. A.* 8 (1977) 1363–1371. doi:10.1007/BF02642850.
- [23] D. McLean, *Grain boundaries in metals*, Clarendon Press, 1957.
- [24] R.H. Fowler, E.A. Guggenheim, *Statistical thermodynamics*, Cambridge University Press
- [25] M. Guttman, Equilibrium segregation in a ternary solution: A model for temper embrittlement, *Surf. Sci.* 53 (1975) 213–227. doi:10.1016/0039-6028(75)90125-9.
- [26] M. Guttman, *Interfacial Segregation and Temper Embrittlement*, in: *Encycl. Mater. Sci. Technol. Second Ed.*, Elsevier, Oxford, 2001

- [27] M. Guttman, Temper embrittlement and ternary equilibrium segregation, *Mater. Sci. Eng.* 42 (1980) 227–232. doi:10.1016/0025-5416(80)90032-4.
- [28] M.P. Seah, E.D. Hondros, Use of a “BET” analogue equation to describe grain boundary segregation, *Scr. Metall.* 7 (1973) 735–737. doi:10.1016/0036-9748(73)90124-5.
- [29] S. Brunauer, P.H. Emmett, E. Teller, Adsorption of Gases in Multimolecular Layers, *J. Am. Chem. Soc.* 60 (1938) 309–319. doi:10.1021/ja01269a023.
- [30] P. Lejček, S. Hofmann, Grain boundary segregation diagrams of  $\alpha$ -iron, *Interface Sci.* 1 (1993) 163–174. doi:10.1007/BF00203606.
- [31] R. Hultgren, D.T. Hawkins, P.D. Desai, Selected values of the thermodynamic properties of binary alloys, American Society for Metals, Metals Park, Ohio, 1973.
- [32] P. Lejček, L. Zheng, S. Hofmann, M. Šob, Applied Thermodynamics: Grain Boundary Segregation, *Entropy.* 16 (2014) 1462–1483. doi:10.3390/e16031462.
- [33] L. Priester, Grain boundaries from theory to engineering, Springer, Dordrecht; New York, 2013.
- [34] L. Movileanu, E.A. Schiff, Entropy-enthalpy Compensation of Biomolecular Systems in Aqueous Phase: a Dry Perspective, *Monatshefte Chem.* 144 (2013) 59–65. doi:10.1007/s00706-012-0839-9.
- [35] U. Ryde, A fundamental view of enthalpy–entropy compensation, *MedChemComm.* 5 (2014) 1324. doi:10.1039/C4MD00057A.
- [36] J.F. Perez-Benito, M. Mulero-Raichs, Enthalpy-Entropy Compensation Effect in Chemical Kinetics and Experimental Errors: A Numerical Simulation Approach, *J. Phys. Chem. A.* 120 (2016) 7598–7609. doi:10.1021/acs.jpca.6b08079.
- [37] P. Lejček, Enthalpy–entropy compensation effect in grain boundary phenomena, *Z. Für Met.* 96 (2005) 1129–1133. doi:10.3139/146.101151.
- [38] P. Lejček, S. Hofmann, V. Paidar, Solute segregation and classification of [100] tilt grain boundaries in  $\alpha$ -iron: consequences for grain boundary engineering, *Acta Mater.* 51 (2003) 3951–3963. doi:10.1016/S1359-6454(03)00219-2.
- [39] J. Janovec, M. Jenko, P. Lejček, J. Pokluda, Grain boundary segregation of phosphorus and silicon in polycrystals and bicrystals of the Fe–2.6Si–0.055P alloy, *Mater. Sci. Eng. A.* 462 (2007) 441–445. doi:10.1016/j.msea.2006.02.464.
- [40] P. Lejček, J. Adánek, S. Hofmann, Anisotropy of grain boundary segregation in  $\Sigma = 5$  bicrystals of  $\alpha$ -iron, *Surf. Sci.* 264 (1992) 449–454. doi:10.1016/0039-6028(92)90201-G.

- [41] S. Hofmann, P. Lejček, J. Adámek, Grain boundary segregation in [100] symmetrical tilt bicrystals of an Fe-Si alloy, *Surf. Interface Anal.* 19 (1992) 601–606. doi:10.1002/sia.7401901112.
- [42] P. Lejček, S. Hofmann, Temperature dependence of the phosphorus segregation at the twin boundary in an Fe-4 at.% Si alloy, *Surf. Interface Anal.* 16 (1990) 546–551. doi:10.1002/sia.7401601113.
- [43] P. Lejček, S. Hofmann, Segregation enthalpies of phosphorus, carbon and silicon at {013} and {012} symmetrical tilt grain boundaries in an Fe-3.5 at.% Si alloy, *Acta Metall. Mater.* 39 (1991) 2469–2476. doi:10.1016/0956-7151(91)90026-W.
- [44] P. Lejček, Characterization of grain boundary segregation in an Fe-Si alloy, *Anal. Chim. Acta.* 297 (1994) 165–178. doi:10.1016/0003-2670(93)E0388-N.
- [45] C.H.P. Lupis, *Chemical Thermodynamics of Materials*, Elsevier, Amsterdam, 1983.
- [46] H.S. Carslaw, J.C. Jaeger, *Conduction of Heat in Solids*, Clarendon Press, 1986.
- [47] A.P. Sutton, V. Vitek, On the Structure of Tilt Grain Boundaries in Cubic Metals I. Symmetrical Tilt Boundaries, *Philos. Trans. R. Soc. Math. Phys. Eng. Sci.* 309 (1983) 1–36. doi:10.1098/rsta.1983.0020.
- [48] H.J. Frost, F. Spaepen, Hard sphere models for the structure of grain boundaries, *J. Phys. Colloq.* 43 (1982) C6-73-C6-82. doi:10.1051/jphyscol:1982608.
- [49] M.F. Ashby, F. Spaepen, S. Williams, The structure of grain boundaries described as a packing of polyhedra, *Acta Metall.* 26 (1978) 1647–1663. doi:10.1016/0001-6160(78)90075-5.
- [50] M.F. Ashby, F. Spaepen, A new model for the structure of grain boundaries: Packing of polyhedra, *Scr. Metall.* 12 (1978) 193–195. doi:10.1016/0036-9748(78)90162-X.
- [51] H. Gleiter, On the structure of grain boundaries in metals, *Mater. Sci. Eng.* 52 (1982) 91–131. doi:10.1016/0025-5416(82)90040-4.
- [52] D.L. Medlin, K. Hattar, J.A. Zimmerman, F. Abdeljawad, S.M. Foiles, Defect character at grain boundary facet junctions: Analysis of an asymmetric  $\Sigma = 5$  grain boundary in Fe, *Acta Mater.* 124 (2017) 383–396. doi:10.1016/j.actamat.2016.11.017.
- [53] A. Biedermann, M. Schmid, B.M. Reichl, P. Varga, Competitive segregation of Si and P on Fe<sub>96.5</sub>Si<sub>3.5</sub> (100) and (110), *Fresenius J. Anal. Chem.* 353 (1995) 259–262. doi:10.1007/BF00322048.
- [54] M. Lavrskyi, H. Zapolsky, A.G. Khachaturyan, Quasiparticle approach to diffusional atomic scale self-assembly of complex structures: from disorder to complex crystals and double-helix polymers, *Npj Comput. Mater.* 2 (2016). doi:10.1038/npjcompumats.2015.13.

- [55] P. Lejček, S. Hofmann, Interstitial and substitutional solute segregation at individual grain boundaries of  $\alpha$ -iron: data revisited, *J. Phys. Condens. Matter.* 28 (2016) 064001. doi:10.1088/0953-8984/28/6/064001.
- [56] P. Lejček, S. Hofmann, Grain boundary segregation, anisotropy and prediction, in: *Encycl. Mater. Sci. Technol.* Pergamon, Amsterdam, 2002.
- [57] H. Hänsel, H.J. Grabke, Grain boundary segregation of phosphorus and carbon in ferritic iron, *Scr. Metall.* 20 (1986) 1641–1644. doi:10.1016/0036-9748(86)90411-4.
- [58] H.J. Grabke, Surface and Grain Boundary Segregation on and in Iron and Steels, *ISIJ Int.* 29 (1989) 529–538. doi:10.2355/isijinternational.29.529.
- [59] W. Wei, H.J. Grabke, The effect of alloying elements on the grain boundary segregation of phosphorus in iron and the intergranular corrosion of the Fe-P system, *Corros. Sci.* 26 (1986) 223–236. doi:10.1016/0010-938X(86)90057-0.
- [60] S. Suzuki, M. Obata, K. Abiko, H. Kimura, Effect of carbon on the grain boundary segregation of phosphorus in  $\alpha$ -iron, *Scr. Metall.* 17 (1983) 1325–1328. doi:10.1016/0036-9748(83)90225-9.
- [61] T. Matsuyama, H. Hosokawa, H. Suto, Tracer Diffusion of P in Iron and Iron Alloys, *Trans. Jpn. Inst. Met.* 24 (1983) 589–594. doi:10.2320/matertrans1960.24.589.
- [62] L. Qingfen, Y. Shanglin, L. Li, Z. Lei, X. Tingdong, Experimental study on non-equilibrium grain-boundary segregation kinetics of phosphorus in an industrial steel, *Scr. Mater.* 47 (2002) 389–392. doi:10.1016/S1359-6462(02)00151-3.
- [63] O.K. von Goldbeck, *Iron-X Binary Phase Diagrams*, Springer Berlin Heidelberg, Berlin, Heidelberg, 1982.

## **Chapter 4. Solute segregation under ion irradiation in Fe-P-C model alloy**

As it was shown in Chapter 1, during the last years, phosphorus segregation in RPV steels and Fe-based model alloys was extensively studied in order to understand the mechanisms of irradiation embrittlement. However, the dependence of the variation of phosphorus segregation with GB geometry has not been studied systematically. This is an open question often ignored in the literature. This chapter will report on the characterization of intergranular segregation after self-ion irradiation of Fe-P model alloys and its possible relationship with GB geometry.

In the first part of the current chapter, the structural and chemical investigations of self-ion irradiated Fe-0.034 at.% P-0.01 at.% C model alloy by STEM-EDX and APT are presented. Five degrees of freedom were determined for each GB using combined APT/TKD method. The relationship between GB geometry and segregation intensity is discussed. Also, phosphorus clusters and its segregation on the dislocation lines are observed. The density of dislocations and voids is determined from the STEM images and considered in the modeling.

In order to gain a better understanding of the mechanism of intergranular segregation, a Faulkner's RIS model for dilute alloys was applied to predict the segregation behavior of phosphorus to GBs in irradiated Fe-0.034 at.% P-0.01 at.% C model alloy. A detailed description of the model and comparison with experimental data is given in the second part of this chapter.

## 4.1 Radiation-induced segregation related to the grain boundary structure

### 4.1.1 Phosphorus segregation as a function of irradiation depth

As explained in Chapter 2, self-ion irradiations were used to get insight in the understanding of the effects of neutron irradiation on phosphorous intergranular segregation. However, because of high electronic energy loss, ions lose energy quickly, giving rise to spatially non uniform energy deposition profile [1]. The penetration distance of 10 MeV  $\text{Fe}^{5+}$  ions into iron target, according to the SRIM calculation, is approximately 2.5  $\mu\text{m}$ . It is thus considered that in the depth range from 300 to 1000 nm there is no influence of sample surface and a limited number of implanted iron ions. But at least, there is an effect of the dose rate and PKA spectrum, in comparison to neutron irradiation condition. Moreover, the method for APT tip preparation used in this work, suffer from uncertainty in the determination of the sample depth extraction. According to the more widely used method, the irradiated surface is located perpendicular to the microtip axis (Fig. 4.1). The layer of Pt on the top allows to the operator to control the depth of milling with high accuracy (below 10 nm).

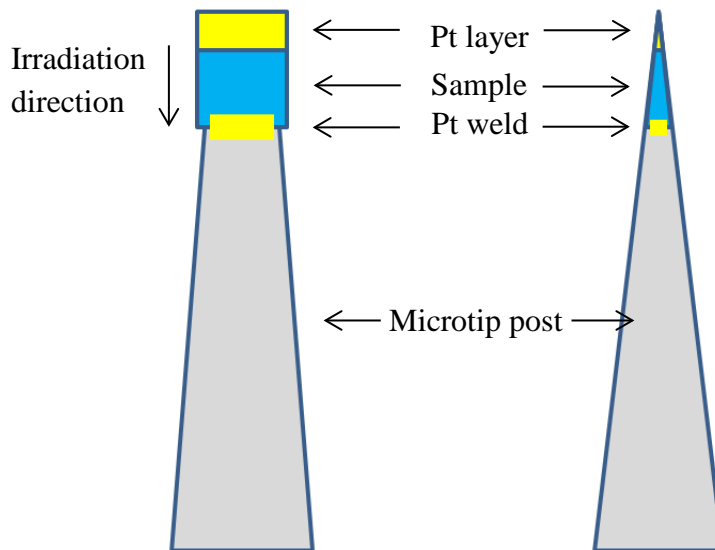


**Fig. 4.1.** Schematic image of the irradiated sample welded to the microtip post. The implanted surface is oriented perpendicular to the axis of microtip post

In our case, in order to control the process of milling by TKD mapping [2,3] and to minimize the 3D atomic reconstruction artifacts, the GB was oriented perpendicular to the tip axis. The delicate part of the machining is the control of the erosion in the irradiated volume

after the milling of the Pt layer, which is the only indicator of the surface location. One must keep in mind that the APT tip apex with a GB in must be formed in a depth range of 0.5 to 1  $\mu\text{m}$  (Fig. 4.2). According to the SRIM calculation, this depth range corresponds to a roughly homogeneous irradiation with a dose rate variation of only  $2.5 \times 10^{-5}$  to  $4 \times 10^{-5}$   $dpa/s$ .

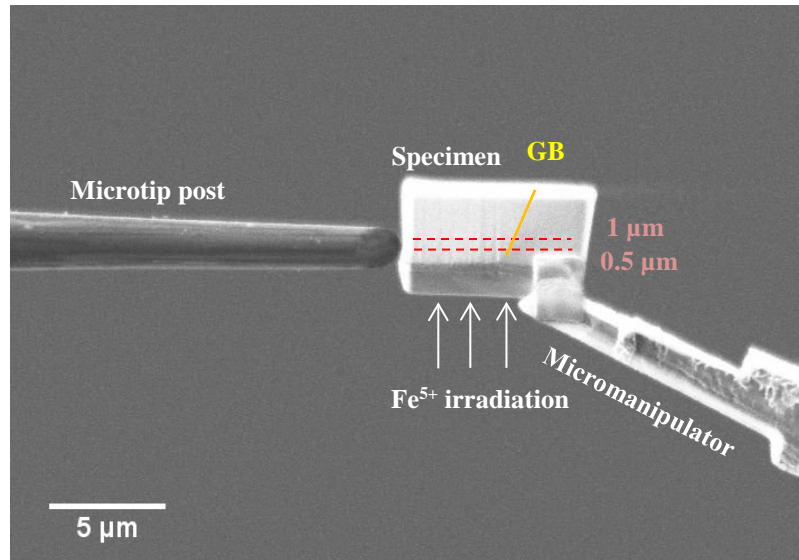


**Fig. 4.2.** The specimen with a size  $10 \times 4 \times 2 \mu\text{m}^3$  is placed onto a W-microtip post using micromanipulator. The homogeneous irradiated part between 0.5 and  $1 \mu\text{m}$  depth is shown by dotted red lines

In order to verify that the phosphorus segregation along GB in the direction of irradiation, especially in the range from 0.5 to  $1 \mu\text{m}$ , is homogenous, TEM lamellae containing GB was prepared. An in situ lift-out technique using DualBeam Focused Ion Beam Scanning Electron Microscope (FIB-SEM) was used to extract a thin foil from across a GB  $43^\circ[100]$  in the Fe-0.034 at.% P-0.01 at.% C model alloy irradiated at  $450^\circ\text{C}$  using Fe ions at a dose rate  $3 \times 10^{-5}$   $dpa/s$ .

Since the foil is a cross section of the irradiated sample, phosphorus GB segregation can be examined as a function of irradiation depth. Phosphorus GB segregation has been measured by Energy-Dispersive X-ray Analysis (EDX) using the GPM's scanning transmission electron microscope with a field emission electron source (FEG-STEM).

The phosphorus concentration is plotted as a function of depth below the surface (Fig. 4.3, red dots). The analysis revealed an approximately constant value of phosphorus segregation in the depth range from 0.3 to  $1.2 \mu\text{m}$ . Thus, the distribution of phosphorus is homogenous in the area of the APT tip preparation, which is between 0.5 and  $1 \mu\text{m}$ .

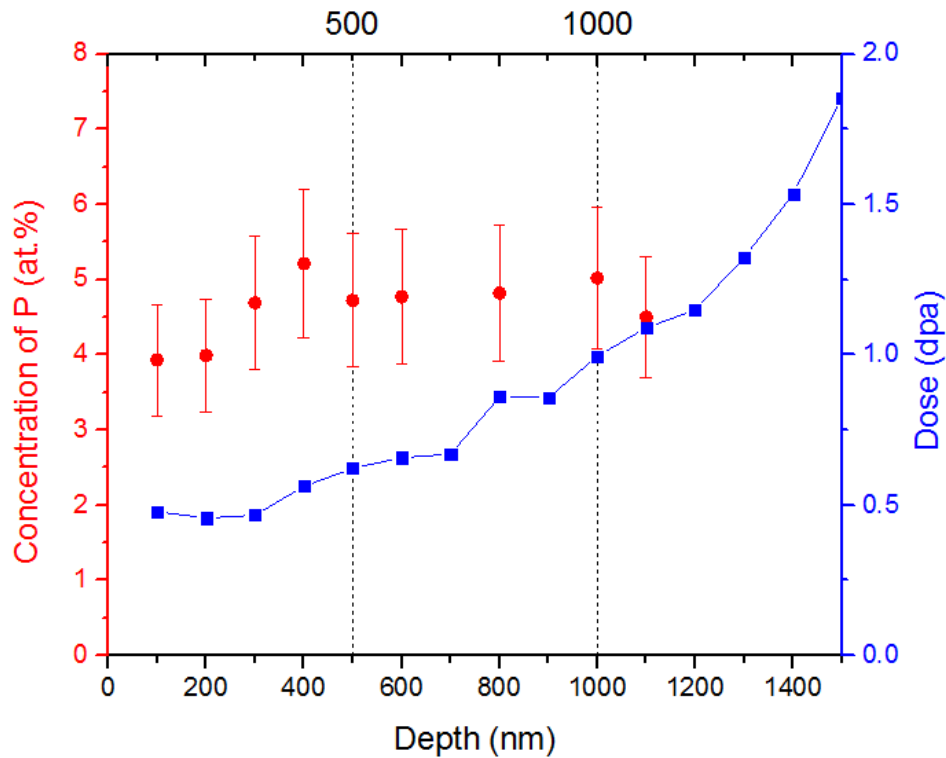


**Fig. 4.3.** STEM-EDX measurement of phosphorus concentration at general  $43^\circ[100]$  GB, as well as dose evolution as a function of irradiation depth

#### 4.1.2 Radiation-induced segregation at grain boundaries

In our study, the effect of irradiation was studied on a Fe-0.034 at.% P-0.01 at.% C model alloy after a stress relieve heat treatment (SRHT) at  $650^\circ\text{C}$  for 2h. This material was irradiated at  $450^\circ\text{C}$  with 10 MeV  $\text{Fe}^{5+}$  ions to three irradiation doses ( $0.075 \pm 0.025$ ;  $0.38 \pm 0.12$ ;  $0.75 \pm 0.25$  dpa). The GB chemistry was examined using APT.

Atom probe analysis revealed that phosphorus and carbon atoms segregate at GBs. Fig. 4.4a presents a typical 3D APT reconstruction, with a clear enrichment of phosphorus atoms at GB. This was obtained in an APT tip prepared from the sample irradiated to 0.75 dpa and containing a HAGB with a misorientation of  $43^\circ[100](11-1)/(3-50)$ . Fig. 4.4b shows that the distribution of phosphorus atoms in the GB plane is homogenous in this HAGB. The different experiments show the same behavior in LAGBs.

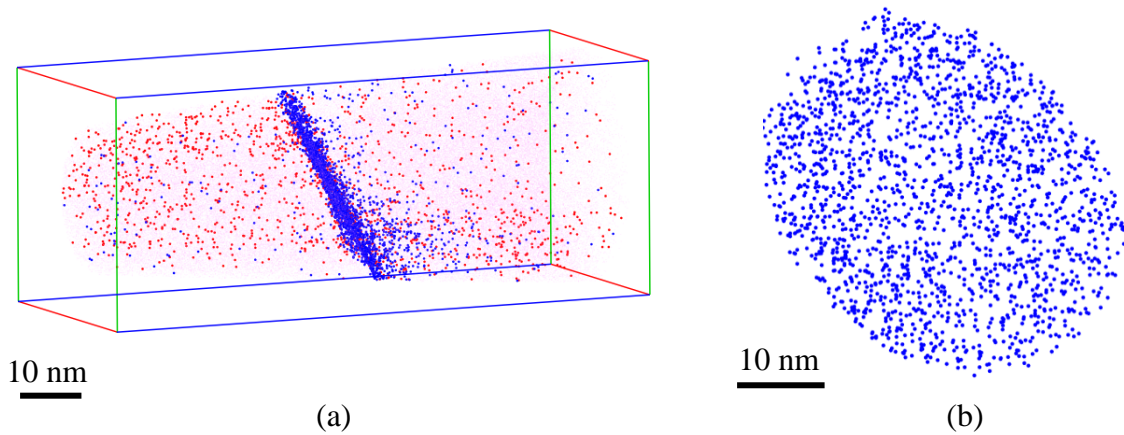


**Fig. 4.4.** (a) 3D APT reconstruction of a small volume of the Fe-0.034 at.% P-0.01 at.% C alloy irradiated at 450°C up to  $0.75 \pm 0.25$  dpa. In figure (a) the phosphorus and carbon atoms distribution clearly reveal the  $43^\circ[100](11-1)/(3-50)$  GB and figure (b) shows the distribution of phosphorus atoms on this GB plane

Five degrees of freedom were determined for each GB using combined APT/TKD method. Monolayer coverages of phosphorus and carbon atoms with the corresponding GB geometry are presented in Table 4.1.

Despite the large dispersion of values for each GB, the mean phosphorus segregation at HAGBs increases with irradiation dose. In the sample irradiated to  $0.075 \pm 0.025$  dpa, phosphorus GB segregation reaches on the average  $0.22 \pm 0.05$  monolayer. With increasing the dose to  $0.38 \pm 0.12$  dpa, phosphorus GB segregation reaches  $0.29 \pm 0.08$  monolayer. The sample irradiated to the highest dose,  $0.75 \pm 0.25$  dpa, shows the most important phosphorus segregation level at boundaries with the average value of  $0.36 \pm 0.14$  monolayers and the highest value of  $0.50 \pm 0.01$  monolayer at  $43^\circ[100](-3-21)/(-521)$  GB. The lowest phosphorus segregation ( $0.15 \pm 0.03$  monolayer) was obtained for the lowest-angle GB, i.e.  $8^\circ[101](-3-23)/(-2-12)$ .

Two APT specimens with different orientations ( $43^\circ[100](11-1)/(3-50)$  and  $43^\circ[100](-3-21)/(-521)$ ) were prepared from one large GB. Indeed, when the GB surface is spatially curved, these two samples, in two different area of the curve surface have different GB plane orientations. Both phosphorus and carbon segregation levels vary significantly from one GB to another. This is an indicator of the strong variations in GB energies depending on their geometries. As we can see from Table 4.1 the phosphorus segregation at  $43^\circ[100](-3-21)/(-521)$  GB is  $\sim 30\%$  higher than at  $43^\circ[100](11-1)/(3-50)$  GB.

As for as carbon segregation is concerned, the segregation level does not change with irradiation dose ( $0.20 \pm 0.05$  monolayer after irradiation to 0.075 dpa,  $0.20 \pm 0.06$  monolayer after 0.38 dpa and  $0.19 \pm 0.04$  monolayer after 0.75 dpa). It seems that both the GB structure

and the phosphorus segregation influence on the value of carbon GB segregation. The lowest carbon segregation ( $0.13 \pm 0.02$  monolayer) was observed in the lowest-angle  $8^\circ[101](-3-23)/(-2-12)$  GB. Other low carbon segregation ( $0.14 \pm 0.01$  monolayer) corresponds with the highest phosphorus GB segregation ( $0.50 \pm 0.01$  monolayer) at  $43^\circ[100](-3-21)/(-521)$  GB after irradiation to  $0.75 \pm 0.25$  dpa. This may indicate the site competition between phosphorus and carbon at the GB.

**Table 4.1.** Summary of GB geometry and related phosphorus,  $C_P^\Phi$ , and carbon,  $C_C^\Phi$ , segregations. Phosphorus and carbon GB segregation in the specimen after stress-relieving heat treatment was averaged over all the analysed HAGBs. Phosphorus GB segregation in the specimen after thermal ageing is a predicted value of equilibrium GB segregation obtained using the segregation kinetics model (see Chapter 3). Carbon GB segregation in the specimen after thermal ageing is the mean experimental value over all the analysed HAGBs.

Treatment	GB structure	$C_P^\Phi$ (monolayer)	$C_C^\Phi$ (monolayer)
Stress-relieving heat treatment at $650^\circ\text{C}$ (experiments)		$0.12 \pm 0.01$	$0.03 \pm 0.01$
Thermal ageing at $450^\circ\text{C}$ (modeling)		$0.17 \pm 0.02$	$0.25 \pm 0.05$
$0.075 \pm 0.025$ dpa	$12^\circ[-331] (22-1)/(3-22)$	$0.20 \pm 0.01$	$0.19 \pm 0.02$
	$31^\circ[01-2] (1-30)/(010)$	$0.17 \pm 0.01$	$0.18 \pm 0.01$
	$42^\circ[113] (-2-50)/(3-2-2)$	$0.27 \pm 0.01$	$0.25 \pm 0.02$
$0.38 \pm 0.12$ dpa	$8^\circ[101] (-3-23)/(-2-12)$	$0.15 \pm 0.03$	$0.13 \pm 0.02$
	$41^\circ[-441] (-24-3)/(1-10)$	$0.21 \pm 0.01$	$0.21 \pm 0.01$
	$45^\circ[41-1] (-151)/(10-1)$	$0.37 \pm 0.01$	$0.25 \pm 0.01$
$0.75 \pm 0.25$ dpa	$12^\circ[1-11] (-344)/(5-45)$	$0.35 \pm 0.02$	$0.18 \pm 0.01$
	$35^\circ[40-3] (52-2)/(51-1)$	$0.21 \pm 0.01$	$0.19 \pm 0.01$
	$43^\circ[100] (11-1)/(3-50)$	$0.36 \pm 0.01$	$0.23 \pm 0.01$
	$43^\circ[100] (-3-21)/(-521)$	$0.50 \pm 0.01$	$0.14 \pm 0.01$

The experimental data from the irradiated specimens was compared with the experimentally determined initial GB segregation and the theoretical equilibrium GB segregation under thermal ageing at  $450^\circ\text{C}$ .

The initial GB segregations (after SRHT) of phosphorus and carbon are  $0.12 \pm 0.01$  and  $0.03 \pm 0.01$  monolayer, respectively. The values were determined experimentally using

APT and the same standard milling procedure as for irradiated samples. Since the GB segregations of phosphorus and carbon at 650°C reach the equilibrium steady-state value in less than 2h (Chapter 3), the presented GB concentrations are taken as the reference equilibrium GB segregation.

In Chapter 3 it has been shown that 1000 h of ageing is not enough to reach the equilibrium phosphorus GB segregation at 450°C. The equilibrium phosphorus GB segregation was calculated using the segregation kinetics model and fitted with experimental data. The value of phosphorus GB segregation at 450°C given in Table 4.1 ( $0.17 \pm 0.02$  monolayer), is the predicted equilibrium GB segregation of phosphorus.

All data from Table 4.1 is illustrated in Fig. 4.5. As it seen, the phosphorus intergranular segregation under irradiation for most of GBs is larger than the equilibrium GB segregation at the same temperature (450°C). One exception is the GB with a low misorientation angle:  $8^\circ$ [101] (-3-23)/(-2-12).

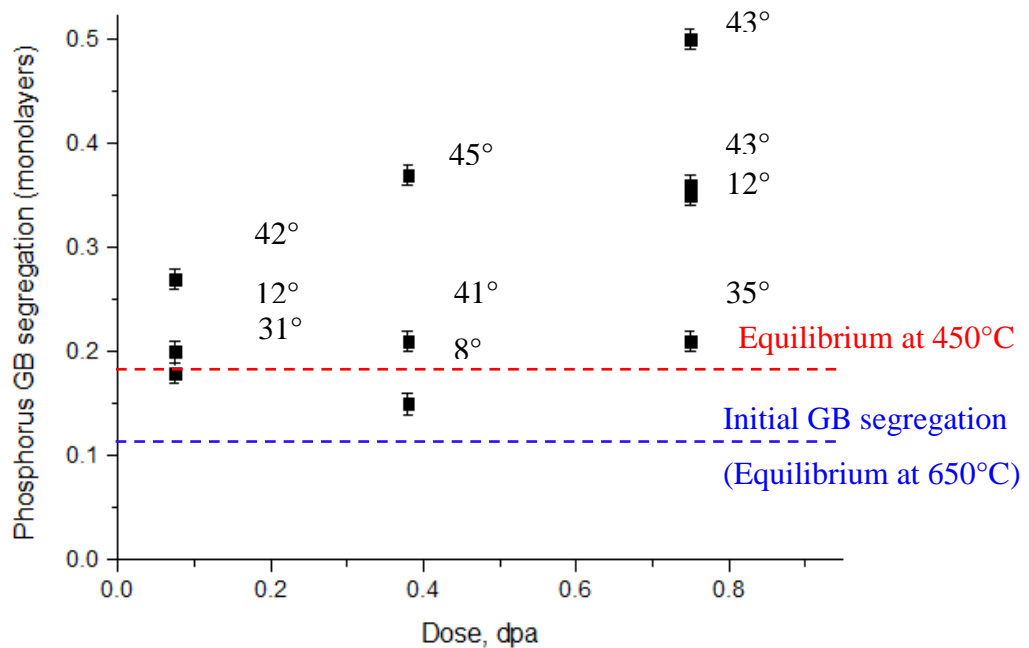


**Fig. 4.5.** Phosphorus GB segregation under irradiation as a function of dose is compared with the average values of measured initial segregation (blue dashed line) and predicted equilibrium segregation at 450°C (red dashed line).

In the irradiated materials, the excess of phosphorus atoms over the equilibrium GB segregation would suggest the presence and influence of flux coupling effect between irradiation point defect and phosphorus atoms, i.e. a radiation-induced segregation (RIS) mechanism. Probably both thermal equilibrium segregation and the kinetic of the non-equilibrium radiation-induced segregation process participate to the phosphorus diffusion.

In order to gain a better understanding of phosphorus segregation mechanism in  $\alpha$ -Fe under given irradiation condition, the analytical model of Faulkner is used (see 4.2). The classical theory of RIS in steels presents a mechanism where point defects migrate to GBs acting as perfect sinks. However, the presence of internal defects may influence this migration process. Thus, the study of internal defects and segregation on them is necessary.

### 4.1.3 Intragranular segregation and precipitation of phosphorus atoms

In the current research we focused our statement on GB segregation. Thus, a study of phosphorus segregation on internal defects was not performed systematically. However, some APT tips prepared to study GB chemistry revealed non-homogenous phosphorus distribution in the grain after irradiation. For instance, in the sample irradiated to  $0.075 \pm 0.025$  dpa, a cluster enriched in phosphorus and carbon atoms was found. As it is shown in Fig. 4.6, a cluster with a non-regular shape and a size about  $12 \pm 1$  nm is detected. The core of a cluster contains  $13.8 \pm 0.3$  at.% of P and  $1.5 \pm 0.1$  at.% of C.

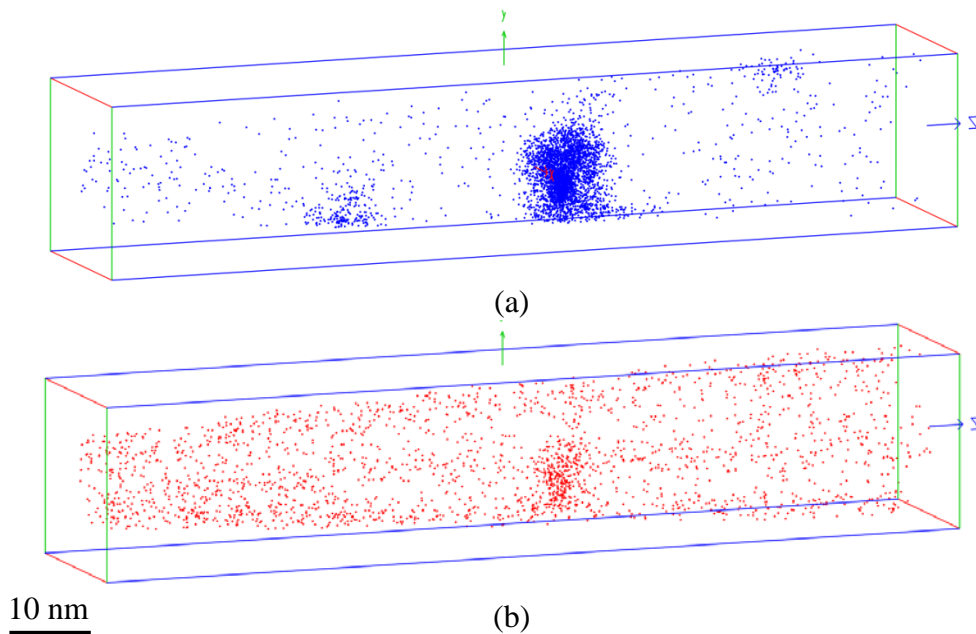


**Fig. 4.6.** 3D reconstruction of an analyzed volume representing the distribution of (a) phosphorus and (b) carbon atoms in a Fe-0.034 at.% P-0.01 at.% C model alloy after ion irradiation to 0.075 dpa

The bulk concentration of phosphorus is far from the solubility limit of P in alpha-iron at 450°C (0.26 at.%) [4], so there is no thermally-enhanced phase transformation at this temperature. The number density of phosphorus clusters in the grains is too low to have good statistic using only APT technique (clusters were observed in only a few of the samples).

However, one may conclude that radiation-induced clustering occurs in ion irradiated Fe-0.034 at.% P-0.01 at.% C model alloy at 450°C.

A few APT analyses demonstrated that phosphorus atoms segregate nearby dislocations. (Fig. 4.7). Visually it seems that dislocations are also enriched in carbon, but there is a very little difference between carbon concentration in a bulk and in the dislocation line.

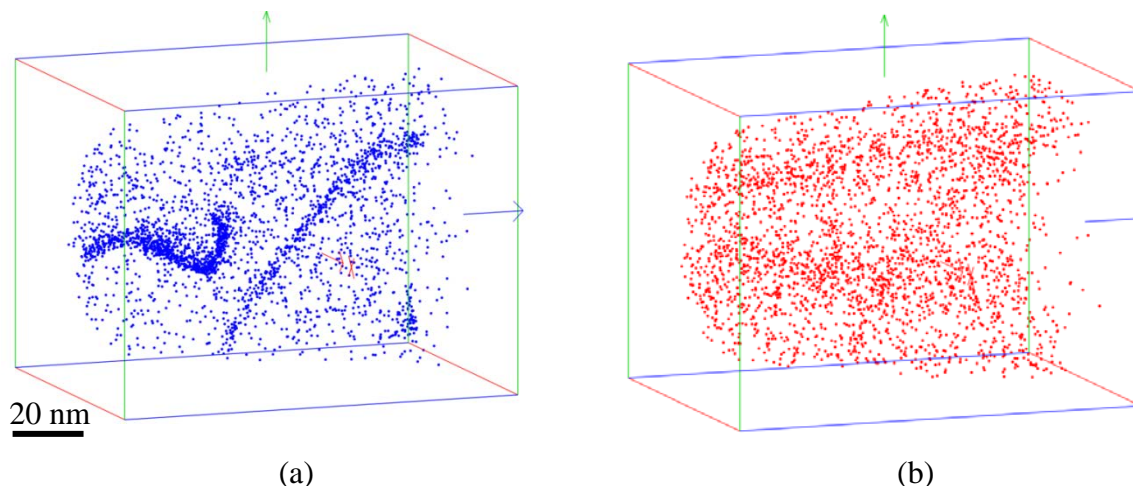


**Fig. 4.7.** 3D reconstruction of an analyzed volume of the Fe-0.034 at.% P-0.01 at.% C model alloy after ion irradiation at 450°C up to 0.075 dpa, showing the presence of dislocations enriched with (a) phosphorus and (b) carbon atoms.

The presence of phosphorus atoms in clusters and nearby dislocations would suggest that these atoms don't contribute to the radiation induced GB segregation. Thus, the high number density of intragranular defects can significantly reduce the flux of point defect-phosphorus complexes toward GB.

Since the number density of dislocations and voids are included in the further GB segregation modelling, it was decided to measure them from STEM images. The site-specific Dual Beam (FIB-SEM) technique was used to extract a thin foil from across a GB  $43^\circ[100]$  in Fe-0.034 at.% P-0.01 at.% C model alloy irradiated to 0.75 dpa at 450°C. The analysis was performed in the GPM's JEM-ARM200F. The images were taken in STEM bright field mode using (110) reflection from  $\langle 111 \rangle$  oriented grain. Comparison of irradiated and unirradiated thin foils prepared with the same SEM/FIB dual beam technique has shown the FIB milling leads to formation of large number of ultra-fine black dots, while dislocation arrays and voids were observed only in the ion irradiated specimen.

Fig. 4.8 shows the STEM bright field images of a cross-sectional foil containing a GB  $43^\circ[100]$ . The thin dark layer at the top of the images corresponds to the Pt layer on the

specimen surface. The matrix damage mainly consists in a dislocation array down to 2  $\mu\text{m}$  depth. This is consistent with SRIM calculation, where the peak damage depth and ion range are about 1.9 and 2.1  $\mu\text{m}$ , respectively.

The dislocation density was measured using the approach given by Ham [5]:

$$\rho = \frac{2N}{L \times t} \quad (88)$$

where  $L$  is the total length of five lines drawn in random directions,  $N$  is the number of intersections of these lines with dislocations and  $t$  is the thickness of the film. The thickness of the lamella was determined from the *thickness over electron wavelength* ( $t/\lambda$ ) map, acquired by energy filtered transmission electron microscopy (EFTEM). The dislocation density in the area between 0.5 and 1  $\mu\text{m}$  below the irradiated surface is  $\rho = 1.4 \times 10^{14}/\text{m}^2$ .

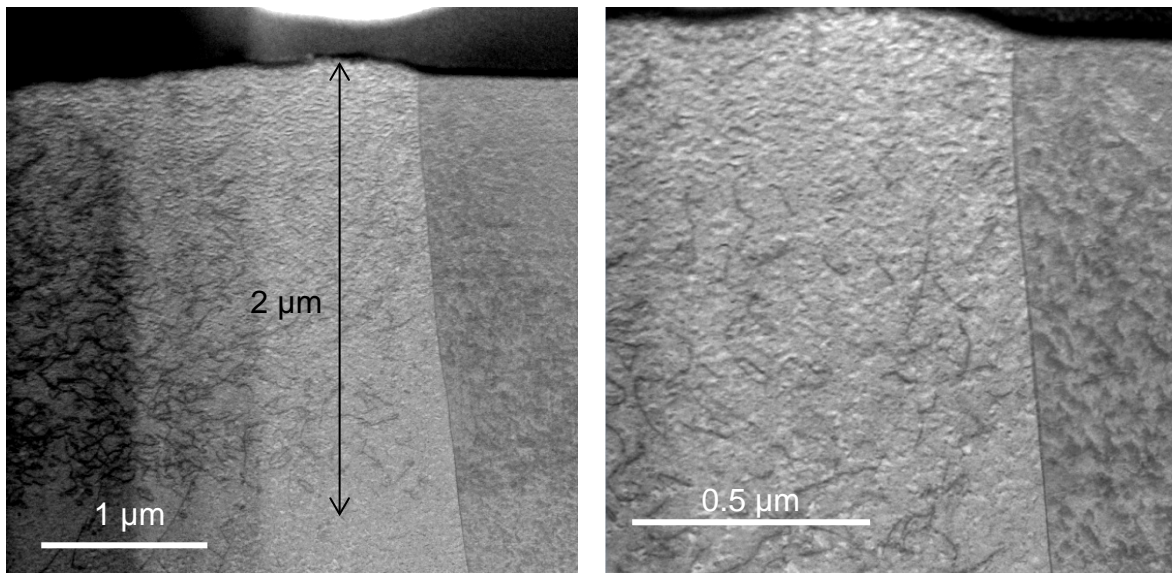


**Fig. 4.8.** STEM bright field image showing the dislocation array near the GB in Fe-0.034 at.% P-0.01 at.% C model alloy irradiated at 450°C to 0.75 dpa at different magnifications

Two beam contrast experiments using reflections with  $\bar{g} = 110$  close to  $\langle 111 \rangle$  zone axis reveal the presence of voids from the surface to a depth beyond 2  $\mu\text{m}$  (Fig. 4.9). A void-denuded zone about 200 nm is observed near GB. The volume-averaged void diameter is about 10 nm; the void number density is  $\sim 10^{21} \text{ m}^{-3}$ . It corresponds to a volume fraction of about 0.17%.

The resolution of STEM-EDX mapping was not enough to detect an eventual segregation of phosphorus at the void interfaces, but some authors reported the occurrence of non-equilibrium solute segregation, giving rise to solute depletion or enrichment at void surfaces in steels [6–8].

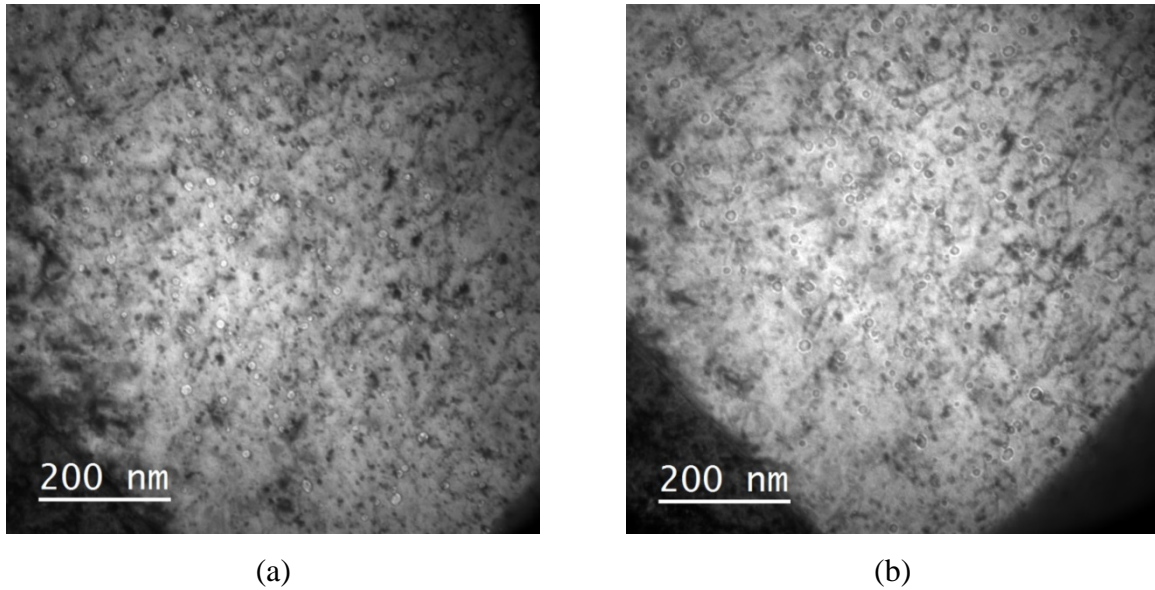


**Fig. 4.9.** TEM bright field (a) under focused and (b) over focused images of voids in the model alloy irradiated at 450°C to 0.75 dpa ( $\bar{g} = 110$ ,  $\bar{z} = \langle 111 \rangle$ ), denuded area near GB (lower left) is about 200 nm.

The number density of dislocations and voids are considered with the mean field approximation and included in the total sink strength, which appears in the radiation-induced segregation model.

## 4.2 Modeling of radiation induced grain boundary segregation

In the present work, the kinetic model of Faulkner [9–13] is used to describe the segregation of solute atoms to grain boundaries in a polycrystalline diluted alloy at a given temperature. In this model, both irradiation-enhanced and irradiation-induced solute diffusion have effect on the final value of the GB solute segregation. It was described in Chapter 1 that in the case of phosphorus in neutron or heavy ion irradiated  $\alpha$ -Fe, the diffusion of solute-interstitials complexes plays a dominant role in irradiation-induced segregation [14–16]. The diffusion of phosphorus-point defect complexes (resulting in non-equilibrium segregation) and enhanced phosphorus diffusion (resulting in equilibrium segregation) and also phosphorus-carbon repulsive interaction were taken into account in calculations.

Due to the fact that RIS is a kinetic process and equilibrium segregation is a thermodynamic process, it was assumed that these two processes are independent of each other. In calculations, the total segregation level was founded as sum of non-equilibrium and equilibrium segregation levels minus the matrix concentration of the solute.

### 4.2.1 Radiation-induced segregation

The irradiation generates an excess of vacancies and self-interstitials. According to the rate theory approach, when the concentration of point defects reaches a steady state, the production rate,  $G$ , is equal to the sum of recombination and the annihilation of point defects [11,17]:

$$BG = K_{VI}C_V^r C_I^r + K_{SV}C_V^r C_S \quad (89)$$

$$BG = K_{VI}C_V^r C_I^r + K_{SI}C_I^r C_S \quad (90)$$

where  $G$  is the point-defect production rate or dose rate;  $B$  is the dose rate efficiency, i.e. the fraction of freely migrating defects escaping from cascade;  $C_V^r$  and  $C_I^r$  are the irradiation-generated vacancy and interstitial concentrations, respectively;  $D_V$  and  $D_I$  are the diffusion coefficients of vacancies and interstitials, respectively;  $C_S$  is the sink concentration in the grain;  $K_{VI}$  is the mutual recombination rate constant;  $K_{SV}$  and  $K_{SI}$  are sink absorption annihilation rate constants for vacancies and interstitials, respectively.

The action of sinks on the point defects ( $P$ ) in the solid can be described through sink strength,  $k_{SP}^2$ , with units of  $\text{cm}^{-2}$  as [18]:

$$\text{absorption rate} = K_{SP}C_P^r C_S = k_{SP}^2 C_P^r D_P \quad (91)$$

so equations (89) and (90) can be rewritten as:

$$BG = K_{VI}C_V^r C_I^r + k_{SV}^2 C_V^r D_V \quad (92)$$

$$BG = K_{VI}C_V^r C_I^r + k_{SI}^2 C_I^r D_I \quad (93)$$

From (92) one may obtain the concentration of irradiation-created point defects,  $C_P^r$ , (where  $P$  can be I (interstitial) or V (vacancy)) as [19,20]:

$$C_P^r = \frac{BGF(\eta)}{D_P k_{SP}^2} \quad (94)$$

where

$$F(\eta) = \frac{2}{\eta} [(1 + \eta)^{1/2} - 1] \quad (95)$$

and

$$\eta = \frac{4K_{VI}BG}{k_{SV}^2 k_{SI}^2 D_V D_I} \quad (96)$$

When recombination rate coefficient,  $K_{VI}$ , is small,  $\eta$  is also small and  $F(\eta) \rightarrow 1$ , i.e. has no effect on irradiation phenomena.  $K_{VI}$  should not be confused by  $B$ , which describes the

mutual recombination *in cascade*, while  $K_{VI}$  is the long-range recombination coefficient given by [18]:

$$K_{VI} = \frac{z_{VI}D_I}{b^2} \quad (97)$$

where  $z_{VI}$  is the combinatorial factor, i.e. number of potential interactions, and  $b$  is the jump distance of interstitials.

Two kind of sinks observed experimentally, voids and dislocations, are considered with the mean field approximation and included in the total sink strength,  $k_{SP}^2 = k_{hP}^2 + k_{dP}^2$ . The void sink strength,  $k_{hP}^2$ , is defined as [20,21]:

$$k_{hP}^2 = 4\pi\bar{r}_h\rho_h \quad (98)$$

where  $\bar{r}_h$  is the void mean radius,  $\rho_h$  is the void number density.

The dislocation sink strength is given by [22,23]:

$$k_{dV}^2 = \sqrt{\rho_d} \left( \frac{6}{R} + \sqrt{\rho_d} \right) \quad (99)$$

$$k_{dI}^2 = \sqrt{Z_I\rho_d} \left( \frac{6}{R} + \sqrt{Z_I\rho_d} \right) \quad (100)$$

for vacancies,  $k_{dV}^2$ , and interstitials,  $k_{dI}^2$ , respectively, where  $Z_I$  is the bias parameter defining the preferential interaction between interstitials and dislocations compared to vacancies,  $R$  is the grain size and  $\rho$  is the dislocation density.

The thermal equilibrium point defect concentration,  $C_p^{eq}$ , is given by [24]:

$$C_p^{eq} = A_p \exp\left(\frac{-E_f^P}{kT}\right) \quad (101)$$

where  $E_f^P$  is the formation energy of point defect,  $A_p$  is a constant correlating with the vibrational entropy of atoms around the vacancy,  $k$  is the Boltzmann's constant and  $T$  is the temperature.

Thus, total steady-state concentration of point defects in the bulk,  $C_{iP}^B$ , is given by:

$$C_{iP}^B = C_p^{eq} + C_p^r = A_p \exp\left(\frac{-E_f^P}{kT}\right) + \frac{BGF(\eta)}{D_P k_{PS}^2} \quad (102)$$

The concentration of solute-point defect complexes,  $C_{iP}^B$ , created in the bulk during irradiation is given by [24]:

$$C_{iP}^B = A_{iP} C_p^B C_i^B \exp\left(\frac{E_b^{iP}}{kT}\right) \quad (103)$$

where  $C_P^B$  is the total point defect concentration in the bulk of grain,  $C_i^B$  is the solute concentration,  $A_{iP}$  is a constant containing geometric and entropy terms,  $E_b^{iP}$  is the solute  $i$  - point defect  $P$  binding energy.

Substituting equation (102) to (103) obtain the value of  $C_{iP}/C_i$  within the bulk of the grains:

$$\left(\frac{C_{iP}}{C_i}\right)^B = A_P A_{iP} \exp\left(\frac{E_b^{iP} - E_f^P}{kT}\right) + A_{iP} \frac{BGF(\eta)}{D_P k_{PS}^2} \exp\left(\frac{E_b^{iP}}{kT}\right) \quad (104)$$

Due to the annihilation of point defects, it can be considered that in the vicinity of sinks, in particular GBs, point defects are present in their equilibrium concentration, i.e.:

$$C_{iP}^\phi = A_{iP} C_P^{eq} C_i^\phi \exp\left(\frac{E_b^{iP}}{kT}\right) \quad (105)$$

Hence, from equation (101) the ratio  $C_{iP}/C_i$  at the boundary is given by:

$$\left(\frac{C_{iP}}{C_i}\right)^\phi = A_{iP} A_P \exp\left(\frac{E_b^{iP} - E_f^P}{kT}\right) \quad (106)$$

As a result, a gradient of point defect concentration between the GB and grain interior appears and drives the point-defect solute complexes to migrate toward the GB. It means that larger supersaturation of point defects induces a larger level of phosphorus segregation at GB.

Dividing equation (104) by equation (106) gives:

$$\frac{(C_{iP}/C_i)^B}{(C_{iP}/C_i)^\phi} = 1 + \frac{BGF(\eta)}{A_P D_P k_{PS}^2} \exp\left(\frac{E_f^P}{kT}\right) \quad (107)$$

The left-hand side of this equation can be rearranged to give:

$$\frac{C_i^\phi}{C_i^B} \cdot \frac{C_{iP}^B}{C_{iP}^\phi} = 1 + \frac{BGF(\eta)}{A_P D_P k_{PS}^2} \exp\left(\frac{E_f^P}{kT}\right) \quad (108)$$

Faulkner [25] has shown that the absolute concentration of the complexes should be related to the point defect-impurity binding energy,  $E_b^{iP}$ , as:

$$\frac{C_{iP}^\phi}{C_{iP}^B} = \frac{E_b^{iP}}{E_f^P} \quad (109)$$

Thus, we have

$$C_i^\phi = C_i^B \frac{E_b^{iP}}{E_f^P} \left[ 1 + \frac{BGF(\eta)}{A_P D_P k_{PS}^2} \exp\left(\frac{E_f^P}{kT}\right) \right] \quad (110)$$

It was assumed by Faulkner [9] that in the multicomponent systems, solutes migrate toward GB independently. However, there is only a finite number of freely-migrating SIAs within the bulk. Thus, the segregating solutes have to compete to form mobile mixed

dumbbells. As it was previously shown [11], the absolute concentration of the complexes is proportional to the solute concentration and the exponential term containing the point-defect – solute binding energy. Hence, in order to consider the competition between  $i$  solutes to create mixed dumbbells the equation (110) is modified into:

$$C_i^\phi = C_i^B \frac{E_b^{iP}}{E_f^P} \left[ \frac{C_i^B \exp\left(\frac{E_b^{iP}}{kT}\right)}{\sum_i C_i^B \exp\left(\frac{E_b^{iP}}{kT}\right)} \right] \left[ 1 + \frac{BGF(\eta)}{A_P D_P k_{PS}^2} \exp\left(\frac{E_f^P}{kT}\right) \right] \quad (111)$$

The kinetics for irradiation-induced non-equilibrium grain boundary segregation for solute  $i$  is given by McLean's formula [26],

$$\frac{C_i^\phi(t) - C_i^B}{C_i^\phi - C_i^B} = 1 - \exp\left(\frac{4D_{iP}t}{\beta_i^2 d^2}\right) \operatorname{erfc}\left(\frac{2\sqrt{D_{iP}t}}{\beta_i d}\right) \quad (112)$$

where  $C_i^\phi(t)$  is the concentration of solute  $i$  at GB as a function of irradiation time at a given irradiation temperature,  $D_c^{iP}$  is the diffusion coefficient of solute  $i$ -point defect complexes,  $d$  is the thickness of grain boundary and  $\beta_i = C_i^\phi / C_i^B$ .

Repulsive interaction between phosphorus and carbon atoms ( $j = 1,2$ ) at GB is considered by assuming that  $C_i^\phi(t)$  is modified to  $C_i^\phi(t)^*$ , according to the relative binding energies between the segregated elements and the grain boundary,  $Q_i^\Phi$ ,

$$C_i^\phi(t)^* = C_i^\phi(t) \left( \frac{C_i^B \exp(Q_i^\Phi / kT)}{\sum_j C_j^B \exp(Q_j^\Phi / kT)} \right) \quad (113)$$

The diffusion coefficients indicated above are given by the following relationships:

$$D_{iV} = D_{0iV} \exp\left(-\frac{E_m^{iV}}{kT}\right) \quad (114)$$

$$D_{iI} = D_{0iI} \exp\left(-\frac{E_m^{iI}}{kT}\right) \quad (115)$$

$$D_V = D_{0V} \exp\left(-\frac{E_m^V}{kT}\right) \quad (116)$$

$$D_I = D_{0I} \exp\left(-\frac{E_m^I}{kT}\right) \quad (117)$$

where  $D_{0iV}$ ,  $D_{0iI}$ ,  $D_{0V}$  and  $D_{0I}$  are the pre-exponential constants for diffusion of solute-vacancy complexes, solute-interstitials complexes, vacancies and interstitials, respectively;

$E_m^{iV}$ ,  $E_m^{iI}$ ,  $E_m^V$  and  $E_m^I$  are the migration energies for diffusion of solute-vacancy complexes, solute-interstitials complexes, vacancies and interstitials, respectively.

## 4.2.2 Thermal equilibrium segregation under irradiation temperature

The increased concentration of irradiation-created vacancies enhances the solute diffusion rate but does not affect the equilibrium segregation level. Thermal equilibrium GB segregation is described using McLean and Guttman models for ternary Fe-P-C system [26,27]. More detailed explanation is given in Chapter 3.

The equilibrium concentration of phosphorus,  $C_P^\phi$ , at a given temperature is expressed as:

$$\frac{C_P^\phi}{1 - C_P^\phi - C_C^\phi} = \frac{C_P^B}{1 - C_P^B - C_C^B} \exp\left(-\frac{\Delta G_P}{RT}\right) \quad (118)$$

where  $C_P^B$  and  $C_C^B$  are the bulk concentrations of phosphorus and carbon, respectively,  $\Delta G_P^0$  is the standard Gibbs energy of intergranular phosphorus segregation,  $R$  is the universal gas constant and  $T$  is the temperature.

The free energy of segregation,  $\Delta G_I$ , in equation (118) is given by:

$$\Delta G_P = \Delta H_P^0 - T\Delta S_P^0 + \alpha'_{PC}(C_C^\phi - C_C^B) \quad (119)$$

where  $\Delta H_P^0$  and  $\Delta S_P^0$  are the standard molar enthalpy and entropy of phosphorus segregation in a dilute binary Fe-P system and  $\alpha'_{PC}$  is the interaction coefficient.

The kinetics of equilibrium GB segregation of phosphorus is given by :

$$\frac{C_P^\phi(t) - C_P^\phi(0)}{C_P^\phi - C_P^\phi(0)} = 1 - \exp\left(\frac{4D_P^*t}{\beta_P^2 d^2}\right) \operatorname{erfc}\left(\frac{2\sqrt{D_P^*t}}{\beta_P d}\right) \quad (120)$$

where  $C_P^\phi(t)$  is the equilibrium phosphorus concentration after irradiation time  $t$ ,  $C_P^\phi(0)$  is the initial GB concentration of phosphorus ( $t = 0$ ), i.e. the segregation level produced during stress relieve heat treatment,  $C_P^\phi$  is the equilibrium concentration,  $D_P^*$  is the irradiation-enhanced diffusion coefficient for phosphorus atoms in presence of irradiation created vacancies,  $d$  is the thickness of concentrated layer and  $\beta_P = C_P^\phi/C_P^B$  is the enrichment ratio.

The approach to evaluate irradiation-enhanced diffusion is to consider the effect of irradiation created vacancies on solute diffusion.

Thus the irradiation-enhanced phosphorus diffusion coefficient can be acquired by [9]:

$$D_P^* = D_P \left( \frac{C_V^{eq} + C_V^{ir}}{C_V^{eq}} \right) \quad (121)$$

where  $C_V^{eq}$  and  $C_V^{ir}$  are the thermal equilibrium vacancy concentration and irradiation-generated vacancy concentration, respectively.

### 4.2.3 Comparison of experimental and theoretical results

Radiation-induced non-equilibrium segregation and thermal equilibrium segregation are considered to be independent each other, because the first is a kinetic process and the second is a thermodynamic process. Thus the total segregation level is considered to be the sum of radiation-induced and thermal segregation levels minus the bulk concentration of the solute.

Parameters used in the theoretical calculations are listed in Table 4.2. The model parameters were selected in order to fit the calculated curves with experimental data obtained from three different doses.

**Table 4.2.** Data used in the theoretical calculations

Symbol	Parameter (unit)	This work	Other values
$G$	Dose rate (dpa/s)	$3 \times 10^{-5}$	
$R$	Grain size (m)	0,0002	
$\rho_d$	Dislocation density ( $m^{-2}$ )	$1.4 \times 10^{14}$	
$\rho_h$	Void number density ( $m^{-3}$ )	$10^{21}$	
$r$	Void mean radius (m)	$5 \times 10^{-9}$	
$B$	Dose rate correction factor	0.01 [28]	
$b$	Jump distance of SIA in $\alpha$ -iron (m)	$1.43 \times 10^{-10}$	
$d$	Grain boundary thickness (m)	$0.5 \times 10^{-9}$	
$A_I$	SIA vibrational entropy	1 [9]	
$A_V$	Vacancy vibrational entropy	1 [9]	
$E_f^V$	Vacancy formation energy (eV)	2.18 [29]	2.02 [16], 2.0 [30], 1.6 [31], 1.4 [24], 1.71 [32]
$E_f^I$	SIA formation energy (eV)	3.0 [9]	3.2 [33], 3.36 [32], 4.3 [31], 3.41 [34]
$E_b^{PI}$	P-SIA binding energy	0.83 [16]	0.58 [35], 1.02 [36], 0.57

	(eV)		[37]
$E_b^{CI}$	C-SIA binding energy (eV)	1.12 [37]	0.58 [38], -0.19 [39], 0.68 [40]
$E_m^{PI}$	P-SIA complex migration energy (eV)	0.87 [10]	0.27 [36], 0.29 [41], 1.24 [36]
$E_m^I$	SIA migration energy (eV)	0.3 [42]	0.34 [36]
$E_m^V$	Vacancy migration energy (eV)	0.7 [29]	1.24 [43], 1.3 [31]
$E_i$	Activation energy for P diffusion (eV)	2.39 [44]	2.62 [45]
$D_0^i$	Pre-exponential factor of P diffusivity (m <sup>2</sup> /s)	$2.9 \times 10^{-4}$ [44]	$7.12 \times 10^{-3}$ [45]
$D_{0c}^{iV}$	Pre-exponential factor of P-vacancy complex diffusivity (m <sup>2</sup> /s)	$4.48 \times 10^{-7}$ [16]	$1.7 \times 10^{-5}$ [46], $4.95 \times 10^{-8}$ [29]
$D_{0c}^{iI}$	Pre-exponential factor of P-SIA complex diffusivity (m <sup>2</sup> /s)	$8 \times 10^{-7}$ [47]	
$D_{0I}$	Pre-exponential factor of SIA diffusivity (m <sup>2</sup> /s)	$5 \times 10^{-6}$ [47]	
$D_{0V}$	Pre-exponential factor of vacancy diffusivity (m <sup>2</sup> /s)	$5 \times 10^{-5}$ [24]	$1.16 \times 10^{-4}$ [29,48]
$Z_I$	Interstitial bias	1.1 [49]	1.2 [31]
$Q_P^\Phi$	P-GB binding energy (eV)	0.52	0.54 [50], 0.4 [51]
$Q_C^\Phi$	C-GB binding energy (eV)	0.83 [50]	0.5 [52]
$\Delta H_I^0$	Standard segregation enthalpy of P (J/mol)	-27000	
$\Delta S_I^0$	Standard segregation entropy of P (J/mol/K)	21.5	
$\Delta H_I^0$	Standard segregation enthalpy of C (J/mol)	-50000 [53]	
$\Delta S_I^0$	Standard segregation entropy of C (J/mol/K)	2 [53]	
$\alpha'_{P-C}$	P-C interaction coefficient (J/mol)	7000 [53]	

The prediction of radiation enhanced and total (combined radiation enhanced and radiation induced) phosphorus segregation in Fe-0.034 at.% P-0.01 at.% C alloy irradiated to three different doses is presented in Fig. 4.10.

Radiation-induced segregation (RIS) caused by phosphorus-interstitial complex diffusion is absolutely dominant below approximately 500°C and equilibrium segregation

dominates above this temperature. The segregation peak occurs in a temperature range between 400 and 450°C. Below these temperatures, the maximum non-equilibrium segregation amount is larger, but kinetics processes are slower, and above these temperatures, the segregation is still lower because of lower maximum segregation values. Consequently, the predictions from the model suggest that the magnitude of the segregation peak increases and shifts to lower temperatures with increasing dose (irradiation time) at the same dose rate.

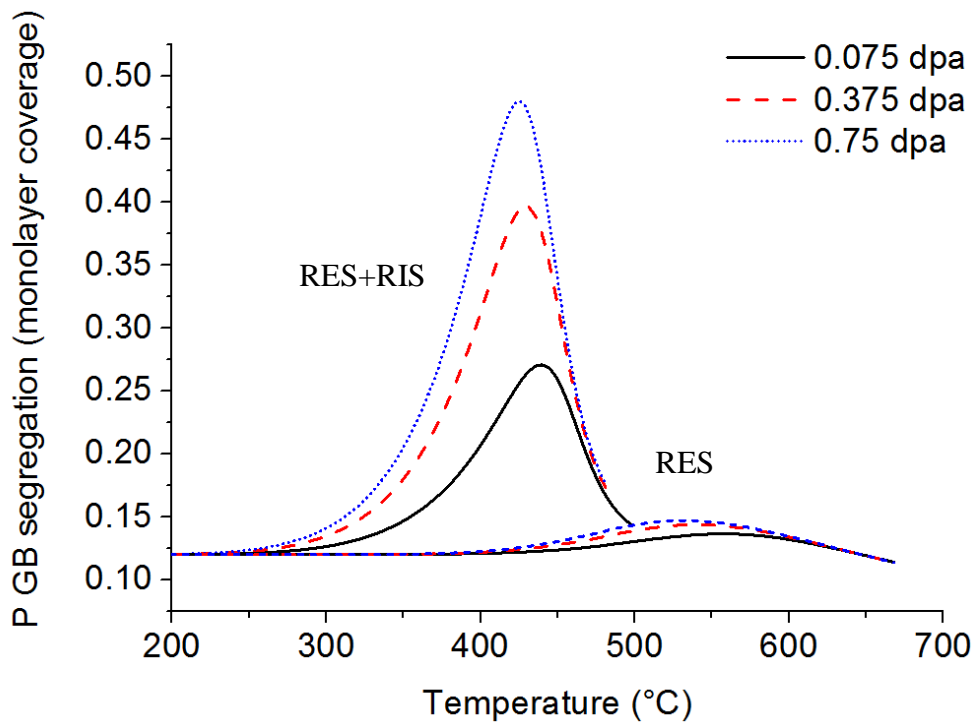


**Fig. 4.10.** Model prediction of radiation-enhanced (RES) and combined radiation enhanced and radiation induced segregations (RES+RIS) of phosphorus in Fe-0.034 at.% P-0.01 at.% C alloy as a function of irradiation temperature and dose (a dose rate is  $3 \times 10^{-5}$  dpa/s)

Experimental studies of low-alloy ferritic steel revealed that in a range from 400°C to 550°C temper embrittlement associated with GB segregation of phosphorus occurs and leads to intergranular fracture [10,45,54]. Thus, Faulkner's model satisfactorily indicates the area of considerable phosphorus segregation.

Phosphorus segregation kinetics modelling is compared with experimental data on phosphorus segregation in Fe-0.034 at.% P-0.01 at.% C model alloy. Fig. 4.11 shows radiation-enhanced segregation (RES) and combined radiation enhanced and induced segregation (RIS+RES) kinetics. The phosphorus GB segregation before irradiation, in the samples after stress relieve heat treatment (SRHT) is  $0.12 \pm 0.01$  monolayer. In figure it is shown by black dash line.

The equilibrium GB segregation of phosphorus at 450°C is  $0.17 \pm 0.02$  monolayer. The diffusion coefficient of phosphorus in steels at this temperature is  $5.8 \times 10^{-21} \text{ m}^2/\text{s}$ . According to the segregation kinetics model of McLean (see Chapter 3), more than 3000 h needs to reach the equilibrium GB segregation. While under ion irradiation, the coefficient of radiation-enhanced diffusion of phosphorus is equal to  $9 \times 10^{-13} \text{ m}^2/\text{s}$ , so the equilibrium GB segregation ( $0.17 \pm 0.02$  monolayers of phosphorus) is reached faster. Therefore, the radiation-enhanced mechanism of segregation is shown by the straight solid pink line, which indicates the equilibrium GB segregation of phosphorus at 450°C. As it was noted before, experimental data exceed the predicted equilibrium value of phosphorus GB segregation at 450°C. One exception is the GB with a low misorientation angle:  $8^\circ[101](-3-23)/(-2-12)$ .

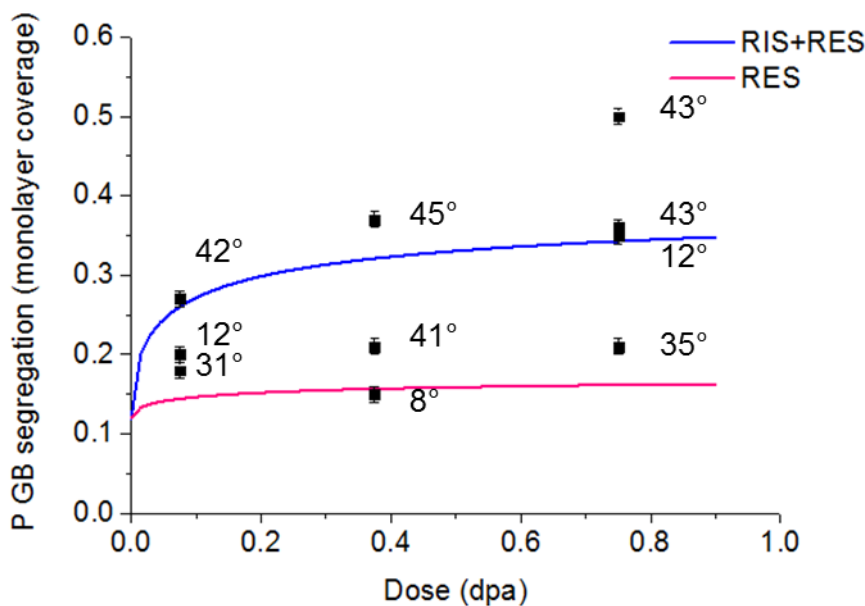


**Fig. 4.11.** Comparison of predicted (solid lines) dose dependence of phosphorus grain boundary segregation in Fe-0.034 at.% P-0.01 at.% C ( dose rate =  $3 \times 10^{-5} \text{ dpa/s}$  ) with experimental data (symbols). The pink and blue solid lines represents kinetics of combined radiation enhanced and induced segregation (RIS+RES) and radiation-enhanced segregation (RES), respectively. The black dash line indicates the level of phosphorus GB segregation before irradiation, in the samples after stress relieve heat treatment (SRHT)

We can say that the experimental results are broadly comparable with RIS-RES model prediction. However, there is a spread of segregation due to GB structure effects, which will be discussed later.

RIS model of Faulkner together with experimental data from thermal aged samples allows to us to distinguish the nature of phosphorus segregation at GBs. For instance, the total amount of phosphorus segregation at  $43^\circ[100] (11-1)/(3-50)$  GB is  $\sim 0.36$  monolayer. Of them:  $\sim 0.12$  monolayer ( $\sim 33\%$  from the total amount) was segregated during stress relieve

heat treatment,  $\sim 0.05$  monolayer ( $\sim 14\%$  from the total amount) is the radiation-enhanced segregation via the vacancy mechanism, and  $\sim 0.19$  monolayer ( $\sim 53\%$  from the total amount) is radiation-induced segregation via phosphorus-interstitial complex diffusion.

Thus, considering the experimental data from the heat treated samples and the results of equilibrium and radiation-induced GB segregation modelling, it is possible to qualitatively distinguish the participation of each mechanism in the formation of the final value of phosphorus GB segregation. Also, Faulkner's model based on coupled interstitial point defect and solute fluxes represented the general behavior of RIS in Fe-0.034 at.% P-0.01 at.% C model alloy and satisfactorily indicates the temperature range where phosphorus GB segregation reaches the maximum level. Furthermore, as it was shown in many works of Faulkner and his colleges [9–11,13,37,55,56], the model also can sufficiently indicates the effects of dose, dose rate, dislocation and void density, grain size and considers the presence other solute elements in the bulk.

### 4.3 Discussion

Faulkner's RIS model along with many others presents the segregation of phosphorus to GBs acting as perfect sinks. However, variation in GB nature may influence the sink efficiency and thus the segregation level. In the current work, the large dispersion of the values is observed. For example, intergranular phosphorus segregation in sample irradiated to 0.75 dpa may vary from 21% to 50%. Moreover, there is some variation of phosphorus segregation along GB.

Due to the complicated structure of GBs (5 DOFs, GB curvature, faceting), there is no simple rule to link a GB geometrical parameter to its segregation level [57]. The segregation variations have been first attributed to the different GB plane orientations. The previous Auger electron spectroscopy analyses, after fracture, demonstrated that larger phosphorus segregation occurs at GBs with high Miller index planes, while the segregation is low for those with low index planes [58–60]. Also, Ogura et al. [58] have found a correlation between the boundary straightness and the phosphorus segregation level: there is lower phosphorus segregation at straight boundaries, and higher at curved GBs.

Fig. 4.12 shows the combined band contrast (BC) and grain boundary (GB) map of the Fe-0.034 at.% P-0.01 at.% C model alloy, which was obtained by EBSD. The red and yellow arrows indicate the straight and curved GBs, respectively.

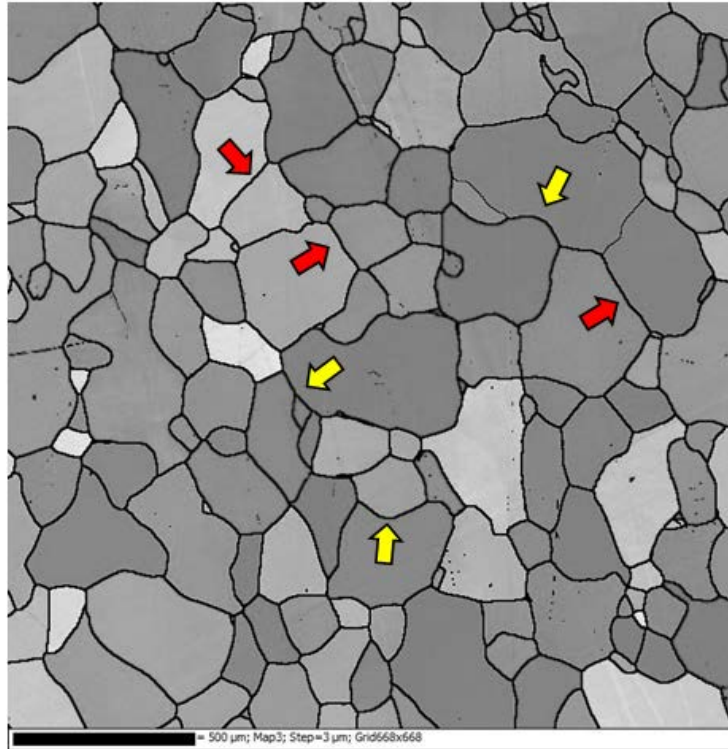


**Fig. 4.12.** The combined band contrast (BC) and grain boundary (GB) EBSD map of the Fe-0.034 at.% P-0.01 at.% C model alloy. The red and yellow arrows indicate the straight and curved GBs, respectively

The GBs, whose traces are observed straight or with boundaries having long straight segment are referred to as *straight boundaries*. However, they are not necessarily straight on an atomic scale. The GBs, whose traces are observed curved, i.e. the GB plane orientation change along the boundary are referred to as *curved boundaries*. However, the curved boundaries may be decomposed in planar segments and presented as a set of facets with low indices [61].

In order to measure the local curvature of GB traces, the concept of curvature at a point on a surface, describing in [62], was used. Fig. 4.13 shows a curve in the XY plane. To define the curvature at a point P place two other points, A and B, on the curve. Construct a circle through these three points. This circle has a center, O, and a radius r. Now let A and B approach P. The point O moves and the radius changes. In the limit as A and B arrive at P, the center approaches the center of curvature for the point P, and the radius becomes the radius of curvature. The curvature of the curve at P is the reciprocal of this radius.

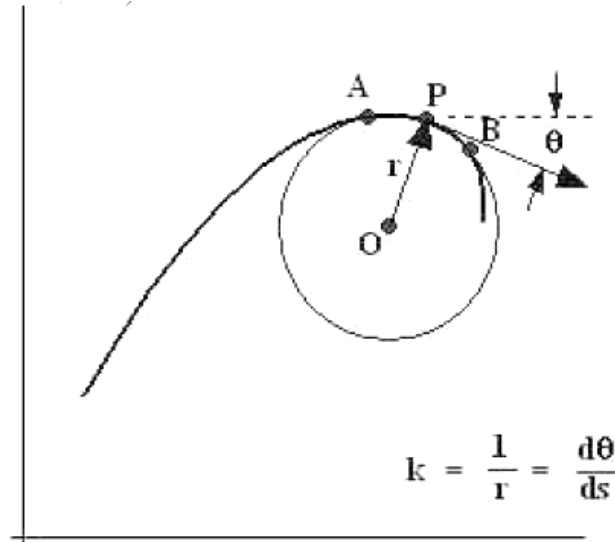


**Fig. 4.13.** Curvature at a point P on a curve in two dimensional space is the reciprocal of the radius of a circle that passes through three adjacent points (A,P and B) on the curve at P [62]

It can also be shown that the curvature is the rate of rotation of the tangent to the curve as the point P moves along the arc length,  $s$ :

$$k = \frac{1}{r} = \frac{d\theta}{ds} \quad (122)$$

where  $\theta$  is the angle between curve and tangent.

In order to check the influence of GB plane orientation and straightness to phosphorus segregation level, the closest low-index plane (deviation angle less than  $10^\circ$ ) and the boundary curvature  $k$  was determined for each GB and given in Table 4.3. For straight GBs the  $k = 0$ .

With regard to the GBs statistics, the GB straightness seems to be the most influential factor. In the sample irradiated to  $0.075 \pm 0.025$  dpa, phosphorus is enriched to  $0.20 \pm 0.01$  monolayers at curved GB with low misorientation angle  $12^\circ[-331]\{221\}/\{211\}$ , which is slightly higher than phosphorus segregation ( $0.17 \pm 0.01$  monolayer) at HAGB  $31^\circ[01-2]\{130\}/\{001\}$ . A similar behavior is observed in the sample irradiated to  $0.75 \pm 0.25$  dpa. The phosphorus segregation ( $0.35 \pm 0.02$  monolayers) at curved  $12^\circ[-335]\{221\}/\{221\}$  GB is higher than the segregation ( $0.21 \pm 0.01$  monolayers) at straight  $34^\circ[10-1]\{211\}/\{311\}$  GB with higher misorientation angle.

In the sample irradiated to  $0.38 \pm 0.12$  dpa, two GBs have a very similar structure: GB  $45^\circ[41-1]\{311\}/\{321\}$  and  $41^\circ[-441]\{311\}/\{311\}$ . Both of them have high misorientation angle, high index rotation axis and high index GB planes. But curved GB  $45^\circ[41-$

$1\{311\}/\{321\}$  has higher phosphorus segregation ( $0.37 \pm 0.01$  monolayer) than straight GB  $41^\circ[-441]\{311\}/\{311\}$  ( $0.21 \pm 0.01$  monolayer).

**Table 4.3.** Summary of GB plane orientations given in nearest low Miller indices, GB curvatures and related phosphorus segregation

Dose (dpa)	$\theta$ (°)	[hkl]	(hkl) <sub>1</sub>	Nearest low Miller indexes	Deviation (°)	(hkl) <sub>2</sub>	Nearest low Miller indexes	Deviation (°)	$k$ , GB curvature ( $10^3 \text{ m}^{-1}$ )	$C_P^\Phi$ (mono-layers)
0.075	12	-331	22-1	{221}	0	3-22	{211}	8	2.9	0.20
	31	01-2	1-30	{130}	0	010	{001}	0	0	0.17
	42	113	250	{120}	4.8	-322	{211}	8	1.5	0.27
0.38	8	101	32-3	{111}	10	21-2	{120}	0	0	0.15
	41	-441	521	{311}	7	251	{311}	7	0	0.21
	45	41-1	15-1	{311}	9.5	-413	{321}	5	0.9	0.37
0.75	12	1-11	-335	{211}	5	5-34	{221}	8	3.6	0.35
	34	10-1	32-2	{211}	8.5	52-1	{311}	7.8	0	0.21
	44	100	11-1	{111}	0	3-50	{120}	4.4	4.5	0.36
	44	100	32-1	{321}	0	-521	{311}	7.8	4.5	0.50

To the author's knowledge, the influence of boundary curvature on the segregation intensity has not been investigated from the theoretical point of view. Thus our results suggest the direction for future theoretical development.

The influence of the GB plane orientation was determined by comparing two samples from a same curved GB. It was found that the GB area with higher nearest Miller indices  $43^\circ[100]\{321\}/\{311\}$  has greater phosphorus segregation level ( $0.50 \pm 0.01$  monolayer) than GB  $43^\circ[100]\{111\}/\{120\}$  with relatively low index GB plane ( $0.36 \pm 0.01$  monolayer).

A possible explanation for this phenomenon can be the presence of larger excess volume for high Miller index GBs [63–65]. According to the structural unit model, the GB excess volume describes how much *expansion* is induced by the presence of a GB in a material [66]. Wolf et al. [67,68] was one of the first who calculated that the low-index GB planes in polycrystal are associated with low-energy and small amount of volume expansion. However, there are some contradictory examples, which showed that low indexed GB plane are not necessarily associated with the low GB energy and segregation [69,70]. Our result is in agreement with the theory of Wolf, but the statistics is low (only one GB).

Thus, our study has distinguished the significant influence of GB plane orientation and curvature on phosphorus segregation level. The main advantage of our results is the atomic-

scale observing, which can support the simulation works at the same scale. The main limitation of the experimental results is low statistics. Clearly, more experimental and theoretical researches are still necessary before obtaining a definitive correlation between GB structure and intergranular segregation.

As it was noted before, the Faulkner's model assumes that the GBs are perfect sinks. This model was useful for us to distinguish the different segregation mechanisms of phosphorus under thermal and irradiation ageing. However, this approach does not enable us to consider GB structure effect, since there is no GB sink efficiency in the model.

Further study is needed to develop the atomic scale model for anticipating the GB energy (sink efficiency) to the boundary structure. Until recently, studies of GB energy have been generally limited a small number of GBs. Most of them has studied symmetrical tilt and twist GBs and presented the GB energy as a function of misorientation angle or boundary coincidence  $\Sigma$  [71–76]. A few atomistic simulations have explored the role of GB plane orientation on the structure of asymmetrical GBs [69,70,72,77]. For general GBs with mixed (tilt and twist) structure the GB energies should be calculated over all five degrees-of-freedom. In recent years, great effort has been devoted to the computational study of GB structure and energy. Several authors [78–82] have reported the GB energy as a function of all macroscopic five crystallographic parameters. Despite of the considerable effort that has been devoted, the computational study of GB is still not trivial. The new approach has to consider the infinite number of different GBs depending on the misorientation between the two grains and GB plane orientation.

The further step is to apply this atomic-scale model to RIS. It has been shown [83–85] that the defect structure at GB and subsequently the sink efficiency can evolve in a complex manner during irradiation. In addition, our results have shown the influence of GB plane curvature on the segregation level. These factors will complicate the prediction of RIS in RPV steel. Moreover, interaction between different solutes at GB should be taken into account.

## Conclusion

In the first part of this chapter, intra granular and intergranular phosphorus segregation in self-ion irradiated Fe-0.034 at.% P-0.01 at.% C model alloy were studied using atomic-scale resolution techniques. The STEM-EDX analysis revealed the homogeneous distribution of phosphorus in the area of the APT tip preparation, which is between 0.5 and 1  $\mu\text{m}$ .

A few APT experiments revealed phosphorus clustering and segregation on dislocation lines. STEM study has shown that during 10 MeV  $\text{Fe}^{5+}$  ion irradiation at 450°C of the Fe-0.034 at.% P-0.01 at.% C model alloy up to 0.75 dpa, irradiation damage becomes apparent in the form of a dislocation array and voids down to 2  $\mu\text{m}$  depth. The number density of dislocations and voids were measured and included in the total sink strength, which appears in the radiation-induced segregation model.

The APT analysis of the Fe-0.034 at.% P-0.01 at.% C after ion irradiation up to 0.75 dpa has shown that the mean phosphorus segregations at HAGBs increases with irradiation dose, while the carbon GB segregation does not change. The phosphorus segregation at high-angle GBs in all irradiated samples is larger than the equilibrium GB segregation of phosphorus at the same temperature. It was suggest the presence and influence of flux coupling effect between irradiation point defect and phosphorus atoms, i.e. a radiation-induced segregation (RIS) mechanism.

Further modeling using Faulkner's model has demonstrated that RIS of phosphorus caused by phosphorus-interstitial complex diffusion is absolutely dominant mechanism in the Fe-0.034 at.% P-0.01 at.% C model alloy under ion irradiation at 450°C using 10 MeV  $\text{Fe}^{5+}$  ions at a dose rate  $3.0 \times 10^{-5}$  dpa/s. Considering the experimental data from the heat treated samples and the results of equilibrium and radiation-induced GB segregation modelling, it was qualitatively distinguished the participation of each mechanism in the formation of the final value of phosphorus GB segregation.

It was found the experimental evidence of the higher phosphorus segregation at curved GBs than at straight one. Also, it was demonstrated that larger phosphorus segregation occurs at GBs with high Miller index planes, while the segregation is low for those with low index planes. In the discussion part it was concluded that analytical models similar to the Faulkner's one oversimplify the RIS process. Therefore, further study is needed to develop the atomic scale model for anticipating the GB properties (energy, sink efficiency, solute segregation) to the boundary structure.

## References

- [1] G.S. Was, R.S. Averback, Radiation Damage Using Ion Beams, in: *Compr. Nucl. Mater.*, Elsevier, 2012: pp. 195–221. doi:10.1016/B978-0-08-056033-5.00007-0.
- [2] K. Babinsky, R. De Kloe, H. Clemens, S. Primig, A novel approach for site-specific atom probe specimen preparation by focused ion beam and transmission electron backscatter diffraction, *Ultramicroscopy*. 144 (2014) 9–18. doi:10.1016/j.ultramicro.2014.04.003.
- [3] K. Babinsky, W. Knabl, A. Lorich, R. De Kloe, H. Clemens, S. Primig, Grain boundary study of technically pure molybdenum by combining APT and TKD, *Ultramicroscopy*. doi:10.1016/j.ultramicro.2015.05.014.
- [4] O.K. von Goldbeck, *Iron-X Binary Phase Diagrams*, Springer Berlin Heidelberg, Berlin, Heidelberg, 1982.
- [5] R.K. Ham, The determination of dislocation densities in thin films, *Philos. Mag.* 6 (1961) 1183–1184. doi:10.1080/14786436108239679.
- [6] E.A. Little, D.A. Stow, Void-swelling in irons and ferritic steels, *J. Nucl. Mater.* 87 (1979) 25–39. doi:10.1016/0022-3115(79)90123-5.
- [7] L.K. Mansur, M.H. Yoo, The effects of impurity trapping on irradiation-induced swelling and creep, *J. Nucl. Mater.* 74 (1978) 228–241. doi:10.1016/0022-3115(78)90362-8.
- [8] I.M. Neklyudov, V.N. Voyevodin, Features of structure-phase transformations and segregation processes under irradiation of austenitic and ferritic-martensitic steels, *J. Nucl. Mater.* 212–215 (1994) 39–44. doi:10.1016/0022-3115(94)90031-0.
- [9] R.G. Faulkner, S. Song, P.E.J. Flewitt, M. Victoria, P. Marmy, Grain boundary segregation under neutron irradiation in dilute alloys, *J. Nucl. Mater.* 255 (1998) 189–209. doi:10.1016/S0022-3115(98)00022-1.
- [10] R.G. Faulkner, S. Song, P.E.J. Flewitt, A model describing neutron irradiation-induced segregation to grain boundaries in dilute alloys, *Metall. Mater. Trans. A*. 27 (1996) 3381–3390. doi:10.1007/BF02595431.
- [11] R.G. Faulkner, N.C. Waite, E.A. Little, T.S. Morgan, Radiation-induced grain boundary segregation in dilute alloys, *Mater. Sci. Eng. A*. 171 (1993) 241–248. doi:10.1016/0921-5093(93)90411-7.
- [12] R.G. Faulkner, Combined grain boundary equilibrium and non-equilibrium segregation in ferritic/martensitic steels, *Acta Metall.* 35(1987) 2905–2914. doi:10.1016/0001-6160(87)90289-6.

- [13] Z. Lu, R.G. Faulkner, *Irradiation Assisted Grain Boundary Segregation in Steels*, Materials Research Society, Warrendale, 2008.
- [14] L. Messina, M. Nastar, P. Olsson, *Ab initio-based investigation of solute-dumbbell transport and radiation induced segregation in Fe-X (X= Cr, Cu, Mn, Ni, P, Si) dilute alloys*, 2015.
- [15] A. Barbu, A.B. Lidiard, *Solute segregation in dilute bcc alloys under irradiation*, *Philos. Mag. A.* 74 (1996) 709–722. doi:10.1080/01418619608243537.
- [16] C. Domain, C.S. Becquart, *Diffusion of phosphorus in  $\alpha$ -Fe: An ab initio study*, *Phys. Rev. B.* 71 (2005) 214109. doi:10.1103/PhysRevB.71.214109.
- [17] K.M. Miller, S.B. Fisher, R.J. White, *Interstitial loop growth in irradiated thin foils*, *J. Nucl. Mater.* 110 (1982) 265–276. doi:10.1016/0022-3115(82)90155-6.
- [18] G.S. Was, *Fundamentals of Radiation Materials Science: Metals and Alloys*, Springer Science & Business Media, 2007.
- [19] P.T. Heald, M.V. Speight, *Point defect behaviour in irradiated materials*, *Acta Metall.* 23 (1975) 1389–1399.
- [20] S.B. Fisher, R.J. White, K.M. Miller, *Quantitative analysis of void swelling in pure copper*, *Philos. Mag. A.* 40 (1979) 239–255. doi:10.1080/01418617908243101.
- [21] F. Laliberte, L. Boldon, L. Liu, *A Review of the Application of Rate Theory to Simulate Vacancy Cluster Formation and Interstitial Defect Formation in Reactor Pressure Vessel Steel.*, *J. Eng. Sci. Technol. Rev.* 8 (2015).
- [22] R. Bullough, M.H. Wood, *Mechanisms of radiation induced creep and growth*, *J. Nucl. Mater.* 90 (1980) 1–21. doi:10.1016/0022-3115(80)90241-X.
- [23] A.D. Brailsford, R. Bullough, M.R. Hayns, *Point defect sink strengths and void-swelling*, *J. Nucl. Mater.* 60 (1976) 246–256. doi:10.1016/0022-3115(76)90139-2.
- [24] T.M. Williams, A.M. Stoneham, D.R. Harries, *The segregation of boron to grain boundaries in solution-treated Type 316 austenitic stainless steel*, *Met. Sci.* 10 (1976) 14–19. doi:10.1179/030634576790431471.
- [25] R.G. Faulkner, *Non-equilibrium grain-boundary segregation in austenitic alloys*, *J. Mater. Sci.* 16 (1981) 373–383. doi:10.1007/BF00738626.
- [26] D. McLean, *Grain boundaries in metals*, Clarendon Press, 1957.
- [27] M. Guttman, *Equilibrium segregation in a ternary solution: A model for temper embrittlement*, *Surf. Sci.* 53 (1975) 213–227. doi:10.1016/0039-6028(75)90125-9.

- [28] L.E. Rehn, Production of freely-migrating defects, *J. Nucl. Mater.* 174 (1990) 144–150. doi:10.1016/0022-3115(90)90228-F.
- [29] L. Messina, M. Nastar, T. Garnier, C. Domain, P. Olsson, Exact ab initio transport coefficients in bcc Fe – X ( X = Cr , Cu , Mn , Ni , P , Si ) dilute alloys, *Phys. Rev. B.* 90 (2014). doi:10.1103/PhysRevB.90.104203.
- [30] L. De Schepper, D. Segers, L. Dorikens-Vanpraet, M. Dorikens, G. Knuyt, L.M. Stals, P. Moser, Positron annihilation on pure and carbon-doped  $\alpha$ -iron in thermal equilibrium, *Phys. Rev. B.* 27 (1983) 5257–5269. doi:10.1103/PhysRevB.27.5257.
- [31] A. Hardouin Duparc, C. Moingeon, N. Smetniansky-de-Grande, A. Barbu, Microstructure modelling of ferritic alloys under high flux 1 MeV electron irradiations, *J. Nucl. Mater.* 302 (2002) 143–155. doi:10.1016/S0022-3115(02)00776-6.
- [32] G.J. Ackland, M.I. Mendeleev, D.J. Srolovitz, S. Han, A.V. Barashev, Development of an interatomic potential for phosphorus impurities in  $\alpha$ -iron, *J. Phys. Condens. Matter.* 16 (2004) S2629–S2642. doi:10.1088/0953-8984/16/27/003.
- [33] A.D. Le Claire, G. Neumann, Diffusion in impurities in Solid Metallic Elements, in: *Diffus. Solid Met. Alloys*, Springer-Verlag, 1990.
- [34] C. Domain, C.S. Becquart, Ab initio calculations of defects in Fe and dilute Fe-Cu alloys, *Phys. Rev. B.* 65 (2001). doi:10.1103/PhysRevB.65.024103.
- [35] A.A. Vasiliev, V.V. Rybin, A.A. Zisman, The nature of the phosphorus atom mobility in bcc iron irradiated at low temperatures, *J. Nucl. Mater.* 231 (1996) 249–253. doi:10.1016/0022-3115(96)00201-2.
- [36] E. Meslin, C.-C. Fu, A. Barbu, F. Gao, F. Willaime, Theoretical study of atomic transport via interstitials in dilute Fe – P alloys, *Phys. Rev. B.* 75 (2007). doi:10.1103/PhysRevB.75.094303.
- [37] R.G. Faulkner, S.-H. Song, P.E.J. Flewitt, Determination of impurity–point defect binding energies in alloys, *Mater. Sci. Technol.* 12 (1996) 904–910. doi:10.1179/mst.1996.12.11.904.
- [38] K. Tapasa, A.V. Barashev, D.J. Bacon, Y.N. Osetsky, Computer simulation of carbon diffusion and vacancy–carbon interaction in  $\alpha$ -iron, *Acta Mater.* 55 (2007) 1–11. doi:10.1016/j.actamat.2006.05.029.
- [39] C. Domain, C.S. Becquart, J. Foct, Ab initio study of foreign interstitial atom (C, N) interactions with intrinsic point defects in  $\alpha$ -Fe, *Phys. Rev. B.* 69 (2004). doi:10.1103/PhysRevB.69.144112.
- [40] B.-J. Lee, A modified embedded-atom method interatomic potential for the Fe–C system, *Acta Mater.* 54 (2006) 701–711. doi:10.1016/j.actamat.2005.09.034.

- [41] H. Hurchand, S.D. Kenny, C.F. Sanz-Navarro, R. Smith, P.E.J. Flewitt, The influence of P solutes on an irradiated  $\alpha$ -Fe matrix, *Nucl. Instrum. Methods Phys. Res. Sect. B Beam Interact. Mater. At.* 229 (2005) 92–102. doi:10.1016/j.nimb.2004.11.010.
- [42] P. Paufler, R. W. Cahn, P. Haasen (eds). *Physical metallurgy 3rd revised and enlarged edition*. North-Holland physics publishing, (1985) 270–270. doi:10.1002/crat.2170200229.
- [43] M. Kiritani, H. Takata, K. Moriyama, F.E. Fujita, Mobility of lattice vacancies in iron, *Philos. Mag. A.* 40 (1979) 779–802.
- [44] L. Qingfen, Y. Shanglin, L. Li, Z. Lei, X. Tingdong, Experimental study on non-equilibrium grain-boundary segregation kinetics of phosphorus in an industrial steel, *Scr. Mater.* 47 (2002) 389–392. doi:10.1016/S1359-6462(02)00151-3.
- [45] H. Nakata, K. Fujii, K. Fukuya, R. Kasada, A. Kimura, Grain Boundary Phosphorus Segregation in Thermally Aged Low Alloy Steels, *J. Nucl. Sci. Technol.* 43 (2006) 785–793. doi:10.1080/18811248.2006.9711160.
- [46] S. Song, R.G. Faulkner, Diffusion Characteristics of Interstitial and Vacancy Based Complexes, *Defect Diffus. Forum.* 143–147 (1997) 149–154. doi:10.4028/www.scientific.net/DDF.143-147.149.
- [47] R.A. Johnson, N.Q. Lam, Solute segregation in metals under irradiation, *Phys. Rev. B.* 13 (1976) 4364–4375. doi:10.1103/PhysRevB.13.4364.
- [48] L. Messina, M. Nastar, N. Sandberg, P. Olsson, Systematic electronic-structure investigation of substitutional impurity diffusion and flux coupling in bcc iron, (2015).
- [49] Y. Katoh, T. Muroga, A. Kohyama, R.E. Stoller, C. Namba, Rate theory modeling of defect evolution under cascade damage conditions: the influence of vacancy-type cascade remnants on defect evolution, *J. Nucl. Mater.* 233–237 (1996) 1022–1028. doi:10.1016/S0022-3115(96)00088-8.
- [50] D. Meade, Grain boundary segregation of impurity elements in reactor pressure vessel steels, PhD thesis, Loughborough University, 1998. Available at: <https://dspace.lboro.ac.uk/dspace-jspui/handle/2134/16934> (accessed May 29, 2017).
- [51] R. Wu, A.J. Freeman, G.B. Olson, On the electronic basis of the phosphorus intergranular embrittlement of iron, *J. Mater. Res.* 7 (1992) 2403–2411. doi:10.1557/JMR.1992.2403.
- [52] N.R. Rhodes, M.A. Tschopp, K.N. Solanki, Quantifying the energetics and length scales of carbon segregation to  $\alpha$ -Fe symmetric tilt grain boundaries using atomistic simulations, *Model. Simul. Mater. Sci. Eng.* 21 (2013) 035009. doi:10.1088/0965-0393/21/3/035009.

- [53] P. Lejček, S. Hofmann, Segregation enthalpies of phosphorus, carbon and silicon at {013} and {012} symmetrical tilt grain boundaries in an Fe-3.5 at.% Si alloy, *Acta Metall. Mater.* 39 (1991) 2469–2476. doi:10.1016/0956-7151(91)90026-W.
- [54] S. Song, Z. Yuan, D. Shen, L. Weng, Effects of phosphorus grain boundary segregation and hardness on the ductile-to-brittle transition for a 2.25Cr1Mo steel, *J. Wuhan Univ. Technol.-Mater Sci Ed.* 22 (2007) 1–6. doi:10.1007/s11595-005-1001-x.
- [55] R.G. Faulkner, R.B. Jones, Z. Lu, P.E.J. Flewitt, Grain boundary impurity segregation and neutron irradiation effects in ferritic alloys, *Philos. Mag.* 85 (2005) 2065–2099. doi:10.1080/14786430412331331853.
- [56] Z. Lu, R.G. Faulkner, P.E.J. Flewitt, The role of irradiation-induced phosphorus segregation in the ductile-to-brittle transition temperature in ferritic steels, *Mater. Sci. Eng. A.* 437 (2006) 306–312. doi:10.1016/j.msea.2006.07.114.
- [57] L. Priester, *Grain boundaries from theory to engineering*, Springer, Dordrecht; New York, 2013.
- [58] T. Ogura, C.J. McMahon Jr., H.C. Feng, V. Vitek, Structure-dependent intergranular segregation of phosphorus in austenite in a Ni-Cr steel, *Acta Metall.* 26 (1978) 1317–1330. doi:10.1016/0001-6160(78)90147-5.
- [59] S. Suzuki, K. Abiko, H. Kimura, Phosphorus segregation related to the grain boundary structure in an Fe-P alloy, *Scr. Metall.* 15 (1981) 1139–1143. doi:10.1016/0036-9748(81)90175-7.
- [60] G.O. Williams, V. Randle, J.R. Cowan, P. Spellward, The role of misorientation and phosphorus content on grain growth and intergranular fracture in iron–carbon–phosphorus alloys, *J. Microsc.* 213 (2004) 321–327. doi:10.1111/j.0022-2720.2004.01301.x.
- [61] D.L. Medlin, K. Hattar, J.A. Zimmerman, F. Abdeljawad, S.M. Foiles, Defect character at grain boundary facet junctions: Analysis of an asymmetric  $\Sigma = 5$  grain boundary in Fe, *Acta Mater.* 124 (2017) 383–396. doi:10.1016/j.actamat.2016.11.017.
- [62] J.C. Russ, R.T. Dehoff, *Practical Stereology*, Springer US, Boston, MA, 2000. doi:10.1007/978-1-4615-1233-2.
- [63] M. Koiwa, H. Seyazaki, T. Ogura, A systematic study of symmetric tilt-boundaries in hard-sphere f.c.c. crystals, *Acta Metall.* 32 (1984) 171–182. doi:10.1016/0001-6160(84)90214-1.
- [64] C. Li, D.B. Williams, The relationship between grain-boundary structure and segregation in a rapidly solidified Fe-P alloy, *Philos. Mag.* 85 (2005) 2023–2032. doi:10.1080/14786430412331325030.

- [65] J.J. Bean, K.P. McKenna, Origin of differences in the excess volume of copper and nickel grain boundaries, *Acta Mater.* 110 (2016) 246–257. doi:10.1016/j.actamat.2016.02.040.
- [66] H.J. Frost, F. Spaepen, Hard Sphere models for the structure of grain boundaries, *J. Phys. Colloq.* 43 (1982) C6-73-C6-82. doi:10.1051/jphyscol:1982608.
- [67] D. Wolf, S. Yip, *Materials Interfaces: Atomic-level Structure and Properties*, Springer Science & Business Media, 1992.
- [68] D. Wolf, Structure and energy of general grain boundaries in bcc metals, *J. Appl. Phys.* 69 (1991) 185–196. doi:10.1063/1.347741.
- [69] M.A. Tschopp, D.L. McDowell, Asymmetric tilt grain boundary structure and energy in copper and aluminium, *Philos. Mag.* 87 (2007) 3871–3892. doi:10.1080/14786430701455321.
- [70] M.A. Tschopp, D.L. McDowell, Structural unit and faceting description of  $\Sigma 3$  asymmetric tilt grain boundaries, *J. Mater. Sci.* 42 (2007) 7806–7811. doi:10.1007/s10853-007-1626-6.
- [71] Y. Shibuta, S. Takamoto, T. Suzuki, A Molecular Dynamics Study of the Energy and Structure of the Symmetric Tilt Boundary of Iron, *ISIJ Int.* 48 (2008) 1582–1591. doi:10.2355/isijinternational.48.1582.
- [72] K.L. Merkle, D. Wolf, Low-energy configurations of symmetric and asymmetric tilt grain boundaries, *Philos. Mag. A.* 65 (1992) 513–530. doi:10.1080/01418619208201536.
- [73] A. Sutton, R. Balluffi, Overview no. 61 On geometric criteria for low interfacial energy, *Acta Metall.* 35 (1987) 2177–2201. doi:10.1016/0001-6160(87)90067-8.
- [74] W. Gui-Jin, V. Vitek, Relationships between grain boundary structure and energy, *Acta Metall.* 34 (1986) 951–960. doi:10.1016/0001-6160(86)90068-4.
- [75] D.N. Seidman, Subnanoscale Studies of Segregation at Grain Boundaries: Simulations and Experiments, *Annu. Rev. Mater. Res.* 32 (2002) 235–269. doi:10.1146/annurev.matsci.32.011602.095455.
- [76] V.R. Coffman, J.P. Sethna, Grain boundary energies and cohesive strength as a function of geometry, *Phys. Rev. B.* 77 (2008). doi:10.1103/PhysRevB.77.144111.
- [77] D. Wolf, Structure-energy correlation for grain boundaries in f.c.c. metals—IV. Asymmetrical twist (general) boundaries, *Acta Metall. Mater.* 38 (1990) 791–798. doi:10.1016/0956-7151(90)90031-B.
- [78] J. Li, S.J. Dillon, G.S. Rohrer, Relative grain boundary area and energy distributions in nickel, *Acta Mater.* 57 (2009) 4304–4311. doi:10.1016/j.actamat.2009.06.004.

- [79] H. Beladi, N.T. Nuhfer, G.S. Rohrer, The five-parameter grain boundary character and energy distributions of a fully austenitic high-manganese steel using three dimensional data, *Acta Mater.* 70 (2014) 281–289. doi:10.1016/j.actamat.2014.02.038.
- [80] E.R. Homer, S. Patala, J.L. Priedeman, Grain Boundary Plane Orientation Fundamental Zones and Structure-Property Relationships, *Sci. Rep.* 5 (2015) 15476. doi:10.1038/srep15476.
- [81] V.V. Bulatov, B.W. Reed, M. Kumar, Grain boundary energy function for fcc metals, *Acta Mater.* 65 (2014) 161–175. doi:10.1016/j.actamat.2013.10.057.
- [82] H.-K. Kim, W.-S. Ko, H.-J. Lee, S.G. Kim, B.-J. Lee, An identification scheme of grain boundaries and construction of a grain boundary energy database, *Scr. Mater.* 64 (2011) 1152–1155. doi:10.1016/j.scriptamat.2011.03.020.
- [83] B.P. Uberuaga, L.J. Vernon, E. Martinez, A.F. Voter, The relationship between grain boundary structure, defect mobility, and grain boundary sink efficiency, *Sci. Rep.* 5 (2015). doi:10.1038/srep09095.
- [84] F.J. Pérez-Pérez, R. Smith, Preferential damage at symmetrical tilt grain boundaries in bcc iron, *Nucl. Instrum. Methods Phys. Res. Sect. B Beam Interact. Mater. At.* 180 (2001) 322–328. doi:10.1016/S0168-583X(01)00439-6.
- [85] X.-M. Bai, B.P. Uberuaga, The Influence of Grain Boundaries on Radiation-Induced Point Defect Production in Materials: A Review of Atomistic Studies, *JOM.* 65 (2013) 360–373. doi:10.1007/s11837-012-0544-5.



## Conclusion and Perspectives

The main objective of the current PhD work was to develop and combine theoretical tools and experimental methods to quantify experimentally, understand mechanisms and model phosphorus intergranular segregations in steels as a function of grain boundary (GB) nature and ageing conditions (thermal ageing, irradiation). For a better understanding of the mechanisms and to simplify the identification of the influence of each parameter, a ternary model alloy (Fe – 0.034 at.% P – 0.01 at.% C) was investigated instead of complex commercial steel.

Atom Probe Tomography (APT) analysis of as-received material revealed the homogenous distribution of phosphorus and carbon atoms at the scale of an atom probe reconstructed volume. The bulk concentration of phosphorus and carbon varies from one volume to another, however the mean values ( $0.032 \pm 0.01$  at.% of phosphorus and  $0.007 \pm 0.004$  at.% of carbon) are close to the nominal composition.

All the samples were annealed at  $650^{\circ}\text{C}$  during 2 h. Such treatment was intended to simulate stress relieve heat treatment (SRHT), which is performed on RPV steel to decrease the residual stresses. To ensure that the equilibrium is reached after 2 h, a heat treatment in the same conditions but during 24 h was performed. After that, some samples were ion irradiated. The irradiations were performed at  $450^{\circ}\text{C}$  with 10 MeV  $\text{Fe}^{5+}$  ions under a flux of  $(1.2 \pm 0.4) \times 10^{11}$  ions/cm<sup>2</sup>/s. Three irradiation durations were used (2500s, 12500s, 25000s) which corresponds respectively to doses 0.075, 0.357 and 0.75 dpa at a sample depth of about 750 nm. To allow better differentiation between thermal and radiation-induced segregations in irradiated material, some other samples were thermally aged at the irradiation temperature ( $450^{\circ}\text{C}$ ) during 1000 h after SRHT.

After generalities on mechanisms of irradiation damage in Fe and Fe-based alloys and on structure of GBs in polycrystals in the chapter 1, the chapter 2 focusses on physical principles of different techniques namely: Atom Probe Tomography (APT), Scanning Transmission Electron Microscopy (STEM), Scanning Electron Microscopy (SEM), Focused Ion Beam (FIB), Electron Backscatter Diffraction (EBSD), Transmission Kikuchi Diffraction (TKD).

The main technique used in the current study is APT. This instrument provides the three dimensional distribution of phosphorus and carbon atoms at GB at atomic scale. However, the concentration profiles of carbon and phosphorus atoms across GB are biased by

some aberrations due to the field evaporation. The measured width of phosphorus intergranular segregation (8 atomic layers) is more than expected for equilibrium segregation (one or two atomic layers). It is supposed that the enlargement of the phosphorus intergranular segregation width is mainly caused by reconstruction artefacts. The lower evaporation field of Fe atoms at GB leads to an apparent higher atom density near GBs. At the same time, the higher evaporation field of solute atoms (phosphorus and carbon) results in an asymmetrical concentration profile across GBs. This interpretation of experimental observations was confirmed by the simulation of the field evaporation of a needle containing a GB. In order to minimize the influence of APT artifacts, the Gibbsian interfacial excess was measured and converted to a fraction of a monolayer, assuming that the phosphorus atoms reside in a single close-packed (110) plane of a BCC  $\alpha$ -iron.

The APT samples were prepared using SEM/FIB dual beam and TKD. The combination of the three-dimensional APT reconstruction with the TKD indexing allows to determine the five macroscopic degrees of freedom of a GB which are sufficient to give a complete geometrical description by the notation  $\theta^\circ [uvw](h_1k_1l_1)/(h_2k_2l_2)$ .

The chapter 3 is dedicated to equilibrium segregation of phosphorus and atoms to GBs in the Fe-0.034 at.% P-0.01 at.% C model alloy at 650°C (SRHT) and 450°C (thermal ageing). The APT analysis of the samples after annealing at 650° has established that:

- The equilibrium phosphorus segregation to HAGBs at 650°C is  $0.12 \pm 0.01$  monolayer coverage. The time needed to reach the equilibrium GB segregation is less than or equal to 2h.
- The carbon atoms can segregate to GBs during air-cooling from the high temperature (650°C), if the specimen size is big enough to decrease the cooling rate. The carbon intergranular segregation after air-cooling of the samples with the sizes of  $20 \times 20 \times 20 \text{ mm}^3$  and  $4 \times 4 \times 20 \text{ mm}^3$  is  $0.30 \pm 0.01$  and  $0.03 \pm 0.01$  monolayer coverage, respectively.

The measured phosphorus GB segregation after 1000 h of thermal ageing at 450°C is  $0.14 \pm 0.01$  monolayer. To know how far we are from equilibrium GB concentration the Guttman's model of equilibrium GB segregation was used. The thermodynamic parameters were taken from the works of Lejček and co-workers [1]. The model was first verified at 650°C. The predicted equilibrium phosphorus GB segregation at 650°C ( $0.21 \pm 0.01$  monolayer) was much higher than the experimentally observed ( $0.10 \pm 0.01$  monolayer). Since the parameters given by Lejček were obtained by AES experiments, while APT was used in the current work, it was decided to use both techniques to measure the GB segregation

in the same material. The comparative study of phosphorus intergranular segregation after SRHT at 650°C using APT and Auger Electron Spectroscopy (AES) has shown that the mean value of phosphorus GB segregation measured by AES is equal to  $(1.4 \pm 0.5)10^{14}$  atoms/cm<sup>2</sup>, which is in good agreement with the mean segregation of phosphorus at HAGBs obtained by APT ( $(1.6 \pm 0.7) 10^{14}$  atoms/cm<sup>2</sup>). These results confirm that the intergranular cracking in AES follows the GBs with the highest phosphorus segregation (i.e. the HAGB). ). Based on that fact, it was supposed that the difference between theoretical prediction and experimental data is a result of GB segregation quantification. In the current work, the Gibbsian interfacial excess measured by APT is converted to a fraction of a monolayer, assuming that the phosphorus atoms reside in a single close-packed (110) plane of BCC  $\alpha$ -iron, while Lejcek et al. have estimated the atomic density of GB plane from AES analysis of pure iron surface [2]. Since the (110) plane is the highest density plane in a bcc iron, our assumption underestimates the phosphorus GB segregation.

The Guttman's model for equilibrium intergranular segregation in multicomponent system was applied to the Fe-0.034 at.% P-0.01 at.% C model alloy. The thermodynamic parameters were calculated using Lejcek's model for the segregation enthalpy and entropy at different GBs (special, vicinal, general). The final expression for temperature dependence of the free Gibbs energy of phosphorus segregation at general GBs in BCC iron is  $\Delta G_P = -27000 - 21.5 \cdot T + 7000 \cdot (C_C^\phi(T) - C_C^B)$ , where  $C_C^\phi(T)$  and  $C_C^B$  are the carbon concentration at GB and in the bulk, respectively. The phosphorus-carbon interaction coefficient was taken from the literature. The interaction is reported as repulsive. However, the nature of this repulsive interaction isn't clear. Is it the chemical repulsive forces or site competition between phosphorus and carbon atoms? Since there is no experimental high-resolution observation of the phosphorus segregation at GB in BCC iron, allowing us to distinguish undoubtedly the position of phosphorus atoms (interstitial or substitutional) the problem remains open. The atomic-scale simulation of phosphorus segregation at GBs in BCC iron using the Quasi particle Approach (QA) [3] performed by Antoine Vaugeois (GPM, Rouen) has shown that the phosphorus atoms initially situated in the lattice positions can move to the interstitial sites close to the GB. Thus, the simulation showed us that the phosphorus can segregate interstitially. However, other questions are still open. Does the position of phosphorus atoms in GB depend on the annealing temperature? Could phosphorus atoms situated both at substitutional and interstitials sites? How they interact with carbon atoms?

However, as the repulsive interaction between phosphorus and carbon atoms at GB was repeatedly observed in the literature [4–9] and since, according to the QA simulation, the interstitial segregation of phosphorus is energetically favorable, both repulsive interaction and site competition between phosphorus and carbon atoms at GB were taken into account in modeling. The theoretical value of equilibrium GB segregation of phosphorus at 450°C is equal to  $0.17 \pm 0.02$  monolayer, which is slightly higher than the values measured by APT after 1000 h of ageing ( $0.14 \pm 0.01$  monolayer). This observation is coherent with the calculations of phosphorus intergranular segregation kinetics which has shown that the time needed to reach the equilibrium phosphorus GB segregation at 450°C in the Fe-0.034 at.% P-0.01 at.% C model alloy is about 3000h (or 125 days).

The study of equilibrium phosphorus segregation after SRHT and thermal ageing at irradiation temperature was important to separate the different contributions of phosphorus intergranular segregation in irradiated samples.

The Chapter 4 reports on the characterization of intergranular segregation of phosphorus after self-ion irradiation of Fe-0.034 at.% P-0.01 at.% C model alloy up to 0.75 dpa and its possible relationship with GB crystallography.

The APT analysis of the model alloys after ion irradiation up to 0.75 dpa has shown that:

- The mean level of phosphorus segregated at GB increases with irradiation dose (respectively  $0.22 \pm 0.05$ ,  $0.29 \pm 0.08$  and  $0.36 \pm 0.14$  monolayer for 0.075 dpa, 0.38 dpa and 0.75 dpa).
- Irradiation dose has no effect on the level of carbon GB segregation ( $0.20 \pm 0.05$ ,  $0.20 \pm 0.06$  and  $0.19 \pm 0.04$  monolayer after irradiation to 0.075 dpa, 0.38 dpa and 0.75 dpa, respectively)

The phosphorus segregation at high-angle GBs in all irradiated samples is larger than the equilibrium GB segregation of phosphorus at the same temperature ( $0.17 \pm 0.02$  monolayer). The excess of phosphorus atoms over the equilibrium GB segregation would suggest the presence and influence of flux coupling between supersaturated point defects and phosphorus atoms, i.e. a radiation-induced segregation (RIS) mechanism.

A few APT experiments revealed phosphorus clustering and segregation on dislocation lines. STEM study has shown that during 10 MeV Fe<sup>5+</sup> ion irradiation at 450°C of the Fe-0.034 at.% P-0.01 at.% C model alloy up to 0.75 dpa, irradiation damage becomes apparent in the form of a dislocation array and voids down to 2 μm depth. The number density

of dislocations and voids were measured and included in the total sink strength, which appears in the radiation-induced segregation model.

Further modeling of RIS in the Fe-0.034 at.% P-0.01 at.% C model alloy under given irradiation conditions has demonstrated that:

- The radiation-induced segregation (RIS) caused by phosphorus-interstitial complex diffusion is absolutely dominant below approximately 500°C and the radiation-enhanced segregation dominates above this temperature. The segregation peak occurs in a temperature range between 400 and 450°C.
- The irradiation at 450°C using 10 MeV Fe<sup>5+</sup> ions at a dose rate  $3.0 \times 10^{-5}$  dpa/s results in the RIS of phosphorus to GB, however, the radiation-enhanced mechanism also participate.

RIS model of Faulkner together with experimental data from thermally aged samples allows to us to distinguish the nature of phosphorus segregation at GBs. For instance, the total amount of phosphorus segregation at 43°[100] (11-1)/(3-50) GB is ~ 0.36 monolayers. Among them, ~ 0.12 monolayers (~ 30% from the total amount) was segregated during stress relieve heat treatment, ~ 0.04 monolayers (~ 10% from the total amount) is the radiation-enhanced segregation via the vacancy mechanism, and ~ 0.20 monolayers (~ 60% from the total amount) is radiation-induced segregation via phosphorus-interstitial complex diffusion.

The experimental evidence of higher RIS of phosphorus at curved GBs than at straight one was shown. Also, it was demonstrated that larger phosphorus segregation occurs at GBs with high Miller index planes, while the segregation is low for those with low index planes.

Based on a literature review and our experimental results, it can be said that there is no simple rule to link a GB geometrical parameter to its segregation level. The complicated structure of real GBs in polycrystal (5 DOFs, GB curvature, faceting) requires more powerful instruments, such as computer simulation, which can reconstruct any structure and give large statistics. But to support or assess these predictions, experimental studies at the same scale, i.e. atomic scale, of grain boundaries with complete description of their structures and chemistries are needed. We believe that this work is one of these supports, and the methodology to perform systematic analysis of grain boundaries (GB structure, quantitative measurement of segregations) will be applied to the further works.

## References

- [1] P. Lejček, *Grain Boundary Segregation in Metals*, Springer Berlin Heidelberg, Berlin, Heidelberg, 2010.
- [2] P. Lejček, Characterization of grain boundary segregation in an Fe-Si alloy, *Anal. Chim. Acta.* 297 (1994) 165–178. doi:10.1016/0003-2670(93)E0388-N.
- [3] M. Lavrskyi, H. Zapolsky, A.G. Khachatryan, Quasiparticle approach to diffusional atomic scale self-assembly of complex structures: from disorder to complex crystals and double-helix polymers, *Npj Comput. Mater.* 2 (2016). doi:10.1038/npjcompumats.2015.13.
- [4] H. Hänsel, H.J. Grabke, Grain boundary segregation of phosphorus and carbon in ferritic iron, *Scr. Metall.* 20 (1986) 1641–1644. doi:10.1016/0036-9748(86)90411-4.
- [5] H.J. Grabke, *Surface and Grain Boundary Segregation on and in Iron and Steels*, *ISIJ Int.* 29 (1989) 529–538. doi:10.2355/isijinternational.29.529.
- [6] H. Erhart, H.J. Grabke, Equilibrium segregation of phosphorus at grain boundaries of Fe–P, Fe–C–P, Fe–Cr–P, and Fe–Cr–C–P alloys, *Met. Sci.* 15 (1981) 401–408. doi:10.1179/030634581790426877.
- [7] W. Wei, H.J. Grabke, The effect of alloying elements on the grain boundary segregation of phosphorus in iron and the intergranular corrosion of the Fe–P system, *Corros. Sci.* 26 (1986) 223–236. doi:10.1016/0010-938X(86)90057-0.
- [8] K. Ebihara, M. Yamaguchi, Y. Nishiyama, K. Onizawa, H. Matsuzawa, Effect of carbon on irradiation-induced grain-boundary phosphorus segregation in reactor pressure vessel steels using first-principles-based rate theory model, *J. Nucl. Mater.* 414 (2011) 328–335. doi:10.1016/j.jnucmat.2011.05.001.
- [9] S. Suzuki, M. Obata, K. Abiko, H. Kimura, Effect of carbon on the grain boundary segregation of phosphorus in  $\alpha$ -iron, *Scr. Metall.* 17 (1983) 1325–1328. doi:10.1016/0036-9748(83)90225-9.

# Appendices

## Appendix 1. Field evaporation model

A model simulating the field evaporation of surface atoms of thin needle and their subsequent trajectories from toward a detector was developed at GPM by F. Vurpillot and M. Gruber [1,2]. It represents the atom probe tip as a stack of atoms in the shape of cylinder terminated by a hemispherical cap of radius  $R$ . The tip is subjected to an electric potential,  $V_0$ . Far from the tip, an electrode is placed with a potential equal to 0.

The distribution of the electric potential around simulated volume can be calculated by numerically solving the Laplace equation using a finite difference algorithm:

$$\Delta V = 0 \quad (123)$$

The space between the tip and electrode is divided into a regular cubic grid of discrete points. Each points is defined by its coordinates  $i, j$  and  $k$ . The potential in each point is noted  $V_{i,j,k}$ . For each point, the local Laplace equation is solved. Thus, the value of the potential at each point is determined by the six first neighbors of this point,

$$V_{i,j,k} = \frac{1}{6} (V_{i+1,j,k} + V_{i-1,j,k} + V_{i,j+1,k} + V_{i,j-1,k} + V_{i,j,k+1} + V_{i,j,k-1}) \quad (124)$$

This condition has to be satisfied in each point above the tip surface. The electric field distribution near the surface was then derived ( $E = -\nabla V$ ).

In order to represent a thermally activated process of evaporation, the atom to be evaporated is chosen via a residence time algorithm [3]. The choice of the evaporated atom is obtained by calculating the relative rate of evaporation for every atom,

$$k_i^r = \frac{K_i}{\sum_{S=1}^N K_S} \quad (125)$$

where the  $K_i$  is the probability of evaporation for atom  $i$  and  $\sum_{S=1}^N K_S$  is the sum of evaporation probability for all atoms. Then, these relative evaporation rates are cumulated in a list in order to have a segment of probability of length equal to unity ( $\sum k_i^r = 1$ ). Therefore, a given atom is defined by a part of segment of length  $k_i^r$ . Then a random atom  $i$  from the section  $[0,1]$  is chosen to be field evaporated. The probability to have an atom with the highest rate  $k_i$  is high, but not systematic.

The trajectories of ions are calculated by using the first principle of dynamics ( $F = eE = m \frac{d^2 r}{dt^2}$  with  $E(E_x, E_y, E_z)$ ). An iterative algorithm with a first-order approximation

is applied. The components of the position vector  $r(x, y, z)$  at time  $t$  within very small interval  $\delta t$  may be defined as:

$$x(t + \delta t) \cong x(t) + v_x(r, t)\delta t \quad (126)$$

Expressions of  $y$  and  $z$  are similar to that of  $x$ .  $v_x, v_y$  and  $v_z$  are the components of the velocity vector  $v$ :

$$v_x(r, t + \delta t) \cong v_x(r, t) + e/mE_x(r)\delta t \quad (127)$$

$v_y, v_z$  are written in a similar way.

More details about the model can be found in ref [1,2,4].

The ion trajectories allow to calculate the coordinates of the impact on the virtual detector. So that a dataset similar to the one of a real APT analysis is obtained and can be treated with the same tools that for actual experiments.

## Appendix 2: Nanoscale secondary ion mass spectrometry

This study combines Atom Probe Tomography and Transmission Kikuchi Diffraction techniques to reveal the GB structure – solute segregation relationship in a Fe-0.034 at.%P-0.01 at.%C model alloy. TKD is used to characterize the grain boundary geometry. APT is used to characterize GB segregation in three dimensions at near-atomic scale. However, APT is limited by a small analysis volume ( $\sim 100 \times 100 \times 300 \text{ nm}^3$ ) and the difficult and time-consuming specimen preparation (using dual-beam focused-ion-beam (FIB)/scanning electron microscope (SEM)), which restricts the number of investigated GBs.

Nanoscale Secondary Ion Mass Spectrometry (NanoSIMS) technique is supposed to be used for improving the statistics of measurements. NanoSIMS has an advantage of analyzing a larger surface (tens of square micrometers) with very high sensitivity (down to atom ppb in favorable cases) and high resolution (down to 50 nm).

The physical principle of SIMS is presented in Fig. A.1. NanoSIMS directs a focused ion beam (typically in the 0.1-50 keV range [5]) at the solid's surface of interest. These ions, defined as primary ions, create a collision cascade in the target. As a result, atoms near the surface are sputtered. A small fraction of sputtered atoms (between  $10^{-5}$  to  $10^{-2}$  [6]) are ionized. The sputtered and ionized atoms are referred as “secondary ions”.

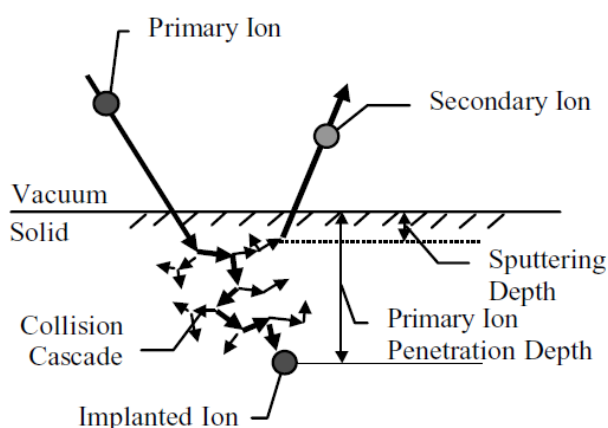


Fig. A.1. The physical principle of SIMS. Impacting primary ions on a sample surface create the collision cascade with displaced atoms. Some of these secondary atoms are ionised and leave the surface [7]

These are focused by a magnetic field and directed into a mass spectrometer. Thus, for a given number of primary ions impacting the surface per second, a number of secondary ions of a given isotope reaches the detector and is counted each second [6].

In this work, NanoSIMS analyses were performed using the Cameca NanoSIMS 50. A focused 16 keV  $\text{Cs}^+$  primary ion beam scanned over the surface of the sample and sputtered negative secondary ions. Secondary ions were detected on four detectors simultaneously for the four following ions:  $^{16}\text{O}^-$ ,  $^{12}\text{C}^-$ ,  $^{31}\text{P}^-$  and  $^{54}\text{Fe}^{16}\text{O}^-$ .

In order to get quantitative information, the method proposed by F. Christien and co-workers was used [8]. They investigated the sulphur segregation in Ni-S alloy and found a linear correlation between the sulphur bulk concentration and the measured intensity of the  $^{32}\text{S}^-$  ion. Thus, the concentration of solute in a GB,  $C_{GB}$ , can be found using one standard sample and the following proportional equation:

$$C_{GB} = \frac{I_{GB}}{I_{std}} C_{std} \quad (128)$$

where  $I_{GB}$  is the signal intensity at GB,  $C_{std}$  is the known solute concentration of the standard material and  $I_{std}$  is in the signal intensity obtained from the standard material.

According to this method, the signal of  $^{31}\text{P}^-$  ion were acquired on the three Fe-xP model alloys (where  $x = 0.016, 0.034, 0.074$  at.%). The summed counts for individual raster scans (raster size is  $20 \times 20 \mu\text{m}$ ) were recorded until steady-state of the signal reached (Fig. A.2).

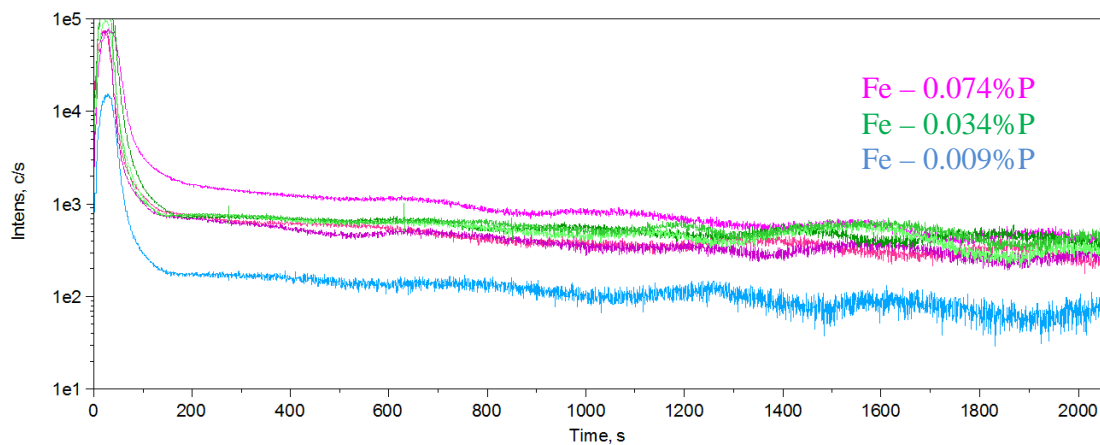


Fig. A.2. Intensity of  $^{31}\text{P}^-$  signal as a function of time on the Fe- xP alloys ( $x=0.016, 0.034, 0.074$  at.%). Sputtered area:  $20 \times 20 \mu\text{m}$ . Primary beam current: 90 pA

The correlation graph between steady-state  $^{31}\text{P}^-$  intensity (counts/sec) and phosphorus concentration (at. %) in a bulk was plotted (Fig. A.3). It was found the reasonable proportionality between phosphorus bulk concentration and  $^{31}\text{P}^-$  steady-state signal averaged over different grains.

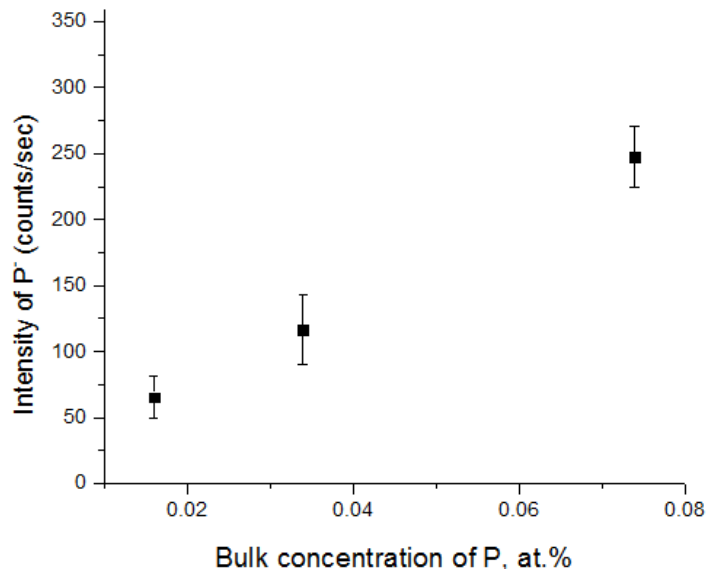


Fig. A.3. Steady-state  $^{31}\text{P}^-$  intensity versus P concentration obtained from NanoSIMS measurement for Fe-xP model alloys with  $x = 0.016, 0.034, 0.074$  at.%

Since the dependence of the signal intensity from the bulk concentration is linear, concentration of phosphorus at GB can be found using equation (128). In our case the standard and analysed samples are the same, thus equation (128) transform to

$$C_{GB} = \frac{I_{GB}}{I_{bulk}} C_{bulk} \quad (129)$$

where  $C_{bulk}$  is the bulk concentration

In order to quantify the GB segregation, the NanoSIMS mapping was done. A  $256 \times 256$  pixel images were acquired by rastering the primary beam over the sample surface, recording the number of secondary ion counts within the defined dwell time at each pixel. The images of GB area were recorded with different sets of parameters (dwell time (0.5...15 ms/sec), aperture size (100...500  $\mu\text{m}$ ), primary beam current (1...2 pA)). Image processing was carried out using ImageJ software (U.S. National Institutes of Health, Bethesda, MD), using the OpenMIMS plugin (National Resource for Imaging Mass Spectrometry, Harvard University, Cambridge, MA), to extract deadtime-corrected data from linear profiles drawn onto the images.

However, no segregation of phosphorus or carbon could be detected in the GB, indicating that the segregation of phosphorus is below the detection limit of NanoSIMS at this condition. Despite of that, we suppose that the similar approach can be used to study and quantify the intergranular segregation in microscale.

## References

- [1] F. Vurpillot, Etude de la fonction de transfert pointe -image en sonde atomique tomographique. PhD thesis, Université de Rouen, 2001.
- [2] M. Gruber, Etude de l'évaporation par effet de champ en sonde atomique tomographique: application à la métrologie de l'instrument. PhD thesis, Université de Rouen, 2012.
- [3] A.B. Bortz, M.H. Kalos, J.L. Lebowitz, A new algorithm for Monte Carlo simulation of Ising spin systems, *J. Comput. Phys.* 17 (1975) 10–18. doi:10.1016/0021-9991(75)90060-1.
- [4] D. Blavette, F. Vurpillot, P. Pareige, A. Menand, A model accounting for spatial overlaps in 3D atom-probe microscopy, *Ultramicroscopy*. 89 (2001) 145–153. doi:10.1016/S0304-3991(01)00120-6.
- [5] P. van der Heide, *Secondary Ion Mass Spectrometry: An Introduction to Principles and Practices*, John Wiley & Sons, Hoboken, USA, 2014. doi:10.1002/9781118916780.
- [6] P. Hoppe, S. Cohen, A. Meibom, NanoSIMS: technical aspects and applications in cosmochemistry and biological geochemistry, *Geostand. Geoanalytical Res.* 37 (2013) 111–154.
- [7] D.S. McPhail, Applications of Secondary Ion Mass Spectrometry (SIMS) in Materials Science, *J. Mater. Sci.* 41 (2006) 873–903. doi:10.1007/s10853-006-6568-x.
- [8] F. Christien, C. Downing, K.L. Moore, C.R.M. Grovenor, Quantification of grain boundary equilibrium segregation by NanoSIMS analysis of bulk samples, *Surf. Interface Anal.* 44 (2012) 377–387. doi:10.1002/sia.4806.

# Résumé

L'objectif principal de ce travail de thèse était de développer et de combiner des outils théoriques et des méthodes expérimentales pour quantifier expérimentalement, comprendre les mécanismes et modéliser la ségrégation intergranulaire du phosphore dans les alliages ferritiques en fonction de la nature des joints de grains (GB) et des conditions de vieillissement (vieillissement thermique ou irradiation). Pour une meilleure compréhension, et pour faciliter l'identification des paramètres pertinents, un alliage modèle ternaire (Fe-0.034 at.% P-0.01 at.% C) a été étudié. Pour étudier efficacement les mécanismes de ségrégation intergranulaire, il est nécessaire de combiner des techniques complémentaires permettant une description précise et représentative des joints de grains avant et après vieillissement. Il s'agit de l'objectif principal de la thèse. Le second objectif est d'appliquer l'approche ainsi développée à l'étude de l'influence des conditions de vieillissement et de la géométrie des joints de grains sur la ségrégation intergranulaire dans l'alliage modèle vieilli thermiquement ou irradié aux ions. Le troisième objectif est d'étudier la ségrégation intergranulaire du phosphore à l'équilibre et hors-équilibre afin d'améliorer la prédictibilité de la fragilisation sous irradiation des aciers de cuve des réacteurs à eau sous pression (PWR).

Tous les échantillons ont préalablement été recuits à 650°C pendant 2h. Ce traitement vise à simuler un traitement thermique de relaxation des contraintes (SHRT), utilisé sur les aciers de cuve des PWR. Pour s'assurer que l'équilibre est atteint après 2h, un traitement thermique dans les mêmes conditions, mais de 24h, a été réalisé. Après ça, une partie des échantillons a été irradiée aux ions. Les irradiations ont été réalisées à 450°C avec des ions Fe<sup>5+</sup> de 10 MeV sous un flux de  $(1.2 \pm 0.4) \times 10^{11}$  ions/cm<sup>2</sup>/s. Trois durées d'irradiation ont été retenues (2500s, 12500s, 25000s) correspondant respectivement à des doses de 0.075, 0.36 et 0.75 dpa à une profondeur d'environ 750 nm. Pour permettre une meilleure différenciation entre la contribution de la température et celle de l'irradiation à la ségrégation intergranulaire, une autre partie des échantillons a subi un vieillissement thermique à la température d'irradiation (450°C) pendant 1000 h.

Le chapitre 1 décrit tout d'abord de manière générale les mécanismes d'endommagement sous irradiation dans le fer et alliages ferreux. La structure de joints de grains dans les polycristaux est ensuite présentée. Enfin, le chapitre se concentre sur les principes physiques des différentes techniques d'analyse utilisées dans ce travail: Sonde Atomique Tomographique (APT), Microscopie Électronique en Transmission à Balayage (STEM), Microscopie

Électronique à Balayage (SEM), Faisceau d'Ions Focalisés (FIB), Diffraction des Électrons Rétrodiffusés (EBSD) et Diffraction de Kikuchi en Transmission (TKD).

La technique principale de ce travail est l'APT. Cet instrument permet d'obtenir une représentation à l'échelle atomique en 3 dimensions de la distribution du phosphore et du carbone aux joints de grains. Les échantillons d'APT sont préparés en utilisant un SEM/FIB couplées à la TKD. La combinaison de la reconstruction 3D obtenues par APT avec l'indexation des grains déterminée par TKD permet de déterminer les cinq degrés de liberté macroscopiques d'un joint de grain, ce qui suffit à avoir une description géométrique complète. Un GB est ainsi défini par la notation  $\theta^\circ[uvw](h_1k_1l_1)/(h_2k_2l_2)$ .

Le chapitre 3 est dédié à la ségrégation intergranulaire du phosphore à l'équilibre dans l'alliage modèle Fe-0.034 at.% P-0.01 at.% à 650°C (SRHT) et à 450°C (vieillessement thermique). L'analyse par APT des échantillons après recuit à 650°C montre que le taux de recouvrement d'une monocouche par le phosphore dans les joints de forte désorientation est de  $0.12 \pm 0.01$  à 650°C. Les résultats de sonde atomique obtenus sur les GB de forte désorientation à 650°C ont été comparés à des mesures de Spectroscopie des Electrons Auger (AES). Les valeurs mesurées par AES et APT sont en très bon accord, respectivement  $(1.4 \pm 0.5)10^{14}$  atomes/cm<sup>2</sup> et  $(1.6 \pm 0.7) 10^{14}$  atomes/cm<sup>2</sup>.

Le modèle de Guttman a ensuite été utilisé pour déterminer le taux de ségrégation du phosphore à l'équilibre à 450°C. Les paramètres thermodynamiques de ce modèle ont été ajustés sur des données de la littérature obtenues par (AES). La valeur théorique de ségrégation à l'équilibre du phosphore dans les joints de grains à 450°C est égale à  $0.17 \pm 0.02$  monocouche, ce qui est significativement plus élevé que les valeurs mesurées par APT après 1000 h de vieillissement ( $0.14 \pm 0.01$  monocouche). Cette observation est cohérente avec les calculs de la cinétique de ségrégation intergranulaire du phosphore qui montrent que le temps nécessaire pour atteindre l'équilibre à 450°C dans l'alliage modèle Fe-0.034 at.% P-0.01 at.% C est d'environ 3000h (125 jours).

L'étude de la ségrégation à l'équilibre du phosphore après SRHT et vieillissement thermique à température d'irradiation était importante pour séparer les différentes contributions à la ségrégation intergranulaire du phosphore dans les échantillons irradiés.

Le chapitre 4 présente les résultats obtenus sur la ségrégation intergranulaire du phosphore après irradiation aux ions fer de l'alliage modèle Fe-0.034 at.% P-0.01 at.% C jusqu'à 0.75 dpa. Les relations entre le taux de ségrégation hors équilibre et la géométrie des joints de grains sont également abordées.

L'analyse APT de l'alliage modèle après irradiation ionique jusqu'à 0.75 dpa a montré que le niveau moyen de ségrégation du phosphore dans les joints de grains augmente avec la dose d'irradiation. La dose d'irradiation n'a pas d'effet sur le niveau de ségrégation du carbone.

La ségrégation du phosphore aux joints de grains de forte désorientation dans les échantillons irradiés est systématiquement plus importante que la ségrégation du phosphore à l'équilibre à la même température ( $0.17 \pm 0.02$  monocouche). L'excès d'atomes de phosphore suggère l'existence d'un couplage entre les flux de défauts ponctuels sursaturés et des atomes de phosphore. Autrement dit, un mécanisme de ségrégation induite par l'irradiation (RIS) semble contribuer à la ségrégation intergranulaire du phosphore dans ces conditions d'irradiation.

Pour avoir une meilleure compréhension des mécanismes de ségrégation intergranulaire, le modèle de RIS développé par Faulkner a été appliqué à l'alliage modèle Fe-0.034 at.% P-0.01 at.% C irradié aux ions. La modélisation a montré que la RIS résultant de la diffusion du complexe phosphore-interstitiel est largement dominante pour des températures inférieures à 500°C, dans les conditions d'irradiation utilisées ici. Le maximum de ségrégation apparaît dans une gamme de température située entre 400 et 450°C.

Compte tenu des données de la littérature et de nos résultats expérimentaux, il apparaît qu'il n'y a pas de règle simple pour relier un paramètre géométrique du joint de grains à son taux de ségrégation. La structure complexe des joints de grains (5 degrés de liberté, courbature, facettage) requiert des instruments tels que la simulation numérique afin prédire au mieux la ségrégation intergranulaire en fonction de la structure des GB. Ces calculs doivent s'appuyer sur des études expérimentales à la même échelle, fournissant à la fois une description complète de la structure des GB et leur chimie. Nous pensons que ce travail est un de ces supports, et que la méthodologie pour réaliser des études systématiques des joints de grains (structure, mesures quantitatives de ségrégation) sera utilisée dans de futurs travaux.

